Photo-engineered Optoelectronic Properties of Transparent Conductive Oxides *via* Reactive Laser Annealing (ReLA): The Consequence of Defects.

JAMES ARTHUR HILLIER

A thesis submitted in partial fulfilment of the requirements of Nottingham Trent University for the degree of Doctor of Philosophy

School of Science and Technology

Nottingham Trent University

September 2021

Copyright Statement

The copyright in this work is held by the author. You may copy up to 5% of this work for private study, or personal, non-commercial research. Any re-use of the information contained within this document should be fully referenced, quoting the author, title, university, degree level and pagination. Queries or requests for any other use, or if a more substantial copy is required, should be directed to the author.

Abstract

The ongoing development of nanofabrication capabilities ever increases our ability to exploit the light-matter interactions occurring on the nanoscale, promising radical breakthroughs in many technological sectors. This research field, namely plasmonics, faces a major roadblock in respect to realistic applications. Specifically, to translate the potential of plasmonics into practical optical devices, the right set of materials are required; materials that can overcome the loss issue and expand the operational window towards the infrared and (IR) near-IR (NIR) spectral ranges. Transparent conductive oxides (TCOs) are appealing alternatives due to their transparency, refractory character, and maturity in electronic devices. Importantly, their non-stoichiometric character allows for the modulation of their optoelectronic properties through the manipulation of their defects. This research developed the knowledge of the optoelectronic properties of TCOs, *via* spectroscopic ellipsometry (SE) while examining high-throughput methods to tune their transport properties towards the requirements of IR plasmonics. Specifically, this research investigated, for the first time, the utility of reactive laser annealing (ReLA) to probe the crystal structure and donor state variations of sputtered tin-doped indium oxide (ITO) thin films. The demonstration of ReLA comprised an investigation of the role of the laser processing parameters (*e.g.,* laser fluence, number of pulses and ambient composition) with an extensive characterisation methodology comprising: four-point probe, Hall Effect, X-ray diffractometry, energy-dispersive X-ray spectroscopy and X-ray photon spectroscopy. In this way, ReLA is established as a novel and versatile tool to tailor the properties of TCO films towards the requirements of potential plasmonic applications. Furthermore, SE in the wide spectral range between $0.034 - 6.5\ \mathrm{eV}$ was employed to get insights on the properties of seed TCO films and the laser-induced modifications, revealing how and why TCOs present challenges both for further elucidating the still not fully known mechanisms that govern their optoelectronic behaviour and for their integration into far-IR plasmonic devices.

Acknowledgements

First and foremost, I would like to thank my Director of Studies and mentor, Dr. Nikolaos Kalfagiannis for giving me this opportunity to perform this research and for his guidance, insights, and unwavering support in this journey. His efforts have not only contributed greatly to the achievements of this work but to my development as a researcher and Greek-speaking άνθρωπος. To my 2nd supervisor, Dr. Demosthenes Koutsogeorgis, I give special thanks for his constant supervision, encouragement, and patience and for handing me the tools (both literally and figuratively) to thrive in a lab.

My sincere gratitude is also extended to our collaborators across the world, without whom this research would not have been possible: Associate Prof. Christopher Mellor at the University of Nottingham – UK, for providing access, training and supervision for the use of the NIR-VIS-UV spectroscopic ellipsometry (SE) system, Prof. Wayne Cranton and Prof. Alexei Nabok at Sheffield Hallam University – UK, for providing access, training and supervision for the use of the Hall Effect and NIR-VIS SE systems', Prof. Sophie Camelio at the Université de Poitiers – France, for providing access to their ellipsometry suite and finally Prof. Panos Patsalas at the Aristotle University of Thessaloniki – Greece, for performing the measurements and subsequent back-ground removal and peak fitting for X-ray photoelectron spectroscopy and for his insights and offered guidance. I would also like to thank the experts in ellipsometry at J. A. Woollam (Andrew Martin, Dr. Tom Tiwald, Dr. Joel Mohrmann and Dr. Ron Synowicki) for their provision of the CompleteEASE™ software beta with IR capabilities and for their collaboration and insights into the finer details of SE.

I would like to express my sincere gratitude to my comrades at iSMART and MTIF, new and old (in order of appearance, no favourites!): Dr. Jacob Spear, Chris Mutton, Dr. Henry Pegram, Dr. Joseph Pally, Dr. Neranga Abeywickrama, Dr. Gary Mudd, Jodie West, Ryan Toms, Michael Brown, Christina Koutsiaki, Luke Blyth, Josh Barkby, Matthew Spink, and Thomas Howe, for their support, friendship, advice, cathartic moaning sessions and intermittent celebrations. For Jodie specifically, thanks for allowing me to make your home all sticky and for Christina, well, τα ξέρεις.

Finally, it would be amiss not to thank my family and of course, my fellow shire-folk: Ginger, Rolando Bloom, Burney, Martini, Killjoy, Yazmin Rice, The perfectly candid man, The Friday Prince, Benji, I'm Dave Lewzey, Yoshi, Brian's lodger, Claire, Michelle, Player, Paddington Bear, Fierce Peirce and Scatty Patty for simply being awesome, unapologetically making me who I am (*i.e.* blame them), bearing with me becoming a bit of a ghost these past few years and, hopefully, being there on the road ahead, no matter where we might be swept off to.

"We are the wood elves".

List of Publications

List of Journal Papers

1. Kalfagiannis, N., Stoner, J. L., **Hillier, J.**, Vangelidis, I. and Lidorikis, E. Mid- to far-infrared sensing: SrTiO3, a novel optical material. J. Mater. Chem. C 7, 7851–7857 (2019).
2. **J. A. Hillier,** S. Camelio, W. Cranton, A. Nabok, C. J. Mellor, D. C. Koutsogeorgis and N. Kalfagiannis. When Ellipsometry Works Best: A Case Study with Transparent Conductive Oxides, ACS Photonics. 7, 10 (2020).

List of Journal Papers under preparation

1. **J. A. Hillier,** P. Patsalas, S. Camelio, W. Cranton, A. Nabok, C. J. Mellor, D. C. Koutsogeorgis and N. Kalfagiannis. “Photo-engineered optoelectronic properties of indium tin oxide *via* reactive laser annealing (ReLA): the consequence of defects”. *To be submitted in Applied Surface Science, November 2021.*
2. **J. A. Hillier,** S. Camelio, W. Cranton, A. Nabok, C. J. Mellor, D. C. Koutsogeorgis and N. Kalfagiannis. “Ultrafast Multi-Beat Reactive Laser Annealing (UMBReLA) – Tailoring TCOs towards IR plasmonic applications”. *To be submitted in Optical Materials Express, December 2021.*

List of Conference Presentations

1. **J.A. Hillier**, D.C. Koutsogeorgis, S. Camelio, N. Kalfagiannis. "Controlled Environment Excimer Laser Annealing (CEELA) – A novel strategy for low-loss materials engineering for IR plasmonics". **An oral presentation at the 9th International symposium on Transparent Conductive Materials (TCM2018), 12th - 17th October 2018 (Crete - Greece). Award for best oral presentation was received for this presentation.**
2. **J. A. Hillier**, D. C. Koutsogeorgis, S. Camelio, P. Patsalas, W. M. Cranton, A. Nabok, and N. Kalfagiannis. "Controlled Environment Excimer Laser Annealing (CEELA) – Low-Loss Materials Engineering for IR plasmonics". **An oral and a poster presentation at School of Science & Technology 12th Annual Research (STAR) Conference, 16th - 17th May 2019 (Nottingham Trent University, Nottingham – UK).**
3. **J. A. Hillier**, D. C. Koutsogeorgis, S. Camelio, P. Patsalas, W. M. Cranton, A. Nabok, and N. Kalfagiannis. "Controlled Environment Excimer Laser Annealing (CEELA) – Low-Loss Materials Engineering for IR plasmonics". **A poster presentation at the European Materials Research Society (E-MRS) Spring Meeting, 31st May – 3rd June, (Nice – France).**
4. **J. A. Hillier**, D. C. Koutsogeorgis, S. Camelio, P. Patsalas, W. M. Cranton, A. Nabok, and N. Kalfagiannis. "Reactive Ambient Environment Excimer Laser Annealing (RAELA): Engineering of Low-Loss Transparent Conducting Oxides for IR plasmonics". **A poster presentation at the Materials Research Society (MRS) Fall Meeting & Exhibit, December 1st – 6th, 2019 (Boston, Massachusetts – USA).**
5. **J. A. Hillier**, "Reactive Laser Annealing (ReLA) to overcome the material limitations of plasmonics" **An oral presentation at the Institute of Physics (IoP) Three Minute Wonder Science Communication Competition East Midlands Regional heat, 11 March 2020, Leicester - UK. A prize for best oral presentation was received for this presentation, and a place was secured in the national heat to take place in the Royal Institution, London – UK (scheduled for September 2021).**
6. **James A. Hillier**, Sophie Camelio, Wayne Cranton, Alexei V. Nabok, Christopher J. Mellor, Demosthenes C. Koutsogeorgis, and Nikolaos Kalfagiannis. **An oral presentation at the E-MRS Spring Meeting, May 31st – June 4th, 2021 (Virtual Conference).**

List of Abbreviations

Abbreviation	Meaning
4pp	Four-point probe
AC	Alternating current
AZO	Aluminium-doped zinc oxide
BB-XRD	Bragg-Brentano XRD
BES	Binding energy spectrum
CB	Conduction band
CBM	Conduction band minimum
CMOS	Complementary metal–oxide–semiconductor
CPPB	Critical point parabolic band
DC	Direct current
DFT	Density-functional theory
EBS	Electronic band structure
EDX	Energy-dispersive X-ray spectroscopy
EMA	Effective medium approximation
ENZ	Epsilon near zero
FIB	Focused ion beam
FoM	Figure of merit
FWHM	Full-width half-maximum
GBS	Grain boundary scattering
GI-XRD	Grazing-incidence XRD
GLS	Gaussian-Lorentzian Sum
GZO	Gallium-doped zinc oxide
ICS	Ionised cluster scattering
IIS	Ionised impurity scattering
IRSE	Infrared spectroscopic ellipsometry
IRT	IR transmission
ITO	Indium tin oxide or tin-doped indium oxide
KK	Kramers-Kronig
LA	Laser annealing
LSPR	Localised surface plasmon resonance
MSE	Root mean squared error
NIR-VIS-UV	Near-infrared to visible to ultraviolet
ORS	Optical reflection spectroscopy
ReLA	Reactive laser annealing
RF	Radio frequency
RT	Room temperature
SE	Spectroscopic ellipsometry
SEM	Scanning electron microscopy
SPP	Surface plasmon polariton
TA	Thermal annealing
TCO	Transparent conductive oxide
TE	Transverse electric
TEM	Transmission electron microscopy
TM	Transverse magnetic
UMBReLA	Ultrafast multi-beat reactive laser annealing
UV	Ultraviolet
VASE	Variable angle spectroscopic ellipsometry
VB	Valence band
VBM	Valence band maximum
VdP	Van der Pauw
VIS	Visible
XPS	X-ray spectroscopy
XRD	X-ray diffractometry
IR	Infrared
NIR	Near infrared

List of Symbols

Symbol	Description
a	Lattice parameter
A	Area or Absorptance
A_L	Oscillator amplitude
B	Magnetic field strength
c	Speed of light (2.998×10^8 ms^{-1})
C_V	Specific heat capacity
d	Distance, thickness or d-spacing
D_{Gr}	Grain size / average vertical diameter
E	(Photon) energy
e	Charge of the electron (1.602×10^{-19} C)
E_0	Peak position
E_B	Potential barrier height or Binding energy
E_G	Band gap
E_K	Kinetic energy
E_p	(Unscreened) plasma energy
E_{ps}	Screened plasma energy
ΔE_{BGR}	Bandgap renormalisation shift
ΔE_{BM}	Burstein-Moss shift
F_e	Electrostatic force
F_L	Lorentz force
F_{IIS}	Screening function
f_j	4pp correction factors
Fa	Faraday number
$\hbar$	Reduced Planks constant (6.582×10^{-16} eVs)
H	Magnetic field
I	Wave intensity or Current
j	Current density, Spin quantum number or counting term
J_L	Laser fluence / energy density
Jo	Joule number
K	Spring constant or dimensionless Scherer constant
$\tilde{k}$	Complex wavevector ($\tilde{k} = k_1 + ik_2$)
k_b	Boltzmann constant (1.381×10^{-23} JK^{-1})
K_T	Thermal conductivity
l_e	Mean free path for electrons
L_t	Heat diffusion length
m_e^*	Effective mass of the electron ($m^* m_e$)
m^*	Effective mass ratio
m_e	Mass of the electron
$\tilde{n}$	Complex refractive index ($\tilde{n} = n + i\kappa$)
n	(Real) refractive index
n	Principle quantum number of an orbital OR a counting term
N_L	Density of Lorentz oscillators
N	Free carrier concentration
N_{Hall}	Hall carrier concentration
N_{opt}	Optical carrier concentration
N_{ICS}	Transition concentration for clusters of ionised impurities.
N_{IIS}	Transition concentration for ionised impurities
$\mathrm{O}_2\%$	Oxygen to argon ratio
P	Sputtering power
p	Pressure
q	Charge density
Q_t	trap density
r	Spatial vector or displacement
R	Reflectivity
r_F	Fresnel reflection coefficient
R_H	Hall coefficient
r_{Hall}	Hall scattering factor
R_{sh}	Sheet resistance
R_{VIS}	Visible Reflectance
s	Spacing
S	Spin
S_{Drude}	Free carrier detectability
t	Time / duration
t_F	Fresnel transmission coefficient
T	Temperature or Transmittance

Symbol	Description
v	Velocity
V	Voltage
V_H	Hall voltage
w	Width
Y	Young's modulus
Z	Ionised impurity charge
α	Absorption coefficient
α_{ICS}	Transition coefficient for clusters of ionised impurities.
α_{IIS}	Transition coefficient for ionised impurities
β_G	Gaussian component of the peak broadening
β_L	Lorentzian component of the peak broadening
γ	Damping coefficient / relaxation rate
Γ	Full-width half-maximum
γ_p	Drude / plasma damping coefficient
Δ	Ellipsometric angle related to phase of ρ_f
δ_p	Penetration depth
δ_S	Stress
ε_0	Permittivity of free space (8.854×10^{-12} Fm^{-1})
$\tilde{\varepsilon}$	Complex dielectric function or permittivity ($\tilde{\varepsilon} = \varepsilon_1 + i\varepsilon_2$)
$< \tilde{\varepsilon} >$	Complex *pseudo*-permittivity ($< \tilde{\varepsilon} > = < \varepsilon_1 > + i < \varepsilon_2 >$)
ε_∞	High-frequency permittivity
ϵ_{MaS}	Macro-strain
ϵ_{mS}	Micro-strain
θ	Angle
2θ	Bragg collection angle
κ	Extinction coefficient
λ	Wavelength
μ_0	Permeability of free space (1.257×10^{-6} Hm^{-1})
μ_r	Relative permeability of a material
μ	Free carrier mobility
μ_{Hall}	Hall mobility
μ_{opt}	Optical carrier mobility
μ_1	Ionised cluster inhibited mobility
μ_{max}	Lattice limited mobility
μ_{min}	Ionised impurity inhibited mobility
ξ	Electric field
ρ	Resistivity
ρ_{4pp}	DC resistivity measured by four-point probe
ρ_{VdP}	DC resistivity measured in Van dep Pauw configuration
ρ_{opt}	Optical resistivity
ρ_f	Ratio of reflection of the s- and p-polarisation states from a sample
ρ_M	Material density
σ	Conductivity
τ	Average time between collisions or mean free time
τ_{opt}	Optical mean free time
τ_{GS}	Peak integral breadth due to grain size
τ_{mS}	Peak integral breadth due to micro-strain
ϕ	Work function
χ_e	Electric susceptibility
Ψ	Ellipsometric angle related to the amplitude of ρ_f
ω	(Photon) angular frequency
ω_0	Resonant frequency
ω_p	Plasma frequency

Table of Contents

Copyright Statement ii

Abstract iii

Acknowledgements iv

List of Publications v

List of Abbreviations vii

List of Symbols viii

Table of Contents x

1. Introduction 1

1.1. Motivation of the present work 1

1.2. Research aim 7

1.3. Research objectives 7

1.4. Overview of research methodology 7

1.5. Significant contribution to the field of IR plasmonics 10

1.6. Structure of the thesis 11

2. Background and Literature Review 12

2.1. Optical properties of solids 12

2.1.1. Electromagnetism 12

2.1.2. Optics 13

2.1.3. Lorentz model 15

2.1.4. Drude theory 18

2.1.5. Surface electromagnetic waves 20

2.2. Transparent conductive oxides 23

2.2.1. Overview 23

2.2.2. Crystal Structure of TCOs 27

2.2.3. Electronic band structure and optoelectronic properties of TCOs 29

2.2.4. Doping strategies 32

2.2.5. Scattering Mechanisms and Carrier Transport Properties of TCOs 34

3. Experimental Methods 38

3.1. Material Fabrication and Processing 38

3.1.1. Magnetron Sputtering 40

3.1.2. Excimer Laser Annealing 43

3.2. Characterisation techniques 47

3.2.1. Structural 48

3.2.2. Morphological 52

3.2.3. Compositional 54

3.2.4. Electrical 57

3.2.5. Optical 62

4. Elucidating the optoelectronic properties of RT sputtered TCOs. 71

4.1. Seed material deposition 71

4.1.1. Target Acquisition 71

4.1.2. Sputtering optimisation 72

4.1.3. Experimental Seed Films 78

4.1.4. Structure of seed TCO films 80

4.1.5. Uniformity of seed TCO films 82

4.1.6. Carrier transport mechanisms of seed TCO films 85

4.2. Optical modelling of the seed TCOs 88

4.2.1. Fitting “ideal” films with IR-VIS-UV SE 88

4.2.2. Accounting for multiple carrier species in the optical model 99

4.2.3. Accounting for depth Inhomogeneity of the carrier transport properties 104

4.2.4. Accounting for non-parabolicity of the conduction band 110

4.2.5. Optical vs Hall carrier transport mechanisms 113

4.3. Concluding Remarks 114

5. Uncovering the physical mechanisms behind ReLA of ITO 115

5.1. Introduction 115

5.2. Reactive laser annealing of the optimised ITO film 116

5.2.1. Influence of ReLA on the optoelectronic characteristics 116

5.2.2. Influence of ReLA on the microstructure and morphology 119

5.2.3. Influence of ReLA on the compositional properties 121

5.2.4. Building a model for the ReLA process 126

5.3. Reactive laser annealing of the un-optimised ITO film 132

5.3.1. Influence of ReLA on the optoelectronic characteristics 132

5.3.2. Influence of ReLA on the microstructure and morphology 138

5.3.3. Influence of ReLA on the compositional properties 143

5.4. Concluding remarks 145

6. Ultrafast Multi-Beat Reactive Laser Annealing of ITO 147

6.1. Introduction 147

6.2. Influence of ReLA fluence 147

6.3. Influence of number of pulses 157

6.4. Influence of ReLA ambient composition 163

6.5. Concluding Remarks... 166

7. When ellipsometry really works 168

7.1. Introduction 168

7.2. Simulating ellipsometric data 168

7.3. Computational Limits and Noise 169

7.4. Substrate and Film Thickness 170

7.5. Additional Oscillators within and outside the measurement range 172

7.6. Influence of the carrier mobility 172

7.7. Limits of SE for TCOs 174

7.7.1. Limitations of SE to determine the carrier concentration. 174

7.7.2. Quantifying the limits of NIR-VIS-UV SE 178

7.8. Concluding Remarks... 183

8. Conclusions and Future Perspectives 184

8.1. Introduction 184

8.2. Conclusions 184

8.3. Future perspectives.. 187

9. References 189

1. Introduction

Transparent conducting oxides (TCOs) have been proposed as material components, that are able to overcome the current roadblock to plasmonic applications in the infrared (IR). This roadblock is primarily defined by the high electronic losses of the noble metals in the IR, which limit their plasmonic capabilities in the IR and demands significant compromises in the nanoparticle dimensions and device design. This work aims to expand the spectral domain for the exploitation of plasmonic phenomena with negligible optical loss, which is made possible by engineering the defects of TCOs *via* nanosecond laser annealing (LA) in reactive ambient environments. The research presented in this Ph.D. thesis is focused on investigating the potential of reactive-LA (ReLA) as a powerful tool to control the quality and opto-electronic properties of TCOs, improving the efficiency of such materials as plasmonic components.

1.1. Motivation of the present work

Plasmonics deals with the light-matter interactions at the nanoscale, where electromagnetic fields are confined to sub-wavelength dimensions through driven oscillations of the conduction electrons, known as “plasmons” [1,2]. Two key phenomena of such light-matter interactions that arise from the resonant condition of the plasmons are the surface plasmon polariton (SPP) modes in planar surfaces and localised surface plasmon resonance (LSPR) modes in confined media, like nanoparticles. These modes can be exploited to enhance the local electric field by orders of magnitude and confine light below the diffraction limit [3]. Exploitation of plasmonic phenomena has been demonstrated to present novel applications for nanophotonics [4,5], thermal photovoltaics [6,7], biosensing [8,9], cancer treatment [5], optical encoding [10], photo-catalysis [11] and waveguiding [12]. Vitally, the quality and operating frequency of the LSPR is dependent upon the nano-architecture, local dielectric environment and, importantly, the constituent materials [13].

To date, a key part of plasmonic research has focused on the device design, and less attention has been paid to fully examining the constituent material components [6,14–19]. It follows that the research field would benefit greatly from the adoption of an approach to elucidate the role of materials in plasmonic devices, or strategies to optimise the material components for particular device requirements [20–23]. Therefore, to expand plasmonic capabilities for potential devices, there exist a requirement for new materials that can broaden the window of low loss plasmonic responses. Traditionally, gold (Au) and silver (Ag) have been the obvious choice as plasmonic material components due to their unrivalled conductivity, chemical stability and un-retarded LSPR in the visible spectral range [9,24–28]. However, their melting point is low and they suffer from high-diffusivity, making them unsuitable for high-

temperature devices [29,30]. Furthermore, the noble metals suffer from inherent optical losses from interband transitions that are close to their plasma energy as well as high electronic losses from free carrier absorption. The spectral tunability of the noble metals is limited and the LSPR peak for Au or Ag nanoparticles cannot be extended to the ultraviolet (UV), reducing their effectiveness for chemical sensing and photo-catalysis applications [31,32]. There are a handful of conductive materials that can extend their plasmonic operation into the near- and mid-UV such as aluminium (Al), magnesium (Mg), ruthenium (Ru), rhodium (Rh) and recently molybdenum nitride (MoN)) [33]. However, mono-elemental metals cannot be doped in order to change their optoelectronic properties. Therefore, there are a plethora of materials for the middle (NIR-VIS-UV) range but for the far edges of the spectrum we require better knowledge of the optical properties and need to find other strategies to expand towards the far-UV and mid- to far-IR. Extension of the plasmonic response into the IR can only be achieved by varying the size, the shape, and the distribution of the nanoparticles. This process must compromise with increasing losses due to the response of the high concentration of free carriers. In fact, the free electrons can be considered both the blessing and the curse of plasmonic materials. They are required to fulfil the fundamental criterion for plasmonics (a spectral region of negative real permittivity) but are also responsible for high losses limiting the spectral range of operation.

Fig. 1-1 illustrates this point by presenting the (a) real and (b) imaginary parts of the complex permittivity for a small selection of alternative plasmonic material candidates: tin-doped indium oxide (ITO; cyan line) and aluminium-doped zinc oxide (AZO; purple line). Two frequently used mono-elemental metals, Ag (pink line) and Al (gold line), are also shown for comparison. The point where the real permittivity, ε_1, crosses zero and becomes negative (the screened plasma energy; $E_{ps} = E(\varepsilon_1 = 0)$) is indicated for each material by the vertical-coloured lines. Below this energy, plasmonic phenomena can be exploited. However, the imaginary permittivity, ε_2, rapidly increases below this energy due to the absorption of free carriers. This absorption results in optical losses which can limit the efficiency of potential plasmonic devices. The losses are lowest in the epsilon near zero (ENZ) regime just below the plasma energy. To better illustrate this region, in Fig. 1-1 an arbitrary "low-loss limit" is defined as the cut-off where epsilon is not "near zero". It should be noted that the width of this region is completely dependent on the chosen low-loss limit, which can be highly sensitive to a particular desired application. Purely for illustrative purposes, this limit is chosen to be $\varepsilon_2 = 3$ and is shown with the horizontal dashed black line in Fig. 1-1b. The resulting "region of low loss plasmonics" or ENZ region is presented as the shaded areas in Fig. 1-1b. Therefore, there is a fixed and narrow spectral window where "low-loss" plasmonic phenomena can be efficiently exploited.

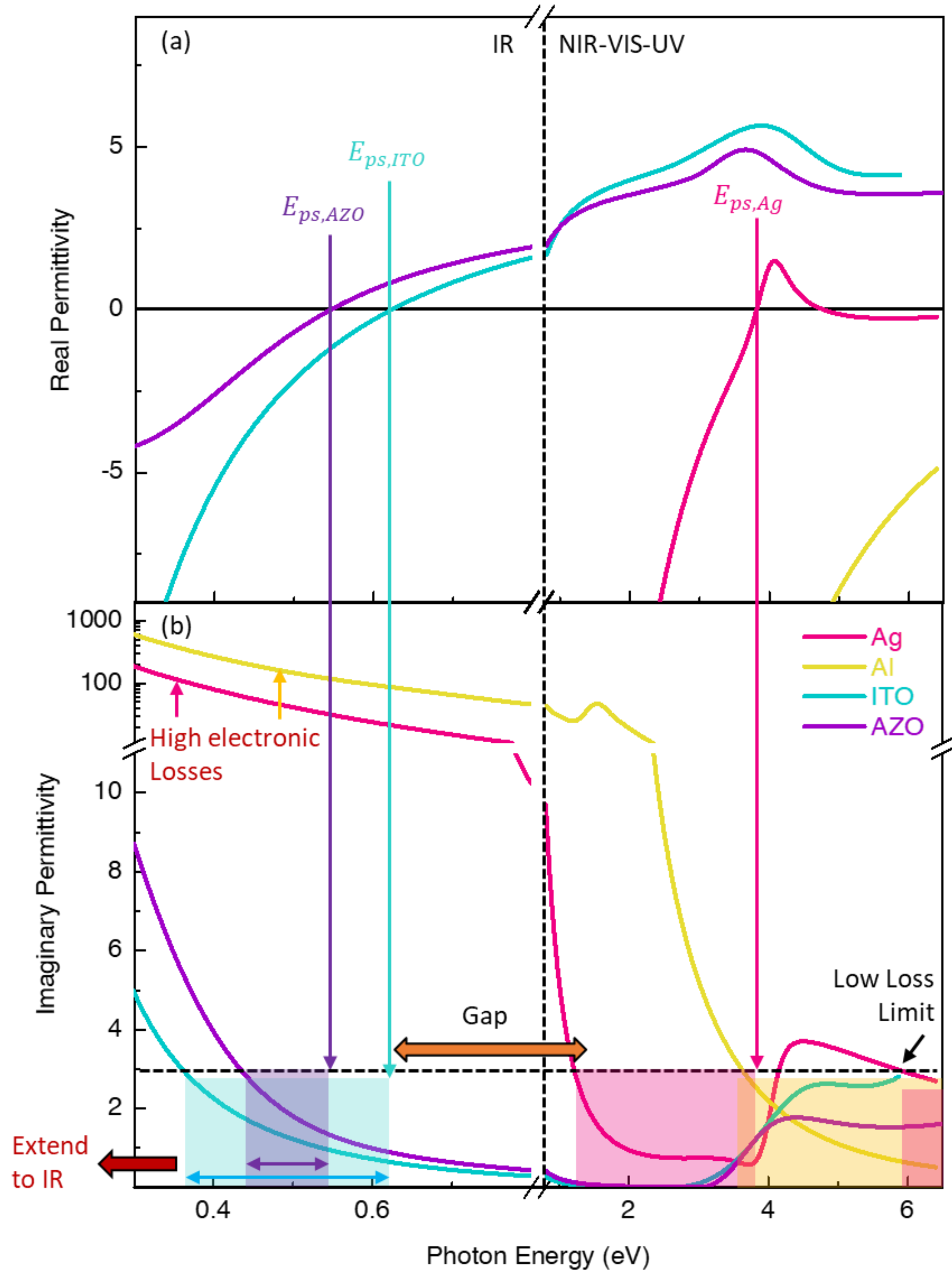

Fig. 1-1. (a) Real and (b) imaginary parts of the complex permittivity for Ag (pink line), Al (gold line), ITO (cyan line) and AZO (purple line). The screened plasma energy, $E_{ps} = E(\varepsilon_1 = 0)$, is indicated for each material by the vertical-coloured lines. In (b), the illustrative "low-loss limit" of $\varepsilon_2 = 3$ is shown with the horizontal dashed black line and the defined "region of low loss plasmonics" or "epsilon-near-zero region" (ENZ) is presented as the pink, gold, cyan and purple shaded areas for Ag, Al, ITO and AZO, respectively. The gap not covered by the example noble metals or metal oxides and the gap further into the IR are indicated with the orange and red arrows, respectively. Note the change in scale in the x-axis at $0.8\ \mathrm{eV}$ used to exaggerate the IR region and in the y-axis at 11, where the scale becomes logarithmic, to exaggerate the low loss region.

It is apparent from Fig. 1-1 that there exists a gap in the NIR not covered by the example materials (orange double-arrow in Fig. 1-1b). The noble metals are inhibited by their high electronic losses in the NIR, and the example metal oxides have a too low screened plasma energy, preventing the expansion of plasmonic applications that require lower losses or seek to operate in technologically important windows in the IR such as the telecommunications window ($1.55\ \mu m$; $0.8\ eV$) [29,30]. Additionally, another gap exists due to the increasing optical losses of the metal oxides, further into the IR (red arrow in Fig. 1-1b). In response to this challenge, the research community have begun to adopt a materials science based strategy to systematically explore alternative materials, such as heavily-doped semiconductors [34,35], conductive polymers [36–39] and transition metal nitrides [40,41] which provide application-specific desirable characteristics [15,28,41]. To aid in the hunt, an attempt can be made to screen and predict the properties of various classes of materials by a careful examination of their chemical, structural and electronic properties. For example, to fill the gap of low loss plasmonic responses and thus expand plasmonic capabilities for potential optical devices operating in the NIR and IR, materials with both lower and higher carrier concentration are required. In particular, development and optimisation of highly tuneable and easily fabricated nanostructured plasmonic materials is considered a key goal for the nanophotonics industry [30].

Over the last decade, the applicability of TCOs as material building blocks for plasmonic devices has been increasingly apparent. Candidates for IR plasmonic applications are the TCOs such as tin-doped indium oxide (ITO), aluminium-doped zinc oxide (AZO) and gallium-doped zinc oxide (GZO), to name but a few [27,28,42]. TCOs are used in optoelectronic devices such as flat-panel displays due to their transparency, refractory character and their capacity for dynamic tuning of their opto-electronic behaviour through application of electric fields *via* the Pockels effect [30,43,44]. An important additional asset of TCOs is the fact that they are compatible with complementary metal–oxide–semiconductor (CMOS) fabrication techniques, unlike the noble metals [15,42,45,46]. This allows for the utilisation of well-matured manufacturing techniques and integration into current electronic devices. Vitally, the optoelectronic properties of TCOs are sensitive to the fabrication techniques and conditions, which enables one to tailor the optoelectronic properties of TCOs towards specific device requirements [47,48]. Due to the fulfilment of many such desirable criteria, the role of TCOs for IR plasmonics has become increasingly apparent in recent years [19,28,40,49–51]. Table 1-1 presents a selection of the most critical and desired material properties for plasmonic applications.

Table 1-1. Critical and Desirable material properties of plasmonic applications and those possessed by TCOs [9,24–28].

Property	Critical	Desirable	Noble Metals	TCOs
Carrier density	✓		Ag, Au	✓
Spectral position of LSPR	✓		Ag, Au	✓
Low electrical losses	✓		Ag, Au	✓
Low dielectric losses	✓		Ag	✓
Chemical inactivity		✓	Au	✓
Functionalisation ability		✓	Au	✓
Static (bulk) tunability		✓		✓
Dynamic tunability		✓		✓
Optical transparency		✓		✓
CMOS compatibility		✓		✓
Refractory character		✓		✓
Cheap and scalable fabrication		✓		✓

Importantly, TCOs fill the operational gap of materials in the IR and their doping can be controlled to modulate their optoelectronic properties and reduce electronic losses in desired operation windows, improving device performance [51]. This can be achieved with cheap and simple post-growth annealing processes such as thermal annealing (TA) [52], which alleviates the need for cost-ineffective and time-consuming doping processes [28]. Such modifications have been achieved through TA in reactive atmospheres which has been shown to improve the free carrier mobility and transparency by inducing or enhancing the crystallisation of the seed films and by probing donor state variations [52–56]. However, TA of thin films suffers from long dwell times and high thermal budget, making the process cumbersome and unable to be utilised for films where the characteristics of the substrate must be preserved (*i.e.* flexible displays or manufactured chips with heat-sensitive components) [43,57–60]. Therefore, alternative methods that can deliver rapid and selective thermal treatment are urgently required. Laser annealing (LA) offers rapid, precise and selective energy delivery able to probe the material structure and composition and enables micro-patterning of the material elements required for the exploitation of plasmonic phenomena [61–63]. LA operates through application of a highly spatially and temporally localised energetic heating and offers a significantly increased level of control over the manipulation of material properties. This is possible from accessing an array of LA parameters such as pulse length, pulse frequency, pulse number, laser energy/fluence [61] and wavelength in addition to those available to TA such as environmental temperature, pressure and composition [64,65]. The wide range of the LA parameters that are available to control are illustrated in Fig. 1-2 and are broken down into those related to the laser unit, laser beam and local environment.

Recent results have demonstrated the ability of LA to overcome the limitations associated with TA and thereby offer an ultra-fast, scalable and low thermal budget post-growth processing technique to enhance the crystallinity of TCOs [59,63,66,67]. Research into LA of TCOs, so far, has focused only on the optimisation of the electrical properties of TCOs towards the specific needs of electronic devices [56,57,63–65, and references within].

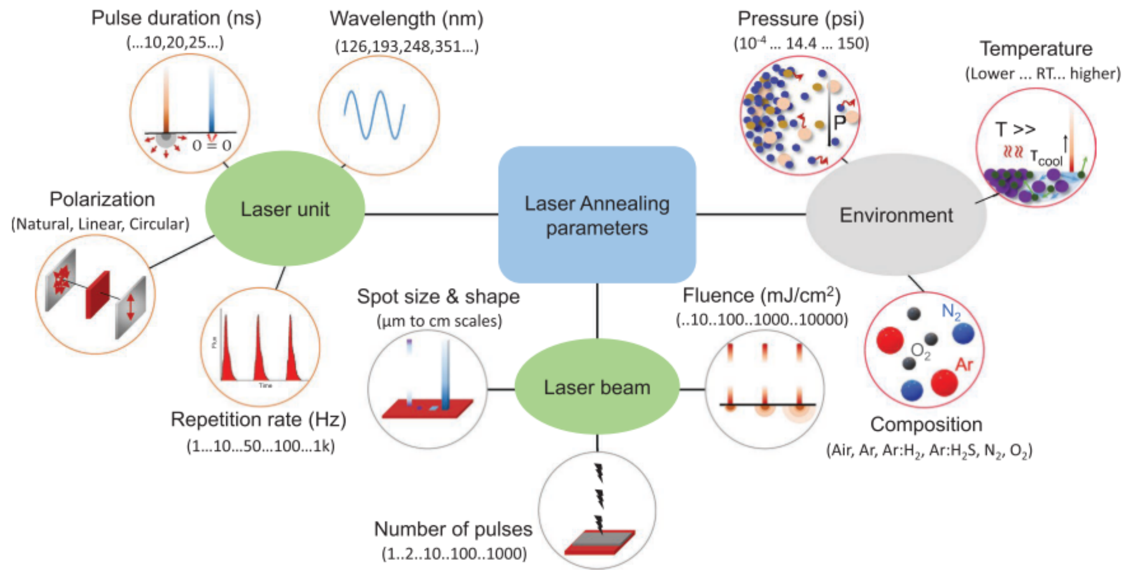

Fig. 1-2. The key LA experimental parameters. Reused with permission from [71].

1.2. Research aim

The overarching objective of this research was to investigate how LA in reactive environments can probe the defect state variations of key TCO materials to tailor their opto-electronic properties and investigate their applicability to plasmonics.

1.3. Research objectives

The realisation of this aim came into fruition through the following objectives:

1. **Develop and optimise seed TCOs suitable for plasmonics.** Sourcing of the seed materials *via* radio-frequency magnetron sputtering, with extensive reviewing of the reported optimisation of the materials, deposition techniques and parameters for plasmonic and electronic applications.
2. **Build the knowledge of the IR opto-electronic properties of room-temperature deposited TCOs.** Performing characterisation of the seed TCOs *via* IR spectroscopic ellipsometry and establishing the benefits and limitations of ellipsometry as a technique to extract the optoelectronic properties of metal oxides.
3. **Investigate the underlying mechanisms that govern the reactive LA (ReLA)-induced alteration of the structure and opto-electronic properties of TCOs:** Processing the seed ITO, AZO and GZO materials with LA in reactive ambient environments (reactive LA; ReLA) and performing characterisation of the opto-electronic, compositional, structural, and morphological properties of the laser processed TCOs using an extensive set of independent techniques. Contribution of this knowledge to the successful employment of LA as a post-growth process for tailoring the spectral features in various TCOs.
4. **Reveal the influence of ReLA-induced modifications on the plasmonic operation of TCOs.** Utilise the wide set of seed and laser processed films to establish a library of potential TCO-based plasmonic devices achievable *via* ReLA using a set of figures of merit (FoMs) for plasmonic operation.

1.4. Overview of research methodology

In this research, room temperature (RT) radio frequency (RF) magnetron sputtering, and LA were utilised to fabricate TCO materials. RF magnetron sputtering is the most widely adopted deposition technique for industrial and research applications, largely due to the ability to finely control the deposition parameters and thus tune the structural, compositional and as a result the optoelectronic properties of the thin film. Sputtering is also applicable to a wide range of materials, can be applied to large-area deposition and can operate without external substrate heating (enabling the use of heat sensitive substrates). Sputtering operates by bombarding a target material with energetic gas ions inside a vacuum chamber, removing (sputtering) the

target atoms that subsequently can travel in the low pressure environment and deposit onto a substrate, resulting in the growth of a dense and uniform film [72,73].

Thin film deposition of TCOs with no external substrate heating generally requires a post-deposition thermal annealing (TA) process in order to enhance the characteristics for better optoelectronic device performance [74,75]. However, the TA process is cumbersome and requires long dwell times to achieve the desired results. To overcome these limitations, in this work laser annealing (LA) is instead adopted for post-deposition processing. LA is very attractive for this purpose due to the very short processing times and the ability to process very small areas across a low depth. In LA, the lased photons with energy higher than the materials' band gap irradiate and are absorbed by the annealed material. The photon energy is rapidly converted into a highly localised heating with a thermal gradient between the surface and underlying layers [76,77]. LA is often performed at atmospheric conditions (pressure and composition), where the role of the laser beam and laser unit parameters (Fig. 1-2) on the resulting film properties are investigated in turn [59,61,66,78]. The influence of the ambient environment is rarely examined [59]. However, for TCOs it is well understood that the stoichiometry, especially the concentration of oxygen vacancies in the film, plays a key role in the resulting optoelectronic properties [48]. Indeed, control over the ambient composition has been demonstrated to tune the carrier concentration, and thus plasma energy, by manipulating such defects during TA [52–55,79] and utilisation of a high-pressure environment minimises the detrimental effects of ablation [61]. This work seeks to combine the advantages of TA in reactive (oxidising and reducing) atmospheres and LA, by performing the laser processing within reactive, pressurised environments to probe the crystal structure and defect composition of TCOs. This process is considered analogous to the use of "reactive" elements during sputter deposition (*i.e*. reactive sputtering [80,81]) and as such is designated here as "reactive laser annealing" (ReLA). ReLA is investigated as a novel tool to control and tune the optoelectronic properties of TCOs towards the requirements of potential IR plasmonic devices.

To assess the prospects of potential materials with plasmonic behaviour in the infrared (IR), one requires precise knowledge of the influence of optical phonons and/or defect states. This assessment relies on knowledge of the materials' complex permittivity, best determined *via* spectroscopic ellipsometry (SE). SE is a highly sensitive characterisation technique that measures the relative phase change and amplitude in a beam of polarised reflected (or transmitted) light from a material [82]. It gains its sensitivity and accuracy from its self-referencing nature meaning that no reference material is required. Measuring the data across a wide range of photon energy and at various angles (variable angle SE or VASE) further increases the sensitivity. SE is commonly

used to characterise both thin films and bulk materials and has proven to be the primary technique to determine the optical constants of a material. It is very sensitive to many material properties and has been used to determine:

1. Optical constants [83,84].
2. Thin film thickness [85].
3. Free carrier transport mechanisms of conductive materials [86].
4. Interband transitions and the band gap [87].
5. Surface and interfacial roughness [88].
6. Crystallinity [89,90].
7. Inhomogeneity [91,92].
8. Anisotropy [93,94].

IRSE is a rapidly growing technology that combines the chemical sensitivity of IR transmission (IRT) measurements with the thin film sensitivity of SE. The extended spectral range gives more sensitivity to the free carrier absorption and can be used to determine multiple material properties in addition to those available to the standard SE in the NIR-VIS-UV:

1. IR optical constants [95].
2. Free carrier transport mechanisms for semiconducting materials [96].
3. Molecular vibrations and phonon absorption [97,98].
4. Defect states [99,100].
5. Majority free carrier type (n or p) [101].
6. Free carrier concentration depth profiles [102].
7. Phonon-plasmon coupling [103–105].

In this work, both IR and NIR-VIS-UV are utilised to expand the measured spectral range to $0.034 - 6.5\ \mathrm{eV}$ and thus take advantage of the enhanced sensitivity of each range to specific material properties (*i.e.*, thickness, roughness, interband absorption for NIR-VIS-UV SE and free carrier absorption and phonons for IRSE). At the time of writing, the use of SE across such a wide spectral range is at the forefront of research capabilities.

The methodology follows a five-pronged approach.

1. Optimise and fabricate seed TCO thin films.
2. Elucidate the properties of seed TCOs with SE across the IR and NIR-VIS-UV.
3. Explore the capabilities and limitations of SE for TCOs.
4. Investigate the physical mechanisms behind ReLA.
5. Investigate capabilities of ReLA for tailoring properties of TCOs towards the requirement of IR plasmonics.

1.5. Significant contribution to the field of IR plasmonics

This research study has investigated the utilisation of ReLA for the defect engineering of three key TCOs (ITO, AZO and GZO) in order to tailor the materials' optoelectronic properties towards the requirements of plasmonic applications in the IR. During this research, many significant contributions to the field of material science, metal oxide research, IR plasmonics and ellipsometry have been made:

1. The transport properties of ITO, AZO and GZO were collated *via* both SE and Hall Effect and used to determine the relation of both the effective mass and the carrier mobility to the carrier concentration for room-temperature sputter deposited TCOs.
2. The limitations of SE were investigated with a theoretical experiment to detail the limits of IR and NIR-VIS-UV SE due to noise, effect of a substrate, oscillators outside of the spectral range, oscillators within the spectral range and grain boundary scattering.
3. This investigation was used to explain the experimental results for ITO, AZO and GZO films to establish the "limitations of SE" for such materials.
4. An "application-specific" limitation of SE was outlined that could be applied to various materials and application requirements.
5. The impact of the IR spectral features and scattering mechanisms of ITO, AZO and GZO on the fundamental applicability of these materials for IR plasmonics was revealed. For example, the role of grain boundary scattering was found to ensure that amorphous TCOs (room temperature deposited ITO, IGZO and others) were vital for mid to far-IR plasmonics.
6. The ReLA-induced conversions of optoelectronic, morphological, structural, and compositional properties of ITO were uncovered.
7. Complex optical models, involving multiple carrier species, film inhomogeneity and non-parabolic bandgap were built to explain ellipsometric results and validated with additional experimental techniques. This revealed information of the properties of TCOs that was only available *via* IRSE and has not been fully understood before in the literature.
8. An understanding of the physical mechanisms behind the ReLA process was built.
9. An extensive picture of the role of the laser fluence, number of pulses and ambient composition on the conversion of the structural and optoelectronic properties of ITO was established.

1.6. Structure of the thesis

This thesis is composed of seven chapters organised as follows:

1. Chapter 1 presents the research motivation, aim, and objectives, as well as an overview of the research methodology and contribution to the field. Finally, the chapter outlines the thesis structure.
2. Chapter 2: provides the background knowledge which is required to explain and discuss the results of this project. The basics regarding the optical properties of materials are outlined and then the reader is guided in more detail through the concepts of plasmonics. Following this, the fundamental structural, compositional, and electrical properties of TCOs are summarised, with an emphasis on how these properties effect the optoelectronic behaviour of TCOs.
3. Chapter 3 details all the experimental characterisation and computational techniques utilised in this research project.
4. Chapter 4 presents the fabrication of a wide set of TCO seed materials and the investigation of the optical, electronic, and structural properties of the as-deposited films. An in-depth overview of the ellipsometric modelling is detailed in order to gain knowledge of the IR optical properties of TCOs and the influence of the scattering mechanisms on the transport properties for a wide range of TCO films.
5. Chapter 5 presents and discusses the results for the laser processing of ITO in reactive ambient environments. The optoelectronic modifications are related to changes in the film composition therefore build a deep understanding of the physical mechanisms behind ReLA.
6. Chapter 6 is devoted to investigating the full capabilities of ReLA by utilising an extended range of fluences, multiple laser pulses and a wider range of ambient environments to assess the ability of ultrafast, multi-beat ReLA (UMBReLA) to manipulate the transport properties of ITO.
7. Chapter 7 utilises the new insights into the optical properties of TCOs developed throughout the thesis to perform a theoretical investigation of the limitations of SE to extract the transport properties of TCOs.
8. Chapter 8 presents the conclusions and key outcomes of this body of work. It also suggests future work on oxides materials deposition, LA, and applications.

2. Background and Literature Review

This chapter provides the background information on the fundamentals of the optical properties of solids alongside an introduction to plasmonics. It then gives an overview on the key properties of TCOs and expands on the techniques utilised for fabrication and processing of TCOs, before providing a more detailed look at the specific structural, morphological, compositional, electrical, and optical of ITO, AZO and GZO.

2.1. Optical properties of solids

2.1.1. Electromagnetism

The fundamentals of the optical properties of solids naturally arise from Maxwell's equations, which describe the interaction of electromagnetic fields with matter. They are written as [106,107]:

$$\nabla \cdot \boldsymbol{D}(\boldsymbol{r},t) = q(\boldsymbol{r},t) \tag{2-1}$$

$$\nabla \cdot \boldsymbol{B}(\boldsymbol{r},t) = 0 \tag{2-2}$$

$$\nabla \times \boldsymbol{\xi}(\boldsymbol{r},t) = -\frac{\partial \boldsymbol{B}(\boldsymbol{r},t)}{\partial t} \tag{2-3}$$

$$\nabla \times \boldsymbol{H}(\boldsymbol{r},t) = \frac{\partial \boldsymbol{D}(\boldsymbol{r},t)}{\partial t} + \boldsymbol{j}(\boldsymbol{r},t) \tag{2-4}$$

where $\boldsymbol{D}$ is the electric displacement, $\boldsymbol{B}$ the magnetic induction, $\boldsymbol{\xi}$ the electric field and $\boldsymbol{H}$ the magnetic field. They are functions of the spatial vector $\boldsymbol{r}$ and of time t. q and j are the charge and current density, respectively. Note that Eqs. (2-1) to (2-4) are Maxwell's equations in differential form and with SI units. $\boldsymbol{D}$ and $\boldsymbol{H}$ are defined as:

$$\boldsymbol{D}(\boldsymbol{r},t) = \varepsilon_0 \boldsymbol{\xi}(\boldsymbol{r},t) + \boldsymbol{P}(\boldsymbol{r},t) \tag{2-5}$$

$$\boldsymbol{H}(\boldsymbol{r},t) = \frac{1}{\mu_0}\boldsymbol{B}(\boldsymbol{r},t) - \boldsymbol{M}(\boldsymbol{r},t) \tag{2-6}$$

where $\boldsymbol{P}(\boldsymbol{r},t)$ is the electric polarisation and $\boldsymbol{M}(\boldsymbol{r},t)$ is the magnetisation. $\varepsilon_0 \approx 8.854 \times 10^{-12}\ \mathrm{Fm^{-1}}$ and $\mu_0 = (\varepsilon_0 c^2)^{-1} \approx 1.257 \times 10^{-6}\ \mathrm{Hm^{-1}}$ are the permittivity and permeability of free space, where $c \approx 2.998\ \mathrm{ms^{-1}}$ is the speed of light in a vacuum [108].

To describe the response of matter to such fields (in a linear and isotropic medium, without charges and currents), Eqs. (2-1) to (2-4) are supplemented with the constitutive relations [106,108] that are combined with Eqs. (2-3) and (2-4) (following an assumption of a time-harmonic field) to give:

$$\boldsymbol{D}(\boldsymbol{k},\omega) = \varepsilon_0 \varepsilon_r(\boldsymbol{k},\omega)\boldsymbol{\xi}(\boldsymbol{k},\omega) \tag{2-7}$$

$$\boldsymbol{B}(\boldsymbol{k},\omega) = \mu_0 \mu_r(\boldsymbol{k},\omega)\boldsymbol{H}(\boldsymbol{k},\omega) \tag{2-8}$$

$$\boldsymbol{j}(\boldsymbol{k},\omega) = \frac{\boldsymbol{\xi}(\boldsymbol{k},\omega)}{\rho_{opt}(\boldsymbol{k},\omega)} \tag{2-9}$$

where $\boldsymbol{k}$ and ω are the wavevector and the angular frequency of the applied field, respectively. $\varepsilon_r(\boldsymbol{k},\omega)$ and $\mu_r(\boldsymbol{k},\omega)$ are the dimensionless relative permittivity and permeability of a material, respectively. ε_r is often referred to as the dielectric constant. $\boldsymbol{j}(\boldsymbol{k},\omega)$ is the current density and $\rho_{opt}(\boldsymbol{k},\omega)$ is the "optical" resistivity, defining the current induced by an electric field, for a material. By noting that $j = I/A$, $\xi = V/l$ and $R = \rho l/A$ (where I is the current, A is the area, V is the voltage, l is the length and R is the resistance), Eq. (2-9) is seen to be the identical, vector form, of Ohm's law [108].

A wavevector and frequency dependence of ε_r, μ_r and ρ_{opt} is observed in Eqs. (2-7) to (2-9). For wavelengths, $\lambda = 2\pi c/\omega$, much smaller than material dimensions, the wavevector dependence can be neglected as the effect of the spatial dispersion is usually very weak. In this chapter, while we consider the optical properties of bulk materials, we will make this simplification. However, for plasmonics, the case is different as we will deal with particles with sizes comparable to λ. The frequency dependence of ε_r, μ_r and ρ_{opt} is always vital to consider and is at the root of many optical phenomena. The frequency-dependent $\varepsilon_r(\omega)$ or simply $\varepsilon(\omega)$ is referred to as the dielectric function or the permittivity of a material. If only non-magnetic materials are considered ($\mu_r(\omega) = 0$ for all ω) and the material is uniform and isotropic, the Helmholtz wave equation is derived [109]:

$$\nabla^2\boldsymbol{\xi}(\boldsymbol{r}) + \frac{\omega^2}{c^2}\varepsilon(\omega)\boldsymbol{\xi}(\boldsymbol{r}) = 0 \tag{2-10}$$

If, instead, a material with current sources ($\boldsymbol{j} \neq 0$) was considered, one would obtain:

$$\nabla^2\boldsymbol{\xi}(\boldsymbol{r}) + \frac{\omega^2}{c^2}\left(\varepsilon(\omega) + i\frac{1}{\rho_{opt}(\omega)\omega\varepsilon_0}\right)\boldsymbol{\xi}(\boldsymbol{r}) = 0 \tag{2-11}$$

By comparing Eq. (2-10) and Eq. (2-11), it is found that with the addition of current sources the permittivity becomes complex: $\varepsilon(\omega) \rightarrow \tilde{\varepsilon}(\omega) = \left(\varepsilon_1(\omega) + i\left(\rho_{opt}(\omega)\omega\varepsilon_0\right)^{-1}\right)$. This is because the sources oscillate with the driving electric field, attenuating the field as it propagates through the material. Thus, the imaginary part of the permittivity defines the magnitude of the absorption. Vitally, the frequency-dependent properties of the material can be described by this complex permittivity (or complex dielectric function): $\tilde{\varepsilon}(\omega) = \varepsilon_1(\omega) + i\varepsilon_2(\omega)$.

2.1.2. Optics

Optics is the study of electromagnetic waves and how they propagate in vacuum and, more importantly, how they interact (propagate, reflect, or attenuate) with materials. The simplest electromagnetic waves are the plane waves [110]:

$$\boldsymbol{\xi}(\boldsymbol{r},t) = \boldsymbol{\xi}_0 e^{i(\tilde{\boldsymbol{k}}\cdot\boldsymbol{r}-\omega t)} \tag{2-12}$$

$$\boldsymbol{H}(\boldsymbol{r},t) = \boldsymbol{H}_0 e^{i(\tilde{\boldsymbol{k}}\cdot\boldsymbol{r}-\omega t)} \tag{2-13}$$

where the $\boldsymbol{\xi}_0$ and $\boldsymbol{H}_0$ are the electric and magnetic field amplitudes, respectively, and are generally constant complex vectors. The wavevector $\widetilde{\boldsymbol{k}}$ is also, generally, complex such that $\widetilde{\boldsymbol{k}} = \boldsymbol{k}_1 + i\boldsymbol{k}_2$. Again, the complex nature of the vectors implies a decay in amplitude in the direction of propagation. For a homogeneous electromagnetic plane wave with $\widetilde{\boldsymbol{k}} = (k_1 + ik_2)\underline{\hat{\boldsymbol{e}}} = \tilde{k}\underline{\hat{\boldsymbol{e}}}$, where $\underline{\hat{\boldsymbol{e}}}$ is a real unit vector in the direction of propagation, and when there is no charge or current density (so that all properties of $\tilde{\varepsilon}(\omega)$ arise from the material), one derives:

$$\tilde{\varepsilon}(\omega)\boldsymbol{k} \cdot \boldsymbol{\xi}_0 = 0 \tag{2-14}$$

$$\boldsymbol{k} \cdot \boldsymbol{H}_0 = 0 \tag{2-15}$$

$$\boldsymbol{k} \times \boldsymbol{\xi}_0 = \omega\mu_0\boldsymbol{H}_0 \tag{2-16}$$

$$\boldsymbol{k} \times \boldsymbol{H}_0 = -\omega\varepsilon_0\tilde{\varepsilon}(\omega)\boldsymbol{\xi}_0 \tag{2-17}$$

From Eqs. (2-14) and (2-15) it is seen that $\boldsymbol{k}$ is perpendicular to $\boldsymbol{\xi}_0$ and H_0 and we have a transverse wave. By combining Eqs. (2-16) and (2-17) we arrive at the dispersion relation:

$$\tilde{k}(\omega) = \sqrt{\tilde{\varepsilon}(\omega)}\frac{\omega}{c} = \tilde{n}(\omega)\frac{\omega}{c} \tag{2-18}$$

where $\tilde{n}(\omega) = \sqrt{\tilde{\varepsilon}(\omega)} = n(\omega) + i\kappa(\omega)$ is the complex refractive index. $n(\omega)$ is the normal refractive index that determines the phase velocity, $v(\omega)$, of a plane wave through a material ($n(\omega) = c/v(\omega)$, where c is the speed of light). $\kappa(\omega)$ is the extinction coefficient that determines the absorption coefficient, $\alpha(\omega)$, through the following equation:

$$\alpha(\omega) = 2\frac{\omega}{c}\kappa(\omega) \tag{2-19}$$

where $\alpha(\omega)$ describes how the wave intensity, $I(\delta)$, is attenuated from it's original value, I_0, as it propagates along the z direction through a material with increasing depth, δ, as according to Beer's law [111]:

$$I(\delta) = I_0 e^{-\alpha(\omega)\delta} \tag{2-20}$$

which is used to define the penetration depth, $\delta_p = \alpha^{-1}$, at the point where $I(z) = I_0 e^{-1}$. The refractive index and the extinction coefficient can be used to calculate the real and imaginary parts of the complex permittivity, $\varepsilon_1(\omega)$ and $\varepsilon_2(\omega)$, respectively (and vice-versa):

$$\varepsilon_1(\omega) = n^2(\omega) - \kappa^2(\omega) \tag{2-21}$$

$$\varepsilon_2(\omega) = 2n(\omega)\kappa(\omega) \tag{2-22}$$

$$n^2(\omega) = \frac{1}{2}\sqrt{{\varepsilon_1}^2(\omega) + {\varepsilon_2}^2(\omega)} + \frac{\varepsilon_1(\omega)}{2} \tag{2-23}$$

$$\kappa^2(\omega) = \frac{1}{2}\sqrt{{\varepsilon_1}^2(\omega) + {\varepsilon_2}^2(\omega)} - \frac{\varepsilon_1(\omega)}{2} \quad - \frac{\varepsilon_1(\omega)}{2} \tag{2-24}$$

In this work, the real and imaginary permittivity will be used to assess materials. The imaginary permittivity is also indicative of absorption, scaled by the real refractive index. The real permittivity plays a more complex role that will reveal itself later in this chapter.

2.1.3. Lorentz model

The complex permittivity defines the optical properties of a material and is influenced by all forms of absorption at all photon frequencies. Each form of absorption is defined by an oscillator that describes the physical mechanism behind any light-matter interaction. The classical example is for a negatively charged electron bound to a positively charged ion (*i.e.*, a hydrogen atom). Fig. 2-1 presents a schematic diagram of such a case [110]. This oscillator model, known as the Lorentz model [107], is akin to the case of a classic damped oscillator with a restoring force that is characterised by a resonant frequency, ω_0.

The equation of motion for the electron is response to an external electric field, $\boldsymbol{\xi}(t)$, is:

$$\frac{d^2\boldsymbol{r}(t)}{dt^2} + \gamma\frac{d\boldsymbol{r}(t)}{dt} + {\omega_0}^2\,\boldsymbol{r}(t) = \frac{e}{m_e^*}\boldsymbol{\xi}(t) \tag{2-25}$$

where $\boldsymbol{r}(t)$ is the displacement of the electron from the ion at time, t. γ is the damping coefficient and m_e^* and e are the effective mass and charge of the electron, respectively. As the spring constant is K, it follows that $\omega_0 = \sqrt{K/m_e^*}$. Setting the electric field to that of an electromagnetic plane wave ($\boldsymbol{\xi}(t) = \boldsymbol{\xi}_0(\omega)e^{-i\omega t}$) and solving for $\boldsymbol{r}(t) = \boldsymbol{r}_0(\omega)e^{-i\omega t}$ gives:

$$\boldsymbol{r}_0(\omega) = \frac{e}{m({\omega_0}^2 - \omega^2 - i\gamma\omega)}\,\xi_0(\omega) \tag{2-26}$$

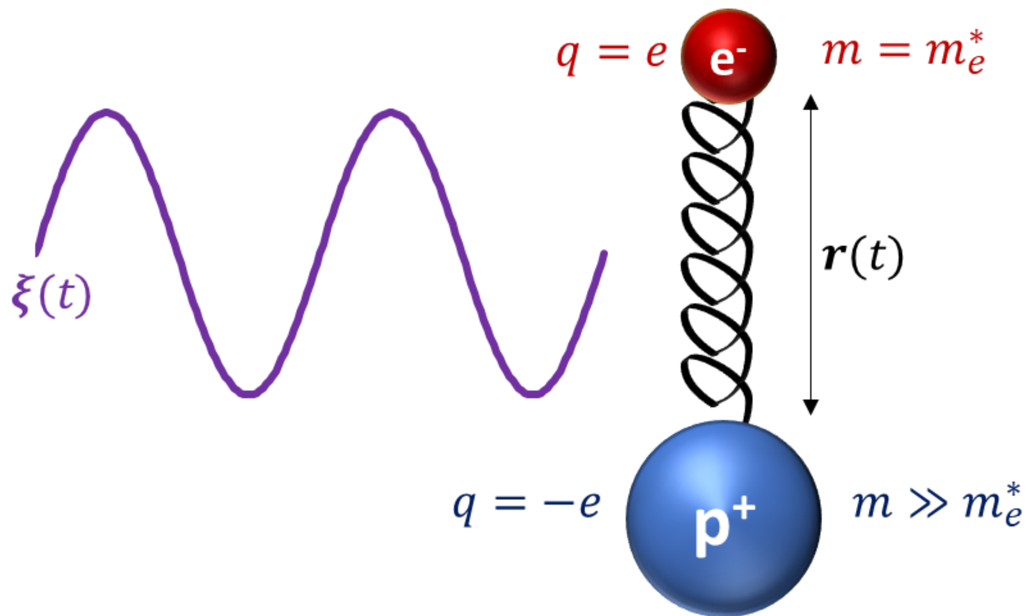

Fig. 2-1. Schematic of the Lorentz oscillator model of an electron (red sphere) bound to the positively charged ion (blue sphere) by a spring with spring constant, K. The electron oscillates with a displacement, $\boldsymbol{r}(t)$, in response to the driving electromagnetic field, $\boldsymbol{\xi}(t)$ (purple line).

As the electric dipole moment of an electron is given by $e\boldsymbol{r}_0(\omega)$, the complex permittivity is obtained to be:

$$\tilde{\varepsilon}(\omega) = 1 + \frac{N_L e^2}{\varepsilon_0 m_e^*} \frac{1}{({\omega_0}^2 - \omega^2 - i\gamma\omega)} \tag{2-27}$$

where N_L is the number of Lorentz oscillators per unit volume. For a real material, one must consider all other transitions besides the single Lorentz oscillator here. To do this, the electric displacement (Eq. (2-5)) is separated into the resonant part, $\boldsymbol{P}(\omega) = \varepsilon_0(\tilde{\varepsilon}(\omega) - 1)\boldsymbol{\xi}(\omega)$, and the background part, $\boldsymbol{P}_b(\omega) = \varepsilon_0(\varepsilon_\infty - 1)\boldsymbol{\xi}(\omega)$. The resonant part describes the Lorentz oscillator in question ($\tilde{\varepsilon}(\omega)$ is given by Eq. (2-27)). The background contributions are represented by a high-frequency permittivity, ε_∞. This allows for the expression of the complex permittivity to be:

$$\tilde{\varepsilon}(\omega) = \varepsilon_\infty + \frac{f_L^2}{{\omega_0}^2 - \omega^2 - i\gamma\omega} \tag{2-28}$$

where $f_L^2 = N_L e^2/\varepsilon_0 m_e^*$ is indicative of oscillator amplitude, A_L. At the resonant condition:

$$\varepsilon_2(\omega = \omega_0) = A_L = \frac{f_L^2}{\gamma\omega_0} \tag{2-29}$$

Therefore, Eq. (2-28) can be alternatively written as:

$$\tilde{\varepsilon}(\omega) = \varepsilon_\infty + \frac{(A_L\gamma\omega_0)}{{\omega_0}^2 - \omega^2 - i\gamma\omega} \tag{2-30}$$

or, expressed by its individual real and imaginary components, as:

$$\varepsilon_1(\omega) = \varepsilon_\infty + \frac{(A_L\gamma\omega_0)({\omega_0}^2 - \omega^2)}{({\omega_0}^2 - \omega^2)^2 + (\gamma\omega)^2} \tag{2-31}$$

$$\varepsilon_2(\omega) = \frac{A_L(\gamma^2\omega_0\omega)}{({\omega_0}^2 - \omega^2)^2 + (\gamma\omega)^2} \tag{2-32}$$

so that A_L approximately equals $\varepsilon_2(\omega)$ at its peak value ($\omega = \omega_0$). The approximation that $\varepsilon_2(\omega = \omega_0) = \varepsilon_{2,max}$ holds for $\gamma \ll \omega_0$. This allows for the plotting of each component of the complex permittivity in Fig. 2-2, for an example Lorentz oscillator with $\varepsilon_\infty = 1$, $A = 10$, $\gamma = 0.1$ eV and $E_0 = \hbar\omega_0 = 3$ eV. Here forth, the photon energy, E (expressed in eV), is used in place of ω (usually expressed in s^{-1}). The fingerprint line shape of the real and imaginary permittivity for a Lorentz oscillator is observed. Here, a detailed examination of the line shape of the Lorentz oscillator is outlined as the principles here apply, qualitatively, to most of the other oscillators which define a materials' complex permittivity and that are utilised in computational analysis of ellipsometric data (Chapter 3.2.5). The imaginary permittivity resembles a bell-shaped curve with an amplitude, A_L, and full-width half-maximum (FWHM), γ, centred on E_0 (vertical dashed black line in Fig. 2-2). As E tends towards zero (left hand side Fig. 2-2) or towards infinity (right hand side Fig. 2-2), ε_2 tends towards zero. The real part of the permittivity has a more complex line shape. From low to high (left to right), an increase of ε_1 is observed as E approaches the oscillator (up to $\approx E_0 - \gamma$). This region is known as the normal dispersion region [107].

For $E_0 - \gamma < E < E_0 + \gamma$, the real permittivity rapidly decreases and can go negative, defining the anomalous dispersion region. For $E > E_0 + \gamma$, the normal dispersion region is re-entered and ε_1 becomes positive again as it tends towards ε_∞. It is observed that as $E \rightarrow 0$, the real permittivity tends to a value larger than ε_∞. Returning to Eq. (2-29) and inputting $E = \hbar\omega \rightarrow 0$ gives:

$$\varepsilon_1(E \rightarrow 0) = \varepsilon_\infty + A\frac{\gamma(\mathrm{eV})}{E_0(\mathrm{eV})} \tag{2-33}$$

This relation explains the origin of ε_∞. At infinite energy, where there are no physical mechanisms that interact with light, $\varepsilon_1 = 1$ (so that the electric susceptibility, $\chi_e = \varepsilon - 1 = 0$). For every oscillator above the region of concern, ε_1 is increased for energies below the oscillator. Specifically, for a total number, N_L, of distinct Lorentz oscillators, n, above the region of concern:

$$\varepsilon_\infty = 1 + \sum_{\mathrm{n}}^{N_L} \frac{A_\mathrm{n}\gamma_\mathrm{n}}{{E_{0,\mathrm{n}}}^2} \tag{2-34}$$

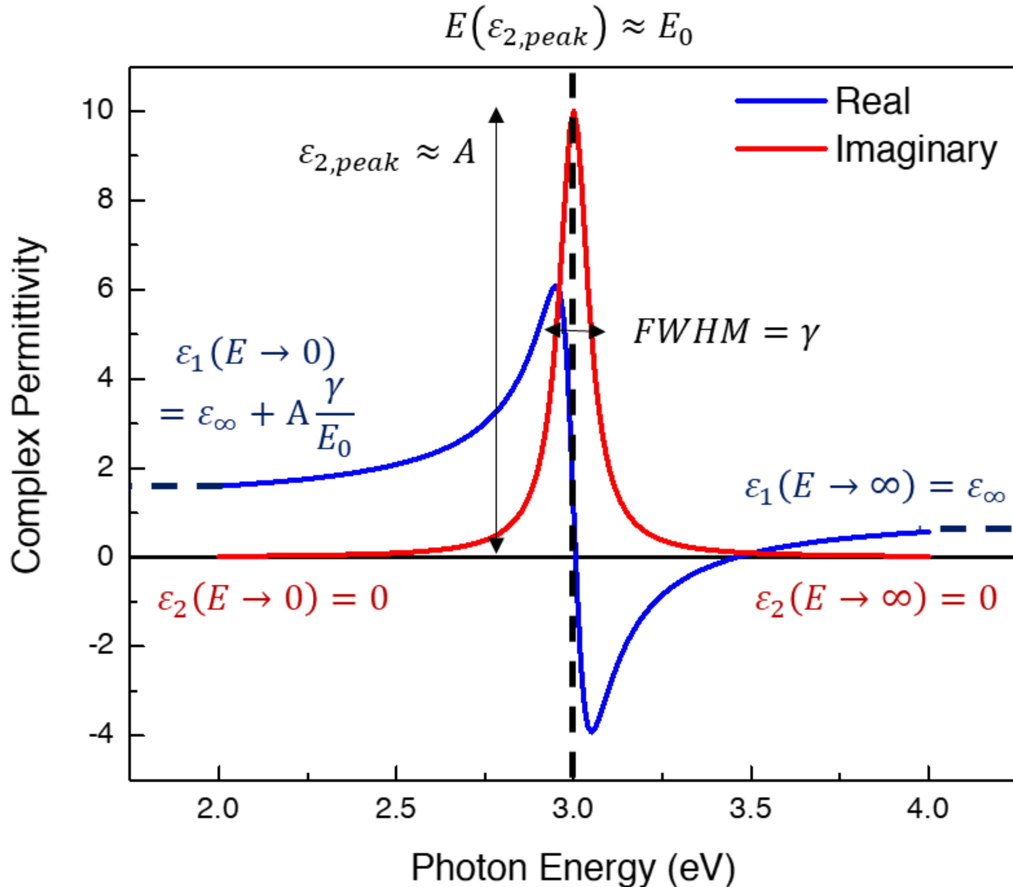

Fig. 2-2. The real (blue solid line) and imaginary (red solid line) permittivity of an example Lorentz oscillator with peak energy, $E_0 = 3.0$ eV (vertical dashed line), peak broadening (or FWHM) $\gamma = 0.1$ eV (double arrow), peak amplitude $A = 10$ and high-energy permittivity, $\varepsilon_\infty = 1$.

2.1.4. Drude theory

The work outlined throughout this thesis is primarily concerned with conductive materials where the electrons are not only bound to the atoms but also exist as a free electron cloud within the material. The simplest classical description, which frequently leads to the same results as more elaborate quantum mechanical approaches [112], is the Drude model [113]. The Drude model can be approached as a special case of the Lorentzian harmonic oscillator model where, as the electrons are "free", there is no restoring force (*i.e.,* $\omega_0 = \sqrt{K/m_e^*} = 0$). If one considers a conductive material with no other centres of absorption within the region of interest, then $\tilde{\varepsilon}(\omega)$ becomes:

$$\tilde{\varepsilon}(\omega) = \varepsilon_\infty - \frac{\omega_p^2}{\omega^2 + i\gamma_p\omega} \tag{2-35}$$

which is often expressed by its individual real and imaginary components:

$$\varepsilon_1(\omega) = \varepsilon_\infty - \frac{\omega_p^2}{\omega^2 + \gamma_p^2} \tag{2-36}$$

$$\varepsilon_2(\omega) = \frac{\omega_p^2\gamma_p}{\omega\left(\omega^2 + \gamma_p^2\right)} \tag{2-37}$$

where ω_p is the plasma frequency (in s^{-1}). The plasma energy (in eV), $E_p = \hbar\omega_p$, is given by:

$$\left(E_p(\mathrm{eV})\right)^2 = \left(\hbar(eV \cdot s)\,\omega_p(\mathrm{s}^{-1})\right)^2 = \hbar^2\frac{N_e e^2}{\varepsilon_0 m_e^*} \tag{2-38}$$

where N_e is the free carrier density and will be simply referred to as N henceforth. The Drude damping coefficient, γ_p, is inverse to the average time between collisions or mean free time, τ:

$$\gamma_p(\mathrm{eV}) = \frac{\hbar}{\tau(s)} \tag{2-39}$$

In reality, γ_p and τ are both temperature [114] and frequency [115] dependent and are determined by impurities, imperfections, electron-phonon scattering and/or electron-electron scattering [113,116]. These scattering events inhibit the carrier transfer across the material and effectively "slow" the carriers, reducing carrier mobility, μ, which is calculated from τ by [113]:

$$\mu = \frac{e\tau}{m_e^*} \tag{2-40}$$

where $m_e^* = m^* m_e$ is the effective mass of the carrier, m^* is the effective mass ratio and m_e the mass of an electron (or hole). This enables one to calculate the resistivity, ρ, *via* the fundamental relation between the conductivity, σ, carrier concentration and mobility, given by [113]:

$$\rho = \frac{1}{\sigma} = \frac{1}{Ne\mu} \tag{2-41}$$

Vitally, the Drude contribution of the free carrier to the permittivity can thus be expressed (in terms of the photon energy, $E = \hbar\omega$ in eV) equivalently by the "optical" resistivity,

ρ_{opt}, and mean free time, τ_{opt}, (Eq. (2-42)) or, if the effective mass is known, the "optical" carrier concentration, N_{opt}, and mobility, μ_{opt} (Eq. (2-43)).

$$\tilde{\varepsilon}(E)_{Drude} = -\frac{\hbar^2}{\varepsilon_0\rho_{opt}(\tau_{opt}E^2 + i\hbar E)}\frac{\hbar^2}{\varepsilon_0\rho(\tau E^2 + i\hbar E)} \quad (2\text{-}42)$$

$$\tilde{\varepsilon}(E)_{Drude} = -\frac{\hbar^2 N_{opt}e^2\mu}{\varepsilon_0(m_e^*\mu_{opt}E^2 + ie\hbar E)}\frac{\hbar^2 Ne^2\mu}{\varepsilon_0(m_e^*\mu E^2 + ie\hbar E)} \quad (2\text{-}43)$$

The optical resistivity can be compared with values of the "DC" resistivity (ρ_{4pp} and ρ_{VdP}) determined by measuring the electrical potential distribution created in a material with a current-injecting electrode with a varying current density [113,117]. The optical carrier concentration can be compared with results from Hall Effect measurements. The "optical" values represent the case where the electrons are responding to an oscillating electric field and thus the induction of an alternating current (AC) opposed to the generally measured response to a direct current (DC).

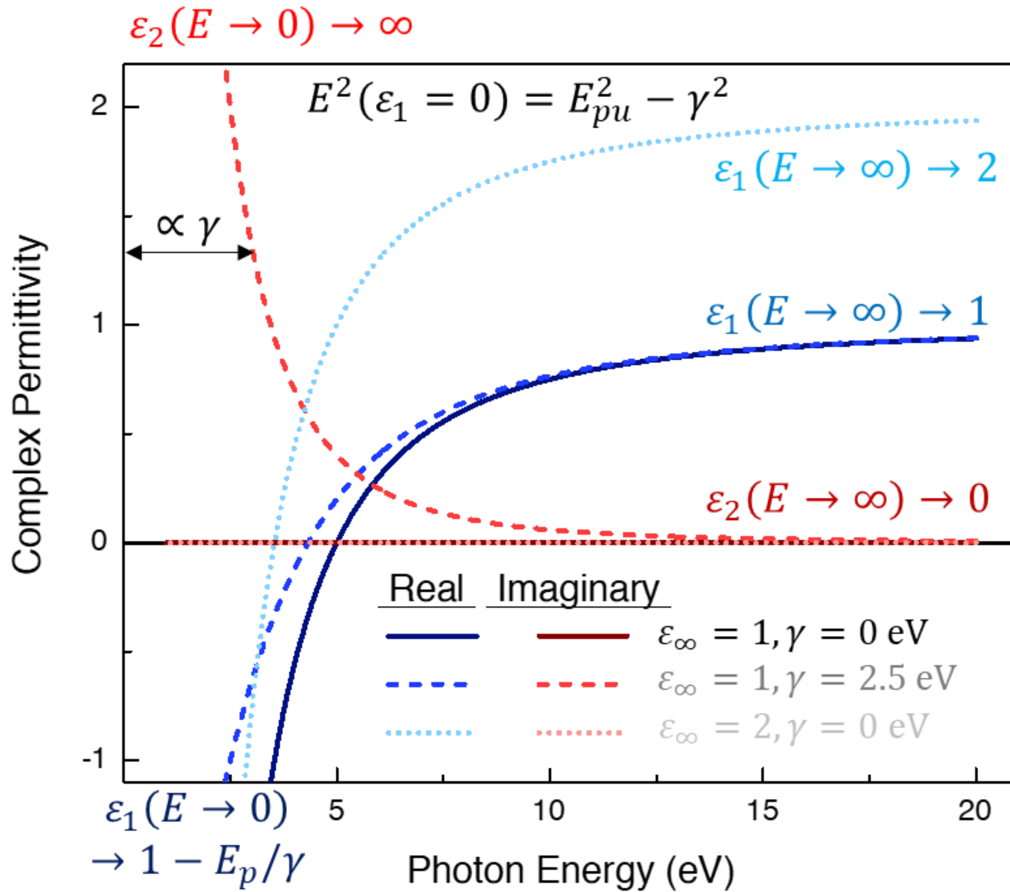

Fig. 2-3. The real (blue lines) and imaginary (red lines) permittivity for three example Drude terms with $\varepsilon_\infty = 1$ and $\gamma_p = 0$ eV (dark-shaded solid lines), $\varepsilon_\infty = 1$ and $\gamma_p = 2.5$ eV (regular-shaded dashed lines) and $\varepsilon_\infty = 2$ and $\gamma_p = 0$ eV (light-shaded dotted lines). The blue and red labels indicate the values of ε_1 and ε_2, respectively, as $E \to 0$ and $E \to \infty$.

The real (blue lines) and imaginary (red lines) parts of the complex permittivity for three example Drude terms are presented in in **Error! Reference source not found.**. The first case is for an ideal, Drude, metal with no other centres of absorption ($\varepsilon_\infty = 1$) and no electronic damping ($\gamma_p = 0$ eV, $\tau = \infty$) and is shown with the dark blue and dark red solid lines. As there is no damping, there is no absorption at any photon energies (*i.e.,* $\varepsilon_2(E) = 0$). The real permittivity follows a negatively inverse trend which tails to unity for $E \to \infty$, as $\varepsilon_1(E, \gamma_p = 0) = 1 - E_p/E$. For this case, $E = E_p$ when $\varepsilon_1 = 0$. Therefore, if the effective electron mass is known, the carrier concentration can be calculated, using Eq. (2-38), from where the real permittivity crosses the x-axis [118], $\varepsilon_1(E = E_p) = 0$, which defines the unscreened plasma energy, E_{pu} [118].

2.1.5. Surface electromagnetic waves

In order to exploit the extraordinary optical behaviour that drives the excitement for plasmonic applications, one must consider the phenomena that occur when the free electrons are bound at an interface or to the physical dimensions of a nanostructure [2].

Surface plasmon polaritons

At the boundary between a thin metal film and a dielectric medium with a complex permittivity's $\tilde{\varepsilon}_M$ and ε_D, respectively, there exist a new excitation of a collective oscillation that are described as surface plasmons or surface plasmon polaritons (SPPs) [119]. The SPPs have a reduced resonant energy of $E_p/\sqrt{2}$ and the dispersion relation for the SPPs is given by [119]:

$$\tilde{k}_x(E) = k_0 \sqrt{\frac{\tilde{\varepsilon}_M(E)\varepsilon_D(E)}{\tilde{\varepsilon}_M(E) + \varepsilon_D(E)}} \tag{2-44}$$

where $k_0 = E/\hbar c$ is the free space wavevector and k_x is the in-plane wavevector. For the mode to be bound at the surface the normal component of the wavevector must be imaginary (so the power does not propagate away from the surface) and thus combinations of ε_M and ε_D must satisfy the condition that $k_{x,i} > \sqrt{(\varepsilon_i)}k_0$. For p-polarised surface waves between a metal and a dielectric this means that $\tilde{\varepsilon}_M$ must be negative and in the last section it was seen that this condition is fulfilled when $E < E_p$. It should be noted that there is no equivalent of the bulk plasmon for SPPs. That is, while bulk plasmonic modes are an inherent property of a material, surface plasmon polaritons only exist when combined with a photon field [119]. The surface electromagnetic waves are propagating waves that are bound to the interface between the metal and dielectric that consist of repeated loops of the electromagnetic field. An illustration of a propagating SPP is given in Fig. 2-4a, where the red lines indicate the loops of the electromagnetic field. When the metal film is an ideal Drude metal, the wave would propagate forever along the interface. However, when the supporting media (the metal) is lossy, the field decays in the direction of propagation. In either case, the magnitude of the field (Fig. 2-4b)

decays away from the interface in both directions. The decay length in the direction of propagation, L_P, is defined as the distance where the field intensity $I = |\xi|^2$ decays to $I(L_P) = I_0 e^{-1}$ and is given by Eq. (2-45) whereas the decay length normal to the interface into the dielectric, L_D, or into the metal, L_M, are defined as the distance that the field amplitude, ξ, decays to $\xi(L_M) = \xi_0 e^{-1}$ and is given by Eq. (2-46).

$$L_P = \frac{1}{2k_{2,x}} \tag{2-45}$$

$$L_{zj} = \frac{1}{k_{2,zj}} \tag{2-46}$$

where $zj = M$ or D.

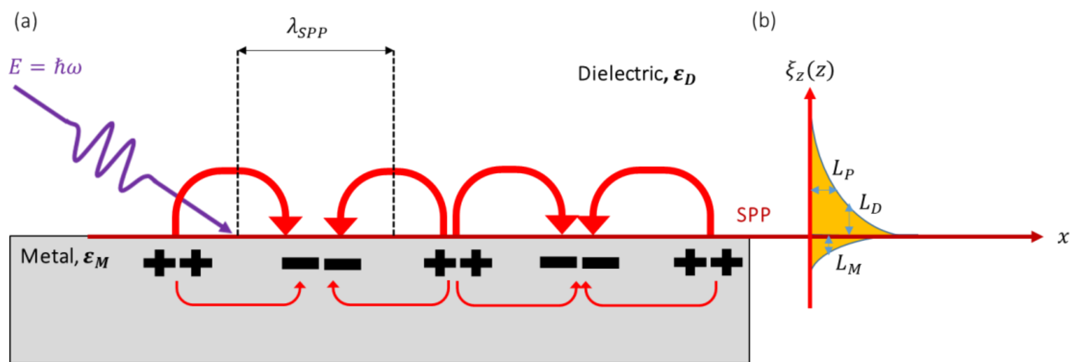

Fig. 2-4. Illustration of surface plasmon polariton propagation. The incident photon (purple line) interacts with the free electrons at the interface of a metal (grey slab) and dielectric (white space), creating loops of electromagnetic field (red loops) around the substrate and giving rise to a propagating surface plasmon polariton with a characteristic wavelength λ_{SPP}(dark red arrow). The electromagnetic field strength, $\xi(z)$, decays exponentially into the dielectric and metal (yellow region in (b)). Adapted from [120].

Localised surface plasmon resonance

An additional, and generally more useful [2,3], plasmonic phenomena, is the interaction between light and metallic nanoparticles with dimensions smaller than the wavelength. The nanoparticle scatters the incoming light leading to a non-propagating collective oscillation of the conduction electrons (a localised plasmon) at a specific frequency known as the localised surface plasmon resonance (LSPR). The nanoparticle becomes an electric dipole and surface charges are created from the oscillation of the free electrons bound to the surface of the nanoparticle. An illustration of a localised plasmon at the resonant condition is given in Fig. 2-5.

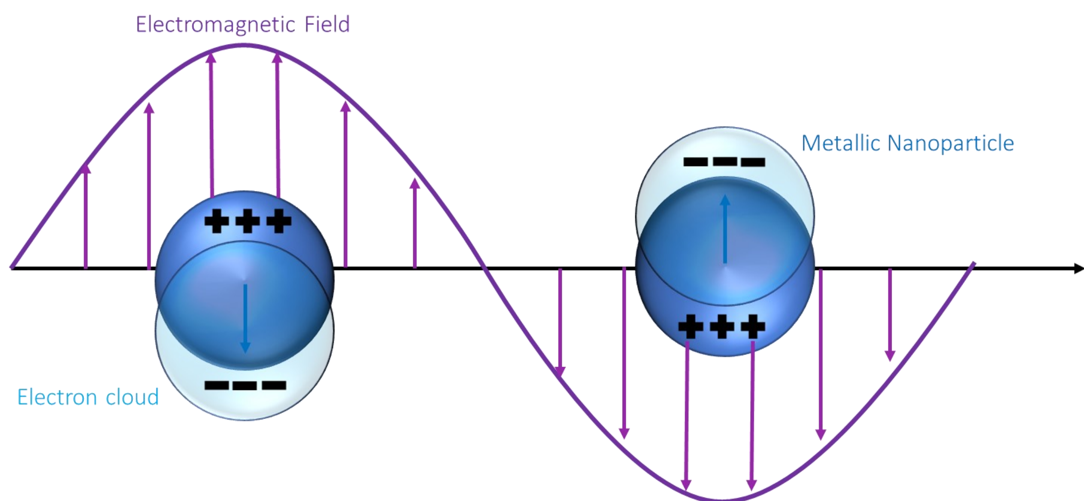

Fig. 2-5. Schematic illustration of LSPR. The purple line is the electric field strength, and the blue spheres represent the metallic nanoparticles. The electron cloud (light blue spheres) moves collectively in response to the driving field and creates a dipole within the nanoparticle. Adapted from [120].

2.2. Transparent conductive oxides

2.2.1. Overview

Transparent conductive oxides (TCOs) are an exciting class of materials which exhibit visible transparency alongside a good electrical conductivity ($\sim 10^3$ $\mathrm{Scm^{-1}}$) [48] and have been applied in many applications such as photovoltaic cells [121,122], flat panel displays [122,123], flexible electronics [49,124], energy-saving windows [125,126] and most recently in plasmonics [19,28,40,49–51]. Vitally, TCOs are a key element in a range of "green" technologies that will be of paramount importance in order to overcome our contemporary climate crisis [125–127]. TCOs are defined largely by their unique optical properties and so a typical optical reflectance, transmission, and absorption spectra for a TCO thin film on top a transparent substrate is presented in Fig. 2-6.

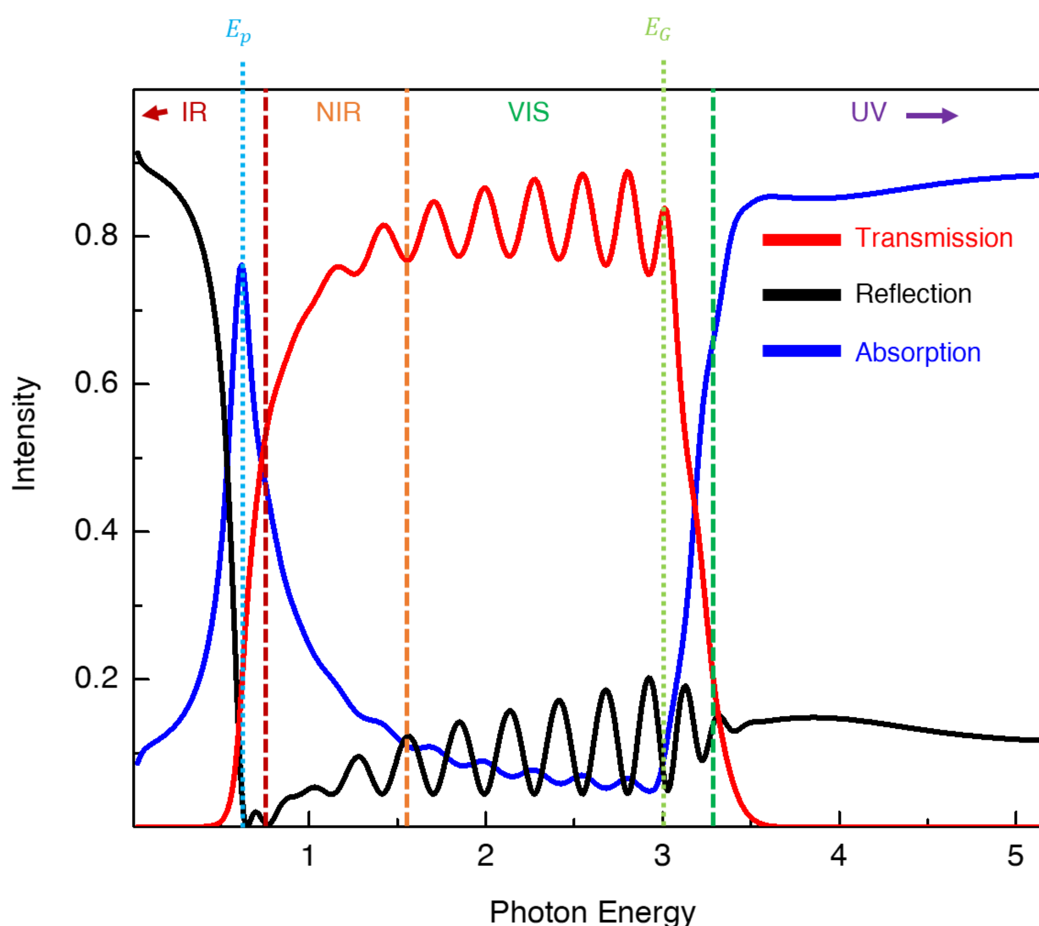

Fig. 2-6. Typical absorption (blue solid line), reflection (black solid line) and transmission (red solid line) spectra for a TCO thin film on a transparent substrate. The dark red, orange, and green dashed lines indicate the IR-NIR, NIR-VIS and VIS-UV boundaries, respectively. The screened plasma energy (where $\varepsilon_1 = 0$) and the band gap are shown by the light blue and light green dotted lines, respectively.

At high photon energy, E, above the band gap, $E_G \approx 3.0$ eV, the film is highly absorbing due to the interband transitions from the valence band (VB) to the conduction band (CB). The large E_G is attributed to the large electronegativity of oxygen and low energy of the VB states [48]. As large E_G materials, TCOs naturally exhibit a high transparency in the visible. This is apparent from the low absorption and the interference pattern observed from $1.4 - 3.0$ eV. As E decreases into the NIR, the absorption increases (with transmission and reflection correspondingly decreasing) up to a maximum value at the plasmon resonance energy, E_p. Above E_p, the film becomes entirely reflective.

As discussed in Section 2.1.4, the absorption at E_p is due to the collective oscillations of "free" conduction band electrons (plasmons) originating from defect energy levels lying close to the CB minimum (CBM) [113]. The defect levels are present in nonstoichiometric TCOs resulting from intrinsic charged interstitial dopants or vacancies within the crystal structure and/or from intentional (or unintentional) substitutional doping [128–134]. A non-zero thermal energy in the system promotes these electrons to the CB, giving rise to the conductivity of TCOs. However, in Fig. 2-6 it is observed that the presence of free carriers in the CB also acts to increase the absorption in the NIR. For a perfect metal with no interband transitions, where there is no damping of the response of the free electrons to a driving electromagnetic field (*i.e.,* $\gamma_p = 0$), the material is perfectly transparent to photons with $E > E_p$ and perfectly reflective when $E < E_p$. The high reflectivity in the IR arises from interaction of the light with the plasma and can be understood by considering that the real permittivity, ε_1, is negative below E_p. If we assume that the carrier damping is small ($\gamma \approx 0$), then $n = \sqrt{\varepsilon_1}$ is imaginary and the reflectivity, $R = |(\tilde{n} - 1)/(\tilde{n} + 1)|^2$, is unity [110]. A non-zero γ_p, as expected for real materials, introduces some free carrier absorption that varies as $\sim E^{-2}$ so that R is less than unity in IR [110]. Materials like metals with a very high free carrier concentration, N, have E_p in or above the visible and are opaque to light (a general property of metals). Those with no free carriers (dielectrics) are transparent (ignoring vibrational states) below E_G. Consequently, the source of the interest for TCOs as a distinctive class of materials is due to their large E_G alongside a relatively high N [48].

The key challenge of TCO material engineering is to effectively uncouple the visible transparency and conductivity. This challenge is partly addressed through a brute-force empirical approach exploring many different TCO material candidates and fabrication techniques, delineating the relationship between the fabrication and processing methodology to the resulting material properties [48,135–143]. An alternative theory-based route has been undertaken to provide insights into the fundamental microscopic nature of the role of the chemical structure, band structure, bonding and film morphology on the carrier transport

mechanisms and opto-electronic properties of TCOs [144–152]. Due to the relation between the conductivity, carrier concentration and mobility (Eq. (2-41)), an additional route to increase the conductivity without sacrificing (and potentially enhancing) the visible and NIR transparency arises from the ability to increase the mobility of the electrons within the lattice. This effectively can reduce the FWHM of the plasmon absorption peak in Fig. 2-6. This has been a key focus of TCO material engineering over the past two decades [46,56,76,152–154, and references within], where empirical techniques of optimising deposition and post-deposition annealing parameters have been employed to provide TCOs with conductivities and transparencies close to their theoretical limits [137,156]. Furthermore, in the last few years the community has explored a more extensive material discovery approach that acknowledges the limitations of the conventional TCO material set (doped binary indium, zinc, and tin oxides). This approach is founded on a realisation that new materials can pave the way to the next generation of optoelectronic devices with not only high transparency and conductivity but also an array of other intrinsic properties (work function, thermal and chemical reactivity/diffusivity) which are deemed critical for particular applications [48].

Indium oxide and Zinc oxide

Indium oxide ($\mathrm{In_2O_3}$) and zinc oxide (ZnO) are n-type direct band gap ($\sim 3.5\ \mathrm{eV}$) semiconductors with high transparency in the visible spectral range ($\sim 80\%$ or higher) [48,135]. These values are however only a rough indication as thin film properties depend highly on the specific fabrication conditions. $\mathrm{In_2O_3}$ is currently the front-runner TCO material candidate due largely to the superior conductivity ($\sim 10^3\ \mathrm{Scm^{-1}}$) and transparency ($> 85\%$) of tin-doped indium oxide (ITO) and due to the presence of shallow oxygen vacancy defect states, which also enables the effective conducting behaviour in undoped $\mathrm{In_2O_3}$ [157]. Interest in ZnO extends beyond its classification as a TCO, due to its "prototype" direct band gap semiconductor nature that places it in competition with gallium nitride, GaN, and for the ease of nanorod production with ZnO [158]. ZnO also has a high exciton binding energy, making it ideal for light-emitting diodes [159,160]. Furthermore, it is an attractive material for microelectronic applications due to its deposition as a polycrystalline material at room temperature and ease of doping [48]. Aluminium and gallium doped ZnO (AZO and GZO, respectively) have gained increasing interest due to their high conductivity (comparable to ITO), chemical stability against hydrogen plasma processing (common to photovoltaic manufacturing) and easy post-deposition etch-ability [48]. Vitally, ZnO-based devices are highly cost effective and environmentally advantageous as a replacement to $\mathrm{In_2O_3}$-based electronics as indium is a much rarer element in the earth's crust [161] and accounts for the largest percentage of the total cost of photovoltaics [162].

TCOs as plasmonic material building blocks.

As discussed in the previous chapter, TCOs present a range of beneficial properties for plasmonics. Importantly, TCOs are non-stoichiometric in nature, meaning that they contain intentional, unintentional and/or intrinsic dopants. By manipulating the defect composition by varying the film growth and or post-processing parameters, N can be altered. Due to the proportionality between E_p and N (Eq. (2-38)), a new route for materials engineering and optimisation of TCOs is available. Here, there exist more freedom than for electronic applications because now N is not only treated as a property to maximise (while not neglecting transparency or mobility) but one to selectively control in order to tune the un-retarded plasmonic resonance frequency. Much is published on optimising material fabrication, processing and nano structuring in order to maximise the quality of the plasmonic response [19,51,55,163] and further studies have demonstrated a wide tunability of plasmonic responses, with minimal losses, for TCOs. [52,164]. However, these studies have only briefly covered the material design itself. To advance the impact of TCOs for plasmonic applications, a greater knowledge base on the charge transport mechanisms is required. A controlled and scalable manner of probing the defect composition is therefore becoming of utmost importance. A recent review of TCOs [165], with a focus on electronic applications, declared that optimising the mobility of TCOs was better served by focusing on the fabrication of TCOs and not the post-deposition processing. However, this may not be the case from a plasmonic perspective; seeking wide tunability of the un-retarded plasma resonance energy or for seeking new techniques to probe the material defect composition.

In the following paragraphs, the current perspective on the role of the crystal structure, defect chemistry and doping mechanisms on the optoelectronic properties of TCOs will be given. The focus will be on three of the main TCO candidates for both optoelectronic and plasmonic applications: tin-doped indium oxide, also known as indium tin oxide (ITO), aluminium-doped zinc oxide (AZO) and gallium-doped zinc oxide (GZO). Subsequently, an overview will be given for the most promising fabrication and processing strategies to achieve TCO thin films with high-quality plasmonic behaviour with wide tunability of the plasmonic response. An increased emphasis is given to the use of post-deposition techniques, specifically thermal annealing (TA) in controlled, reactive environments and on the recent developments of laser annealing (LA) as a robust, selective, and low-thermal-budget approach to probe material characteristics.

2.2.2. Crystal Structure of TCOs

Indium Oxide

The structure of $\mathrm{In_2O_3}$ and ITO are closely related. The indium, In, and oxygen, O, atoms are prevalently bounded by ionic bonding and the $\mathrm{In_2O_3}$ films have a cubic bixbyite structure (Space group Ia3), with a unit cell (lattice parameter, $a = 1.0118$ nm) containing 80 atoms [48]. *32* of the lattice sites are occupied by cations (In or tin, Sn, for ITO) at two types of non-equivalent six-fold coordination sites. A quarter of the cations occupy trigonally compressed octahedral "b" sites (where oxygen vacancies are found along the body diagonal – two opposite corners of cube). The other three quarters of atoms occupy distorted octahedral "d" sites, where oxygen vacancies appear on two opposite corners of a single face. The In atoms sit in the centre of the b- and d-site cubes with only 6 oxygen atoms as nearest neighbours, due to the two intrinsic oxygen vacancies in the structure. The complex structure is represented schematically in Fig. 2-7. The structure can also be regarded as an imperfect crystal of fluorite structure by extracting 16 oxygen atoms for 1 bixbyite unit cell [48,166]. The electrostatic forces between the atoms are skewered by the presence of the intrinsic oxygen vacancies, which causes the cation-oxygen distances to depend on the atom site. This means the atoms do not sit exactly on the corners of the lattice as shown in Fig. 2-7, where we also present the cation-oxygen distances for each bond.

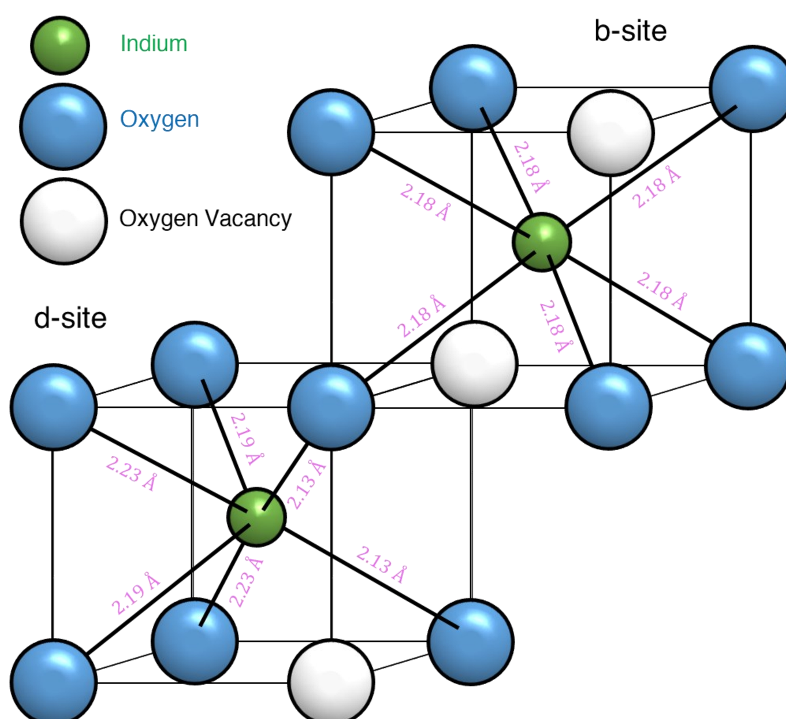

Fig. 2-7. Illustration of the structure of $\mathrm{In_2O_3}$. The blue and green spheres indicate oxygen and indium atoms, respectively. The white spheres indicate an intrinsic oxygen vacancy within the unit cell. Adapted from [166] with the cation-oxygen distances taken from [167].

In_2O_3 films are generally polycrystalline [168,169] with a grain size of ~ 10 nm [170]. In general, the better electrical properties are obtained when the grain size is larger and therefore either deposition onto a preheated substrate or post-deposition annealing is employed [171]. However, even in the amorphous state, In_2O_3-based materials often show quite high free electron mobility [172] that only slightly improves upon crystallisation. The existence of a high conductivity while in the amorphous state may be a little surprising and will be explored shortly.

Zinc Oxide

ZnO crystallises in three distinct crystal structures: cubic zinc blende, rocksalt and hexagonal wurtzite. The zinc blende structure is only stable when deposited on highly mismatched substrates or onto a zinc sulphide buffer layer [173]. The rocksalt structure can be formed at very high pressures (~ 10 GPa) but reverse to the wurtzite structure at lower pressure (2 GPa) [173]. The hexagonal wurtzite is the most thermodynamically stable and thus most observed. The bonds form a tetrahedral geometry where each oxygen ion is bound to the four nearest neighbours of Zn ions (and vice-versa). This structure is presented in Fig. 2-8. Due to the hexagonal lattice, the lattice is described by two lattice parameters a and c, which are 3.2495 Å and 5.2069 Å, respectively, for undoped, unstressed ZnO [174]. During thin film deposition of ZnO, the deposited atoms generally prefer to crystallise along the (002) plane of the wurtzite structure (*i.e.*, the crystallographic c-axis is perpendicular to the substrate surface).

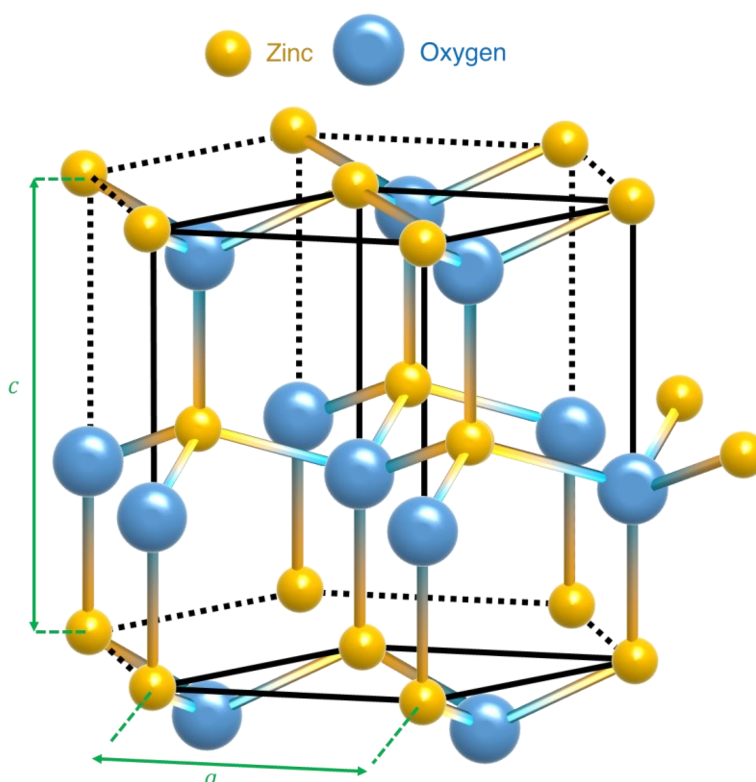

Fig. 2-8. Illustration of the structure of ZnO. The yellow and blue spheres indicate zin and oxygen atoms, respectively. Adapted from [175].

2.2.3. Electronic band structure and optoelectronic properties of TCOs

Most of the interesting optoelectronic properties of TCOs are determined by the electronic band structure (EBS). Therefore, a reliable model of the EBS is necessary to understand the optoelectronic properties on the microscopic level. The plot of the electron energy against the electron wave vector is known as a band structure diagram and is related to the fundamental crystal structure and defect composition of a material. The EBS can become very complicated due, primarily, to the complexity of the structure. Work has been done using first-principles density-functional theory (DFT) calculations to produced detailed EBS for In_2O_3, ZnO, and their doped counterparts, revealing the roles of crystal symmetry, electronic configuration of the cations and strength of the hybridisation between cation states [130,144,176]. However, the key properties of In_2O_3 and ZnO can be elucidated by assuming isotropic parabolic conduction bands to create a simplified schematic EBS model. The simplified EBS models for (a) stoichiometric In_2O_3, (b) oxygen deficient $In_2O_3$and (c) ZnO are presented in Fig. 2-9. During the formation of metal oxides, ionic bonding arises from the charge transfer that occurs between the metal (with lower ionisation energy) and oxygen atoms (with higher electron affinity energy). The conduction band minimum (CBM) comprises unoccupied ns orbitals of metal cations (where n is the principal quantum number of the orbital) and the valance band maximum (VBM) of occupied $2p$ orbitals of metal cations (white and blue buckets in Fig. 2-9). The high strength of the metal-oxide bond results in a high heat of formation and a wide band gap for metal oxides ($E_G = E_{CBM} - E_{VBM}$; purple arrow in Fig. 2-9) [48].

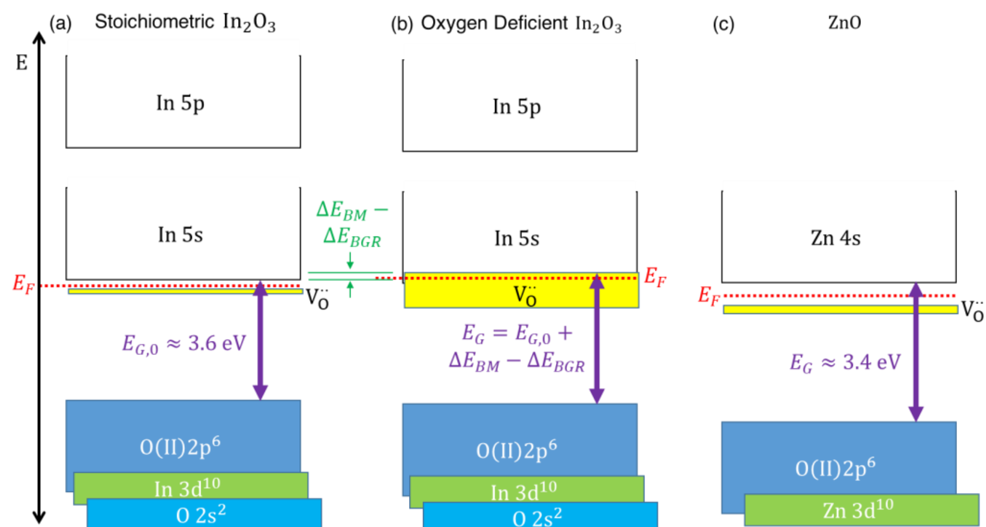

Fig. 2-9. Schematic energy-band model for the simplified electronic band structure of (a) stoichiometric In_2O_3, (b) oxygen deficient In_2O_3 and (c) ZnO. The states for each band are labelled within the band. The fermi level is indicated by the dotted red line and the optical band gap by the purple arrow. The effect of the Burstein moss shift on the bandgap for oxygen deficient In_2O_3 is indicated with the two green lines. Adapted from [177].

Hosono *et al.* [178,179] adopted this understanding of the electronic structure of TCOs to explain the origin of the high electron mobility for amorphous semiconducting oxides. For covalent semiconductors such as Si, the CBM is comprised of directional and anisotropic sp^3 orbitals that are highly sensitive to changes in the bonding angle. Therefore, when such materials are in the amorphous state the local distortions would lead to a high density of localised traps below the CBM, which can trap or scatter free carriers. The carrier mobility is greatly diminished due to the carrier transport only being possible by "hopping" between trap states within the band gap [180,181]. For TCOs, however, the bonds are ionic and the CBM consist of unoccupied, large, and widely spread valence orbitals of metal cations. Vitally, this gives rise to a large overlap between adjacent cation orbitals that does not change with the bonding angle, and thus the conduction pathways are preserved for amorphous TCO films. A schematic of the mechanism for carrier transport across the ns orbitals for the case of a (a) crystalline and (b) amorphous metal oxide is presented in Fig. 2-10.

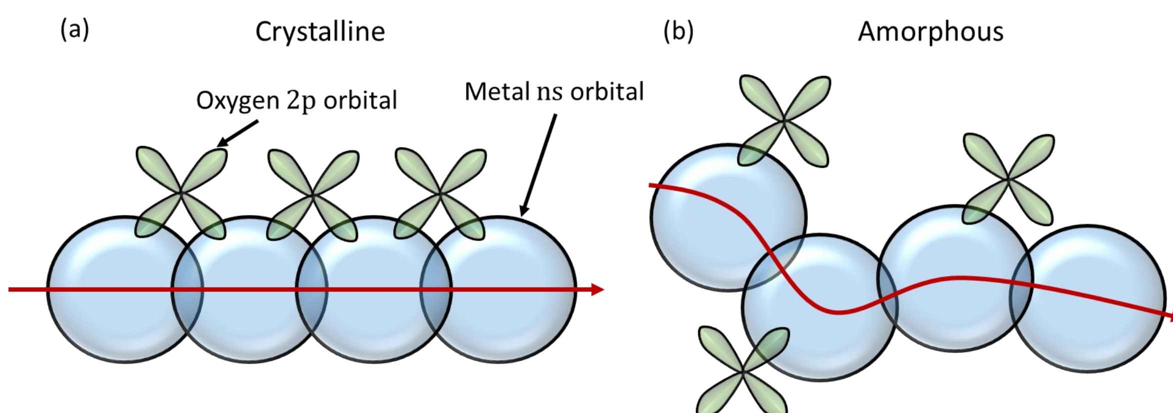

Fig. 2-10. Schematic of the free carrier transport path for (a) crystalline and (b) amorphous TCOs. The blue spheres indicate the spherical metal ns orbitals and the green "butterflies" indicate the oxygen 2p orbitals. The red line shows the conduction pathway of a carrier through the material. Adapted from [48].

The band structure of Indium Oxide

The first realistic calculation of the EBS for In_2O_3 was performed by Odaka *et al.* [182] and subsequently improved by Mi *et al.* [183] and Mryasov and Freeman [184]. In Fig. 2-9a, the form of the EBS is simplified by only considering direct band transitions at the centre of the Brillouin zone. In_2O_3 has a single free-electron-like CBM formed by the In5s and In5p electron states with a direct minimum band gap and a reasonably low effective mass of $0.18\,m_e$ for stoichiometric In_2O_3 [185]. The upper valence bands have the wrong symmetry to allow optical transitions to the conduction band and there exist a minimum band gap at 2.9 eV that is direct and forbidden [186]. The forbidden nature results in the first allowed transition occurring at 0.8

eV below the VBM, resulting in an "optical" band gap of ~3.6 eV. Importantly, the second gap between the 5s and 5p states prevents inter-CB transitions of electrons due to photons in the visible range [187]. The VB is formed by the filled $In3d^{10}$ and $O2p^{6}$ and $O2s^{2}$ electron states.

The free carrier concentration of undoped In_2O_3 is related to the stoichiometry due to the presence of oxygen vacancies [188]. These defects have an energy state just below the CBM and if the system is oxygen depleted and density of electrons exceeds the critical Mott Density [189,190], the states become degenerate and an impurity band forms which can overlap the CB (Fig. 2-9b). This results in the formation of a free electron cloud that can be described classically by Drude theory (Section 2.1.4) and denotes the onset of metallic conductivity. The Mott criterion for In_2O_3 is estimated to be 7.21×10^{18} cm^{-3} [191]. This process also increases the optical band gap as the electrons populate the bottom of the CB, blocking transitions from the VB to these states and thus increasing the energy required for electrons to jump from the VB. This is known as the Burstein-Moss shift or effect [192], which is inversely proportional to the effective mass [193], and is presented schematically in Fig. 2-9b. This effect is however partly reduced due to increased electron-electron and electron-donor interactions that "renormalise" the energy of the elections in the conduction band. The CBM is consequently pushed down while the VBM shifts up and the band gap is narrowed [194]. The overall optical band gap, as a function of N, can be expressed as:

$$E_G(N) = E_{G,0} + \Delta E_{BM}(N) - \Delta E_{BGR}(N) \quad (2\text{-}47)$$

$$\Delta E_{BM}(N) = \frac{\hbar^2}{2m_{VC}^*}(3\pi N)^{\frac{2}{3}} + \hbar\Sigma \quad (2\text{-}48)$$

where $E_{G,0}$, $\Delta E_{BM}(N)$and $\Delta E_{BGR}(N)$ are the stoichiometric band gap, Burstein-Moss shift, and bandgap renormalisation effect, respectively. The increase in N does not always constitute an increase in σ as the oxygen vacancies act as centres for ionised impurity scattering (IIS) that can significantly reduce the free carrier mobility. The carrier scattering mechanisms are explored in more detail in the next section.

The band structure of Zinc Oxide

The band gap of ZnO has been found to be ~3.4 eV [48,135,173]. Due to the lower atomic number of Zn compared to Sn (one row up on the periodic table) the CB consist of $Zn4s^1$ states and the VB of filled $O2p^6$, $Zn3d^{10}$ and $O2s^2$ states [183]. Importantly, for ZnO the oxygen vacancy defects are understood to be deeper within the band gap and undoped ZnO cannot exceed the Mott critical density with oxygen deficiency alone and requires additional doping to become conductive [150]. The Bohr radius of ZnO is estimated to be 0.90 ± 0.01 nm [195] which allows for an estimation of the Mott critical density of ZnO as $(2 \pm 1) \times 10^{19}$ cm^{-3} using the

simple, universal framework for describing the metal-non-metal transition developed by Edwards *et al.* [196]. However, at room temperature the intrinsic defects can be promoted to the CB establishing the semiconducting behaviour of oxygen deficient ZnO [197,198], resulting in the equivalent Burstein-Moss and band gap renormalisation effects as described for $\mathrm{In_2O_3}$.

It should be noted that the origins of the conductivity of TCOs is still under intensive debate [131,199–203]. This debate primarily revolves around the role of the oxygen vacancies as the key shallow donor in TCOs. An interesting theory suggest that shallow hydrogen-related defects play an important role in explaining the conductivity of metal oxides, which is in contrast to the common belief of the oxygen vacancies as the dominant source of free carriers [201]. For ZnO in particular, such proposed mechanisms have been experimentally verified by direct spectroscopic observation of its muonium counterpart [204] and electron paramagnetic resonance and Hall measurements [205]. The hydrogen can be present during growth of annealing as it is ubiquitous, or can even be introduced intentionally [205,206]. The common conception that oxygen vacancies play a key role arises from how the conductivity of TCOs have a strong dependence the partial pressures of oxygen during the growth or annealing [207]. Vitally, however, it has been shown that the oxygen partial pressure sensitivity can be better explained by hydrogen substituting oxygen in the multicentre configuration [208].

For $\mathrm{In_2O_3}$, however, experimental validation of the role of hydrogen defects as the primary source of the conductivity is still disputed. There have been many theoretical, DFT-based calculations of the EBS of $\mathrm{In_2O_3}$ that suggest the deep nature of oxygen vacancy defect states and that hydrogen interstitials form the shallow donor state that promotes conductivity [132,147,209]. However, a theoretical understanding for the role of the oxygen partial pressure during thin film growth and annealing on the conductivity of $\mathrm{In_2O_3}$ has not, yet, been thoroughly established. Therefore, in this work the conductivity of $\mathrm{In_2O_3}$ and ITO are explained, where possible, by variations of the oxygen vacancy concentration.

2.2.4. Doping strategies

As seen, the low resistivity at room temperature that is required for optoelectronic applications can be realised by the creation of oxygen vacancies, lattice defects and/or hydrogen doping. These possibilities can be achieved by adjusting the oxygen partial pressure and sputtering parameters during reactive sputtering or by performing a post-deposition annealing in vacuum or a reducing atmosphere [210,211]. However, the films produced with such processes exhibit undesirable properties, such as a relatively high resistivity. The high resistivity is due, in part, to the inability to consistently increase the oxygen deficiency of $\mathrm{In_2O_3}$ while maintaining film stability and preventing reoxidation ambient conditions. To decrease the

resistivity further, extrinsic dopants are added to the metal oxides during deposition. Such dopants are either metals with an oxidation number 3 on substitutional metal lattice sites or halogens with an oxidation number -1 on oxygen lattice sites [212].

Due to the intrinsic oxygen vacancies and interstitial In, $\mathrm{In_2O_3}$ is an anion-deficient n-type conductor even without external doping [213]. Doping with Sn further increases N due to the higher valence of $\mathrm{Sn^{4+}}$ (in comparison to $\mathrm{In^{3+}}$) [56,177]. In such cases, the charge imbalance is addressed by the formation of oxygen interstitials and/or vacancies. As mentioned, Sn and O (specifically the interstitial O) can form neutral or charged defect clusters (depending on their stoichiometry). These defects have even been proposed to explain the conductivity of $\mathrm{In_2O_3}$ [214,215]. Due to the charge of oxygen defects they may also form complexes with $\mathrm{Sn^{4+}}$ dopants which reduces the ideal contribution of electrons [216]. Alternative but less common doping strategies for $\mathrm{In_2O_3}$ include the use of titanium (Ti) [142], zinc (Zn) [217], cerium (Ce) [151], copper (Cu) [218] and zirconium (Zr) [219], to name but a few [165], as the substitutional dopant. Further studies have explored the using intentional hydrogen (H) doping of $\mathrm{In_2O_3}$ [206,220,221].

AZO and GZO are the most prevalent forms of n-type ZnO based TCOs where aluminium (Al) and gallium (Ga) take the role of substitutional dopants of Zn, akin to Sn in ITO. The substitutional dopants complement the effect of the native defects such as Zn interstitials, oxygen vacancies and shallow H donors. As with $\mathrm{In_2O_3}$, many other dopants [165] have been explored, such as: In [222], silicon (Si) [223], scandium (Sc) [224], yttrium (Y) [224], fluorine (F) [225] and hafnium (Hf) [226]. Each dopant has its own advantages and disadvantages [48].

2.2.5. Scattering Mechanisms and Carrier Transport Properties of TCOs

A meticulous investigation of the different carrier scattering mechanisms at play is required to fully explain the optoelectronic properties of doped $\mathrm{In_2O_3}$ and ZnO. The individual mechanisms are [58,227,228]:

1. Scattering due to lattice vibrations,
2. Ionised impurity scattering,
3. Dislocation scattering,
4. Grain boundary scattering,
5. Neutral impurity scattering.

The total mobility, μ, is obtained by taking into account each contribution *via* Matthiessen's rule [229]:

$$\frac{1}{\mu(N)} = \sum_{\mathrm{i}} \frac{1}{\mu_i} \tag{2-49}$$

where μ_i is the mobility as limited by a particular scattering mechanism.

Ionised Impurity Scattering

In TCOs, the metal-like conductivity arises from the high carrier concentration that originates from the high number of both native (*i.e.,* oxygen vacancies) and intentional (*i.e.,* Sn, Al and Ga) donors. The donors contribute free electrons to the CB and leave behind localised, ionised impurities in order to preserve the net charge neutrality of the material [230]. The positively charged ionised impurities create a localised Coulomb potential that leads to electron scattering during their transport. Conwell and Weisskorf [231] were the first to derive the formula for the ionised impurity scattering (IIS) limited mobility, μ_{IIS} [232]:

$$\mu_{IIS}(N_Z, Z, T) = \frac{128\sqrt{2\pi}(\varepsilon_r\varepsilon_0)^2(k_B T)^{\frac{3}{2}}}{\sqrt{m_e^*}Z^2 e^3 N_Z} \cdot \frac{1}{F_{IIS}(Z, N_Z, T)} \tag{2-50}$$

where ε_r and ε_0 are the relative static permittivity and permittivity of free space, respectively, k_b is the Boltzmann constant, T the temperature, m_e^* the effective carrier mass and e the carrier charge. Z and N_Z are the charge and concentration of the ionised impurity, respectively, and F_{IIS} is the screening function, given by:

$$F_{IIS}(Z, N_Z, T) = \ln\left(1 + \left[\frac{12\pi\varepsilon_r\varepsilon_0 k_B T}{Ze^2 N_Z^{\frac{1}{3}}}\right]^2\right) \tag{2-51}$$

Vitally, the Z dependence of μ_{IIS} infers that the intrinsic doping of oxygen vacancies ($Z = 2$) leads to a $\sim$2 times lower mobility than the extrinsic metal substitutional dopants where $Z = 1$ and that metal interstitial dopants with $Z = 3$ gives rise to even lower mobilities.

However, this approach does not take into account the screening of ionised impurities by the charge carriers, which has the effect of altering the screening function to become [228]:

$$F_{IIS}(\zeta) = \ln(1+\zeta) - \frac{\zeta}{1+\zeta()} \tag{2-52}$$

with

$$\zeta(Z, N_Z, T) = \frac{96\pi^2 \varepsilon_r \varepsilon_0 m_e^*}{N_Z} \left(\frac{k_B T}{he}\right)^2 \tag{2-53}$$

where h is Planck's constant. For degenerate semiconductors, where N is high (such as the TCOs investigated in this work), or at low temperature, the expressions from considering a truncated Coulomb potential, given by Eqs. (2-54)-(2-55), are used instead of Eqs. (2-52)-(2-53) [233]:

$$\mu_{IIS}(N, N_Z, Z) = \frac{3(\varepsilon_r \varepsilon_0)^2 h^3}{Z^2 m_e^{*2} e^3} \cdot \frac{N}{N_Z} \frac{1}{F_{IIS}(\zeta_d)} \tag{2-54}$$

where F_{IIS} is the screening function of Eq. (2-52) but ζ is replaced with ζ_d:

$$\zeta_d(N) = (3\pi^2)^{\frac{1}{3}} \frac{\varepsilon_r \varepsilon_0 h^2 N^{\frac{1}{3}}}{m_e^* e^2} \tag{2-55}$$

Eq. (2-54) takes into account that not all impurities may be ionised ($N \neq N_Z$), but at room temperature the assumption that $N = N_Z$ is justified and the second term becomes unity, so that μ_{IIS} is dependent only on N and Z. Importantly, the temperature dependence of μ_{IIS} disappears for such a deviation and the temperature invariance of μ is often used to characterise materials where IIS is dominant [228]. However, this model still fails to account for the significant decrease in the mobility that is found for TCOs with $N > {\sim}5 \times 10^{20}\ \mathrm{cm}^{-3}$. The cause for the more intense scattering above this threshold has been ascribed to impurity clustering based on a statistical argument outlined by Dakhovskii *et al.* [228], although a full theoretical formulation of such interactions has, as of yet, not been established. Furthermore, for real materials there potentially exist many types of ionised impurity species (oxygen vacancies, interstitial oxygen atoms, interstitial hydrogen atoms, substitutional metal atoms, interstitial metal donors *etc.*). Therefore, the theoretical modelling is insufficient to describe the combined effect of IIS and so the $\mu(N)$ relation for TCOs has been fit with an empirical formula of Masetti *et al.* [234].

$$\mu(N) = \mu_{min} + \frac{\mu_{max} - \mu_{min}}{1 + \left(\frac{N}{N_{IIS}}\right)^{\alpha_{\mathrm{IIS}}}} - \frac{\mu_1}{1 + \left(\frac{N_{ICS}}{N}\right)^{\alpha_{\mathrm{ICS}}}} \tag{2-56}$$

where μ_{max} is indicative of the lattice mobility ($\mu_{max} \approx \mu_L$), μ_{min} the ionised impurity inhibited mobility ($\mu_{min} \approx \mu_{IIS}(N = N_{ref2})$) and $\mu_{min} - \mu_1$ of the ionised cluster inhibited mobility. N_{IIS} and IIS, are the transition concentration and coefficient, respectively, for ionised impurities while N_{ICS} and α_{ICS} are the transition concentration and coefficient, respectively, for clusters of ionised impurities.

Neutral Impurity Scattering

Not all impurities effectively donate electrons to the CB, and thus remain as neutral impurities within the lattice. The origins of the neutral impurities have been presumed to arise from two kinds of crystallographic faults: point defect aggregates and locally strained areas. For ITO these local areas are associated with low grade oxides of $\mathrm{In_2O_3}$ ($\mathrm{In_2O_{3-x}}$) [235] and/or Sn-oxide defect complexes such as $[\mathrm{Sn_2O_i''}][\mathrm{Sn_2O_4}]^{\mathrm{x}}$ [236]. For ZnO, neutral oxygen vacancies and zinc-oxygen dimer vacancies and hydrogen vacancies have been explores as the source of neutral impurities [150]. These defects result in carrier scattering that is described by the neutral impurity limited carrier mobility, μ_{NIS} [237]:

$$\mu_{NIS}(N) = \frac{\mathrm{m_e^*}e^3}{20\varepsilon_r\varepsilon_0\hbar^3 N_{NI}} \tag{2-57}$$

where N_{NI} is the concentration of neutral impurities.

Grain Boundary Scattering

There is a high density of grain boundaries associated with polycrystalline films, such as room temperature deposited AZO and GZO [136,238,239]. The mechanism behind the scattering of carriers by grain boundaries is referred to as grain boundary scattering (GBS) and was first modelled by Seto in 1975 [240]. Fig. 2-11 presents the schematic diagram of Seto's model in three cases: a low, mid-range and high-N.

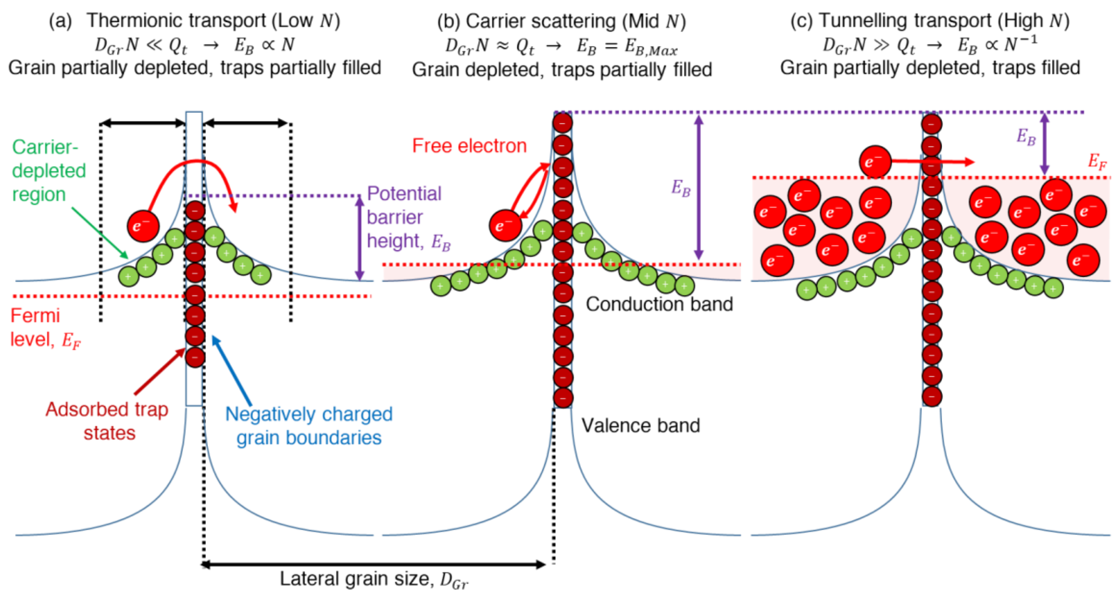

Fig. 2-11. Schematic band diagrams in the grains for different doping concentrations: (a) very few carriers, (b) similar carrier density and trap density and (c) a very high number of free carriers. The free carriers, trap states and depleted holes are shown as the red, dark red and green dots, respectively. The fermi energy and the potential barrier height are indicated by the dotted red and purple lines, respectively. Adapted from [241].

The grain boundaries are attractive sites for the diffusion of ionised trap states. This results in the formation of negatively charged grain boundaries [242], causing band bending and the creation of potential barriers between grains (purple dashed lines in Fig. 2-11) and carrier depleted regions on either side of the grain boundary (green dots in Fig. 2-11). Thus, the formation of negatively charged grain boundaries can impede the transport of carriers between grains [228,243]. The effect of the grain boundaries is strongly dependent on N, the grain size, D_{Gr}, and the trap density, Q_t. Specifically, for very low N ($\ll Q_t/D_{Gr}$) the number of trap states associated with the donor states is low so that the grains are only partially depleted, the traps partially filled and the potential barrier height, E_B, is low. This allows for thermionic transport of the carriers across the grain boundary, only marginally reducing μ. For intermediate N ($\approx Q_t/D_{Gr}$), the grain is fully depleted, and the traps are partially filled. Therefore, E_B is too high to allow for thermionic transport and the carriers are completely scattered by the grain boundaries so that $\mu \approx 0$. Finally, for heavily doped films the high number of free carriers exceeds the number of traps states so that only a small portion of the grain is carrier depleted. The free carriers effectively screen the grain boundary, reducing the width of the potential barrier and enabling tunnelling transport. Baccarani *et al.* [244] improved on Seto's model by including continuous energy at the depletion zone:

$$\mu_{GBS}(N) = \mu_0(N) \exp\left(-\frac{E_B(N)}{k_b T}\right) \tag{2-58}$$

for which the formulation of $E_B(N)$ changes depending on whether the grain is fully depleted and the traps are partially filled (Fig. 2-11a-b; Eq. (2-59)), or the grain is partially depleted while the traps are fully filled (Fig. 2-11c; Eq. (2-60)) [240].

$$E_b(N) = \frac{e^2 Q_t^2}{8\varepsilon_r \varepsilon_0 N}, \quad for \;\; LN > Q_t \tag{2-59}$$

$$E_b(N) = \frac{e^2 {D_{Gr}}^2 N}{8\varepsilon_r \varepsilon_0}, \quad for \;\; LN < Q_t \tag{2-60}$$

$$\mu_0(N) = \frac{e D_{Gr}}{\sqrt{2\pi m_e^* k_b T}} \tag{2-61}$$

Scattering by grain boundaries is expected to play a subordinate role if the mean free path, l_e, of electrons much smaller than the crystallite size, as most electrons would scatter before they reach a grain boundary [245]. l_e can be calculated using a highly degenerate electron gas model [246–248]:

$$l_e(N) = \tau(N) v_F(N) \tag{2-62}$$

where v_F is the Fermi velocity, given by [113]:

$$v_F(N) = (3\pi^2)^{\frac{1}{3}} \frac{\hbar}{m_e^*} N^{1/3} \tag{2-63}$$

3. Experimental Methods

3.1. Material Fabrication and Processing

Thin film materials are adopted for a vast range of applications and are an essential ingredient of modern electronics. Furthermore, one of the most promising solutions to the fast approaching fundamental speed and bandwidth limitations, which arise from the miniaturisation of semiconductor devices, circuits and components, is to replace the electronic signals with light [3]. As explored, plasmonics can extend our ability to make new, faster, and smaller information technology devices by going beyond the diffraction limit. This inherently drives the need for even thinner films and/or nanoparticle templates. One of the most promising methods for the fabrication of such plasmonic architectures is a top-down approach that takes advantage of modern thin film deposition and photolithography techniques [249,250]. There exist a wide variety of well-established methods for thin film fabrication, each with its own strengths and weaknesses such as the cost, scalability, reproducibility as well as the ability to produce films with a high enough "quality" for a particular application. Vitally, the deposition technique and conditions define the resulting physical properties of the thin film. Deposition techniques can be broadly classified into three key groups: chemical vapour deposition, physical vapour deposition and wet chemical deposition [75,251]. TCOs have been deposited with various solution and vacuum based methods. In recent years, solution-based techniques such as spin-coating have shown an increasing promise for cost-effective and scalable applications. However, there is generally a requirement for post-deposition processing with long dwell times ($> 1\ \mathrm{hr}$) and at high temperatures ($> 350\ °\mathrm{C}$) in order to form the metal oxide framework as well as increase the material densification to the standards required for electronic device applications [252,253]. For TCOs, sputter deposition is the most well-established technique with a long history of producing high-quality, large-area, uniform and pure films within research and industry. Extensive reviews of the sputtering of TCOs have been given elsewhere [48,49,170,173]. Therefore, it is the primary deposition technique utilised in this work.

Fig. 3-1. Commonly used thin film deposition techniques, adapted from [75,251].

Post-growth annealing is usually a required step used to enhance the structural and optoelectronic properties of room temperature sputtered TCOs. Due to its simplicity, thermal annealing (TA) is the most common approach. Vitally, TA of TCOs in various ambient environments has been shown to be able to probe the defect composition and thereby tune to optoelectronic properties of TCOs [51,254]. However, TA requires long dwell time and/or high temperatures and, due to the bulk heating, demands the use of expensive rigid substrates [59,65,70]. Laser annealing (LA) overcomes these issues by offering an ultra-rapid processing with heating selectivity [61,255]. A more extensive review of the theory and experimental details for LA is given in the next chapter (Section 3.1.2). It should be noted that only limited studies have been reported on laser annealing of ITO, AZO and GZO. Such studies have been recently reviewed and summarised by Yarali, Koutisaki and colleagues [61]. Furthermore, at the time of writing there are currently no studies into the use of reactive environments to tune the optoelectronic properties of TCOs towards the requirements of IR plasmonics.

This remainder of this chapter gives an overview of the deposition (Section 3.1.1), post-deposition processing (Section 3.1.2) and characterisation (Section 3.2) techniques utilised in this project.

3.1.1. Magnetron Sputtering

Sputtering is a type of physical vapour deposition that deposits a material onto a substrate by removing (sputtering) atoms from the surface of a solid target *via* energetic gas ion (plasma) bombardments [72,73]. Sputtering is a well-established technique for mass production and research of various thin film materials due its simple, safe, and scalable nature and ability to produce films with high uniformity, purity, and substrate adherence. Furthermore, sputtering of good quality TCO films is possible with a low (or no) substrate heating, ensuring minimal thermal effects during deposition [256–258]. There exist a high level of reproducibility and control on the sputtering process due to the small set of tuneable deposition parameters that govern the properties, thickness and composition of the deposited films [259]. The drawbacks of sputtering are that high or ultra-high vacuum systems are required (expensive for set-up and operation), there is poor utilisation of the target materials and that a large portion of the energy of the sputtering gas ions become heat in the target that requires effective cooling. With an understanding of the physics of the sputtering process, it is possible to infer what the effect of changing each deposition parameter can have on the resulting film properties. Therefore, a brief overview of the sputtering process is given below.

Firstly, the sputtering chamber is pumped down to high or ultra-high vacuum. Within the vacuum chamber, an electric field is created between the substrate holder and chamber walls (anode) and the target material (cathode). A sputtering gas that is non-reactive, has sufficiently heavy ions and a relatively low ionisation potential (typically argon, Ar) [72] is then introduced to the chamber. The “primary” electrons, travelling between the anode and cathode, collide with the argon atoms producing ionised or excited Ar species. An additional electron, e^{-}, is produced alongside each Ar^{+} ion and may participate in further ionisations. The excited Ar^{*} atoms will return to their ground state subsequently emitting a photon, which can be seen within the chamber as a glow discharge. The positively charged Ar^{+} ions are accelerated towards the target resulting in a sequence of bombardments:

i. Sputtering (removal) of neutrally charged or ionised atoms from the target surface,
ii. “Secondary” electron emission from the target material,
iii. Reflection of argon ions as energetic neutrals,
iv. Implantation of highly energetic argon ions into the target material.

Finally, the sputtered species travel around the chamber. The low-pressure environment of the chamber ensures a relatively large mean free path (*i.e.*, few collisions) and thus most of the kinetic energy of the sputtered species is retained as they arrive at the substrate. The neutrally charged species arrive at the substrate like “upside down snowfall”,

where the incorporation of the species into the film is largely defined by the energy of the species as it reaches the film. The sputtering deposition rate can be enhanced by introducing a permanent magnetic field just behind the target. This qualifies the process as "magnetron sputtering". Generally, a magnetic field strength of $20 - 50\ \mathrm{mT}$, with field lines mostly parallel to the target surface, is used to sufficiently confine electrons to the target surface without affecting the Ar^+ ions [73]. This increases the plasma density close to the target surface, resulting in higher sputtering rates and preventing secondary electrons from travelling near the substrate (avoiding unintentional substrate damage and/or heating).

There are two key categories of magnetron sputter-deposition systems that are defined by how they are powered. In this work, a radio frequency (RF) power is used instead of a direct current (DC) power. This is because, despite its more cost-effective and simple nature, DC sputtering is hindered by the positive charges that accumulate at the target surface during sputtering [72,260]. RF sputtering overcomes this issue by applying an alternating electric field with a high operating frequency ($13.56\ \mathrm{MHz}$) that can achieve a quick polarity alternation. This results with an alternation between Ar^+ and e^- bombardment of the target ensuring that the positive charges that are accumulated due to Ar^+ bombardments are neutralised during the positive half of the RF signal. Vitally, the quick polarity alternation ensures that the Ar^+ ions are unaffected as their mass is much greater than that of the electrons. A further classification of sputtering is whether the technique is "non-reactive" or "reactive". The former refers to the above where only non-reactive gasses such as Ar are present in the chamber during deposition. The latter denotes that there exist one, or multiple additional elements introduced to the chamber which may interact with the material in order to manipulate its compositional properties [75,251].

Experimental Details

In this work, TCO thin films were deposited onto (100) oriented n-type Si wafers $(1 - 10\ \Omega\mathrm{cm})$ *via* RF reactive magnetron sputtering, with no intentional substrate heating. 3” $(7.62\ \mathrm{cm})$ ceramic targets $(99.99\%$ purity) of $10\ \mathrm{wt.\%}\ \mathrm{Sn} - \mathrm{In_2O_3}$, $2\ \mathrm{wt.\%}\ \mathrm{Al_2O_3} - \mathrm{ZnO}$ and $5\ \mathrm{wt.\%}\ \mathrm{Ga_2O_3} - \mathrm{ZnO}$ were utilised to deposit tin-doped indium oxide (ITO), aluminium-doped zinc oxide (AZO), and gallium-doped zinc oxide (GZO), respectively. The sputtering system is illustrated in Fig. 3-2 and consists of:

1. A sputtering chamber with two water-cooled magnetron-equipped electrodes (for ceramic targets with a $3''$ diameter and $5\ \mathrm{mm}$ thickness) and a rotating substrate holder (for $4''$ wafers). The electrodes are tilted in a “sputter-up” geometry with a fixed target-substrate distance of $\sim 10\ \mathrm{cm}$ and are “aimed” at $2/3$ across the substrate surface in order to enhance the sputtered atoms surface mobility and film uniformity and reduce film damage that can arise from substrate-facing-target arrangements [72].
2. A load lock chamber with a transferable sample holder arm, which can be isolated from the main chamber *via* a knife valve, which enables loading and unloading of samples without venting the main chamber.
3. A two-fold pumping system comprising a diffusion and rotary pump (in series connection) that can evacuate the main chamber to $\sim 10^{-7}\ \mathrm{mbar}$ and ensure a steady pressure during deposition. The pressure within the chamber during sputter ignition and deposition is regulated *via* a baffle valve. The rotary pump pumps the load lock chamber to $\sim 40\ \mathrm{mTorr}$ before opening the knife valve, to minimise pressure build up in the main chamber.
4. A water-cooling system cools both the diffusion pump (higher flow circuit) and the electrodes (lower flow circuit). The lower flow circuit can be isolated from the main circuit for maintenance without requiring the disabling of the diffusion pump.
5. An $13.56\ \mathrm{MHz}$ RF power source with a variable power of $0 - 330\ \mathrm{W}$ (in steps of $1\ \mathrm{W}$) and an output impedance of $50\ \Omega$.
6. Tuning and matching units that tune the plasma impedance to the RF power impedance, ensuring maximum power transfer from the RF power source to the plasma.
7. Three mass flow controllers (Ar, $2\%\ \mathrm{O_2}$ in Ar, and $\mathrm{O_2}$) with a corresponding gas supply and regulation system capable of providing accurate and steady flow and mixing of the desired deposition gasses.
8. A red diode laser reflected from the centre of the sample to an external sensor enabling live interferometric monitoring of the film thickness.

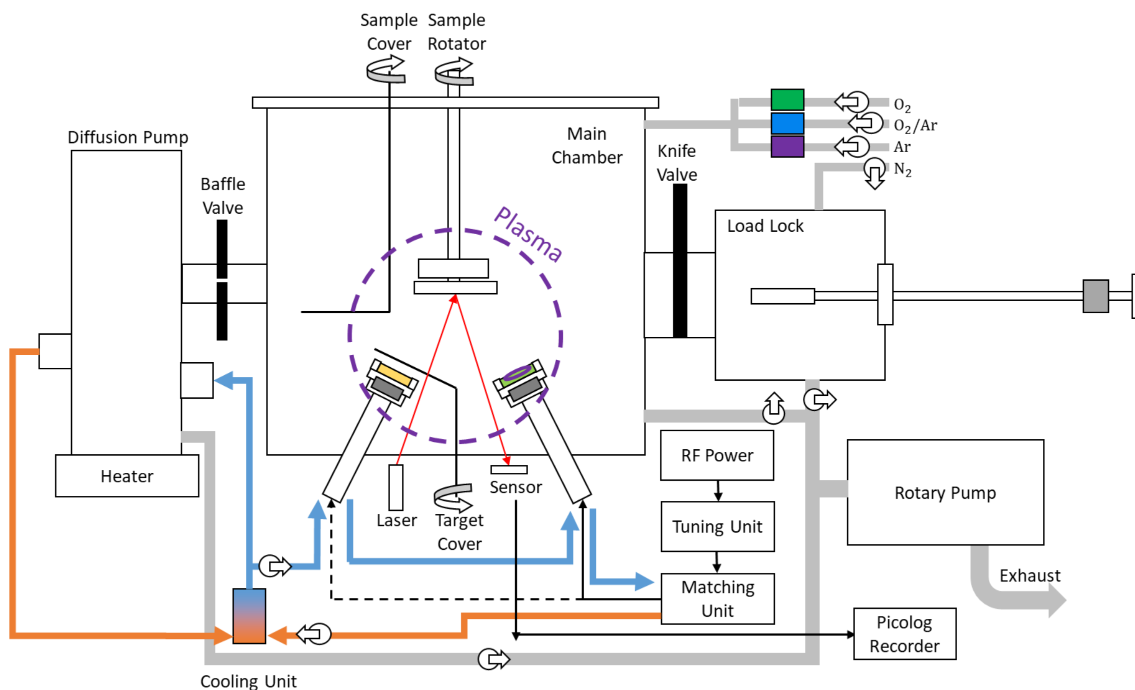

Fig. 3-2. Schematic diagram RF magnetron sputtering system (during sputtering) used in this work, consisting of a main chamber with two sputtering electrodes, a sample rotator, sample cover, target cover and interferometry system. The electrodes are powered with an RF power supply attached to a tuning and matching unit, ensuring maximum power transfer. A knife valve connects the main chamber to a load lock with an N_2 inlet and a baffle valve connects the main chamber to a diffusion pump which is subsequently pumped with a rotary pump. The main chamber has three gas inlets for O_2, 2% O_2 in Ar and Ar. The electrodes and diffusion pump are cooled with an internal cooling system. The blue and orange arrows indicate the flow of the water from cold to hot, respectively. The purple circle with dashed edges indicates the region of plasma.

3.1.2. Excimer Laser Annealing

Generally, thin films grown with physical vapour techniques such as sputtering do not immediately possess the desired physical properties, especially when grown at room temperature [61]. This can be the result of the kinetic energy during growth resulting in less energy for atomic rearrangement and so the entropy and defect density are high. To alleviate this, post-growth annealing techniques are employed to further optimise the structural, compositional, and thus optoelectronic properties of thin film materials. The annealing involves increasing the temperature of the thin film to a desired temperature, T, and keeping it at this temperature for a specific "dwell time", t_d, before allowing the film to slowly, or rapidly, cool down to room temperature. While the film is heated, the thermal energy enables a rearrangement of the atoms and can alter the film microstructure, stoichiometry, and the

density and/or distribution of defects. For example, it has been shown that manipulation of the ambient environment (particularly the oxygen content) during thermal annealing can probe the oxygen content within the film in the form of creating and removing oxygen vacancies, enabling one to tune the carrier concentration, N [51,254].

The most common techniques for annealing of TCOs are indirect annealing techniques such as conventional furnace heating and rapid thermal annealing [61,164,261–266]. For such techniques, the film is said to be indirectly annealed as the processing heat is generated externally and transferred to the film by radiation, conduction or convection [64]. However, in recent decades the remarkable capabilities of more "direct" annealing techniques, such as laser annealing (LA), to improve the optoelectronic properties of TCOs have become more and more apparent [59, and references within]. The direct nature of the annealing refers to the fact that the processing heat is generated within the processed film itself. During LA, the heat arises from the film absorbing high energetic photons. Vitally, the use of high energy lasers such as excimer lasers allows for an ultra-fast (few ns) annealing process that is able to match the high thermal energy demand of metal-oxides and the thermal dose is spatially localised, allowing for micro-patterning of the annealed areas and the use of heat sensitive substrates [59,61]. LA has recently become a well-established technique for the processing of metal-oxides to improve their optoelectronic characteristic for a range of novel optoelectronic devices such a thin film transistors, light emitting diodes, sensors and photovoltaics [59,70,253,267–271], to name but a few [61]. However, research into the effect of the LA environment to probe the defect composition of TCOs (as seen for TA) is currently lacking [61].

Excimer laser annealing (ELA), simply referred to as LA henceforth, uses UV photons with energies larger than the optical bandgap of a material to promote an intense light photon absorption. Due to the high energy, the excited electrons perform a multi-phonon cascade emission as they de-excite. The emitted phonons carry the laser energy as thermal energy throughout the film, dramatically increasing the temperature within the film and producing the annealing effect. As the laser pulse profile is usually a few tens of nanoseconds and the de-excitation occurs within the vicinity of a few tens of picoseconds, the annealing processing is ultra-fast [272]. The absorption of the UV photons is dependent on the optical properties of the thin film. Specifically, the absorption coefficient, $\alpha(E)$, and thus the imaginary permittivity (Eq. (2-19)), defines the strength of the absorption and the penetration depth, δ_p, of the laser photons (Eq. (2-20)). If the thin film thickness is much larger than the penetration depth, then most of the laser induced heating described above will only apply to the upper portion of the film. The rest of the film will be, by some extent, more indirectly heated by the diffusion of the

heat from the upper layer. This process will be governed by the thermal diffusivity, D_h, of the material (Eq. (3-1)) [76]:

$$D_h(T) = \frac{K(T)}{\rho_M(T)C(T)} \tag{3-1}$$

where $\rho_M(T)$ is the material density, $K_T(T)$ the thermal conductivity and $C_V(T)$ the specific heat capacity, which are all temperature dependent. The thermal diffusivity is used to estimate the heat diffusion length, $L_t(T)$, from Eq. (3-2), which is defined as the distance that the laser-generated heat propagates throughout the annealed sample.

$$L_h(T) \approx \sqrt{D_h t_p} \tag{3-2}$$

where t_p is the laser pulse duration. The two-fold heating process of the laser photon absorption in the upper film and the heat diffusion throughout the film means that there a temperature gradient between the surface layer with high T and the layers below with lower T. This can result in an inherent depth dependence to the LA process [59]. The temperature dependence of $D_h(T)$ and $L_h(T)$ and the understanding that the heat will continue to diffuse even after the laser pulse stops highlight that there are no simple solutions to determining the thermal distribution during LA. Instead, to find fundamental properties of the thermal dose, such as the peak temperature, one requires numerical solutions to the 1D heat transport equation that takes into account the spatial and temporal profile of the laser pulse alongside the material properties [61].

Experimental Details

The LA system utilised for this research is illustrated in Fig. 3-3. There are three key components of the LA system: (a) the laser source, (b) the beam delivery system and (c) the sample stage. The system is designed in a way that allows for the control over all the LA parameters outlined in Fig. 1-2. The first part (a), the laser source, is a Krypton Fluoride (KrF) excimer laser (Lambda Physik LPX 305i) that emits pulses of un-polarised light with an energy of $5\ \mathrm{eV}$, a pulse duration of $\sim 25\ \mathrm{ns}$ and an average energy per pulse of up to $1.5\ \mathrm{J}$. The beam-delivery system comprises a variable attenuator to adjust the energy of each laser pulse, a beam homogeniser (Exitech Ltd., type EX-HS-700D) to ensure a uniform laser "spot" at the sample, a field lens, a mask stage for different mask sizes, and a projection lens with $\times\ 1.0$, $\times\ 1.7$ or $\times\ 5.0$ magnification. Additional mirrors are used to guide the beam through the system towards the sample. The beam delivery system converts the raw laser beam into a focused, rectangular, laser spot at the sample surface that has a below $\pm 2\%$ uniformity across the irradiated area of the sample. To examine the laser energy delivery, E_L, an energy monitor was placed between the mask and the projection lens between pulses. The energy density or laser fluence, J_L (expressed in $\mathrm{mJcm^{-2}}$), that determines the strength of the annealing is calculated from E_L and the area of

the sample spot, A. Finally, the sample stage, houses the sample and manipulates it as required. A computer controlled xyz translation stage with micro-precision is used to facilitate large area laser processing and allows for micro-patterning. Furthermore, a pressure cell with a UV transparent window surrounds the sample. This enables control over the sample environment (pressure, ambient composition) to achieve the desired annealing result. The pressure cell contains gas inlets for 5% H_2 in N_2, O_2, Ar and N_2 and can support up to 150 psig of each gas, or mixture of gasses, where the pressure is monitored with a pressure gauge. Prior to processing, the pressure cell is vented 3 times using the desired gas mixture to ensure the correct mixture is achieved.

Due to the variation of the laser energy and the requirement of an energy monitor calibration when setting the laser fluence prior to laser processing, the "actual" fluence deviates from the "desired" fluence, and the error is larger than the recorded energy range due to the propagation of the variation with each step. This is recorded by noting how the "desired" monitor energy, $E_{Mon,Desired}$, compares to the desired fluence, $J_{L,Desired}$, (Eq. (3-1)) and subsequently how the "actual" monitor energy, $E_{Mon,Actual}$, prior to annealing compares to $E_{Mon,Desired}$ (Eq. (3-2)).

$$E_{Mon,Desired} = A \cdot c_{Lens+Cell} \cdot J_{L,Desired} \tag{3-1}$$

$$J_{L,Actual} = J_{L,Desired} \cdot \frac{E_{Mon,Actual}}{E_{Mon,Desired}} \tag{3-2}$$

where $c_{Lens+Cell}$ is a correction to the monitor energy due to the change in monitor position during laser processing (*i.e.,* the laser energy loss due to the focus lens and pressure cell window). This depends on the lenses used, and is found, for each lens magnification, by taking the gradient of the monitor position energy against the sample position energy during calibration.

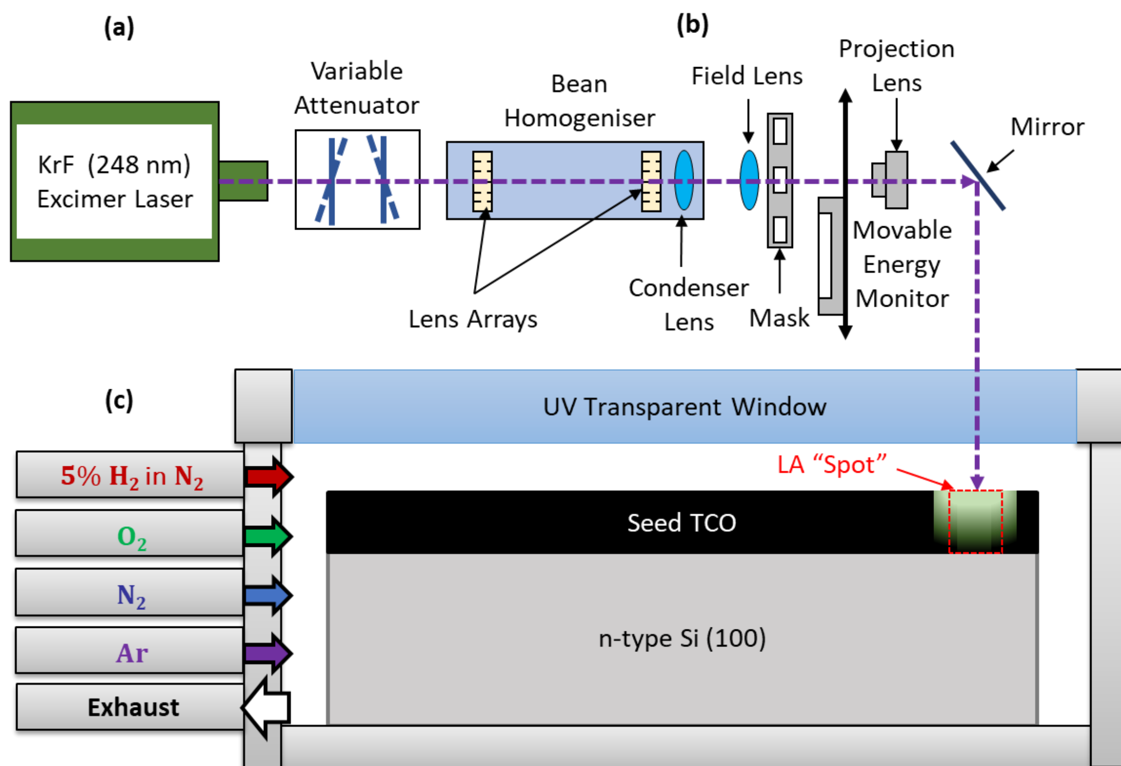

Fig. 3-3. Schematic diagram of the LA system used in this work showing the (a) laser source, (b) beam delivery system consisting of a variable attenuator, beam homogeniser, field lens, mask, projection lens and a movable energy monitor and (c) the sample environment where the thin film TCO (black rectangle) on an n-type Si wafer (grey rectangle) resides inside a pressure cell, with gas inlets for 5% H_2 in N_2, O_2, Ar and N_2 and an exhaust, on an xyz translation stage. The laser processed "spot" defined by the lens magnification and the mask is indicated by the red rectangle with a dashed outline. The annealed region is indicated by the green colour within the film, where there exists an upper layer that increases rapidly in temperature due to the absorption of the KrF laser photons, and a thermal gradient further down into the film resulting from heat diffusion.

3.2. Characterisation techniques

Various characterisation techniques have been employed in order to investigate the structural (Section 3.2.1), morphological (Section 3.2.2), compositional (Section 3.2.3), electrical (Section 3.2.4) and optical (Section 3.2.5) properties of the seed and laser processed TCO thin films. Specifically, the techniques utilised were X-ray diffraction (XRD), scanning electron microscopy (SEM), transmission electron microscopy (TEM), X-ray photoelectron spectroscopy (XPS), electron dispersive X-Ray spectroscopy (EDX), four-point probe (4pp), Van der Pauw (VdP), Hall effect, optical reflection spectroscopy (ORS), IR transmission (IRT), and spectroscopic ellipsometry (SE). In the following section, a comprehensive overview of each technique, alongside specifics for the utilised equipment is presented.

3.2.1. Structural

X-ray diffraction (XRD)

XRD is a popular, non-destructive technique that reveals the microstructural properties of materials [273]. Specifically, XRD can determine the: crystalline phase, grain size, crystallographic orientations, inter-planar spacing of the structure, lattice constants and the micro- and macro-strain. XRD utilises a monochromatic X-Ray beam with a specific wavelength, λ, directed at a sample surface at a known angle of incidence, θ. The X-rays penetrate deeply inside the sample and scatter off the atoms within the material that are arranged in $3\mathrm{d}$ crystallographic planes spaced with distance of d (the d-spacing). Constructive inference of the X-rays occurs when the path difference ($2d\sin(\theta)$) is integer number, n, of X-ray wavelengths [274–277], as defined by Bragg's law (Eq. (3-3)). This is demonstrated schematically in Fig. 3-4.

$$\mathrm{n}\lambda = 2d\sin(\theta) \tag{3-3}$$

XRD can be performed in either two geometries: grazing-incidence XRD (GI-XRD) and Bragg-Brentano XRD (BB-XRD) (also known as $\theta/2\theta$ scan mode). In this work, the BB-XRD geometry is used, where the sample is rotated at an angle θ and the detector at 2θ. A Bragg peak will be present at detector values of 2θ whenever Bragg's law is satisfied. Because the sample and detector angles are mutually dependent, the geometric configuration is maintained, and the measured scattered X-rays always originate from crystallographic planes parallel to sample surface. Vitally for this work, this plane is correlated to the growth and LA process. Conversely, GI-XRD detects crystallographic planes of different angle with respect the film surface (and growth direction) [274–277]. During an XRD measurement, the beam scans across many angles in order to build an X-ray diffractogram that contains the measured intensity as a function of θ. Using Bragg's law, the maxima in the diffractogram provide the d-spacing and thus a collection of maxima across a wide-angle range can be used to determine a particular crystal structure. Consequently, the diffractogram acts as a unique structural fingerprint of the measured sample and we can deduce the material crystal phase.

If the X-ray diffractograms of a bulk, uniform and unstressed material is known (readily available in large XRD libraries), it is possible to derive the macro-strain and the texturing (the degree of preferential orientation) from the peak intensity [278]. Likewise, the average particle diameter (or grain size, D_{gr}) and lattice (micro)-strain can be derived from the from the peak broadening. Vitally, the profile of the grain size and micro-strain have a Gaussian and Lorentzian line shape, respectively. In real films, each factor of broadening is usually present and the convolution of all the broadening sources comprises the measured peak profile.

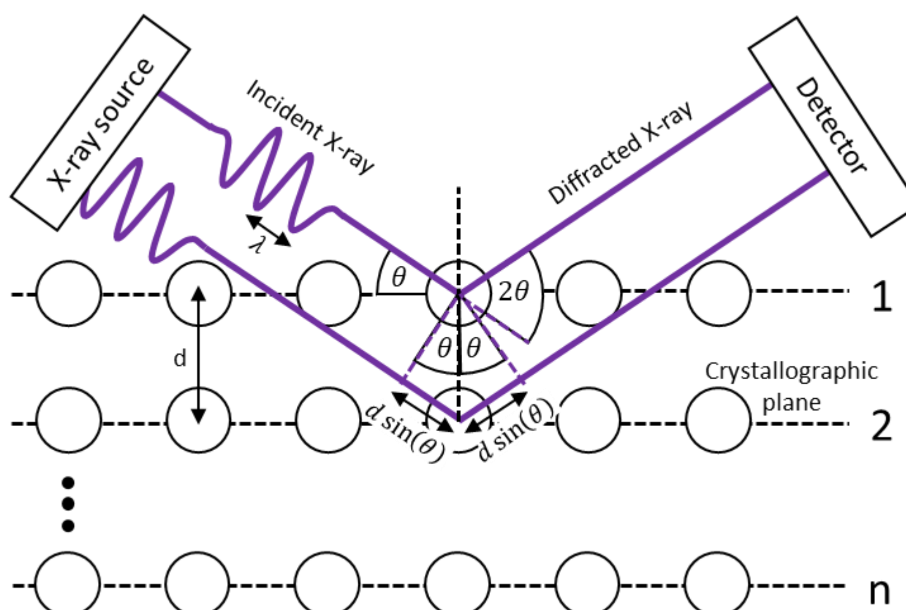

Fig. 3-4. Schematic diagram for Bragg's law of interaction between monochromatic X-ray beams and crystallographic planes within the X-ray diffractometer consisting of a Cu K_α X-ray source providing x-ray photons with $\lambda = 1.5418$ $\AA$ (purple lines), a $\theta - 2\theta$ goniometer stage and a multi-channel detector. The 1^{st}, 2^{nd} and n^{th} crystallographic planes are presented, with the black arrows indicating the spacing d and the additional path length $2d\sin(\theta)$ for diffraction from the 2^{nd} plane.

Subsequently, to quantify the grain size and micro-strain, it is necessary to deconvolute the peak profile into the individual components. Two key methods are commonly applied to achieve this. Specifically, Williamson-Hall analysis and Voigt-function analysis [275]. To determine the two components of the broadening, Williamson-Hall analysis requires multiple large-intensity peaks, from the same material, across a wide-angle range [279]. If only one large peak exists, then Voigt-function analysis is essential. The Voigt function is a convolution of a Gaussian and Lorentzian peak and thus allows us to deconvolute the Bragg peak broadening (after considering the instrumental broadening) into the Gaussian and Lorentzian components.

For thin films, with generally small values of D_{Gr} (< 500 nm) diffraction peak is broadened by an amount dependent on average grain size. This arises from the fact that large grains contain larger number of planes, and thus there are many X-rays scattered at surface that are subject to destructive interference with rays from deeper in the grain. For small grains there are conversely a small number of planes, which leads to incomplete destructive interference for X-rays scattered from sample surface and results in the peak broadening with a Lorentzian distribution. This model was first laid down mathematically by Scherrer [280], who established a formula for the grain size from the peak broadening:

$$D_{Gr} = \frac{K\lambda}{\tau_{GS}\cos\left(\frac{2\theta}{2}\right)} \tag{3-4}$$

where K is a dimensionless constant with a value of 0.94 [275] and τ_{GS} is the peak integral breadth due to grain size (radians). The integral breadth (defined as total area under the peak divided by peak height) has been reported to be more accurate for determining D_{Gr} than the full-width half-maximum (FWHM) of the Lorentzian component, β_L, normally presented instead of τ_{GS} in Eq. (3-4). D_{Gr} related integral breadth is given by [281]:

$$\tau_{GS} = \beta_L \frac{\pi}{2} \tag{3-5}$$

There also may exist residual stresses within the film, and generally this is inevitable during film deposition / processing due to: variations in the coefficients of thermal expansion and lattice parameters between deposited film and substrate, microstructural defects, foreign atoms (substitutional or sputter gas ions), atomic peening (atoms on film surface pushed into the film [275]. Thin film deformation arises in response to the residual stress and gives rise to a uniform and/or non-uniform strain (macro- and micro-strain, respectively). The macro-strain, ϵ_{MaS}, results in an expanding (or contracting) of the unit cell, a larger (or smaller) d-spacing and thus a shift in the peak position. The biaxial strain model [282] gives that:

$$\epsilon_{MaS} = \frac{d_{film} - d_{bulk}}{d_{bulk}} \tag{3-6}$$

where d_{film} and d_{bulk} are the measured thin film and the literature unstrained d-spacing, respectively. d_{film} is measured from XRD data *via* Bragg's law and d_{bulk} for each crystallographic plane with (hkl) is calculated from Eqs. (3-7) to (3-9), depending on whether the crystal structure is cubic, hexagonal or rhombohedral, respectively [275]. The lattice parameters a, c and α, where relevant, are taken from literature.

$$d_{Cubic} = \frac{a}{\sqrt{h^2 + k^2 + l^2}} \tag{3-7}$$

$$d_{Hexagonal} = \left(\frac{4}{3}\left(\frac{h^2 + hk + k^2}{a^2}\right) + \frac{l^2}{c^2}\right)^{-\frac{1}{2}} \tag{3-8}$$

$$d_{Rhombohedral} = \sqrt{\frac{a^2(1 - 3\cos^2(\alpha) + 2\cos^3(\alpha))}{(h^2 + k^2 + l^2)\sin^2(\alpha) + 2(hk + kl + hl)(\cos^2(\alpha) - \cos(\alpha))}} \tag{3-9}$$

The film stress, δ_S, can be calculated from ϵ_{MaS} *via* Eq. (3-10).

$$\delta_S = Y\epsilon_{MaS} \tag{3-10}$$

where Y is the Young's modulus of the material, taken from literature (193.77 GPa for doped In_2O_3 [249], -233 GPa for doped ZnO [283]).

The micro-strain, ϵ_{mS}, constitutes the Gaussian component of the peak broadening, where the weighted average strain can be estimated from:

$$\epsilon_{mS} = \frac{\tau_{mS}}{4\tan(\theta)} \tag{3-11}$$

where τ_{mS} is the integral breadth due to micro-strain (in radians) and is calculated from [284]:

$$\tau_{mS} = \beta_G \sqrt{\frac{\pi}{4\ln(2)}} \tag{3-12}$$

Experimental Details

The utilised XRD system was an X-Pert PanAnalytical Pro Powder Diffractometer operated in Bragg-Brentano configuration and using Cu K_α radiation ($\lambda = 1.5418\ \AA$). The spot size was set to $5 \text{ x } 5\ \mathrm{mm}$ *via* a $10\ \mathrm{mm}$ mask, 2^{rad} soller slits and a programmable divergence slit. Initial $\sim 12\ \mathrm{hr}$ scans were performed over a wide spectral range ($10° - 90°$) so that the most prominent peaks could be identified and then a reduced range with a larger number of scans per steps was used to cover the range of the prominent peak ($25° - 40°$ for ITO and $32° - 37°$ for AZO and GZO), with a step size of $0.0083556°$. The number of scans per step was adjusted for each material to ensure a low signal to noise ratio of the dominant peak ($2000\ \mathrm{s}$ for ITO and $300\ \mathrm{s}$ for AZO and GZO. The very long step time for ITO was required due to the small sample size and amorphous nature of the room-temperature sputtered ITO films [285,286]. Due to the use of a (100) Si substrate, a large sharp peak was present at $33.0°$. This peak drastically interfered with the fitting process and so was manually removed from the data prior to fitting by negating the intensity between $32.8° - 33.2°$. The instrumental contribution (that arises from a non-ideal optics and focus) was determined from a Si standard and was found to be negligible in comparison to the experimentally observed broadening and so was ignored in the analysis. For the TCOs, the dominant Bragg peak ((222) for ITO and (002) for doped-ZnO films) was deconvoluted using a *pseudo*-Voigt function, $pV(2\theta)$ (Eq. (3-13)), which closely approximates a Voigt function using a summation of Gaussian and Lorentz functions. The classification of the function as *pseudo*-Voigt arises from the summation instead of the convolution used for the Voigt function. The peak-fitting was performed with a Levenberg-Marquardt regression algorithm was used to extract the fitting parameters.

$$pV(2\theta) = I\left(\eta e^{-\pi\frac{(2\theta - 2\theta_j)^2}{\beta_G^2}} + (1-\eta)\frac{\beta_L^2}{(2\theta - 2\theta_j)^2 + \beta_L^2}\right) \tag{3-13}$$

where I is the peak intensity and $2\theta_j$ is the peak position.

Multiple Peaks

If there are multiple peaks, then instead of fitting $\beta_L(\theta_j)$ and $\beta_G(\theta_j)$ individually for each peak the grain size, macro-strain and micro-strain are directly fit to the data, ensuring they remain identical for all peaks. This method is in effect identical, mathematically, to performing Williamson-Hall analysis [279].

$$\beta_L(\theta_j) = \frac{2}{\pi}\frac{K\lambda}{D_{Gr}\cos(\theta_j)} \tag{3-14}$$

$$\beta_G(\theta_j) = 8\tan(\theta_j)\,\epsilon_{mS}\sqrt{\frac{\ln(2)}{\pi}} \tag{3-15}$$

where:

$$\theta_j = \sin^{-1}\left(\frac{\sin(\theta_{j,bulk})}{\epsilon_{MaS}+1}\right) \tag{3-16}$$

3.2.2. Morphological

Electron microscopy

Electron microscopy exploits the wave nature of electrons to overcome the diffraction limits of optical microscopy. Due to the very small De Broglie wavelength of fast moving electrons, resolutions of up to $1\ \mathrm{nm}$ are possible, enabling imaging of individual atoms [117]. Transmission electron microscopy (TEM) measures the transmission of electrons through an ultra-thin sample. TEM is a vital tool to study the structural properties of materials due, largely, to its very high spatial resolution and is commonly utilised to characterise the morphology, crystal structure and defects of various materials, especially on the nanoscale [117]. Due to the interaction of electrons with the sample as they pass through, an image of the sample can be formed on those that are transmitted. The electrons that are transmitted usually hit a fluorescent screen which is then imaged by a CCD camera. The image is created through the combination of an objective, intermediate and projector lens with the objective aperture positioned just above the objective lens to enable dark field imaging. Vitally, the TEM column is kept under a high vacuum environment to negate the chance of atmospheric electron scattering. Scanning electron microscopy combines the high spatial resolution of TEM with the capability for depth of field in the scanning image. SEM detects the secondary or backscattering electrons in order to build the image. Therefore, thick samples can be used, and SEM requires minimal sample preparation in comparison to TEM.

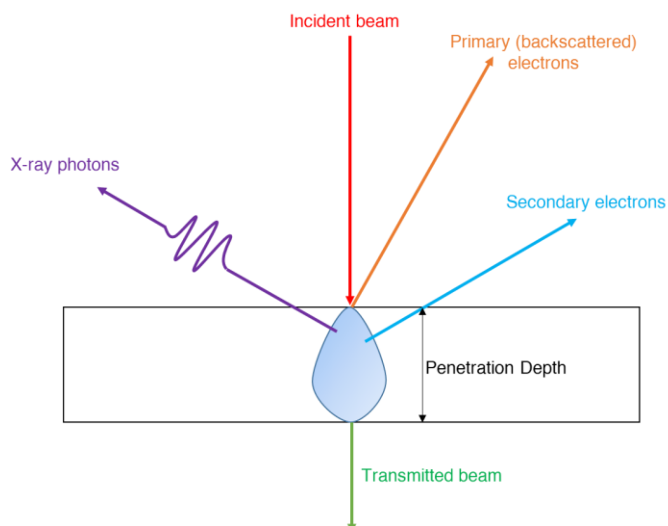

Fig. 3-5. Illustration of electron-matter interactions following bombardment of the material by a beam of fast-moving electrons (red arrow). Primary electrons (orange arrow) are scattered at the surface while secondary electrons (blue arrow) scatter with the "teardrop" covering a penetration depth (black arrow) within the sample, defined by the beam energy and intensity. Characteristic X-ray photons (purple arrow) are emitted from deeper within the teardrop. For very thin slices, a portion of the electron beam is transmitted.

Experimental Details

Cross-sectional images of the transmitted and backscattered electrons for an indicative set of ITO thin films were obtained *via* a high-resolution scanning TEM (FEI™ Talos sTEM) using a Schottky-type field emission gun operated with a tension of $200\ \mathrm{kV}$. Prior to TEM, the films were subject to focused ion beam (FIB) milling process using a JEOL 4500 FIB/SEM. This process used the "trench technique" to thin a small rectangular lamella of material to achieve a sufficiently thin sample that is transparent to the electron beam [287]. The lamella is then extracted and placed onto a TEM grid ready for measurement.

3.2.3. Compositional

Electron dispersive X-Ray spectroscopy (EDX)

Energy dispersive X-ray spectroscopy (EDX) enables qualitative and quantitative characterisation of the chemical composition of the measured ITO samples. EDX analyses the X-ray photons that are emitted when the sample is bombarded with a focused beam of highly energetic electrons within a vacuum (see Fig. 3-5). The X-ray photons are produced when outer-shell electrons fill the core-holes that are produced when the electrons are ejected by the incoming beam. Consequently, the emitted X-rays are characteristic of the atoms from which they are emitted as the photon energy, $E = \hbar\omega$, is dependent on the atomic number [288,289]. An electrical signal that is proportional to the energy of the X-rays is collected by an energy dispersive detector and fed to a software that analyses the energy spectra containing multiple peaks. The position of the peaks (or "X-ray lines") are related to the shell in which the core-hole is created by the incoming electron bombardments and are assigned to a specific element. The intensity of the peaks is related to the concentration of each element.

Experimental Details

EDX was performed for an indicative set of ITO thin films with the FEI™ Talos sTEM during acquisition of lower-resolution SEM measurements alongside the TEM imaging of a selection of seed and laser processed ITO samples. The peak intensity for the X-ray lines of indium, tin, oxygen, and silicon were collected by raster scanning the electron beam across ion beam milled sample slice. This allowed for EDX imaging of the peak intensity related to each relevant element across the entire sample depth.

X-Ray photoelectron spectroscopy (XPS)

X-ray photoelectron spectroscopy (XPS) is one of the most prevalent techniques used to analyse the composition of materials. Alike EDX, XPS can be used to elucidate the precise relative elemental abundances but goes further by providing information of the chemical states of each element (*e.g.,* the oxidation states) and the electronic distribution. The core mechanism that underpins an XPS measurement is the photoelectric effect, illustrated in Fig. 3-6. X-ray photons arrive at the sample and interact with the atoms' electrons transferring all their energy to a bound electron and causing emission of photoelectrons. The kinetic energy of each emitted electron, E_K, is recorded and the binding energy of the electrons in an atomic orbital, E_B, is estimated *via* Eq. (3-17) [290]:

$$E_B = E - E_K - \phi \quad (3\text{-}17)$$

where ϕ is a work function-like term that can be thought of as an instrumental correction factor for the XPS system, representing the minimum energy required to eject and electron from the

highest occupied level to the vacuum. Therefore, the energy of the photoelectrons is related to the atomic and molecular environment that spawned the emission and therefore can serve as a unique fingerprint of each element. The electrons are collected by a detector which can measure E_K using a combination of an electron optic-retardation lens and energy analyser. In order to reduce the chance for photoelectron collision and surface contamination, the sample is kept under ultrahigh vacuum ($< 10^{-7}$ Pa). By performing a scan across a wide range of E, from core to valence levels, multiple photoelectron species can be observed and elemental identification can be performed from the binding energy spectrum (BES) [290,291]. An example BES for ITO is presented in Fig. 3-6, where the specific core level is noted for each peak.

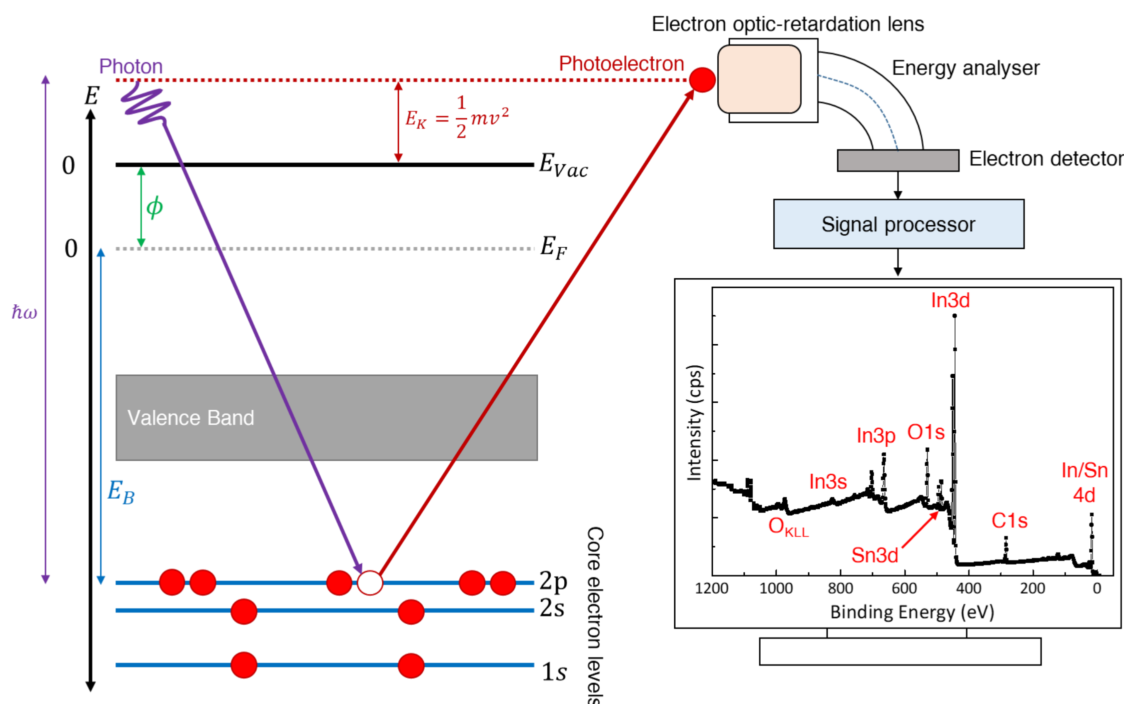

Fig. 3-6. Schematic diagram for X-ray photoelectron spectroscopy (XPS). An incident X-ray photon (purple line), with a photon energy $E = \hbar\omega$, bombards the material and results in the emission of a photoelectron (dark red line) from the core electron levels (blue lines), below the valence band (grey rectangle) with a binding energy, E_B, (blue arrow) below the Fermi level (dashed grey line). The electron escapes the XPS system (with work function, ϕ; green arrow) and arrives at an electron detection system, comprising an electron optic-retardation lens, energy analyser and electron detector, which measures the kinetic energy of the photoelectron, $E_k = \frac{1}{2}mv^2$. The signal is processed with Eq. (3-17) so that the binding energy spectrum (BES) of the material can be output to a display. An example BES for an ITO thin film is presented inside the monitor, where the red labels indicate the specific core level for each peak. Adapted from [59].

To describe each level, the spectroscopic notation is used, labelling each peak with the format '$[\mathrm{n}][\mathrm{l}]_{[\mathrm{j}]}$' where n is the principal quantum number $(1, 2, 3\ldots)$, l is the orbital angular momentum ($\mathrm{s} = 0$, $\mathrm{p} = 1$, $\mathrm{d} = 2$, $\mathrm{f} = 3$) and j is the spin quantum number ($\mathrm{j} = \mathrm{l} + S$, where $S = \pm 1/2$ is the spin). For p, d and f orbitals with momentum $\mathrm{l} > 0$, the interaction between the orbital and electron angular momentum gives rise to a peak splitting, known as a doublet. This splitting can be observed in Fig. 3-6 for the $\mathrm{In3d}$ and $\mathrm{In3p}$ peaks. It should be noted that the penetration depth of the measurement is small, even though the X-rays pass through the entire sample. This is because, due to the relatively short mean free paths of the photoelectrons, only those at the surface can escape to be emitted. Therefore, XPS is a surface technique with a typical depth resolution of $0.5 - 5\ \mathrm{nm}$. Photoelectrons which are created deeper into the sample scatter before reaching the surface and result in a background signal in the BES. However in-situ argon-ion etching can be used in conjunction with XPS for a depth analysis and to remove surface contamination [292].

Experimental Details

XPS measurements were carried out using a Kratos Analytical Ltd. AXIS Ultra XPS system at Aristotle University of Thessaloniki. The system comprises an ultra-high vacuum chamber ($\sim 10^{-9}\ \mathrm{bar}$), a monochromated $\mathrm{Al} - \mathrm{K}_{\alpha 1}$ X-ray beam excitation source ($E = 1486.6\ \mathrm{eV}$), a hemispherical energy analyser and a 128 channel detector. Initially, lower resolution collection was performed for over a wide range of E_B ($0 - 1200\ \mathrm{eV}$) to detect the set of XPS peaks (see Fig. 3-6). This measurement was followed by a high-resolution scan to obtain narrow-range spectra across the regions of interest in the XPS spectrum. The background was removed from the data set to provide the X-ray spectra for each element. The individual elemental singlet or doublet peaks were fit with multiple Gaussian-Lorentzian Sum (GLS) peaks (Eq. (3-18)) with a fixed shape of 0.3 (30% Lorentzian and 70% Gaussian contribution) [293]. The peak positions were taken from literature with an additional shift, shared between each component peak.

$$GLS(E_B, \Gamma, E_0, h) = (1 - 0.3)he^{-4\ln(2)\frac{(E_B - E_0)^2}{\Gamma^2}} + \frac{0.3h}{1 + 4\frac{(E_B - E_0)^2}{\Gamma^2}} \tag{3-18}$$

where h is the height, E_0 the peak position and Γ the FWHM.

3.2.4. Electrical

The electrical properties of the TCO thin films govern their performance in a range of electronic devices [113,117]. They are also fundamentally linked to the optical properties [110,249]. The key parameters which define the electrical properties are the resistivity, ρ, mean scattering time, τ, free carrier concentration, N, and the free carrier mobility, μ. If the effective electron mass, m_e^*, is known, then ρ and τ can be directly translated into N and μ *via* Eq. (2-40) and Eq. (2-41), and vice-versa. ρ can be determined by measuring the electrical potential distribution created in a material with a current-injecting electrode with a varying current density [113,117]. This measurement can be performed in both four-point probe (4pp) and Van dep Pauw (VdP) configurations. N can be determined using the Hall Effect so that μ can be calculated from Eq. (2-41).

Four-point probe (4pp)

The 4pp technique is commonly used to determine the film resistivity due to the simplicity and accuracy of the technique, and the lack of a requirement for any sample preparation [117]. In the 4pp technique, four collinear and equally spaced needle-like metal probes are placed onto the thin film material surface. A current, I, is passed through two outer probes (1 and 4 in Fig. 3-7) and the voltage, V, is measured across two inner probes (2 and 3 in Fig. 3-7). The high input impedance of the voltmeter ensures that a negligible current can flow through the inner probes and thus the resistance impact of the inner probes is eliminated. This allows for measurement of the sheet resistance, R_{sh}, *via* Eq. (3-19):

$$R_{sh} = \rho_{4pp} d_{film} = \frac{\pi}{\ln(2)} \frac{V}{I} \tag{3-19}$$

where V/I is determined from the linear gradient of a set of V across 38 discreet measurements of I. If the film thickness, d_{film}, is known, then the “4pp” resistivity, ρ_{4pp}, can be calculated from:

$$\rho_{4pp} = R_{sh} d_{film} f_1 f_2 f_3 \tag{3-20}$$

where f_1, f_2 and f_3 are a finite sample width, substrate conductivity and film thickness correction factors, respectively [294]. The finite sample width correction is required due to the generally small lateral size of the samples (~ 10 mm) and is calculated for every measurement from the sample width, w, and the probe spacing, s, from Eq. (3-21) [117]:

$$f_1 = \frac{\ln(2)}{\ln(2) + \ln\left(\frac{\left(\frac{w}{s}\right)^2 + 3}{\left(\frac{w}{s}\right)^2 - 3}\right)} \tag{3-21}$$

The substrate conductivity correction is required due to the use of n-type doped silicon substrates and is found empirically for each seed material by measuring the seed films grown

with identical sputtering conditions but deposited onto Si and onto Si with a thermally grown ~ 200 nm intermediate SiO_2 layer. The films with such a dielectric intermediate layer do not need to account the effect of a conducting substrate (*i.e.,* $f_2 = 1.0$) to determine ρ_{4pp}. Subsequently, f_2 for the on-Si films was calculated from $\rho_{4pp,SiO_2}/\rho_{4pp,Si}$. However, due to the generally very conductive nature of the sputtered TCO films ($\sim 10^2 - 10^3\ \Omega^{-1}\text{cm}^{-1}$) compared to the Si film ($\sim 0.1 - 1\ \Omega^{-1}\text{cm}^{-1}$), f_2 was found to be ~ 1.0 in most cases. The film thickness correction factor has been shown to not be required for films with a thickness much less than the probe spacing [117,294]. Due to the very small thickness of the films utilised in this work, the correction for thickness was ignored by setting f_3 to equal 1.0.

Experimental Details

ρ_{4pp} was determined using a Signatone collinear four-point probe station with $1.00 + 0.01$ mm spaced tungsten carbide probes. The probes are spring-loaded to ensure good contact with the sample while minimising potential sample damage and are supplied with a current and the resulting voltage is measured using a dual-channel Model 2636A Keithley SourceMeter.

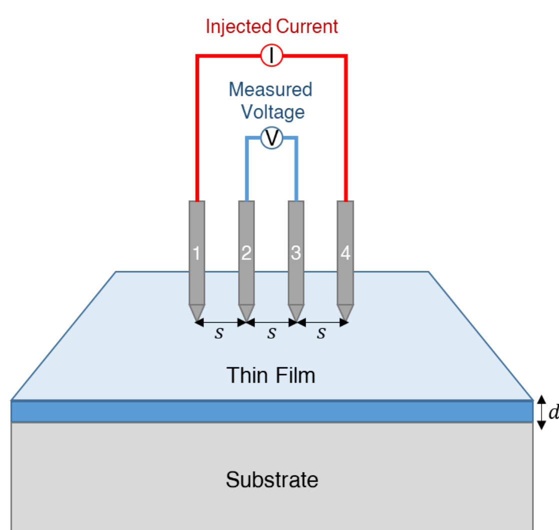

Fig. 3-7. Principle of four-point probe measurements. Four collinear probes with spacing s are placed onto a thin film with thickness, d, (blue slab) on top of a non-conducting substrate (grey slab). A current, I, is passed through two outer probes (red lines) and the voltage, V, is measured across two inner probes (blue lines). Adapted from [117].

Van der Pauw (VdP)

The Van der Pauw (VdP) technique is performed by placing four very small ohmic contacts onto the periphery (preferably in the corners) of the sample surface [295]. Van der Pauw demonstrated that there are two characteristic sheet resistances that are associated with the directionality of the probes. These are defined as R_A and R_B and are illustrated in Fig. 3-8a and Fig. 3-8b, respectively. To reduce the impact of the sample geometry and imperfections in

the contacts, the measurement process is repeated on all sides of the sample and reversing the current direction to yield a total of eight measurements used to calculate R_A and R_B:

$$R_A = \frac{R_{12,43} + R_{21,34} + R_{34,21} + R_{43,12}}{4} \quad (3\text{-}22)$$

$$R_B = \frac{R_{23,14} + R_{32,41} + R_{41,32} + R_{14,23}}{4} \quad (3\text{-}23)$$

where $R_{ij,kl}$ is the measured sheet resistance when I is applied from contact point i to j, while V is measured from contact point k and l:

$$R_{ij,kl} = \frac{V_{\mathrm{kl}}}{I_{\mathrm{ij}}} \quad (3\text{-}24)$$

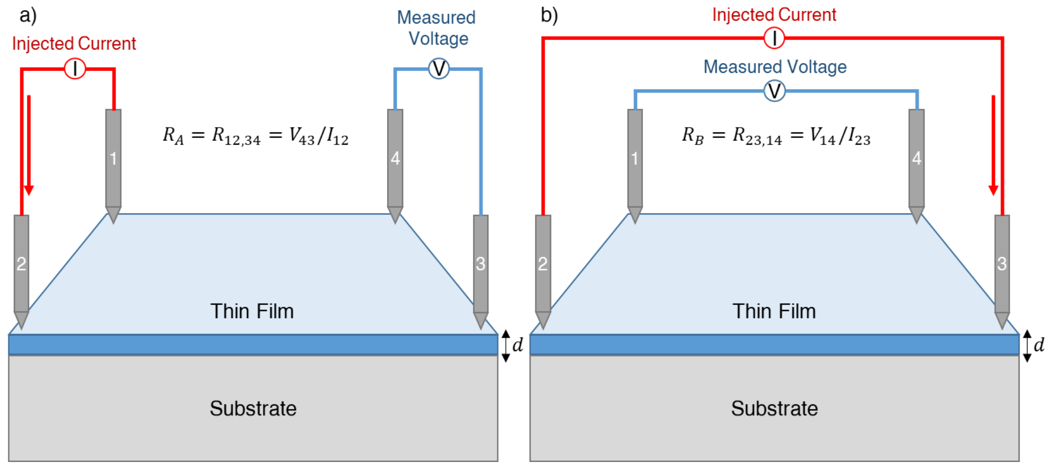

Fig. 3-8. Principle of Van der Pauw measurements. Four collinear probes are placed at the corners of a small (square) sample comprising a thin film with thickness, d_{film}, (blue slab) on top of a non-conducting substrate (grey slab). The supply of a current, I, and measurement of the voltage, V, occur both across the (a) y and (b) x axes of the sample in order to measure the two characteristic sheet resistances of the sample, R_A and R_B, respectively. Adapted from [117].

R_A and R_B are related to R_{sh}through equation Eq. (3-25):

$$\exp\left(-\pi \cdot \frac{R_A}{R_{sh}}\right) + \exp\left(\pi \cdot \frac{R_B}{R_{sh}}\right) = 1 \quad (3\text{-}25)$$

which can be solved numerically for R_{sh} *via* a numerical algorithm by iteration [295]:

$$z_0 = \frac{2\ln(2)}{\pi(R_A + R_B)} \quad (3\text{-}26)$$

$$y_i = \frac{1}{\exp(\pi z_{i-1} R_A)} + \frac{1}{\exp(\pi z_{i-1} R_B)} \quad (3\text{-}27)$$

$$z_i = z_{i-1} - \frac{1 - y_i}{\pi \frac{R_A}{\exp(\pi z_{i-1} R_A)} + \frac{R_B}{\exp(\pi z_{i-1} R_B)}} \quad (3\text{-}28)$$

which is concluded when $(z_i - z_{i-1})/z_i$ is less than a set error limit, $\delta = 0.0005$. The Van der Pauw resistivity, ρ_{VdP}, is then calculated using Eq. (3-20).

Hall Effect

The Hall Effect is underpinned by a combination of the electric and magnetic forces that when charge carriers move with a drift velocity, v_d, along the electric field direction, perpendicular to an applied magnetic field of strength B. The moving change carriers are deflected by the Lorentz force, F_L, (Eq. (3-29)) in the y-direction to one of the sample edges. Fig. 3-9 presents a schematic diagram of this concept.

$$F_L = qv_dB \tag{3-29}$$

where q is the charge of the majority charge carriers. The charge carriers congregate on this side resulting in a build-up of excessive negative (for n-type materials) or positive (for p-type materials) charges. This results in the creation of an electric field, with strength ξ, and electrostatic force, F_e, between the sample sides:

$$F_e = q\xi \tag{3-30}$$

At equilibrium ($F_L = F_e$), $\xi = v_dB$ and a measurable potential difference known as the Hall voltage, V_H, is created between the sample sides:

$$V_H = \frac{\xi}{w} \tag{3-31}$$

where w is the distance between the sample sides. The current, I, is described by the total amount of charge passing through a given cross-sectional area, $A = wd_{film}$:

$$I = Nqv_dwd_{film} \tag{3-32}$$

where N is the free carrier concentration. Eq. (3-32) can be rearranged to give v_d and substituted into Eq. (3-29) to obtain:

$$V_H = \frac{IB}{Nqd_{film}} \tag{3-33}$$

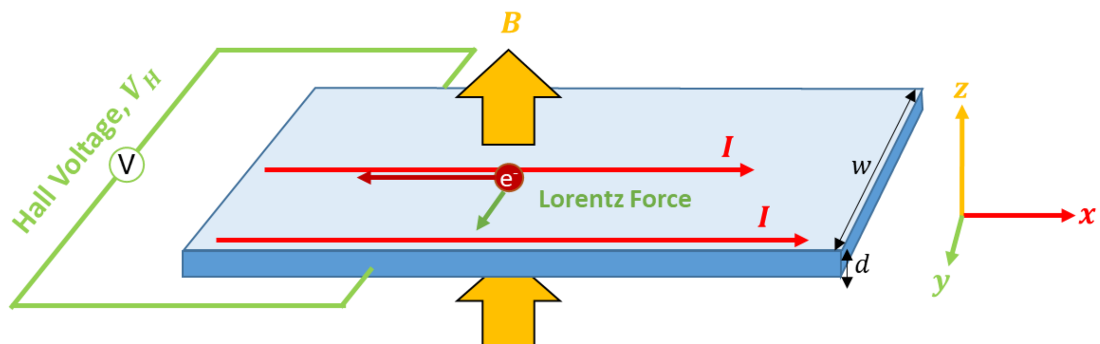

Fig. 3-9. Principle of the Hall Effect. An electron (dark red sphere) moves in response to the electric field, with strength ξ, (dark red arrow) introduced by a current, I (red arrows). When a magnetic field with strength B is introduced, the carriers are deflected by the Lorentz force (green arrow) and build up on one side of the sample, resulting in the creation of a potential difference across each side of the sample that is measured by as the Hall voltage, V_H (green line).

Eq. (3-34) is then used to extract the "Hall coefficient", R_H:

$$R_H = \frac{V_H d_{film}}{IB} = \frac{1}{Nq} \tag{3-34}$$

where the existence of q highlights that the Hall coefficient depends on the sign of the charge unit and therefore indicates the carrier type. All the TCO films investigated in this work are n-type, and so $q = -e$ and the Hall coefficient is negative. From Eq. (3-33) and Eq. (3-34) it is found that, if d_{film} is known, then N can be measured *via* Hall Effect using:

$$N = \frac{1}{e|R_H|} = \frac{|I|B}{et|V_H|} \tag{3-35}$$

Generally, Hall Effect systems use the Van der Pauw configuration where the current is injected on the two opposite contacts, V is measured across the other two opposite contacts and the magnetic field is perpendicular to the sample surface. This is presented in Fig. 3-10. The measurement is repeated for both axes and for reverse current directions, so that the average of the resulting 8 measurements is used to calculate R_H, V_H and N. The "Hall" mobility, μ_{Hall}, can be calculated from ρ_{VdP} by using:

$$\mu_{Hall} = \frac{|R_H|}{\rho_{VdP}} \tag{3-36}$$

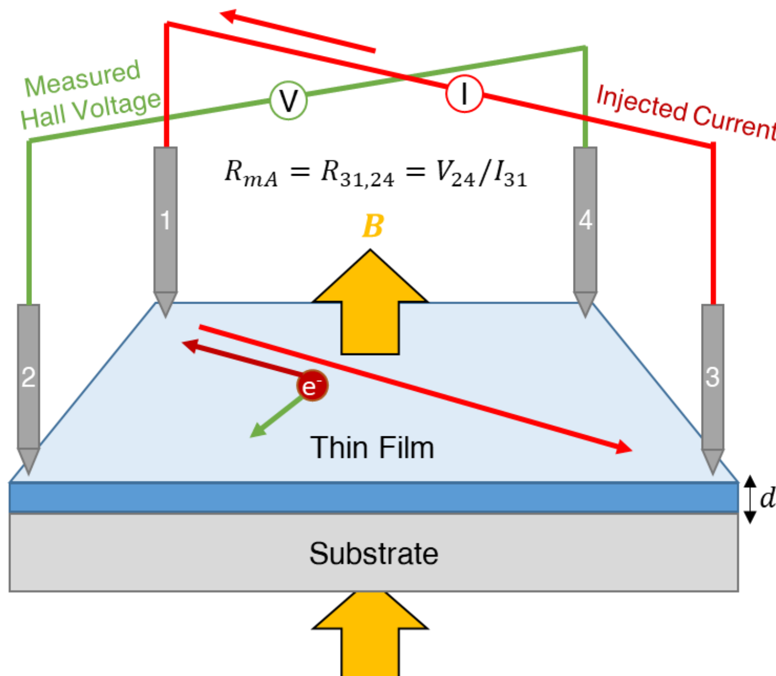

Fig. 3-10. Schematic of the Hall Effect measurement in Van dep Pauw geometry. Four collinear probes are placed at the corners of a small (square) sample comprising a thin film, with thickness d_{film}, (blue slab) on top of a non-conducting substrate (grey slab). A magnetic field, with strength B, is introduced to the sample (yellow arrows). The supply of a current, I, and measurement of the voltage, V, occur across both diagonals of the sample in order to measure the Hall voltage, V_H. Adapted from [117].

μ_{Hall} differs from the "conductivity" mobility, μ, due to complications introduced by energy-dependent scattering mechanisms [117]. The deviations are described by a Hall scattering factor, r_{Hall}, which depends on the dominant scattering mechanism (Section 2.2.5) and is reported to be $3\pi/8$, $315\pi/512$ and 1 for lattice scattering, ionised impurity scattering and neutral impurity scattering, respectively. μ is then calculated from the product of μ_{Hall} and r_{Hall}. However, r_{Hall} is a factor of the temperature and magnetic field strength and there is often a mix of scattering mechanisms present for a particular sample. Due to these complications, henceforth in this work we report only μ_{Hall} and not $\mu = r_{Hall}\mu_{Hall}$.

Experimental Details

The transport properties (N and μ_{Hall}) for ITO, AZO and GZO samples of $\sim 1.0 \times 1.0\ \mathrm{cm}^2$ deposited onto Si were evaluated with an Ecopia HMS-3000 Hall effect measurement system in the Van der Pauw geometry at room temperature with a magnetic field strength of $B = 0.553\ \mathrm{T}$. The measurements were repeated three times for each sample in order to calculate and report the mean value and corresponding standard error. Gold, silver, and indium Ohmic contacts were tested and found not to be required for the ITO, AZO and GZO films due to their low resistivity.

3.2.5. Optical

Optical reflection spectroscopy (ORS)

By setting up boundary conditions for plane waves at a planar interface between two materials characterised by their complex dielectric functions $\tilde{\varepsilon}_i(E)$ and $\tilde{\varepsilon}_t(E)$ (Fig. 3-11), the Fresnel reflection and transmission coefficients at photon energy, E, ($r_F(E)$ and $t_F(E)$ respectively) can be derived [296]. The Fresnel coefficients are defined separately for transverse electric (TE) and transverse magnetic (TM) waves, defined by two cases where the wave is linearly polarised perpendicular (TE) or parallel (TM) to the plane of incidence. TE and TM waves are denoted as s- or p-polarised, respectively, and are indicated within the superscript.

$$r_F^p(E) = \frac{\tilde{\varepsilon}_t(E)k_1(E) - \tilde{\varepsilon}_i(E)k_2(E)}{\tilde{\varepsilon}_t(E)k_1(E) + \tilde{\varepsilon}_i(E)k_2(E)} \tag{3-37}$$

$$r_F^s(E) = \frac{k_i(E) - k_t(E)}{k_i(E) + k_t(E)} \tag{3-38}$$

$$t_F^p(E) = \frac{2k_i(E)}{\tilde{\varepsilon}_t(E)k_i(E) + \tilde{\varepsilon}_i(E)k_t(E)} \tag{3-39}$$

$$t_F^s(E) = \frac{2\tilde{\varepsilon}_t(E)k_i(E)}{k_i(E) + k_t(E)} \tag{3-40}$$

where $k_i(E)$ and $k_t(E)$ are the wavevectors of the incident and transmitted wave perpendicular to the interface. The polarisation dependence of the Fresnel coefficients is a vital component of ellipsometric measurements [297].

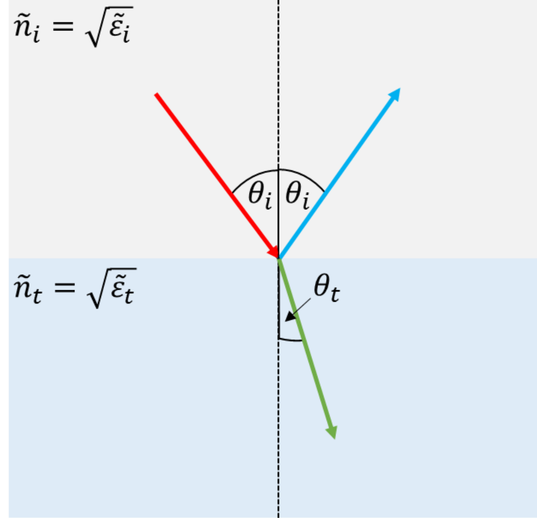

Fig. 3-11. Schematic of light refraction and reflection at a boundary between two regions with different refractive indexes, $\tilde{n}_i$ and $\tilde{n}_t$. The incoming light (red arrow) with an angle of incidence θ_i normal to the interface is either transmitted (green arrow) at a refracted angle, θ_t, or reflected at a reflected angle $\theta_r = \theta_i$. Adapted from [296].

For a non-absorbing incident medium (ε_i is real and positive), the Fresnel coefficients can be used to determine the frequency-dependent reflectance, $R(E)$, and transmittance, $T(E)$, for p- and s-polarised electromagnetic waves [296]:

$$R^P(E) = \frac{|\xi_r(E)|}{|\xi_i(E)|} = \left|\boldsymbol{r}_F^p(E)\right|^2 = \left|\frac{1 - \frac{\varepsilon_i(E)k_t(E)}{\tilde{\varepsilon}_t(E)k_i(E)}}{1 + \frac{\varepsilon_i(E)k_t(E)}{\tilde{\varepsilon}_t k_i}}\right| \tag{3-41}$$

$$R^S(E) = \frac{|\xi_r(E)|}{|\xi_i(E)|} = \left|\boldsymbol{r}_F^p(E)\right|^2 = \left|\frac{1 - \frac{k_t(E)}{k_i(E)}}{1 + \frac{k_t(E)}{k_i(E)}}\right| \tag{3-42}$$

$$T^P(E) = \frac{|\xi_t(E)|}{|\boldsymbol{\xi}_i(E)|} = 1 - R^P(E) = \frac{4\Re\left(\frac{\varepsilon_i(E)k_t(E)}{\tilde{\varepsilon}_t(E)k_i(E)}\right)}{\left|1 + \frac{\varepsilon_i(E)k_t(E)}{\tilde{\varepsilon}_t(E)k_i(E)}\right|} \tag{3-43}$$

$$T^S(E) = \frac{|\xi_t(E)|}{|\xi_i(E)|} = 1 - R^S(E) = \frac{4\frac{k_t(E)}{k_i(E)}}{\left|1 + \frac{k_t(E)}{k_i(E)}\right|} \tag{3-44}$$

At normal incidence, $R(E)$ is identical for p- and s-polarised light and $\theta_i = 0°$ so that:

$$R(E) = \left|\frac{n_i - \tilde{n}_t(E)}{n_i + \tilde{n}_t(E)}\right|, \tag{3-45}$$

where n_i is the refractive index of the non-absorbing incident medium (Air) and $\tilde{n}_t = \sqrt{\tilde{\varepsilon}_t} = n_i + i\kappa_i$ is the complex refractive index of the potentially absorbing material with real refractive index, n_t, and extinction coefficient, κ_t.

For multilayer structures, there exist back-reflections at the material interfaces which lead to interference effects in the collected light (see Fig. 3-12). Determination of the reflection and transmittance of such multilayer structures is achieved with the "Matrix Method" [296]. In this method, 2×2 or 4×4 [298] matrices are used to describe both the reflection and transmission Fresnel coefficients of each individual layer. The final optical response (*i.e.,* the reflectance) is then determined from the multiplication of all the individual matrices. Heavens [299] presented a short description of the method by examining the electric vector of a wave travelling in the direction of incidence, ξ_{n}^{+}, and in the opposite direction, ξ_{n}^{-}, within the n^{th} layer. These waves are described by:

$$\xi_{\mathrm{n}}^{+} = \frac{1}{t_{\mathrm{n}}}(\xi_{\mathrm{n-1}}^{+}\exp(i\theta_{\mathrm{n-1}}) + r_{\mathrm{n}}(\xi_{\mathrm{n-1}}^{-}\exp(-i\theta_{\mathrm{n-1}}))(\xi_{\mathrm{n-1}}^{-}\exp(-i\theta_{\mathrm{n-1}})) \ , \qquad (3\text{-}46)$$

$$\xi_{\mathrm{n}}^{-} = \frac{1}{t_{\mathrm{n}}}(r_{\mathrm{n}}\xi_{\mathrm{n-1}}^{+}\exp(i\theta_{\mathrm{n-1}} -) + (\xi_{\mathrm{n-1}}^{-}\exp(-i\theta_{\mathrm{n-1}})) \ , \qquad (3\text{-}47)$$

where t_n and r_n are the transmission and reflection Fresnel coefficients, respectively. Eq. (3-46) and Eq. (3-47) can be written in matrix form:

$$\begin{pmatrix} \xi_{\mathrm{n}}^{+} \\ \xi_{\mathrm{n}}^{-} \end{pmatrix} = \frac{1}{t_{\mathrm{n}}}\begin{pmatrix} \exp(i\theta_{\mathrm{n-1}}) & r_{\mathrm{n}}\exp(-i\theta_{\mathrm{n-1}}) \\ r_{\mathrm{n}}\exp(i\theta_{\mathrm{n-1}}) & \exp(-i\theta_{\mathrm{n-1}}) \end{pmatrix}\begin{pmatrix} \xi_{\mathrm{n-1}}^{+} \\ \xi_{\mathrm{n-1}}^{-} \end{pmatrix} = \frac{1}{t_{\mathrm{n}}}\mathrm{M}_{\mathrm{n-1}}\begin{pmatrix} \xi_{\mathrm{n-1}}^{+} \\ \xi_{\mathrm{n-1}}^{-} \end{pmatrix} \ , \qquad (3\text{-}48)$$

and for a stack of N layers, it can be derived that:

$$\begin{pmatrix} \xi_{\mathrm{N+1}}^{+} \\ \xi_{\mathrm{N+1}}^{-} \end{pmatrix} = \frac{\mathrm{M}_{\mathrm{N}}\mathrm{M}_{\mathrm{N-1}}\cdots\mathrm{M}_{2}\mathrm{M}_{1}}{t_{\mathrm{N}}t_{\mathrm{N-1}}\cdots t_{2}t_{1}}\begin{pmatrix} \xi_{0}^{+} \\ \xi_{0}^{-} \end{pmatrix} \ , \qquad (3\text{-}49)$$

Finally, the reflectance, $R(E)$, can be calculated from:

$$R(E) = \frac{|\xi_{\mathrm{N+1}}^{-}|^{2}}{|\xi_{\mathrm{N+1}}^{+}|^{2}}. \qquad (3\text{-}50)$$

Experimental Details

In this work, for samples where NIR-VIS-UV SE was unavailable, the VIS-UV optical properties of normal-incidence optical reflectance spectra were measured from $250 - 900\ \mathrm{nm}$ ($1.4 - 5.0\ \mathrm{eV}$) with the Ocean Optics SpectraSuite Software using a VIS-UV (Ocean Optics USB4000) spectrometer, a balanced deuterium-halogen light source (Ocean Optics DH2000BAL) and VIS-UV transparent optical fibres. The set-up is demonstrated schematically in Fig. 3-12. The spectral light intensity of the lamp, $I_L(E)$, was recorded using an $\sim 300\ \mathrm{nm}$ Al thin film deposited onto Si as a reference mirror. The spacing between the optical fibre head and the sample surface was adjusted to ensure a maximum reflected intensity and then the number of counts was adjusted to reduce the peak intensity below the saturation limit of the detector. The light source was then closed in order to record the dark intensity, $I_D(E)$. The source was opened again, the sample were placed under the probe and the reflective light intensity of the measured sample, I_S was recorded.

$R(E)$ was calculated with:

$$R(E) = \frac{I_S(E) - I_D(E)}{I_L(E) - I_D(E)} R_{Al}(E) \tag{3-51}$$

where $R_{Al}(E)$ is the theoretical reflectivity of the Al mirror, determined from ellipsometry.

The J. A. Woollam propriety software of CompleteEase™ was used to solve the matrix method for multiple potentially semi-absorbing layers and a general incident angle. A geometric model is built layer by layer with the optical constants ($\tilde{n}$ or $\tilde{\varepsilon}$) of each layer. The region below the estimated band gap ~ 3 eV is used to fit a constant n and d to the data with a Levenberg-Marquardt nonlinear regression algorithm [300]. For samples with a higher conductivity, the contribution of the free carrier absorption extended into the visible region and was accounted for by factoring in the effect of free carrier absorption on the permittivity. This will be explored in more detail in Section 4.2.

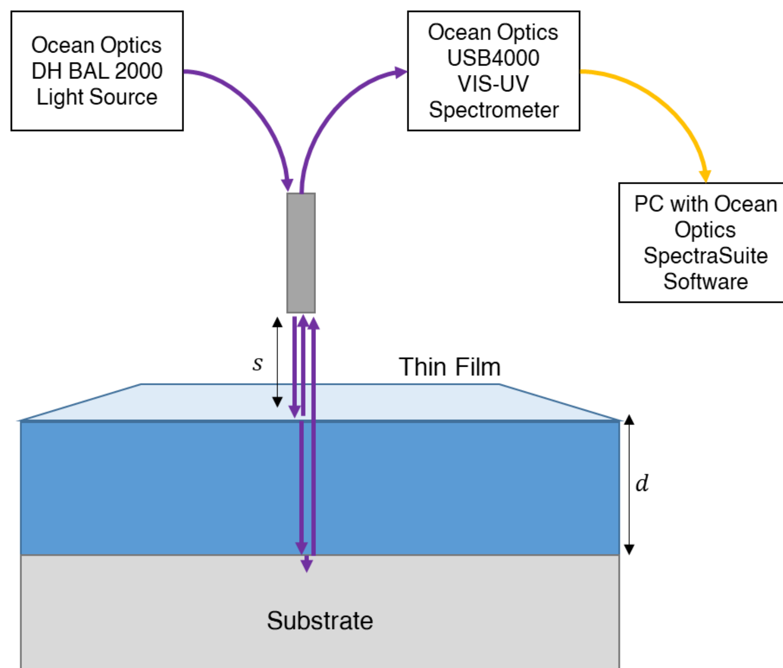

Fig. 3-12. Schematic of the reflectance measurement set-up. Light (purple arrows) is directed from the source to a distance, s, above the surface of a thin film material, with thickness d, (blue slab) on top of a reflective substrate (grey slab) *via* optical fibres. The light immediately reflects from the surface of the thin film, the film/substrate interface or is reflected after one or more back-reflections between the surface and interface. The reflected light travels back into the optical probe and is collected by a spectrometer so that the intensity of reflected light as a function of the photon energy can be analysed. The presence of one or more back-reflections allows for the determination of the film thickness from the spacing on the interference fringes.

Spectroscopic ellipsometry (SE)

Spectroscopic ellipsometry (SE) measures the quantities $\Psi(E)$ and $\Delta(E)$ (also known as ellipsometric angles) which are related to the ratio of reflection of the s- and p- polarisation states from the sample, $\rho_f(E)$ by [297]:

$$\rho_f(E) = \frac{r_p(E)}{r_s(E)} = \tan\big(\Psi(E)\big)\, e^{i\Delta(E)} \tag{3-52}$$

where $r_p(E)$ and $r_s(E)$ are the reflection coefficients of the s- and p-polarised light components, respectively. The real and imaginary parts of the permittivity of the entire sample (considering contribution of the whole stack: substrate/thin film).

The "*pseudo*-permittivity", $< \tilde{\varepsilon}(E,\theta) >$, can be calculated from the measured value of ρ_f at each measured angle, θ [297]:

$$< \tilde{\varepsilon}(E,\theta) >=< \varepsilon_1(E,\theta) > +\mathrm{i} < \varepsilon_2(E,\theta) >= \sin^2(\theta)\left(1 + \tan^2(\theta)\left[\frac{1-\rho_f(E)}{1+\rho_f(E)}\right]^2\right) \tag{3-53}$$

However, $< \tilde{\varepsilon}(E,\theta) >$ is an extrinsic property of the sample that depends on the permittivity of the individual layers and their geometry. Therefore, a combination of a geometric (Fig. 3-14a) and an optical (Fig. 3-14b) model, taking into account the number of layers with the individual layer thickness and permittivity, is required to transform $< \tilde{\varepsilon}(E,\theta) >$ into the optical constants $\tilde{\varepsilon}(E)$ of the "unknown" layer.

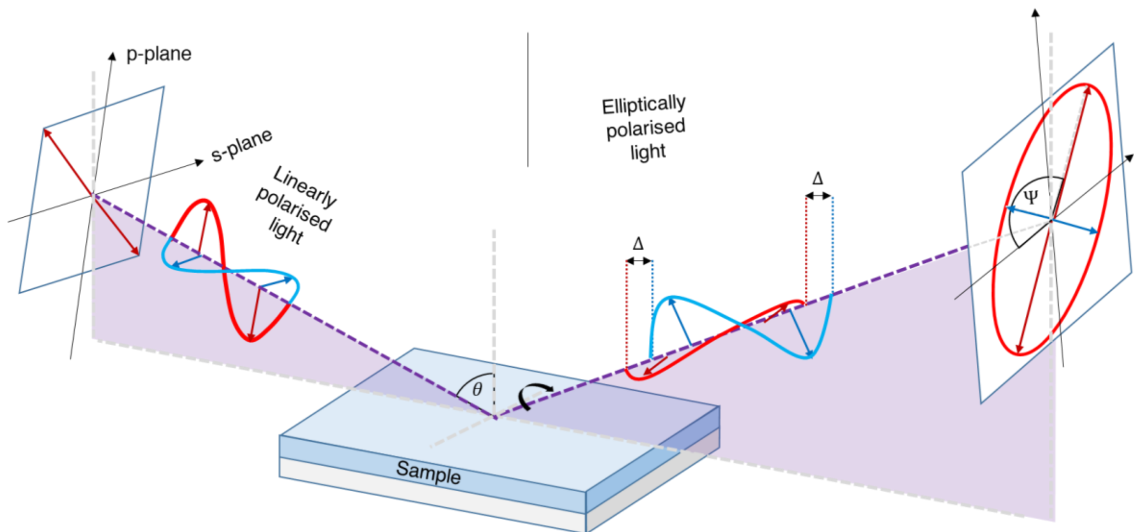

Fig. 3-13. Illustration for the principle of Ellipsometry. Light with a linear polarisation of the electric (red wave) and magnetic (blue wave) reflects off the surface of a sample (blue slab) at an angle, θ. Upon reflection from the sample, the light becomes elliptically polarised and can be described by the amplitude, tan $(\Psi(E))$, and phase, $\Delta(E)$, for the ratio of the p-polarised and s-polarised reflection coefficients.

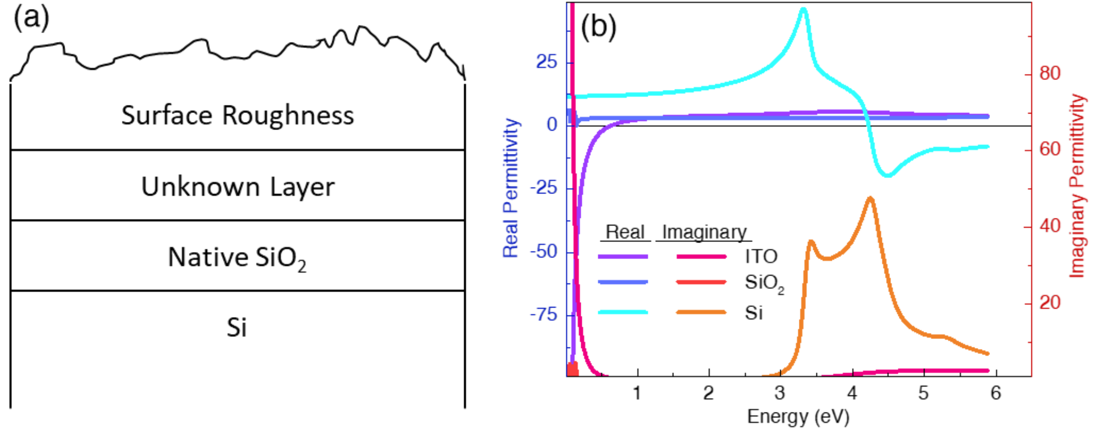

Fig. 3-14. (a) Geometric model of the sample structure and (b) optical model of the real and imaginary permittivity of the individual materials that make up the geometric model used to fit the TCO/Si samples.

The permittivity of Si and the native oxide layer and the thickness of the native oxide are well known [301]. This enables fitting the permittivity and thickness of the thin film layer, defined by a summation of individual oscillators in order to take into account contributions of intraband, interband and optical phonon absorption [102,107]. The permittivity is described by Eq. (3-54) as a summation of the high-frequency permittivity, ε_∞, and additional individual oscillators, $\tilde{\varepsilon}_n(E)$ [302].

$$\tilde{\varepsilon}(E) = \varepsilon_\infty + \sum_{n=1}^{m} \tilde{\varepsilon}_n(E) \tag{3-54}$$

The parameters are fit using an iterative and nonlinear regression algorithm (Levenberg-Marquardt method) [300]. The errors result from the 90% confidence intervals of this algorithm and the “quality” of the fit can be assessed by the resulting root mean squared error (MSE) of the fit, given by Eq. (3-55). The MSE is effectively a summation of the difference between the measured data (subscript “mes”) and the model-generated data (subscript “fit”).

$$\mathrm{MSE} = \sqrt{\frac{10^6}{3\mathrm{n}-\mathrm{m}} \sum_{i=1}^{n} \left[\left(N_{mes_i} - N_{fit_i}\right)^2 + \left(C_{mes_i} - C_{fit_i}\right)^2 + \left(S_{mes_i} - S_{fit_i}\right)^2 \right]} \tag{3-55}$$

where n is the number of data points (individual measured photon energies) and m is the number of fitting parameters. The parameters $N = \cos(2\Psi)$, $C = \sin(2\Psi)\cos(\Delta)$ and $S = \sin(2\Psi)\sin(\Delta)$ are used in place of Ψ and Δ as they are better suited to the MSE definition due to the fact they are always bounded between -1 and 1 and have approximately the same precision and accuracy for rotating compensator ellipsometer configurations [297].

Experimental Details

Optical characterisation was performed with a J. A. Woollam Mark II IR Variable Angle Spectroscopic Ellipsometry (VASE) ($1.6 - 40\ \mu\text{m}$) and a J. A. Woollam Focused M2000-DI VASE ($0.193 - 1.69\ \mu\text{m}$). A schematic diagram of the IR-VASE is presented in Fig. 3-15.

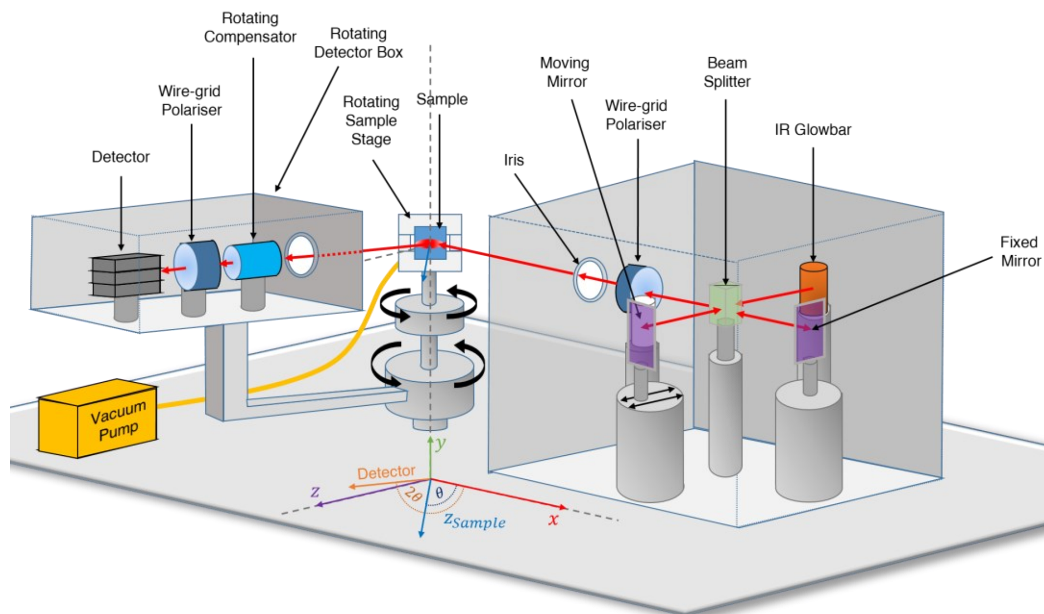

Fig. 3-15. Illustration of the Mark II IR-VASE. The system consists of three main parts: an IR source, the sample manipulator, and the detector. The source comprises an IR glow bar, a beam splitter, a fixed mirror, a moving mirror, a wire-grid polariser, and an iris. This delivers linearly polarised light to the sample surface, which is rotated with by the sample stage to ensure the light is incident at an angle, θ, normal to the sample surface. The sample is vertically mounted on a semi-hollow stage and held in place with a vacuum pump in order to allow measurement of the IR transmission. The detector unit is rotated at an angle of 2θ and houses a rotating compensator, a wire-grid polariser, and a detector. The use of a rotating compensator allows for simultaneous measures of $N(E,\theta)$, $C(E,\theta)$ and $S(E,\theta)$.

It should be noted that the typical back-surface finish of single-side polished Si wafers is insufficiently rough for IRSE measurements. This leads to reflections from the back-surface that are incoherent with the desired reflection from the surface and must either be accounted for in the model or supressed by roughening the back surface [303] or index matching the backside with semi-solid materials such as such as translucent adhesive tape, white glue, grease, paint, and modelling clay [304]. For the TCO films measured with IRSE within this project, the backside of the Si wafers were roughened using a Dremel tool with a diamond head. Dicing tape was used to fix the front-side of the samples down to ensure no residue was left on the surface. For a selection of samples, SE measurements were performed before and after placement onto the dicing tape in order to ensure that the optical properties of the film were unaffected.

Due to the nature of the "inverse problem" of SE, where the sample properties cannot be directly calculated from the measured ellipsometric quantities but the ellipsometry quantities can be calculated from any given sample properties, the precise nature of the fitting is highly dependent on the particular sample of interest [82]. Therefore, a more extensive overview of the optical modelling of TCOs is presented for on a case-by-case basis in Section 4.2.

Infrared transmission (IRT)

The J. A. Woollam Mark II IR-VASE was also utilised to perform IR transmission (IRT) measurements of the spectral transmission, $T_{IR}(E)$, from $1.55 - 35.5\ \mu\mathrm{m}$ $(0.034 - 0.8\ \mathrm{eV})$ at normal-incidence. $T_{IR}(E)$ can be solved following the matrix method outlined above. To facilitate IRT measurements, the TCO films were deposited on double-side polished Si wafers and IRT measurements were acquired prior to back-surface roughening.

$$\mathrm{T}(E) = \frac{\mathrm{n}_0(E)\cos^2(\theta_{\mathrm{N}+1})}{n_{\mathrm{N}+1}(E)\cos^2(\theta_0)} \frac{|\xi_0^+|^2}{|\xi_{\mathrm{N}+1}^+|^2} \tag{3-56}$$

where N is the total number of layers with $\mathrm{N} = 0$ as the layer of the incident light. ξ_0^+ and $\xi_{\mathrm{N}+1}^+$ are calculated from Eqs. (3-44) and (3-45). Where possible, the IRT measurements were appended (with a 33% fit weighting) to IRSE measurements so that both sets of data were fit.

Oscillator Functions

A Drude term describes the contribution of free carriers and is given by Eq. (3-57):

$$\tilde{\varepsilon}_{Drude}(E) = \frac{-\hbar^2}{\varepsilon_o \rho_{opt}\left(\tau_{opt} E^2 + i\hbar E\right)} \tag{3-57}$$

where $\hbar$ is the reduced Planck's constant, e is the elementary charge, ρ_{opt} is the "optical" resistivity, ε_0 is the vacuum permittivity and τ_{opt} is the "optical" carrier mean free time, respectively.

Lorentz functions produced the best fit when utilized for UV absorption centres of the noble metals. They are described by Eq. (3-58):

$$\tilde{\varepsilon}_{Lorentz}(E) = \frac{A_L \gamma E_0}{E_0^2 - E^2 - iE\gamma} \tag{3-58}$$

where A_L is the oscillator amplitude, E_0 is the centre energy and γ is the broadening of the oscillator. The other parameters are defined above.

Gaussian functions produced the best fit when used for IR absorption centres. They are described by Eqs. (3-59) and (3-60).

$$\tilde{\varepsilon}_{Guassian}(E) = A_L \left\{ \begin{array}{c} \left[\Gamma\left(\frac{E - E_0}{\sigma}\right) + \Gamma\left(\frac{E + E_0}{\sigma}\right)\right] \\ +i \cdot \left(exp\left[-\left(\frac{E - E_0}{\sigma}\right)^2\right] - exp\left[-\left(\frac{E + E_0}{\sigma}\right)^2\right]\right) \end{array} \right\} \tag{3-59}$$

where

$$\sigma = \frac{\gamma}{2\sqrt{\ln(2)}} \tag{3-60}$$

and the function Γ is a convergence series used to ensure Kramers-Kronig (KK) consistency for the real permittivity [302]. The other parameters are defined above.

Tauc-Lorentz functions produced the best fit when utilized for UV absorption centres of amorphous materials. They are described by Eqs. (3-61)-(3-64).

$$\tilde{\varepsilon}_{Tauc-Lorentz}(E) = \varepsilon_{1,TL}(E) + i\varepsilon_{2,TL}(E) \tag{3-61}$$

where

$$\varepsilon_{2,TL}(E) = \frac{A_L \gamma E_0 (E - E_G)^2}{En\left(\left(E^2 - {E_0}^2\right)^2 + \gamma^2 E^2\right)}\,, \qquad E > E_G \tag{3-62}$$

$$\varepsilon_{2,TL}(E) = 0\,, \qquad E \leq E_G \tag{3-63}$$

$$\varepsilon_{1,TL}(E) = \frac{2}{\pi} P \int_{E_G}^{\infty} \frac{\xi \varepsilon_{2,TL}(\xi)}{\xi^2 - E^2} d\xi \tag{3-64}$$

where E_G is the band gap and an analytical solution to the Kramers-Kronig integral is applied as presented by Jellison and Modine [305]. The other parameters are defined above.

1D critical point parabolic band (CPPB) functions produced the best fit when utilised for UV absorption centres of the doped ZnO films (AZO and GZO), following the suggestions of Uprety *et al*. [306] They are described by Eq. (3-65) [307].

$$\tilde{\varepsilon}_{CPPB}(E) = A_L e^{i\phi}\left(\frac{\gamma}{2E_0 - 2E - i\gamma}\right)^{\frac{1}{2}} \tag{3-65}$$

where ϕ is the phase projection factor and the other parameters are defined above.

4. Elucidating the optoelectronic properties of RT sputtered TCOs.

This chapter firstly presents the investigation of room temperature (RT) sputter-deposited indium tin oxide (ITO), aluminium-doped zinc oxide (AZO) and gallium-doped zinc oxide (GZO) thin films by radio frequency (RF) magnetron sputtering (Section 4.1). This investigation revealed the optimal deposition parameters which facilitated high quality or “optimised” transparent conductive oxide (TCO) seed films to be utilised in further investigations. The quality was defined by a low resistivity as determined *via* four-point probe (4pp). Furthermore, a low quality (“un-optimised”) or low carrier concentration (“Low-N”) seed materials of each material were chosen for further processing in order grain knowledge of the physical mechanisms behind the optical, structural, and compositional modifications of the films before and after reactive laser annealing (ReLA). Before the photo-induced modifications can be revealed, a detailed understanding of the optical, structural, and compositional properties of the seed films is required. Therefore, in this chapter we also investigate the seed films with 4pp, X-ray diffraction (XRD), Hall Effect and spectroscopic ellipsometry (SE). SE measurements, in particular, are able to elucidate many of the important properties of the material’s optical properties, geometry and carrier transport properties. The process of extracting such information from SE is, however, not trivial and requires careful analysis to ensure the extracted properties reflect physical reality. In response to this Section 4.2 investigates: the methodology used to fit each material (Section 4.2.1), the considerations required for non-ideal features within the measured films (Section 4.2.2 and 4.2.3) and the process of combining Hall Effect and SE to evaluate the changing effective mass and influence of the scattering mechanisms on the carrier transport properties (Section 4.2.4).

4.1. Seed material deposition

4.1.1. Target Acquisition

The initial task, prior to any film deposition, was to acquire sputtering targets with suitable solid solutions to achieve high quality films. The $\mathrm{wt.\%}$ of Sn to $\mathrm{In_2O_3}$ for ITO and of $\mathrm{Al_2O_3}$ and $\mathrm{Ga_2O_3}$ to ZnO for AZO and GZO, respectively, is a key influential parameter that determines the resultant deposited thin films’ electro-optical properties. The guidelines to achieve maximum substitutional solubility are dictated by the Hume-Rothery rules [308]. A sufficient doping level is required to introduce sufficient substitutional Sn, Al or Ga dopants into the $\mathrm{In_2O_3}$ or ZnO lattice. Vitally however, if the doping levels are too high then the dopants could instead occupy interstitial sites or become localised at grain boundaries where they can form ionised clusters and/or sub-oxides within the film. As explored in Section 2.2.5, each of

these factors acts as a scattering mechanism that reduces the carrier mobility, μ, for a particular carrier concentration, N. Furthermore, over-doping can cause additional deterioration of the conductivity by introducing excessive lattice distortion [166,309]. There have been extensive studies on the optimal target doping levels for ITO [247,310–312], AZO [129,264,313,314] and GZO [265,315,316]. Such studies have resulted in a general agreement that to achieve thin films with a low resistivity and a good visible transparency, the optical doping levels for ITO, AZO and GZO sputtering targets should be $10\ \mathrm{wt.\%\ Sn}$, $1-2\ \mathrm{wt.\%\ Al_2O_3}$and $5\ \mathrm{wt.\%\ Ga_2O_3}$. Therefore, 3” ceramic targets (99.99% purity) of $10\ \mathrm{wt.\%\ Sn-In_2O_3}$, $2\ \mathrm{wt.\%\ Al_2O_3-ZnO}$ and $5\ \mathrm{wt.\%}$ $\mathrm{Ga_2O_3-ZnO}$ were acquired from Testbourne Ltd. Following the loading of each target into the sputtering chamber, target conditioning was performed at a low RF power ($\sim 20-60\ \mathrm{W}$) for $\sim 3\ \mathrm{hr}s$ to remove any surface contaminants.

4.1.2. Sputtering optimisation

Beyond the target material selection, the final characteristics of the RF magnetron sputtering deposited films are affected by the system design and deposition parameters [259]. The deposition parameters include, but are not limited to, the substrate to target distance, d_{s-t}, the base pressure, p_{base} the applied RF power, P_{RF}, the oxygen to argon ratio, $O_2\%$ and the deposition pressure p_{dep}. These parameters dictate the kinetic energy, E_K, of the sputtered particles that arrive at the substrate and subsequently the surface mobility of the sputtered particles at the film surface and the deposition rate. The interplay of these factors influences the final microstructural, chemical, morphological and optoelectronic properties of the sputtered film. Due to this interplay between the parameters, the optimisation of the sputtering parameters is not trivial, as altering one parameter may enhance one characteristic of the film and degrade another [257,258,317]. To unveil the influence of the deposition parameters, it is vital to keep all but one parameter constant at a time.

It has been found previously [59,318] that, for the sputtering chamber utilised in this work (Section 3.1.1), the optimal values of $O_2\%$ and p_{dep} for RT deposited AZO onto glass substrates were $0.25\ \%$ and $2.0\ \mathrm{mTorr}$, respectively. An identical process followed by Elhamli [59]. However, in this work n-type ($\rho_{4pp} = 1-10\ \Omega\mathrm{cm}$), (100) orientated silicon wafers were used instead of glass substrates in order to avoid the IR absorption of glass [319]. For this investigation, the $4''$ $\mathrm{Si}\ (100)$ wafers were cleaved into 4 quarters and placed onto the centre of a clean “dummy” wafer prior to deposition. All films were deposited at a substrate rotation of $8\ \mathrm{rpm}$, in order to produce films with acceptable thickness uniformity across the substrate [59]. The substrate to target distance was kept at $\sim 10\ \mathrm{cm}$. The vacuum system was at a base pressure of $< 10^{-7}\ \mathrm{bar}$ (pressure prior to deposition). The $\mathrm{O_2}\%$ was set by adjusting the partial

pressures of Ar and 2% Ar in $\mathrm{O_2}$ supplied to the sputtering chamber. The substrate was covered during the ignition of the plasma (at $20\ \mathrm{W}$) and as the pressure was steadily increased to $25\ \mathrm{mTorr}$. The substrate remained covered (*via* a mechanically adjusted shield) as the sputtering power pressure were incrementally adjusted to the desired value and then left for $\sim 20\ \mathrm{min}$ at the desired deposition parameters for a "pre-sputtering", which is necessary to remove target surface contaminants and ensure reproducibility between consecutive film depositions. During the deposition, the substrate temperature was monitored *via* a chamber thermocouple, to ensure the deposition remained below $\sim 30\ ^{\circ}\mathrm{C}$, and the film thickness and substrate deposition time were monitored *via in-situ* and real-time interferometer measurements, until the desired film thickness was reached. The thickness was cross-checked with optical reflectance spectroscopy (ORS; Section 3.2.5) characterisation and the collinear resistivity, ρ_{4pp}, was measured *via* 4pp (Section 3.2.4).

To investigate the influence of oxygen partial pressure in the optoelectronic properties of ITO, a set of depositions was performed with a constant p_{dep} and P_{RF}, but varying oxygen to argon ratio (0%, 0.12%, 0.25%, and 0.36%). At this stage, the P_{RF} had not yet been optimised, and thus indicative values for p_{dep} and P_{RF} of $2.0\ \mathrm{mTorr}$ and $40\ \mathrm{W}$ were adopted based on literature [286,320]. The results of this investigation for ITO are presented in Fig. 4-1a, where ρ_{4pp} is shown as a function of $\mathrm{O_2}\%$. As $\mathrm{O_2}\%$ was decreased from 0.36% to 0.25%, ρ_{4pp} decreased from $(4.31 \pm 0.06) \times 10^{-4}\ \Omega\mathrm{cm}$ to a minimum value of $(3.89 \pm 0.04) \times 10^{-4}\ \Omega\mathrm{cm}$. This is attributed to the fact that the incorporation of excessive oxygen can fill oxygen vacancies and de-activate substitutional $\mathrm{Sn^{4+}}$ ions on $\mathrm{In^{4+}}$ sites by forming $\mathrm{Sn-O}$ complexes [128,321]. Each process promotes either two or one free electrons to the conduction band, respectively. This increases N and reduces ρ_{4pp} (Eq. (2-41)).

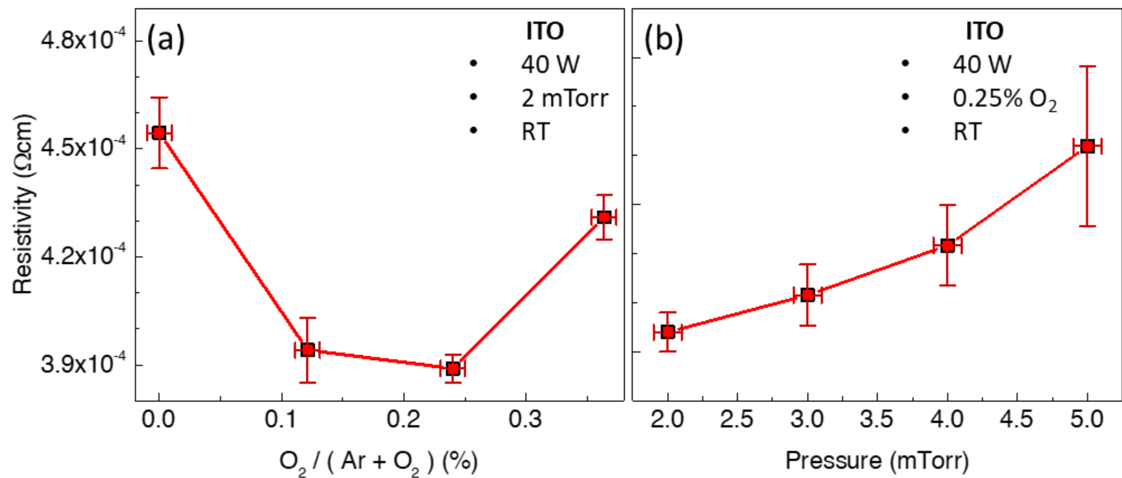

Fig. 4-1. Collinear resistivity, ρ_{4pp}, as a function of the (a) $\mathrm{O_2}$ concentration, $\mathrm{O_2}\%$, and (b) pressure for room-temperature deposited ITO with a sputtering power of $40\ \mathrm{W}$.

For smaller $O_2\%$, however, ρ_{4pp} increased to $(4.5 \pm 0.1) \times 10^{-4}\ \Omega\text{cm}$. This cannot be explained by an increase in N therefore must arise from a decrease in the carrier mobility, μ, brought on by increased carrier scattering by grain boundary, ionised impurity, or ionised cluster scattering (GBS, IIS and ICS, respectively; see Section 2.2.5). The result is an optimal $O_2\%$ of 0.25% to produce films with the lowest resistivity.

To investigate the influence of sputtering pressure in the optoelectronic properties of ITO, a set of depositions was performed with a constant $O_2\%$ and P_{RF}, but various p_{dep} ($1 - 5\ \text{mTorr}$ in steps of $1.0\ \text{mTorr}$). An indicative value of $40\ \text{W}$ was again used for the sputtering power but the $O_2\%$ was set to the optimal value of 0.25%. The results of this investigation are presented in Fig. 4-1b, where ρ_{4pp} is presented as a function of p_{dep}. As p_{dep} increased from $1.0\ \text{mTorr}$ to $5\ \text{mTorr}$, ρ_{4pp} increased from $(3.89 \pm 0.04) \times 10^{-4}\ \Omega\text{cm}$ to $(4.3 \pm 0.2) \times 10^{-4}\ \Omega\text{cm}$. This behaviour can be attributed to the increasing frequency of collisions between the sputtered species in the plasma (decreasing the mean free path) [322]. Subsequently, fewer sputtered particles reach the substrate, and they arrive with lower E_K. Furthermore, increased pressure can result in fewer target bombardments by argon ions. This reduces the sputtering yield and the growth rate [323]. The lower growth rate was observed from the longer deposition time for the film deposited at $5\ \text{mTorr}$. It is reasonable to expect that a lower growth rate could result in higher ρ_{4pp} due to the extra time for oxygen to replenish in the area surrounding the film surface. Therefore, more oxygen atoms are locally available for incorporation into individual growing In_2O_3 unit cells and the likelihood of oxygen vacancies and/or $Sn - O$ complexes forming is increased [53,321,324].

The optimal $O_2\%$ and p_{dep} are identical for ITO and doped-ZnO [59]. For RT sputtering, E_K of the sputtered species as they arrive at the sample surface, which is influenced by a combination of P_{RF} and p_{dep}, is considered the main source of dopant activation energy [323]. Therefore, it is expected that the largest changes to ρ_{4pp} come from variations in P_{RF}. It should also be noted that due to the use of a different substrate (Si) in this work to previous optimisation of doped-ZnO with the same equipment [59], it was necessary to re-identify the optimal P_{RF} for AZO and GZO. To investigate the influence of P_{RF} in the optoelectronic properties of ITO, AZO and GZO a set of depositions was performed with the optimised values for $O_2\%$ and p_{dep} of 0.25% and $2.0\ \text{mTorr}$, respectively. The range of target power was $20 - 100\ \text{W}$, $60 - 140\ \text{W}$ and $40 - 100\ \text{W}$ for ITO, AZO and GZO, respectively (steps of $20\ \text{W}$). The results of this investigation are presented in Fig. 4-2, where ρ_{4pp} is shown as a function of P_{RF} for RT-deposited (a) ITO, (b) AZO and (c) GZO films.

For ITO sputtered at $2\ \mathrm{mTorr}$ (red squares in Fig. 4-2a), as P_{RF} was increased from 20 W to 40 W, ρ_{4pp} decreased from $(5.78 \pm 0.06) \times 10^{-4}\ \Omega\mathrm{cm}$ to $(3.94 \pm 0.04) \times 10^{-4}\ \Omega\mathrm{cm}$. This improvement of the film conductivity with P_{RF} has been ascribed to an enhancement of the crystallinity (resulting in larger μ) and an increase in the oxygen vacancy and Sn^{4+} concentration (resulting in larger N) due to the larger sputtering yield with increased P_{RF} [257,325]. However, for larger P_{RF}, ρ_{4pp} increased, which primarily arises from a reduction in μ due to the dominance of IIS brought about the increased number of free carriers [257]. An additional cause is that the deposition rate at higher P_{RF} is reduced due to re-sputtering of the deposited films by negative oxygen ions which are generated at the oxide target at higher P_{RF} [257].

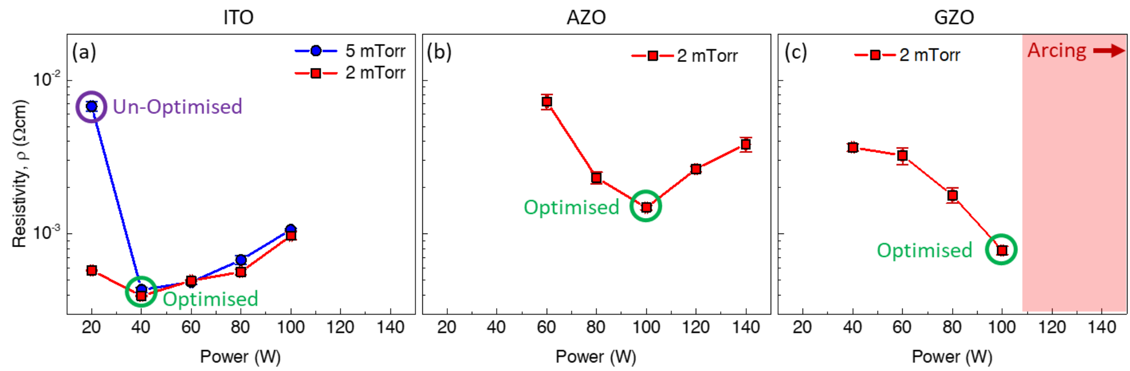

Fig. 4-2. Collinear resistivity, ρ_{4pp}, as a function of the sputtering power, P_{RF}, for (a) ITO, (b) AZO and (c) GZO for room-temperature depositions with a sputtering pressure of $2.0\ \mathrm{mTorr}$ (red square symbols, red line). For ITO, ρ_{4pp} for RT depositions at $5.0\ \mathrm{mTorr}$ are also shown (blue dot symbols, blue line). The red shaded region shows where plasma arcing was observed and thus the deposition was limited to lower power. The chosen P_{RF} for seed "optimised" and "un-optimised" ITO films is indicated by the green and purple circles, respectively.

Later in this work (Chapter 5 and Chapter 6) the influence of ReLA on the optoelectronic, structural, and compositional properties of ITO is thoroughly investigated. To fully test the capability of ReLA and investigate how the film initial condition affect the process, two seed ITO thin films were desired. The first seed material, the "optimised" film, represents the lowest resistivity sample. For the second, an "un-optimised" seed material lower quality material was desired, with ρ approximately a magnitude greater than the optimised film. The variation of P_{RF} from $20 - 100\ \mathrm{W}$ was not sufficient to give a magnitude difference in ρ_{4pp}. Therefore, optimisation of P_{RF} was also performed with $p_{dep} = 5.0\ \mathrm{mTorr}$, shown as the blue dots in Fig. 4-2a. For $P_{RF} \geq 40$, ρ_{4pp} follows a similar trend to that for the films deposited at $2.0\ \mathrm{mTorr}$, with slightly larger resistivities as seen in Fig. 4-1b. However, ρ_{4pp} at 20 W dramatically increases to $(6.8 \pm 0.5) \times 10^{-3}\ \Omega\mathrm{cm}$. This indicates that the increase of ρ_{4pp} with P_{RF} at low sputtering power is highly sensitive to the pressure. The sputtering rate was greatly decreased for this film

and so the high resistivity likely arises from a greatly diminished N, either from a reduced concentration of oxygen vacancies or Sn^{4+} [257].

For AZO, a similar relation stands as for ITO, where ρ_{4pp} initially decreases with P_{RF} before reaching a minimum and then increasing, but the overall trend is shifted to larger P_{RF}. ρ_{4pp} has previously been shown to steadily decrease to an optimal point at 100 W due to an increase in both N and μ with P_{RF} for AZO sputtered at RT onto glass substrates [326]. This increase was correlated with XRD, AFM and XPS data where the increase in μ was attributed to microstructural changes involving an increase in the crystallite size and a reduction in the presence of voids and trapping of oxygen related defects at grain boundaries [59,326,327]. The increase of N was correspondingly attributed to an enhanced ZnO doping efficiency with more "activated" substitutional Al dopants [59,328]. Each of these changes arises from the enhancement of the ion flux and energy for larger P_{RF}, which increases the sputtering yield and growth rate and facilitates the arrival of more energetic species to the substrate that have a high enough E_K to migrate to "better", less entropic, sites on the substrate and/or the growing film.

In Fig. 4-1b, ρ_{4pp} is observed to increase for $P_{RF} > 100$ W, which has also been noted in the literature [326] for RT sputtered AZO on glass substrates. Interestingly, this is not the case for RT deposition of AZO previously achieved by Elhamali [59] in the sputtering chamber utilised in this work, but deposited on glass, where ρ_{4pp} was found to steadily decreased for the entire range of P_{RF} ($40 - 240$ W), flattening out above 180 W [59]. This cannot be assigned to the change in substrate between this work and that of Elhamali [59] and Charpentier [326], who observed a minimum ρ_{4pp} at 100 W, also deposited onto a glass substrate. It is also unlikely to be due to differences in O_2% (0% and 0.25%, respectively), p_{dep} (0.9 mTorr and 2.0 mTorr, respectively) and/or the film thickness (~ 620 nm and ~ 180 nm, respectively) between these two reports, as in this work a minimum is also observed at 100 W with near-identical deposition values to those used by Elhamali [59]. As one of the key influences of P_{RF} is the growth rate, one possible explanation for this discrepancy is the age of the target. This is because as a target is continually used it develops a "racetrack" where the bombardment of the target by the plasma has occurred. Over time, the race track widens and deepens from the erosion, which results in an increase in the sputtering yield and thus growth rate [326]. Therefore, the effective P_{RF} of a system increases with time and may balance out the change in p_{dep} between the work of Elhamali [59], Charpentier [326] and this work. Despite these differences, it has been noted that at high enough P_{RF} and low enough p_{dep}, the sputtered species reach the substrate with high enough E_K to cause bombardments of the resulting film, which re-sputters other particles and introduces an atomic peening effect [329,330], leading to higher stresses in the film [59]. This

previously resulted in the optimal P_{RF} to be at 180 W and not 240 W, where the lowest ρ_{4pp} was observed [59]. In it reasonable to expect that with a higher deposition rate, as found in this work, these effects are exaggerated enough to cause damage to the film, resulting in the larger values of ρ_{4pp} observed at > 100 W. Therefore, the optimal power for RT sputtering of AZO films for this investigation was deemed to be 100 W.

The corresponding case for GZO in presented in Fig. 4-1c. For $P_{RF} = 40 - 100$ W, ρ_{4pp} is observed to decrease from $(3.6 \pm 0.2) \times 10^{-3}$ Ωcm to $(7.8 \pm 0.5) \times 10^{-4}$ Ωcm and no minimum is observed. However, regular "arcing" events were observed on the target surface for $P_{RF} \geq 120$ W. These events comprised a sharp drop in P_{RF} to ~ 20 W for ~ 2 s followed by a sharp rise to ~ 180 W for ~ 4 s, before stabilising back to set-point power. This change in P_{RF} was accompanied by a visible, sharp "lightning ring" covering the racetrack on the target's surface. The frequency of the arcing events was proportional to P_{RF}. The observed phenomena did not abate after many hours of conditioning the target at low P_{RF}, which suggested that the arcing was not due to surface contaminants. The investigation into the physical mechanism behind these arcing events is beyond the scope of this work and so, due to the unknown nature of the arcing event and/or its potential effect on the deposition process, P_{RF} was limited to ≤ 100 W, despite not reaching a global minimum p_{dep} for GZO. Despite this, it is observed for GZO that this minimum is ≥ 100 W, at higher values of P_{RF} than for AZO. The effects of each sputtering parameter on the microstructure of GZO can be expected to be near-identical to that of AZO, as they share the same crystal structure and growth mechanisms [136,258]. Therefore, the change in the required P_{RF} for optimal Ga dopant activation and surface mobility during growth likely arises from the larger atomic mass of Ga (69.72 u) compared to Al (26.98 u) [331], as the larger atomic mass results in lower velocity and thus lower $E_K = \frac{1}{2}mv^2$ [332] of the sputtered species arriving at the sample. As a result of this investigation, the optimal power for RT sputtering of GZO films is designated to be 100 W, below the threshold where arcing phenomena are observed.

In summary, the influence of the deposition conditions on the electronic properties for RT, RF magnetron sputtering of ITO, AZO and GZO was investigated through a combination of a literature survey and experimental calibration. The optimal O_2% and p_{dep} were determined to be 0.25% and 2.0 mTorr for ITO, AZO and GZO. The optimal P_{RF} was found to be 40 W, 100 W and 100 W for ITO, AZO and GZO, respectively. Additionally, the deposition conditions to achieve an "un-optimised" ITO film, to be used to elucidate how the starting conditions effect the ReLA process, were determined to be 20 W at 5.0 mTorr in a mix of 0.25 % oxygen in argon.

4.1.3. Experimental Seed Films

12 seed films were deposited onto 4" Si wafers. The sputtering conditions, film thickness (*via* ORS), collinear resistivity (*via* 4pp) and grain size (*via* XRD) are outlined in Table 4-1. The samples are grouped in three distinct sets, which were exposed to different characterisation techniques depending on the requirements of the investigation (Table 4-2):

1. The **"IR + NIR-VIS-UV SE investigation set"** was produced in order to elucidate the IR optical properties, carrier transport mechanisms (Chapter 4) and the limitations of NIR-VIS-UV SE for TCOs across a range of N (Chapter 7). The set is characterised by three indicative films of each studied material (ITO, AZO and GZO) across a range of N ("High-N", "Mid- N" and "Low- N"). These samples were measured *via* IRSE ($0.034 - 0.8$ eV), at Nottingham Trent University, and NIR-VIS-UV SE ($0.774 - 6.5$ eV), at the University of Nottingham. Hall Effect, 4pp and XRD measurements were employed to aid the fitting process, reveal the best fitting strategy, calculate the effective carrier mass and to calculate the influence of the grain size on the carrier transport mechanisms (Section 4.1.6).
2. The **"ReLA investigation set"** was produced to allow for an investigation into the physical mechanisms that govern the conversion of the optoelectronic properties of ITO during ReLA (Chapter 5). To achieve this, further characterisation of the structural, morphological, and compositional properties of the seed and laser processed films was performed with x-ray photoelectron spectroscopy (XPS), transmission electron microscopy (TEM) and energy dispersive X-ray spectroscopy (EDX). The set is characterised by two indicative ITO films; an "optimised" film with a low resistivity and an "un-optimised" film with a much higher resistivity ($\times \sim 20$). These samples were sputtered onto double-side polished Si wafers, allowing for the appending or IR transmission (IRT) data to the IRSE measurement during fitting. As only the onset of UV absorption was required to determine the band gap of ITO, NIR-VIS SE ($0.774 - 3.4$ eV) was performed at Sheffield Hallam University in place of the full NIR-VIS-UV SE ($0.774 - 6.5$ eV) utilised for the previous set.
3. The **"UMBReLA" investigation set"** was produced to utilise the knowledge gained from the prior investigations in order to elucidate the full capabilities of ReLA with multiple ultrafast pulses (ultrafast multi-beat ReLA or "UMBReLA") to tune the optoelectronic properties of ITO and cover a wider range of epsilon-near-zero (ENZ) for potential applications of IR plasmonics (Chapter 6). Due to limitations introduced by COVID-19 restrictions, NIR-VIS-UV SE was unavailable for such samples, and so visible light reflectance measurements were appended to the IRSE data in order to fit the NIR-VIS-UV optical properties of each sample.

Table 4-1. Details of the varied sputtering conditions and corresponding film properties.

Material	RF Power (W)	Sputtering Pressure (mTorr)	Film Thickness (nm)	Collinear Resistivity $(\times 10^{-4}\ \Omega\mathrm{cm})$
IR + NIR-VIS-UV SE Investigation				
ITO-47 - "High N"	40.0 ± 0.5	2.0 ± 0.1	138 ± 3	5.7 ± 0.6
ITO-38 - "Mid N"	20.0 ± 0.5	2.0 ± 0.1	126 ± 4	13.2 ± 0.2
ITO-39 - "Low-N"	20.0 ± 0.5	5.0 ± 0.1	129 ± 8	180 ± 10
AZO-14 - "High N"	100.0 ± 0.5	2.0 ± 0.1	90 ± 5	19 ± 2
AZO-12 - "Mid N"	80.0 ± 0.5	2.0 ± 0.1	85 ± 6	73 ± 8
AZO-16 - "Low-N"	60.0 ± 0.5	2.0 ± 0.1	90 ± 3	90 ± 10
GZO-09 - "High N"	100.0 ± 0.5	2.0 ± 0.1	182 ± 2	16 ± 0.1
GZO-11 - "Mid N"	80.0 ± 0.5	2.0 ± 0.1	183 ± 1	64 ± 0.5
GZO-13 - "Low-N"	60.0 ± 0.5	2.0 ± 0.1	87 ± 1	90 ± 10
ReLA Investigation				
ITO-57 Optimised ITO	40.0 ± 0.5	2.0 ± 0.1	138 ± 3	3.94 ± 0.04
ITO-58 Un-Optimised ITO	20.0 ± 0.5	5.0 ± 0.1	139 ± 3	68 ± 5
UMBReLA Investigation				
ITO-56 "UMBReLA ITO"	40.0 ± 0.5	2.0 ± 0.1	106.7 ± 0.3	6.1 ± 0.2

Table 4-2. Experimental films and corresponding processing and characterisation techniques.

Material	LA	IRSE	+IRT	+vR	NIR-VIS SE	+UV	4pp	Hall	XRD	XPS	TEM	EDX
IR vs NIR-VIS-UV SE Investigation												
ITO-47 "High N"	✗	✓	✗	✗	✓	✓	✓	✓	✓	✗	✗	✗
ITO-38 "Mid N"	✗	✓	✗	✗	✓	✓	✓	✓	✓	✗	✗	✗
ITO-39 "Low N"	✗	✓	✗	✗	✓	✓	✓	✓	✓	✗	✗	✗
AZO-14 "High N"	✗	✓	✗	✗	✓	✓	✓	✓	✓	✗	✗	✗
AZO-12 "Mid N"	✗	✓	✗	✗	✓	✓	✓	✓	✓	✗	✗	✗
AZO-16 "Low N"	✗	✓	✗	✗	✓	✓	✓	✓	✓	✗	✗	✗
GZO-09 "High N"	✗	✓	✗	✗	✓	✓	✓	✓	✓	✗	✗	✗
GZO-11 "Mid N"	✗	✓	✗	✗	✓	✓	✓	✓	✓	✗	✗	✗
GZO-13 "Low N"	✗	✓	✗	✗	✓	✓	✓	✓	✓	✗	✗	✗
ReLA Investigation												
ITO-57 "Optimised ITO"	✓	✓	✓	✓	✓	✗	✓	✓	✓	✓	✓	✓
ITO-58 "Un-Optimised ITO"	✓	✓	✓	✓	✓	✗	✓	✓	✓	✓	✓	✓
UMBReLA Investigation												
ITO-56 "UMBReLA ITO"	✓	✓	✓	✓	✗	✗	✓	✓	✓	✗	✗	✗

LA: includes laser annealed samples, IRSE: Infrared Spectroscopic Ellipsometry, +IRT: Infrared Transmission appended to IRSE during fit, +vR: visible Reflectance appended to IRSE during fit, NIR-VIS SE: Near-Infrared-Visible Spectroscopic Ellipsometry, +UV: UV range also covered in addition to NIR-VIS SE, 4pp: Four-Point Probe, Hall: Hall Effect, XRD: X-ray Diffraction, AFM: Atomic Force Microscopy, XPS: X-Ray Photoelectron Spectroscopy, TEM: Transmission Electron Microscopy and EDX: Energy Dispersive X-ray Spectroscopy.

4.1.4. Structure of seed TCO films

In order to identify the crystal structure of the seed samples, the ITO, AZO and GZO films were investigated with XRD. Fig. 4-3 presents the X-ray diffractograms for the seed (a) optimised, low ρ, ITO, (b) High-N AZO, (c) un-optimised ITO and (d) High-N AZO GZO films.

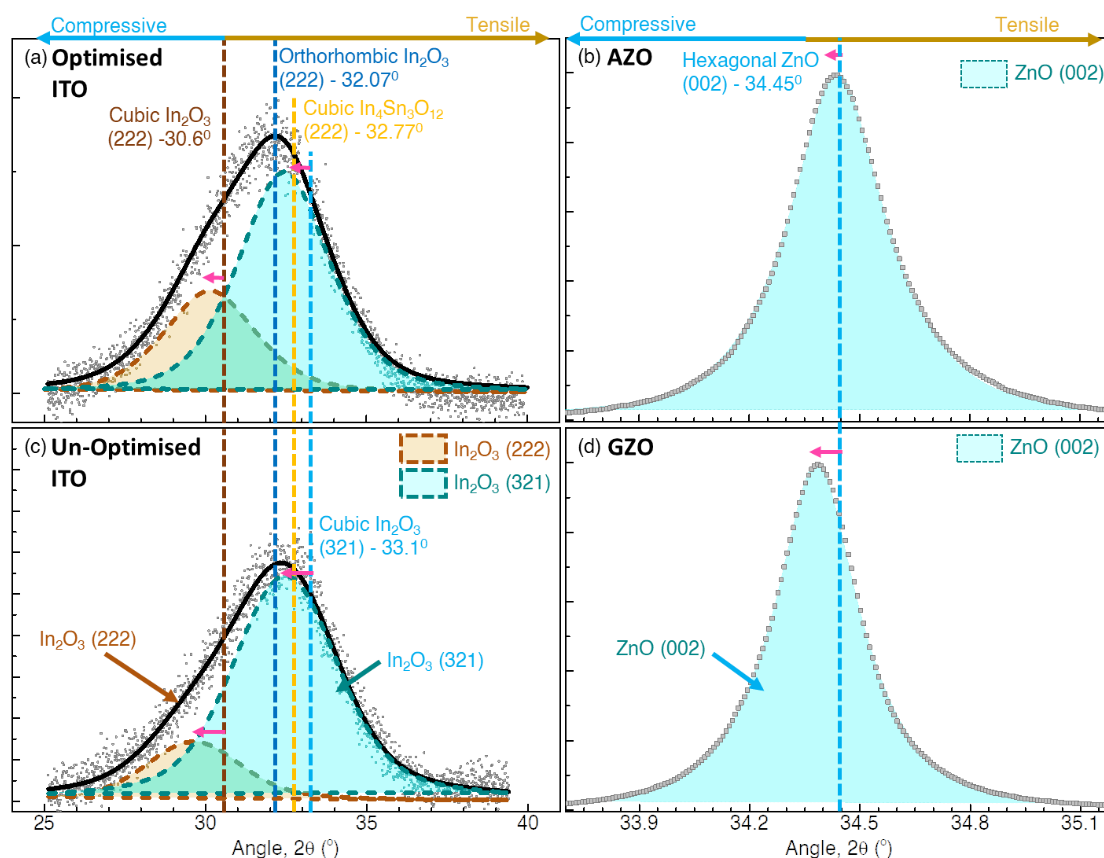

Fig. 4-3. Normalised X-ray diffractograms for (a) "optimised" ITO, (c) "un-optimised" ITO (b) AZO and (d) GZO. The results of fitting two (ITO) or one (AZO and GZO) *pseudo*-Voigt functions are shown as brown and cyan dashed lines with shaded areas. For ITO (a, c), the cumulative fitted peak is indicated by the solid black line and the brown, dark blue, yellow and cyan vertical dashed lines indicate the bulk, unstressed, peak position for the cubic $\mathrm{In_2O_3}$ (222), cubic $\mathrm{In_2O_3}$ (321), rhombohedral $\mathrm{In_4Sn_3O_{12}}$ (222) and the orthorhombic $\mathrm{In_2O_3}$ (211) preferred orientation, respectively. For AZO and GZO (b, d), the cyan dashed line indicates the bulk, unstressed, peak position for the (222) preferred orientation of hexagonal ZnO. The pink arrows indicate the peak shift due to residual stress within the film and the cyan and yellow lines at the top of (a) and (b) indicate how the direction of the shift represents either compressive or tensile stress, respectively. Note that the sharp (100) Si peak at $32.9^0 - 33.1^0$ has been manually removed from all diffractograms to facilitate the fitting process.

For the optimised and un-optimised ITO films (Fig. 4-3a, c), a broad, asymmetric, peak at $\sim 32.5°$ is observed. The existence of such a peak has been noted but the underlying nature of this peak has not been sufficiently explained [169,333–336]. A few possible explanations for the broadening and asymmetry of this peak are that there is a mix of the (expected) cubic (222) $\mathrm{In_2O_3}$ peak / preferred orientation ($a = 1.0118$ nm [157], $2\theta = 30.607°$) alongside:

1. a (321) preferred orientation for cubic $\mathrm{In_2O_3}$ ($a = 1.0118$ nm, $2\theta = 33.127°$ [157]) within the amorphous film (dark blue dashed line in Fig. 4-3a,c),
2. a (222) preferred orientation for rhombohedral $\mathrm{In_4Sn_3O_{12}}$ ($a = \mathrm{b} = 0.94634$ nm, $c = 0.8858\ nm$, $\alpha = 90°$, $2\theta = 32.794°$ [147]) phase, present in amorphous ITO films [138,148,334,335,337] (yellow dashed line in Fig. 4-3a,c),
3. a (211) preferred orientation for orthorhombic $\mathrm{In_2O_3}$ ($a = 0.7912$ nm, $b = 0.5477$ nm, $c = 0.5592$ nm [338], $2\theta_c = 32.07°$) (cyan dashed line in Fig. 4-3a,c).

To account for the peak asymmetry, the diffractograms are fit with two *pseudo*-Voigt functions with shared Lorentzian and Gaussian broadening factors (β_L and β_G, respectively) [284]. A grain size, D_{Gr}, of 3.2 ± 0.3 nm (Eq. (3-4)) is found for the optimised ITO film, confirming that the film is amorphous or, equally, nanocrystalline. The offset of the (222) peak (pink arrow in Fig. 4-3a,c) from the "bulk" value (brown dashed line in Fig. 4-3a,c) indicates that the film is under a tensile stress ($\delta_S = 7.0 \pm 0.3$ GPa) due to the interfacial mismatch between the atomic spacings for the Si and $\mathrm{In_2O_3}$ lattices [339] . Therefore, by assuming the stress within the film is uniform, the "bulk" peak position for the 2^{nd}, larger, peak is calculated to be 33.17 ± 0.04 °. In Fig. 4-3a, this can be seen from how an equal length pink arrow must come from the cyan dashed line, which represents the cubic $\mathrm{In_2O_3}$ (321) peak, in order to produce the as fit peak position. This indicates that this peak is likely due to a (321) preferred orientation for cubic $\mathrm{In_2O_3}$ within the amorphous film. However, it is entirely plausible that all three potential sources exist but cannot be individually resolved. For the AZO (Fig. 4-3b) and GZO (Fig. 4-3d) films, a sharper, more symmetric peak at $34.44 \pm 0.05°$ and $34.38 \pm 0.05°$, respectively, is observed. The lattice parameters for a hexagonal, wurtzite crystal structure of ZnO are $a = 0.32495 \pm 0.0005$ nm and $c = 0.52069 \pm 0.00005$ nm [278]. Eq. (3-8) and Eq. (3-3) are used to calculate a bulk, unstressed d -spacing of $d_{bulk} = 0.2604 \pm 0.0004$ nm and a peak position of $2\theta = 34.45° \pm 0.05°$, respectively, which is indicated by the vertical dashed cyan line in Fig. 4-3b,d. The diffraction peak is much sharper than those for ITO, corresponding to the fact that the structure of AZO and GZO is polycrystalline with a much larger grain size (~ 45 nm). Table 4-3 presents the results of fitting the AZO and GZO samples with a *pseudo*-Voigt peak, as outlined in Section 3.2.1. Both the results for the centre of the seed wafer and the average values for 10 positions from across the entire wafer are given.

Table 4-3. Average grain size, D_{Gr}, film stress, δ_S, and micro-strain, ϵ_{mStr}, for the seed AZO and GZO films.

Fixed Parameters	Unit	AZO (Centre)	AZO (Average)	GZO (Centre)	GZO (Average)
D_{Gr}	nm	43.5 ± 0.3	40 ± 3	48.2 ± 0.5	45 ± 3
δ_S	GPa	-0.209 ± 0.002	-0.17 ± 0.07	-0.769 ± 0.002	-0.5 ± 0.3
ϵ_{mStr}	°	0.375 ± 0.006	0.370 ± 0.005	0.347 ± 0.006	0.36 ± 0.02

4.1.5. Uniformity of seed TCO films

For all samples, some slight non-uniformity in the thickness and ρ_{4pp} was present across the $1/4$ wafers. This non-uniformity introduces a problem for further LA experiments which require a set of laser-processed "spots" of $\sim 1 \times 1$ cm across the full wafer. For example, deviations in the seed film may be mistaken for laser-induced modifications from the seed film to the annealed film. To account for this, an investigation into the non-uniformity of the thickness and ρ_{4pp} across the full $4''$ wafers was undertaken. After deposition of the ITO, AZO and GZO films set for further investigation (Table 4-1), the wafers were cut into ~ 90, $\sim (8 \times 8)$ mm^2 "wafelets". The wafelets were cut along their long edge for each cut, into to reduce any stresses introduce to the film. Importantly, the x and y position, relative to the sample centre, was noted for each wafelet, alongside a unique wafelet identification number (ID). Following this, each wafelet was measured *via* ORS, 4pp and IRT in order to determine the film thickness, visible optical constants, collinear resistivity, "optical" resistivity, "optical" mean free time and IR optical constants, following the analytical methodology outlined in Section 3.2.4 and Section 3.2.5. The thickness, as determined from fitting of ORS data, was used to calculate ρ_{4pp} from the sheet resistance. Furthermore, the thickness, UV oscillators and ε_∞ determined from ORS were fixed during the fitting of IRT data. While fitting IRT data within CompleteEase™, ρ_{4pp} was used as a starting value in order to subsequently fit for ρ_{opt}. The properties of each wafelet were plotted against their x and y position to produce a set of colour maps. The deviation is calculated as the percent difference of the wafelet to the average value.

Fig. 4-4a-c presents a colour map of the thickness of the "UMBReLA" set (Section 4.1.3) of (a) ITO, (b) AZO and (c) GZO across the $4''$ wafer. Fig. 4-4d-f presents the corresponding thickness deviation (in %). For ITO, the thickness range does not deviate more than 8 nm (7.2%) across the wafer and the standard deviation is only 2 nm (1.8%). GZO has a much higher thickness range of 15 nm (15.8%) but this is mostly due to a sharp dip in the thickness at the far edges of the wafer, so that the standard deviation is also low, at 4 nm (4.1%). For AZO, however, the non-uniformity is clearly visible within the colour map and there exist a thickness range of 32 nm (34.2%) and correspondingly high standard deviation of 9 nm (9.7%). All films were deposited had relatively similar deposition rates, and so the source of the significantly higher thickness deviation for AZO is not fully understood.

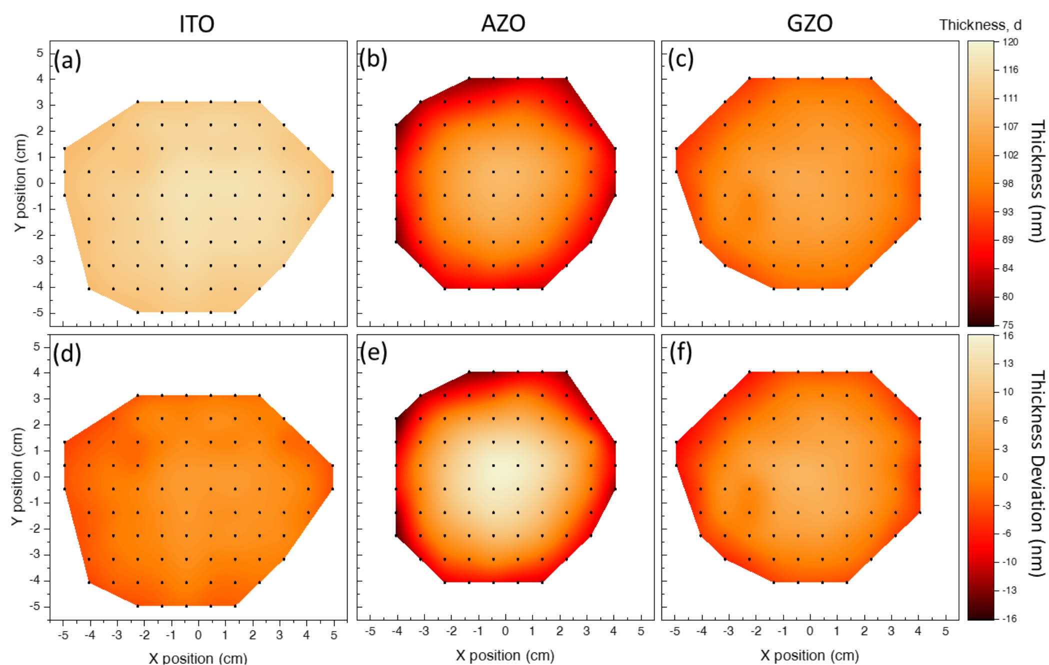

Fig. 4-4. Colour maps of the (a-c) thickness and (d-f) thickness deviation (in %) across a 4´´ Si wafer with an ITO, AZO and GZO thin film coating, respectively.

It is well known that there exist a thickness dependence on the resistivity of ITO [312], AZO [340] and GZO [341] films. Furthermore, the change in thickness across the wafer implies a change in the sputtering rate, which has been noted to drastically affect the resulting film properties (Section 4.1.2). Fig. 4-5a-c presents a colour map for the deviation (in %) of the collinear resistivity, measured *via* 4pp, of the of (a) ITO, (b) AZO and (c) GZO thin films across the 4´´ wafer. Fig. 4-5d-f presents the corresponding deviation of the optical resistivity, measured *via* IR transmission. The thickness, or equivalently the sputtering rate, deviation observed in Fig. 4-4 gives rise to a deviation in ρ_{4pp} across the wafer. The values of ρ_{opt} and ρ_{4pp} generally agree, although the values of ρ_{4pp} are generally slightly lower than ρ_{opt} and show a steeper gradient at the edges. For ITO, the deviation is relatively minor, and the average resistivity is lower towards the centre. For AZO and GZO, conversely, the deviation across the film is larger with a higher resistivity in the centre.

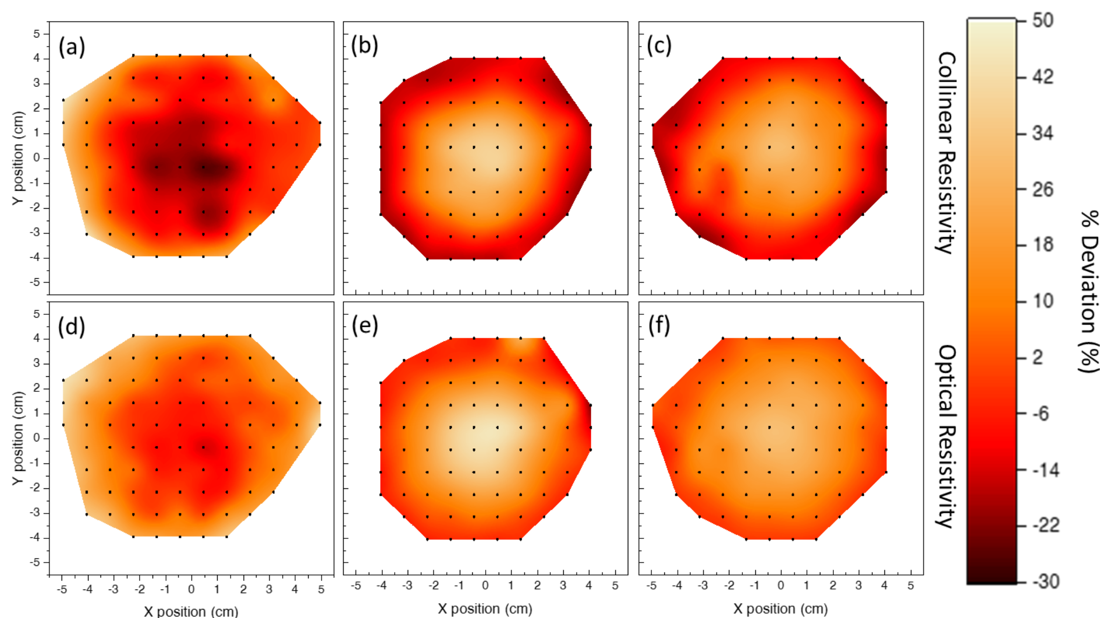

Fig. 4-5. Colour maps of the % deviation for the (a-c) collinear and (d-f) optical resistivity across a 4´ ´ Si wafer with an ITO, AZO and GZO thin film coating, respectively.

Fitting of the IRT measurement also provides the optical mean free time, τ_{opt}, alongside ρ_{opt}. This allows for the calculation of the optical carrier mobility and concentration *via* Eq. (2-40) and Eq. (2-41), from which an understanding of the variations in the transport mechanisms (that are more fundamental properties than the resistivity) can be built. This step requires an assumption of the effective mass to be $0.30\, m_e$ for ITO and $0.28\, m_e$ AZO and GZO [118]. The absolute value of the effective mass does not affect the resulting % deviation, but it is important to note that variations in N_{opt} and μ_{opt} may partially originate from variations in m_e^*. Hall Effect measurements are deemed necessary to determine the effective mass for each wafelet (see Section 4.2.4). Fig. 4-6a-c presents a colour map of the deviation (in %) of the optical carrier concentration of the "UMBReLA" set of (a) ITO, (b) AZO and (c) GZO deposited on a 4´ ´ Si wafer. Fig. 4-6d-f presents the corresponding deviation in the optical carrier mobility. For ITO, it is found that the decrease in ρ_{opt} towards the centre of the wafer arises primarily from an increase in μ_{opt} from $\sim 15\ \mathrm{cm^2/Vs}$ to nearly twice the edge value of $\sim 25\ \mathrm{cm^2/Vs}$ at the centre. The carrier concentration remains near constant with a value of $\sim 4.2\ \mathrm{cm^{-3}}$. For AZO and GZO, the reverse case is found and the increasing ρ_{opt} towards the centre of the film arises from a decrease in N_{opt} while μ_{opt} remains near constant with a value of $\sim 15\ \mathrm{cm^2/Vs}$.

As seen above, N_{opt} remains steady at $\sim 4 \times 10^{20} cm^{-3}$ for ITO while the mobility increases with thickness and sputtering rate, giving rise to a resistivity that decreases with sputtering rate. As the film is amorphous across the entire wafer (Section 4.1.4), structural alterations cannot be used to explain the change in μ_{opt} across the film. Instead, it is noted that

for ITO films with $N > \sim 4 \times 10^{20} cm^{-3}$, the dominant scattering mechanism is ionised cluster scattering (ICS) that has a very large scattering coefficient for ITO films and thus the mobility is highly sensitive to N [234,342,343]. For AZO and GZO, however, D_{Gr} is larger and N_{opt} is lower so that the effects of GBS and ICS are balanced and μ_{opt} is relatively constant with N_{opt}. The effect of the scattering mechanisms on the carrier transport of TCOs is explored further, below.

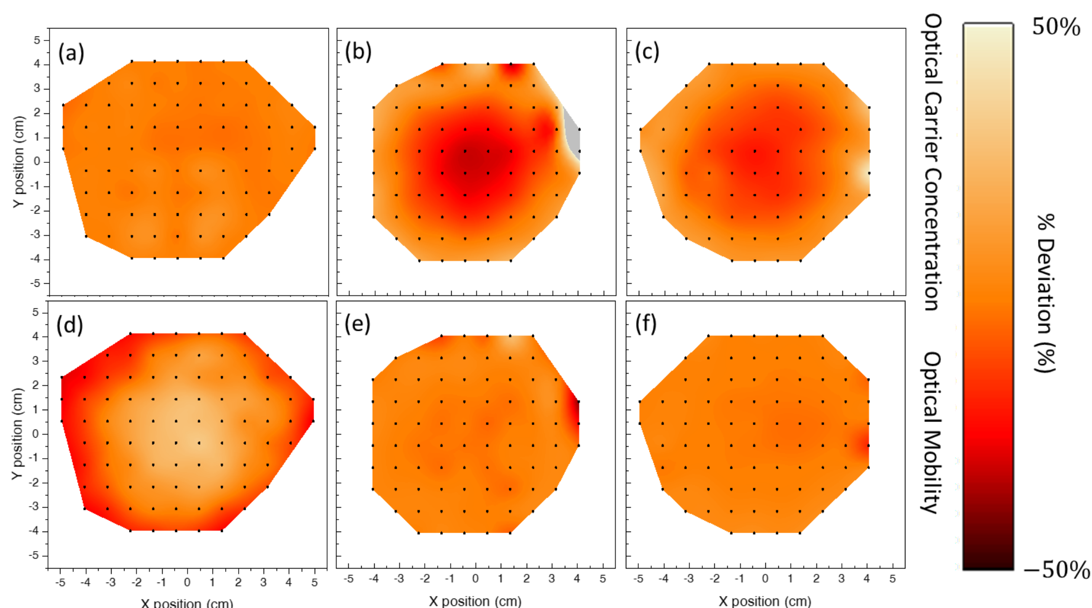

Fig. 4-6. Colour maps of the % deviation for the optical carrier (a-c) mobility and (d-f) concentration across a 4´ ´ Si wafer with an ITO, AZO and GZO thin film coating, respectively.

4.1.6. Carrier transport mechanisms of seed TCO films

In order to further elucidate the mechanisms that govern the transport properties of TCOs, a large set of films were sputtered across the range of sputtering conditions explored in Section 4.1.2. A set of ITO, AZO and GZO thin films were fabricated *via* RT magnetron sputtering on top of test-grade n-type Si wafers (resistivity range: $1 - 20\ \Omega\text{cm}$). For each material, the deposition conditions were varied to produce films with similar crystal structure while covering a range of N. Fig. 4-7 presents the "Hall" carrier concentration, N_{Hall}, and mobility, μ_{Hall}, of the wider set of RT sputtered (a) ITO, (b) AZO and (c) GZO films (grey squares). The yellow squares indicate the optimised ITO, AZO and GZO thin films where Hall Effect was performed for a set of 10 samples covering the entire dimensions of the seed wafers.

The relationship between μ and N follows the trend described by Ellmer *et al.* [343] The $\mu(N)$ relationship is calculated for each material by following Eqs. (2-49) to (2-58) and is presented with the solid lines in Fig. 4-7a-c. This approach accounts for the effects of grain boundary scattering (GBS) (*via* Seto's model) [240] and ionized impurity scattering (IIS) (*via*

Masetti's model) [234] and ignores both dislocation scattering and neutral impurity scattering. When fitting $\mu(N)$ to the experimental data only the parameters N_{ref2} and Q_t were left free, for AZO and GZO, with an additional requirement for α_2 as a free parameter for ITO. The parameters which influence $\mu(N)$ outside the experimental range were taken from Ellmer *et al*. [227], where the experimental points covered a wider range of N. The input of D_{Gr} into Eq. (2-60) and Eq. (2-61) was obtained *via* XRD (see Section 4.1.4).

The influence of the grain size on the $\mu(N)$ relationship is seen in Fig. 4-7a-c. Firstly, a unique behaviour is noted for ITO, while some similarities are palpable for AZO and GZO. The most noticeable deviation between each material is in the region where GBS is dominant, which vastly inhibits the carrier mobility within the "mobility hole" region, where $\mu_{Hall} \approx 0\ \mathrm{cm^2/Vs}$ [240]. The boundaries of this region, with respect to N, result from D_{Gr} and Q_t (Eqs. (2-59) and (2-60)). RT sputtered ITO thin films are nanocrystalline whereas sputtered AZO and GZO films follow a columnar structure with larger grains [70]. As the grain size increases, so does the grain boundary limited mobility, μ_0 (Eq. (2-61)), and therefore the mobility at the low-N limit is larger. However, concurrently, the region where GBS becomes dominant covers a larger range of N. This is vital to consider for plasmonic material components, as materials with a carrier concentration within the GBS region will have poor ability to exploit plasmonic responses in the IR due to their inhibited carrier mobility. The onset of GBS with regard to N is defined by the trap density, Q_t, over D_{Gr} [343,344] so this limit may be reduced to lower N by reducing Q_t. This could be achieved by varying the growth conditions and/or following a post annealing process. Another option would be to take advantage of the ability of the high conductivity of amorphous ITO and IGZO films [48,138] which negates the influence of GBS [240]. This is noted from Fig. 4-7a where, for ITO, there is no region where $\mu_{Hall} \approx 0\ \mathrm{cm^2/Vs}$.

Table 4-4. Fixed and free parameters for ITO, AZO and GZO from fitting the transport properties determined from Hall Effect.

Fixed Parameters	Unit	ITO	AZO	GZO
μ_{max}	$\mathrm{cm^2/Vs}$	210		210
μ_{min}	$\mathrm{cm^2/Vs}$	55	55	55
$\mu_{min}-\mu_1$	$\mathrm{cm^2/Vs}$	5	5	5
N_{ref1}	$\times 10^{17}\ \mathrm{cm^{-3}}$	15	4	4
α_1		1	1	1
α_2		6	4	4
D_{Gr}	nm	2.75	40	45
ε_r		9	8.3	8.3
m_0^*/m_e		0.21 ± 0.02	0.24 ± 0.03	0.26 ± 0.02
C	$\mathrm{eV^{-1}}$	0.4 ± 0.1	0.6 ± 0.2	0.6 ± 0.1
Free Parameters	**Unit**	**ITO**	**AZO**	**GZO**
N_{ref2}	$\times 10^{20}\ \mathrm{cm^{-3}}$	4.9 ± 0.2	1.33 ± 0.06	2.24 ± 0.08
Q_t	$\times 10^{12}\ \mathrm{cm^{-2}}$	3.7 ± 0.8	14.01 ± 0.4	27.7 ± 0.9
D_{Gr}	nm	5.0 ± 0.9	--	--

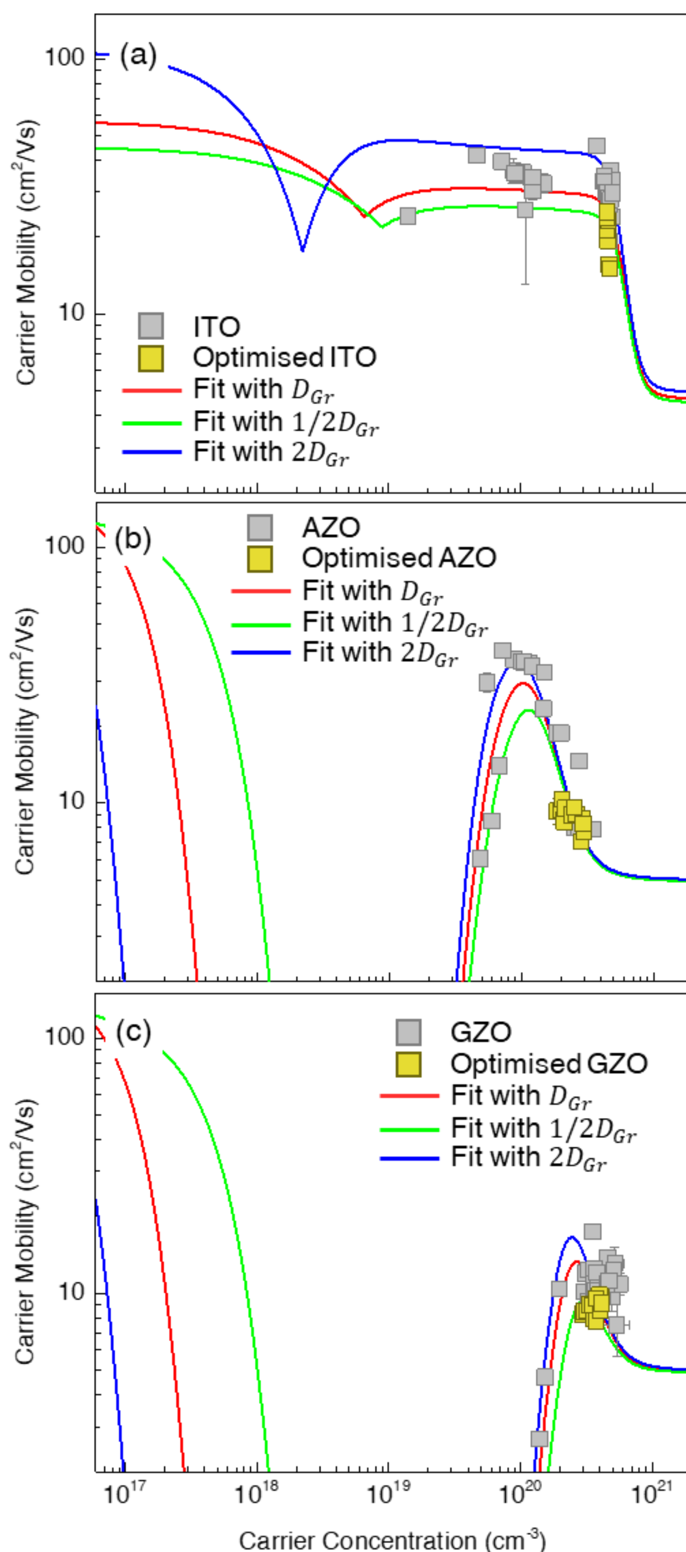

Fig. 4-7. Hall carrier concentration and mobility of sputtered (a) ITO, (b) AZO and (c) GZO films (grey squares). The yellow squares highlight the samples across the wafer of the "optimised" films. The solid red line is the fit to the Hall Effect data. The green and blue lines present the fit of $\mu(N)$ calculated with half and double the measured grain size, respectively, in order to show how the variation of the grain size can explain the deviations of the data points from the theoretical trend.

It is also observed that the samples do not precisely follow the trend of $\mu(N)$ as fit to all experimental datasets. This is because the $\mu(N)$ relation requires the input of a single D_{Gr} parameter for all films. In reality, the varying sputtering conditions required to vary N would influence D_{Gr}. To demonstrate this, Fig. 4-7 presents $\mu(N)$ as calculated using the parameters outlined in Table 4-4 but with D_{Gr} set at $0.5D_{Gr}$ (green line) and $2D_{Gr}$ (blue line). It is observed that nearly all data points lie within the boundaries set by the green and blue lines. Therefore, the deviations of the data points around the theoretical trend can be said to arise from the variation of the grain size between each sample. The most prominent effect of changing D_{Gr} is the shift of the lower boundary of the "mobility hole" region, where $\mu \approx 0\ \mathrm{cm^2/Vs}$. Specifically, the mobility hole is wider for films with larger D_{Gr}. However, D_{Gr} has a negligible effect of μ at high N as ICS becomes the dominant scattering mechanism. As the values of N for the optimised ITO films lie within this region, a variation in D_{Gr} across the wafer or in response to laser processing can be ignored when contemplating the $\mu(N)$ relation.

4.2. Optical modelling of the seed TCOs

In this section, the delicate extraction of the permittivity and transport properties *via* SE is documented. In effect, a step-by-step guide to achieving a good fit of ITO, AZO and GZO is provided. Then, the analytical techniques that provide additional insights into the materials are detailed (Section 4.2.1). Fitting of thin film materials with SE is not always trivial and may be complicated by non-idealities of the film or sample geometry. Because of this, some key sources of non-idealities in SE measurements are investigated and solutions to maintain reliable fittings for such samples (Section 4.2.2 and 4.2.3) are highlighted.

4.2.1. Fitting "ideal" films with IR-VIS-UV SE

This section will guide the reader through the process used to fit SE measurements across the entire IR and NIR-VIS-UV spectral range ($0.034 - 6.5\ \mathrm{eV}$) in order to extract the complex permittivity, $\tilde{\varepsilon}(E) = \varepsilon_1(E) + i\varepsilon_2(E)$, and optoelectronic properties of the TCO films.

ITO

The "High-N" ITO film (see Table 4-1) is used as an example for the simplest case and then the other materials will be investigated in turn. Fig. 4-8a presents the measured $\Psi(E)$ (blue squares) and $\Delta(E)$ (red squares) of the seed "High-N" ITO thin film. Fig. 4-8b presents the corresponding real (blue squares) and imaginary (red squares) *pseudo*-permittivity, $< \tilde{\varepsilon}(E) > = < \varepsilon_1(E) > + i < \varepsilon_2(E) >$. The *pseudo*-permittivity maintains continuity throughout the entire spectral range (as measured independently by two ellipsometers at different spectral ranges). The angular dependence of $< \tilde{\varepsilon}(E) >$ is also small but indicative of a thin film material. The *pseudo*-permittivity alongside, or in-place of, $\Psi(E)$ and $\Delta(E)$ will be presented throughout this

thesis. The first step is to fit the NIR-VIS-UV spectral region, as the process of fitting the NIR-VIS-UV before fitting the IR was found to give the most accurate results [342]. One of the simplest ways fit to the film is to use the Cauchy model, which is used for transparent films where there is no absorption, α, and the refractive index, n, is described by the Cauchy dispersion equation:

$$n(\lambda) = A + \frac{B}{\lambda^2} + \frac{C}{\lambda^4} \tag{4-1}$$

where A, B and C are unitless fitting parameters related to the refractive index and dispersion.

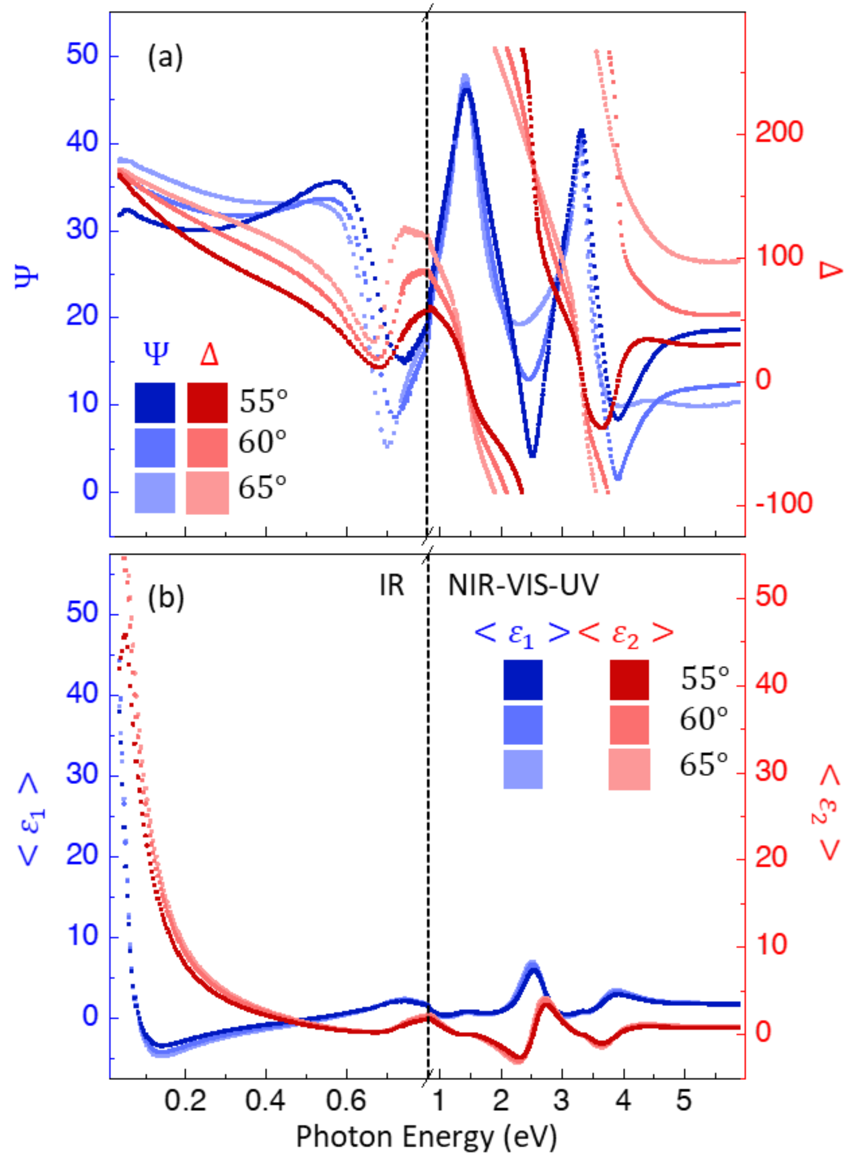

Fig. 4-8. (a) $\Psi(\mathrm{E})$ (blue squares) and $\Delta(\mathrm{E})$ (red squares) and (b) the real ($< \varepsilon_1(E) >$; blue squares) and imaginary ($< \varepsilon_1(E) >$; red squares) *pseudo*-permittivity, of the seed "High-N" ITO thin film at incident angles of $55°$ (darker shade), $60°$ (normal shade) and $65°$ (lighter shade). Note the change of scale in the x-axis at 0.8 eV, where the vertical dashed black line indicates the boundary between the IR and NIR-VIS-UV ranges covered by the two ellipsometers.

TCOs are known to have a large bandgap, E_G, and a high visible transparency, T_{VIS}. Fitting the visible region, with Cauchy model, $(1.0 - 2.5 \text{ eV})$ results in a film thickness, d_{film}, of $127.28 \pm 0.01 \text{ nm}$ and a relatively large root mean-squared error (MSE), which defines how well the data is fit (see Section 3.2.5), of 26.6. However, a model that also considers the intra- and inter-band absorption is required for TCOs. One method to account for a non-zero imaginary permittivity, $\varepsilon_2(E)$, is using a "B-Spline" model, an advanced feature of CompleteEase™ [84], that specifies $\varepsilon_2(E)$ using a series of equally spaced "nodes", or control points. The real permittivity, $\varepsilon_1(E)$, is calculated from $\varepsilon_2(E)$ using the Kramers-Kronig (KK) relations [345,346]. This reduces the freedom of the fitting parameters and constrains them in a way which ensures physical reality. Furthermore, as a KK-consistent B-Spline with $\varepsilon_2 > 0$ is fully representative of a physical, realistic, permittivity of a uniform, "ideal" thin material, it follows that if the data is unable to be fit with such a model, then non-idealities must be present to explain the line-shape.

If the optical constants of the material were all that was required, then the fitting procedure would be complete. The optical constants can also be used to determine figures of merit for particular plasmonic applications [347–349], solve Mie theory for a single spherical nanoparticle [350,351] and to find the band-edge by fitting the linear region of $(\alpha E)^2$ against E [352]. However, no information of the physical mechanisms that govern the light-matter interactions are revealed. To achieve this, a "generalised oscillator" model, describing the permittivity of a material as a summation of various individual oscillators (Section 3.2.5), is required [353]. To fit the measurement with a generalised oscillator model, a summation is made of one Drude and two Tauc-Lorentz oscillators in order to describe both the absorption due to free carriers (intra-band absorption) and inter-band transitions, respectively, as has been suggested by Uprety *et al.* for ITO films [354]. It is important to note that any fit can be achieved, given enough oscillators. "Over-fitting" of the data in this way can complicate the ability to extract useful information from the generalised oscillator model. Potential over-fitting of the data can be investigated *via* the parameter correlation [353], a number between negative and positive unity assigned to each parameter pair where absolute values above 0.90 indicate that the variations in one parameter can be completely accounted for by variations in its correlated counterpart. The parameter correlation can be reduced, increasing the validity of the fit, by reducing the number of free parameters [297]. In some cases, this can be achieved by fixing "known" values during the fit. If no known values exist, then the best strategy is to achieve the best fit with a minimum set of oscillators [297]. A general rule is any added complexity in the model (*i.e.* introducing surface roughness or additional oscillators etc.) is valid as long as it produces a decrease in the MSE by at least $\sim 25\%$ [82], though exceptions to this rule can be made if the parameter is thought to improve the "realness" of the model. The final step to accurately fit the

NIR-VIS-UV SE data is to include a layer of surface roughness, which is described by an effective medium approximation (EMA) consisting of 50% of the layer below and 50% air [301].

Following the fit to the NIR-VIS-UV SE data, the parameters describing the UV absorption and sample geometry are fixed when fitting the IR data. Due to the perfect overlap between the IR and NIR-VIS-UV data (Fig. 4-8), the IR region can potentially be fit by leaving only the Drude oscillator parameters free. This “strategy” is found to give the best results [342], provided that no other absorption mechanism occurs in this spectral range apart from the free carrier absorption. To improve the fit, it was necessary to include an additional IR phonon absorption (described by a Gaussian oscillator) at $\sim 0.045\ \mathrm{eV}$. Due to amorphous structure of the ITO film and the screening of the peak by the free carrier absorption, the $\mathrm{Sn-O}$, $\mathrm{Sn-O-Sn}$ and $\mathrm{In-O}$ optical phonon modes [168,342,355] cannot be individually resolved. The Gaussian oscillator at $\sim 0.045\ \mathrm{eV}$ can be said to represent a convolution of the aforementioned peaks. The inclusion of an additional oscillator at $\sim 0.23 - 0.29\ \mathrm{eV}$ has been reported to improve the fit of ITO [354]. This broader peak at $\sim 0.26\ \mathrm{eV}$ has been ascribed to hydroxide group absorption ($\mathrm{Sn-OH}$ and $\mathrm{O-H}$ stretching), present due to water molecules within the chamber during the initial stage of deposition. Inclusion of this peak can reduce the MSE to 5.59. However, the attribution of this peak to water molecules within a high vacuum chamber is questionable. It is also possible that this peak is instead an artefact that is representative of “non-idealities” of the thin film [82], such as the presence of multiple carrier species or a z-axis inhomogeneity. This will be investigated in more detail in Section 4.2.3. Prior to this, due to the improvement in the fit to ensure more accurate values of the permittivity (also important for the arguments of Chapter 7). To summarise, an ideal thin film with a summation of ε_∞ and one Drude, two Tauc-Lorentz and two Gaussian oscillators with a surface roughness layer is used to fit the “High-N” ITO film. The two Gaussian oscillators peak positions are fixed at $0.042\ \mathrm{eV}$ and $0.28\ \mathrm{eV}$.

The schematic of the geometric model with the general oscillator layers’ parameters is presented in Fig. 4-9c. The orange and blue shaded areas indicate that the parameters were fit in the IR or NIR-VIS-UV, respectively, whereas the grey shaded areas indicate that the value was fixed during fitting. The raw SE data and *pseudo*-permittivity are presented in Fig. 4-9a and Fig. 4-9b, respectively, where the fit with the outlined model is presented as the green solid lines. The different shades of each colour indicate the various incident angles. The structure and format of Fig. 4-9 (data, fit, parametrised geometric model and component-summed ε_2) constitutes a “fitting report”, which will be presented for all following materials. A good fit to the ellipsometric angles and *pseudo*-permittivity is observed throughout the entire spectral range. Fig. 4-9d presents the imaginary permittivity (solid red line) of the High-N ITO film broken

down into its individual oscillators (dashed lines). For comparison, the fit of the B-Spline model to the IR and NIR-VIS-UV measurements is presented with the brown and dark blue dotted lines, respectively. A very good agreement is observed between the generalised oscillator model and B-Spline across the entire measurement range, increasing confidence in the utilised model.

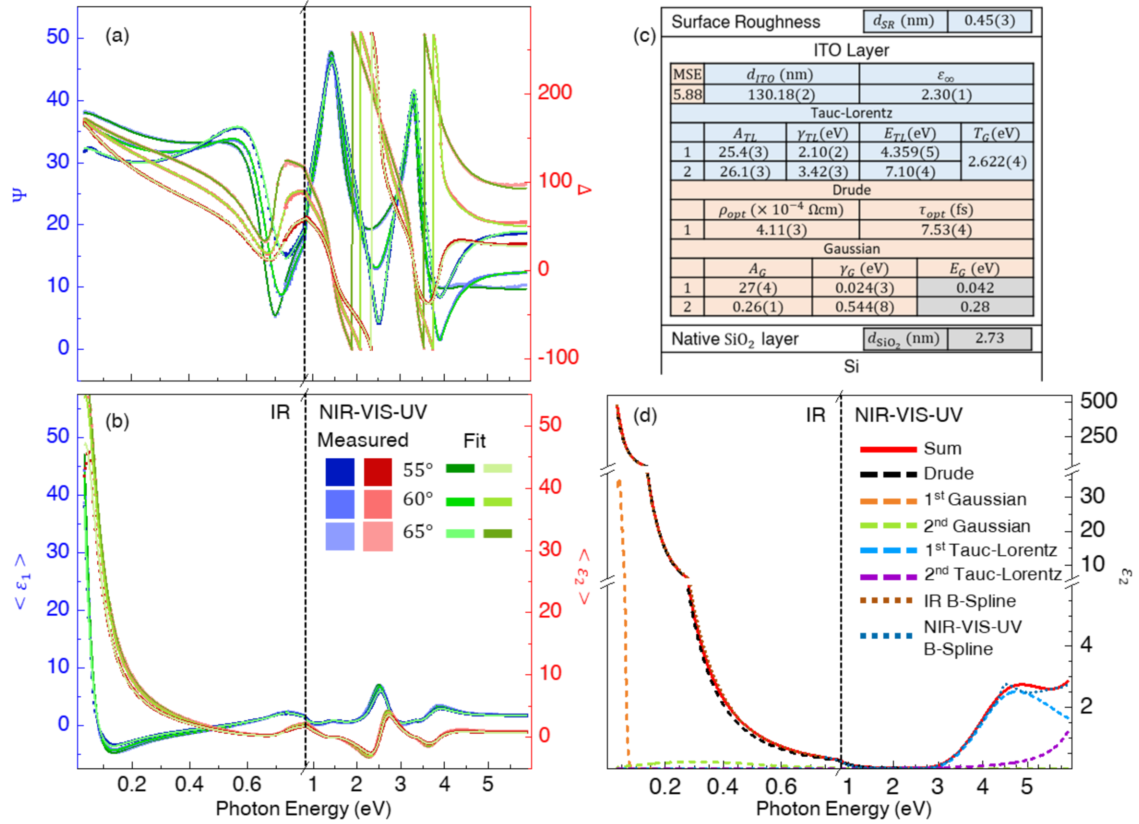

Fig. 4-9. Fitting report for the seed "High-N" ITO thin film. (a) $\Psi(\mathrm{E})$ (blue squares) and $\Delta(\mathrm{E})$ (red squares) and (b) the real ($< \varepsilon_1(E) >$; blue squares) and imaginary ($< \varepsilon_2(E) >$; red squares) *pseudo*-permittivity at incident angles of 55° (darker shade), 60° (normal shade) and 65° (lighter shade). The solid green lines indicate the fit to each collected data set. (c) The parameterised oscillator model utilised to fit the data, where the blue and orange shaded areas indicate that the parameters were fit to the NIR-VIS-UV or IR part of the spectra, respectively, and the grey areas indicate the parameter was fixed during the fit. (d) The as-fit imaginary permittivity, $\varepsilon_2(E)$ (solid red line), of the ITO thin film split into its individual components: a single Drude term (dashed black line), two Gaussian oscillators (dashed orange and green lines) and two Tauc-Lorentz oscillators (dashed blue and purple lines). For comparison, the dotted brown and dark blue lines present the B-Spline fit to the IR and NIR-VIS-UV measurements, respectively. Note the changes of scale in the x-axis of (a), (b) and (c) at $0.8\ \mathrm{eV}$, where the vertical dashed black line indicates the boundary between the IR and NIR-VIS-UV ranges covered by the two ellipsometers.

The approach outlined above was followed in order to produce a fitting report for the "Low-N" ITO film (Fig. 4-10). A more complicated line-shape of $\Psi(E)$ and $\Delta(E)$ is noted, compared to the "High-N" film (Fig. 4-9a). This arises from the reduced screening of the IR oscillators, and allows for fitting of the energy position of the two IR oscillators. The 2^{nd}, broader, peak exist at 0.131 ± 0.003 eV with a broadening of 0.091 ± 0.006 eV, significantly below than the values found previously [342] or used to fit the High-N ITO film. The change in the E_0 with N suggest that this peak is not due to hydroxide group absorption [342] but instead, from defect absorption or an artefact owing to non-idealities within the film (see Section 4.2.3).

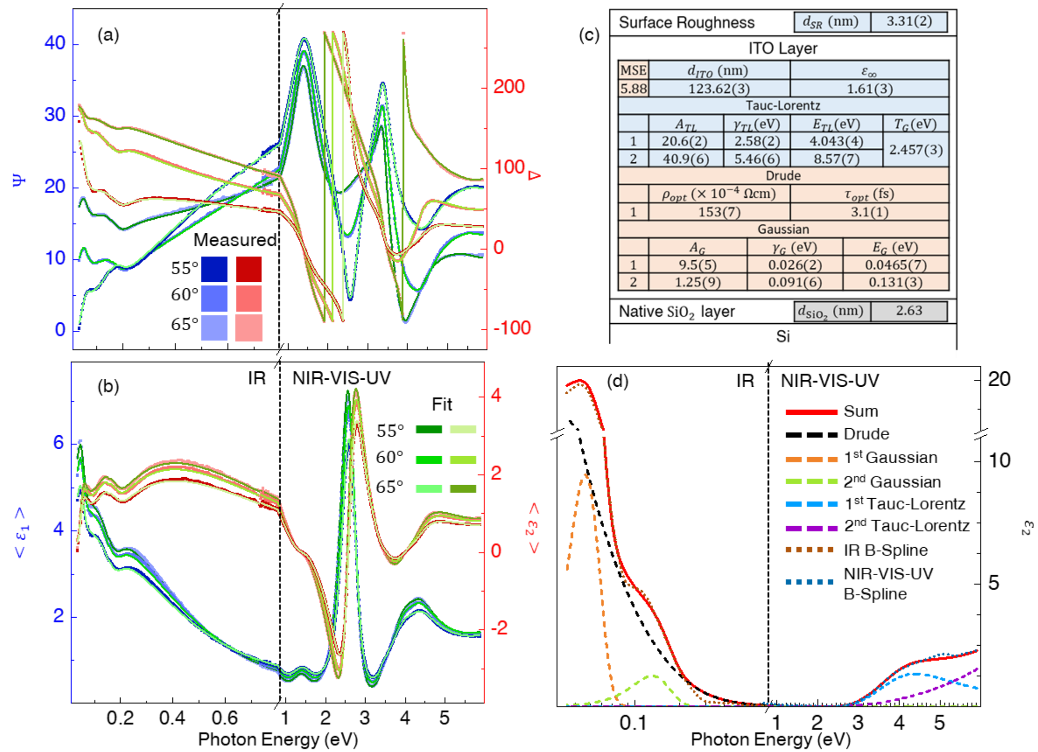

Fig. 4-10. Fitting report for the seed "Low-N" ITO thin film. (a) $\Psi(\mathrm{E})$ (blue squares) and $\Delta(\mathrm{E})$ (red squares) and (b) the real ($<\varepsilon_1(E)>$; blue squares) and imaginary ($<\varepsilon_2(E)>$; red squares) *pseudo*-permittivity at $55-65°$ (darker-lighter shades). The solid green lines indicate the fit to each collected data set. (c) The parameterised oscillator model, where the blue and orange shaded areas indicate that the parameters were fit to the NIR-VIS-UV or IR part of the spectra, respectively, and the grey areas indicate the parameter was fixed during the fit. (d) The imaginary permittivity, $\varepsilon_2(E)$ (solid red line), split into its individual components: a single Drude term (dashed black line), two Gaussian oscillators (dashed orange and green lines) and two Tauc-Lorentz oscillators (dashed blue and purple lines). For comparison, the dotted brown and dark blue lines present the B-Spline fit to the IR and NIR-VIS-UV measurements, respectively. Note the changes of scale in the x-axis of (a), (b) and (c) at 0.8 eV, where the vertical dashed black line indicates the boundary between the IR and NIR-VIS-UV ranges covered by the two ellipsometers.

AZO

The fitting process outlined above was also performed in order to fit the "High-N" and "Low-N" AZO thin films (see Table 4-1). Fig. 4-11a and Fig. 4-12a present the fitting reports for the "High-N" and "Low-N" AZO thin films, respectively.

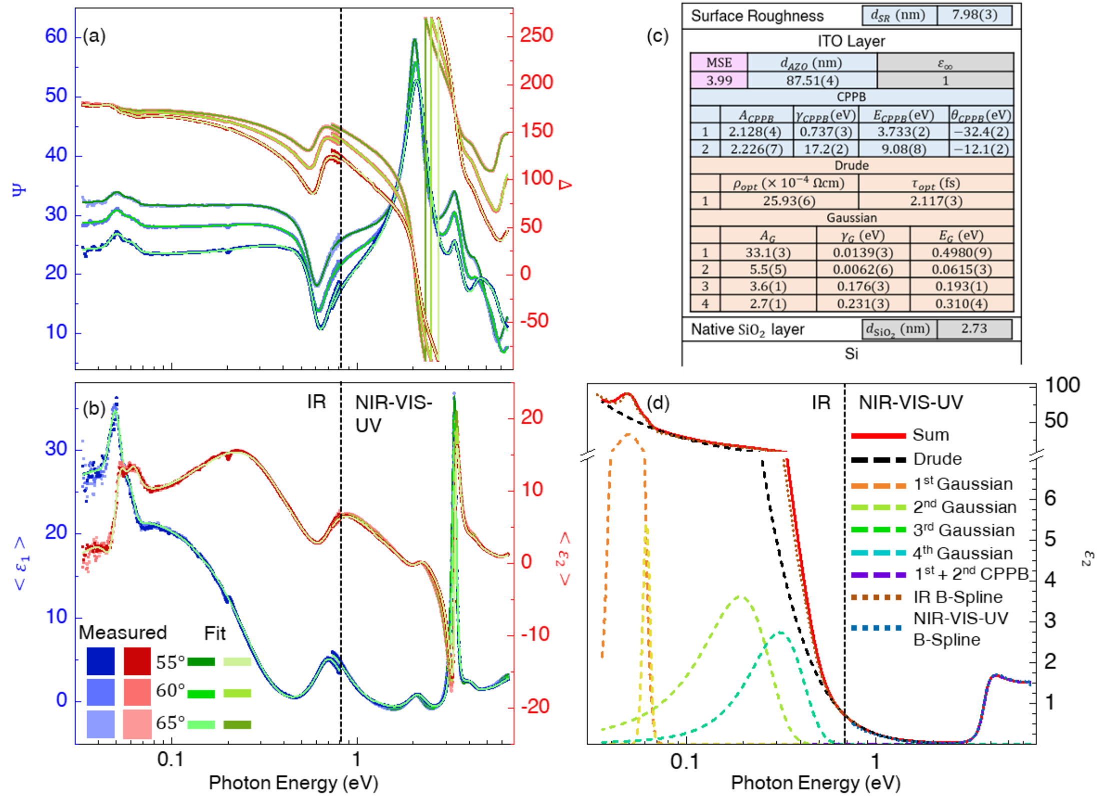

Fig. 4-11. Fitting report for the seed "High-N" AZO thin. (a) $\Psi(\mathrm{E})$ (blue squares) and $\Delta(\mathrm{E})$ (red squares) and (b) the real ($< \varepsilon_1(E) >$; blue squares) and imaginary ($< \varepsilon_2(E) >$; red squares) *pseudo*-permittivity at incident angles of $55°$ (darker shade), $60°$ (normal shade) and $65°$ (lighter shade). The solid green lines indicate the fit to each collected data set. (c) The parameterised oscillator model utilised to fit the data, where the blue and orange shaded areas indicate that the parameters were fit to the NIR-VIS-UV or IR part of the spectra, respectively, and the grey areas indicate the parameter was fixed during the fit. (d) The as-fit imaginary permittivity, $\varepsilon_2(E)$ (solid red line), of the High-N AZO thin film split into its individual components: a single Drude term (dashed black line), four Gaussian oscillators (dashed orange, light green, green and cyan lines) and two CPPB oscillators (dashed purple line). For comparison, the dotted brown and dark blue lines present the B-Spline fit to the IR and NIR-VIS-UV measurements, respectively. Note the changes of scale in the x-axis of (a), (b) and (c) at 0.8 eV, where the vertical dashed black line indicates the boundary between the IR and NIR-VIS-UV ranges covered by the two ellipsometers.

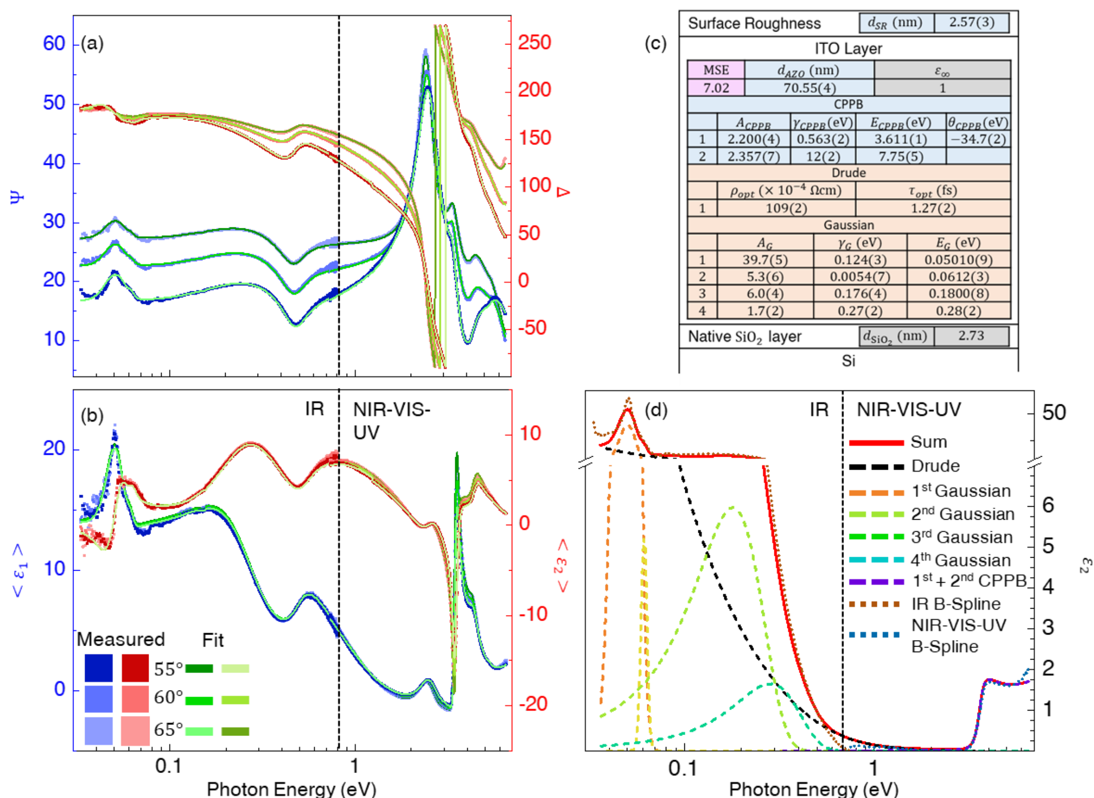

Fig. 4-12. Fitting report for the seed "Low-N" AZO thin. (a) $\Psi(\mathrm{E})$ (blue squares) and $\Delta(\mathrm{E})$ (red squares) and (b) the real ($<\varepsilon_1(E)>$; blue squares) and imaginary ($<\varepsilon_2(E)>$; red squares) *pseudo*-permittivity at incident angles of $55°$ (darker shade), $60°$ (normal shade) and $65°$ (lighter shade). The solid green lines indicate the fit to each collected data set. (c) The parameterised oscillator model utilised to fit the data, where the blue and orange shaded areas indicate that the parameters were fit to the NIR-VIS-UV or IR part of the spectra, respectively, and the grey areas indicate the parameter was fixed during the fit. (d) The as-fit imaginary permittivity, $\varepsilon_2(E)$ (solid red line), of the Low-N AZO thin film split into its individual components: a single Drude term (dashed black line), four Gaussian oscillators (dashed orange, light green, green and cyan lines) and two CPPB oscillators (dashed purple line). For comparison, the dotted brown and dark blue lines present the B-Spline fit to the IR and NIR-VIS-UV measurements, respectively. Note the changes of scale in the x-axis of (a), (b) and (c) at 0.8 eV, where the vertical dashed black line indicates the boundary between the IR and NIR-VIS-UV ranges covered by the two ellipsometers.

For the AZO thin films, two additional Gaussian oscillators were required to fit the more complex IR absorption. The peak at $\sim 0.05\ \mathrm{eV}$ is ascribed to a strong optical phonon absorption of ZnO [356,357]. However, there exists a large broad peak at $\sim 0.2\ \mathrm{eV}$ that is not present to the undoped ZnO [358]. Uprety *et al.* [306] required two additional peaks at $0.11\ \mathrm{eV}$ and $0.16\ \mathrm{eV}$ to fit IRSE measurements of AZO, which they attributed to phonon modes. However, correlation of these peaks to Raman spectra is not possible due to the limited spectral range of current Raman analysis of undoped- and/or doped-ZnO [356–359]. The two broader peaks are shifted to higher energy than noted by Uprety *et al.*, to $0.180 \pm 0.0008\ \mathrm{eV}$ and $0.28 \pm 0.02\ \mathrm{eV}$, respectively, for the Low-N AZO film and to $0.193 \pm 0.001\ \mathrm{eV}$ and $0.310 \pm 0.004\ \mathrm{eV}$, respectively, for the High-N AZO film. As for the case of ITO, the dependence of these peaks on N indicates that the peaks may instead be related to the presence of defect states arising from intentional or unintentional dopants, phonon-plasmon coupling [103,105], multiple carrier species [105] or if they are an artefact arising from a non-uniform structure [173], or anisotropy [163,358]. It should also be noted that a better fit for the UV absorption is achieved for AZO using $1\mathrm{D}$ critical point parabolic band (CPPB) oscillators (Eq. (3-65)) in place of Tauc-Lorentz oscillators, as has been previously reported [306]. The phase parameter of the CPPB function allows for ε_2 to become negative, which is unphysical. This is offset by the 2^{nd} CPPB function and so the summation of the two CPPB oscillators is presented in Fig. 4-11d.

The model used to fit the seed GZO films is almost identical to that used for AZO. Two CPPB oscillators are used to fit the UV absorption (purple dashed lines in Fig. 4-13d and Fig. 4-14d). For the High-N GZO film (Fig. 4-13), an additional Gaussian oscillator is required to fit the sharp phonon absorption at $\sim 0.05\ \mathrm{eV}$. This is likely due to the larger $(\times 2)$ film thickness increasing the sensitivity of SE to the phonon absorption (Table 4-1). The MSE of the fit to the High-N GZO film is 11.7, noticeably higher than for all other films explored so far. This appears to arise from the mismatch of the model and data at very low energy ($0.03 - 0.05\ \mathrm{eV}$ in Fig. 4-13d) and indicates that the assumption of an "ideal" (*i.e.* single carrier species, uniform, isotropic etc.) film may be wrong for this film. For the Low-N GZO film, a much better fit to the data across the entire spectral range is observed (MSE of 3.90). However, from Fig. 4-14d it is noted that there is a discrepancy between the generalised oscillator model and B-Spline generated values for ε_2, especially at $\sim 0.08\ \mathrm{eV}$, where the B-Spline predicts a sharper "trench" between the sharp phonon absorption and the broad absorption peaks at $\sim 0.2\ \mathrm{eV}$. This trench could only be fit within an idealised model using a Gaussian peak with a negative amplitude. While this produces a better fit to the data it is, however, not a reasonable or physical way to describe the film properties and is likely, again, an artefact resulting from non-idealities within the film not accounted for in the model.

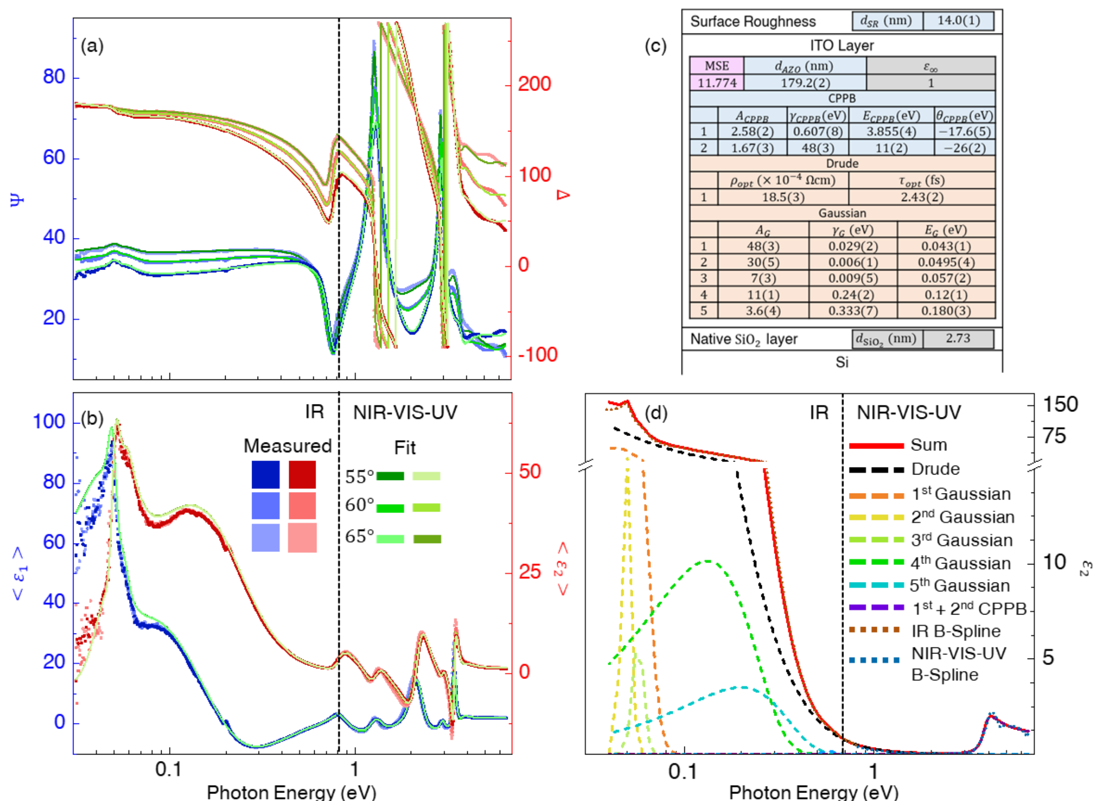

Fig. 4-13. Fitting report for the seed "High-N" GZO thin. (a) $\Psi(\mathrm{E})$ (blue squares) and $\Delta(\mathrm{E})$ (red squares) and (b) the real, $<\varepsilon_1(E)>$, (blue squares) and imaginary, $<\varepsilon_2(E)>$, (red squares) *pseudo*-permittivity at incident angles of 55° (darker shade), 60° (normal shade) and 65° (lighter shade). The solid green lines indicate the fit to each collected data set. (c) The parameterised oscillator model utilised to fit the data, where the blue and orange shaded areas indicate the parameters were fit to the NIR-VIS-UV or IR part of the spectra, respectively, and the grey areas indicate the parameter was fixed during the fit. (d) The as-fit imaginary permittivity, $\varepsilon_2(E)$ (solid red line), of the High-N GZO thin film split into its individual components: a single Drude term (dashed black line), four Gaussian oscillators (dashed orange, light green, green and cyan lines) and two CPPB oscillators (dashed purple line). For comparison, the dotted brown and dark blue lines present the B-Spline fit to the IR and NIR-VIS-UV measurements, respectively. Note the changes of scale in the x-axis of (a), (b) and (c) at $0.8\,\mathrm{eV}$, where the vertical dashed black line indicates the boundary between the IR and NIR-VIS-UV ranges covered by the two ellipsometers.

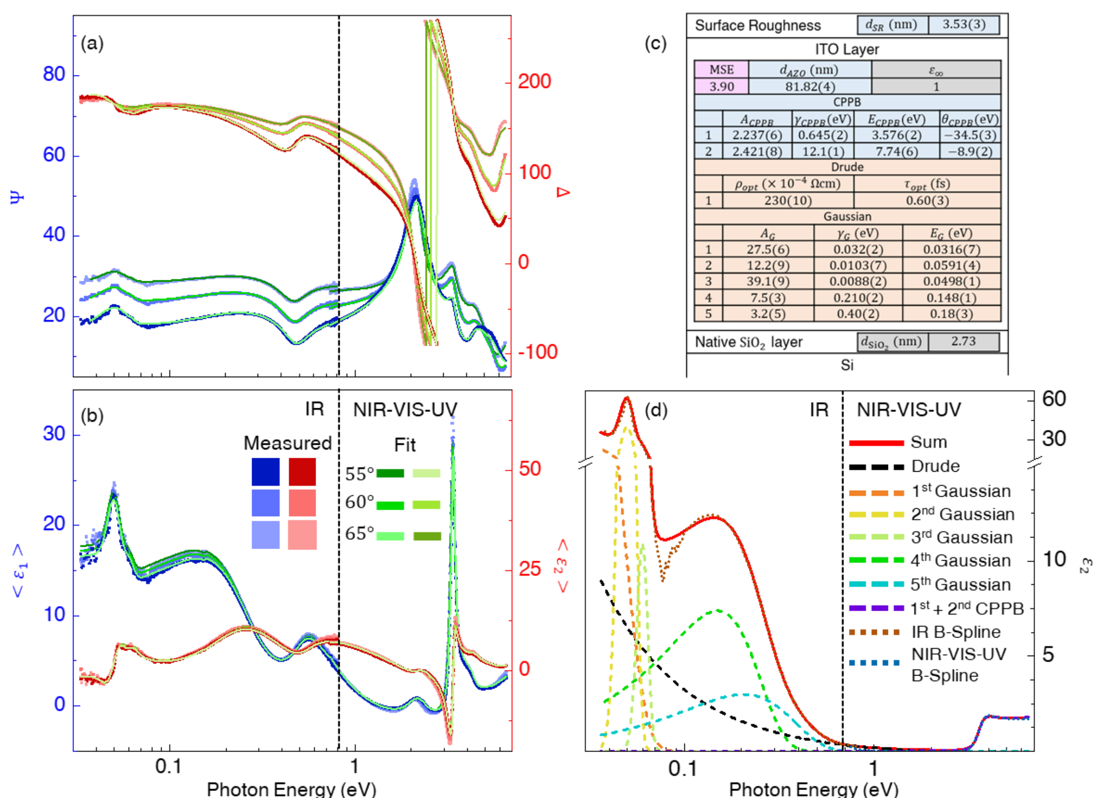

	A_{CPPB}	γ_{CPPB}(eV)	E_{CPPB}(eV)	θ_{CPPB}(eV)
1	2.237(6)	0.645(2)	3.576(2)	−34.5(3)
2	2.421(8)	12.1(1)	7.74(6)	−8.9(2)

	ρ_{opt} ($\times 10^{-4}$ Ωcm)	τ_{opt} (fs)
1	230(10)	0.60(3)

	A_G	γ_G (eV)	E_G (eV)
1	27.5(6)	0.032(2)	0.0316(7)
2	12.2(9)	0.0103(7)	0.0591(4)
3	39.1(9)	0.0088(2)	0.0498(1)
4	7.5(3)	0.210(2)	0.148(1)
5	3.2(5)	0.40(2)	0.18(3)

Fig. 4-14. Fitting report for the seed "Low-N" GZO thin. (a) $\Psi(\mathrm{E})$ (blue squares) and $\Delta(\mathrm{E})$ (red squares) and (b) the real ($<\varepsilon_1(E)>$; blue squares) and imaginary ($<\varepsilon_2(E)>$; red squares) *pseudo*-permittivity at incident angles of $55°$ (darker shade), $60°$ (normal shade) and $65°$ (lighter shade). The solid green lines indicate the fit to each collected data set. (c) The parameterised oscillator model utilised to fit the data, where the blue and orange shaded areas indicate that the parameters were fit to the NIR-VIS-UV or IR part of the spectra, respectively, and the grey areas indicate the parameter was fixed during the fit. (d) The as-fit imaginary permittivity, $\varepsilon_2(E)$ (solid red line), of the Low-N GZO thin film split into its individual components: a single Drude term (dashed black line), four Gaussian oscillators (dashed orange, light green, green and cyan lines) and two CPPB oscillators (dashed purple line). For comparison, the dotted brown and dark blue lines present the B-Spline fit to the IR and NIR-VIS-UV measurements, respectively. Note the changes of scale in the x-axis of (a), (b) and (c) at 0.8 eV, where the vertical dashed black line indicates the boundary between the IR and NIR-VIS-UV ranges covered by the two ellipsometers.

In summary, this section detailed the process used to fit the "IR + NIR-VIS-UV SE" set of seed TCO thin films where $\Psi(E)$ and $\Delta(E)$ were measured in the IR and NIR-VIS-UV spectral ranges. If the films represented an ideal case for a homogeneous and isotropic film with a single charge carrier species, a good fit across the entire spectral range was produced for all films and the resulting values of $\varepsilon_2(E)$ agreed with the values extracted from directly fitting the permittivity to the data. If the only requirement of the fitting of ellipsometric data was to extract the permittivity, as is required to calculate indicative plasmonic figures of merit and/or test the limitations of SE (Chapter 7), then the values extracted from assuming an ideal film suffice for further analysis. However, to gain insights into the physical mechanisms that dictate the optoelectronic properties of TCOs and how ReLA can probe these mechanisms, a more in-depth analysis of the SE data, considering various non-idealities, is required.

The remainder of this chapter investigates the ways that the film can deviate from the "ideal" (*i.e.,* uniform, isotropic, smooth) case investigated above. Each non-ideality is introduced on a case-by-case basis by investigating a particular sample that possesses such qualities and the process of including treatments of the non-ideality within the model are detailed. The investigated non-idealities are: the presence of multiple free carrier species (required for the optimised an un-optimised ITO films; Section 4.2.2), an inhomogeneity in the form of a gradient of optical constants in the film growth direction (required for the un-optimised ITO films; Section 4.2.3) and an N-dependent effective carrier mass (Section 4.2.4).

4.2.2. Accounting for multiple carrier species in the optical model

The first non-ideality was encountered while fitting the seed optimised and un-optimised ITO thin films. The seed optimised ITO thin film (Table 4-1) used for investigations into the effect of ReLA (Chapter 5) is presented here as an exemplar case. The optimised ITO film was optically characterised *via* IRSE $(0.034 - 0.8\text{ eV})$, NIR-VIS SE $(0.775 - 3.4\text{ eV})$, ORS $(0.775 - 3.4\text{ eV})$ and $(0.034 - 0.8\text{ eV})$. The ORS and IRT measurements were appended to the SE data during fitting with a fit weighting of 30%. This helps reduce the chance for over-fitting of the data and is key to identifying particular non-idealities [82].

Fig. 4-15 presents the fitting report for the seed optimised ITO thin film using an "ideal" model with a single Drude term, two Gaussian oscillators and a single Lorentz oscillator. For this and all following fitting reports in this section, the *pseudo*-permittivity, $< \tilde{\varepsilon} >=< \varepsilon_1 > +i < \varepsilon_2 >$, is alone is presented for the SE data in Fig. 4-15a. The corresponding IR transmittance, T_{IR}, (blue squares) and visible reflectance, R_{VIS}, (red squares) spectra are presented in Fig. 4-15c. The fit to T_{IR} and R_{VIS} alongside the calculation of the absorbance, $A = 1 - (T + R)$, are shown as the solid dark green, light green and grey lines, respectively. The dotted lines indicate that

the values have been calculated outside the spectral range from $\tilde{\varepsilon}(E)$. The sharp drop in T_{IR} at ~ 1 eV is due to the absorption of the 0.5 mm Si wafer. The schematic of the geometric model with the general oscillator layers' parameters shown is presented in Fig. 4-15b, where the error of the last digit is shown in the parentheses. The pink colour indicates that the fit was performed with the IR transmission and visible reflectance appended to the IRSE measurement. The grey colour indicates the value was fixed during the fit. Fig. 4-15d presents ε_2 (solid red line) of the optimised seed ITO film broken down into its individual oscillators (dashed lines).

A relatively good fit (MSE of 7.29) is observed across most of the measured spectral range. However, there is a deviation between the measured and modelled values of at low energy (particularly an over-estimation of $< \varepsilon_1 >$). Due to the limited spectral range of the NIR-VIS SE, only the tail of UV absorption is observed. This is not quite enough to reliably measure E_G, but the slope at $3.55 - 3.66$ eV in $(\alpha E)^2$ vs E can be used to compare the shift in E_G between films. As for the High-N ITO film, the Gaussian peaks representing IR phonons were fixed to the peak positions reported by Uprety *et al.* [354]. It was noted previously that peak positions can shift with N (Section 4.2.1) and so it is desirable for the peak positions to be free parameters during the fit. Leaving the Gaussian oscillators free, however, results in an erroneous fit where the error of the peak position, amplitude and broadening become much greater than the fit values despite a slight ($\sim 10\%$) improvement of the fit so that the modelled ε_1 better matches the measured value. Vitally, for such a fit the 1^{st} phonon peak becomes shifted to ~ 0 eV and the fit is improved further if the Gaussian oscillator is replaced with a Lorentzian. A Lorentzian peak centred at 0 eV is a Drude oscillator (Section 2.1.4), which may indicate that a 2^{nd} Drude term is present in the film and is being mistaken for a phonon absorption centred at ~ 0 eV. To account for this possibility, a new fit is performed using an additional Drude term alongside the 1^{st} Drude term and the two Gaussian oscillators. **Error! Reference source not found.** presents the fitting report for the optimised ITO film (as for Fig. 4-15) using this modified model.

An improvement to the fit is noted ($\mathrm{MSE} = 7.01$), and visual inspection of the fit highlights that $< \varepsilon_1 >$ is no longer over-estimated at low E. Furthermore, the inclusion of the additional Drude term (an additional oscillator) reduces the parameter correlation and prevents the IR oscillators from being unresolved. The 1^{st} phonon peak fits to 0.049 ± 0.001 eV, very close to its expected value of 0.045 eV [168,342,355].

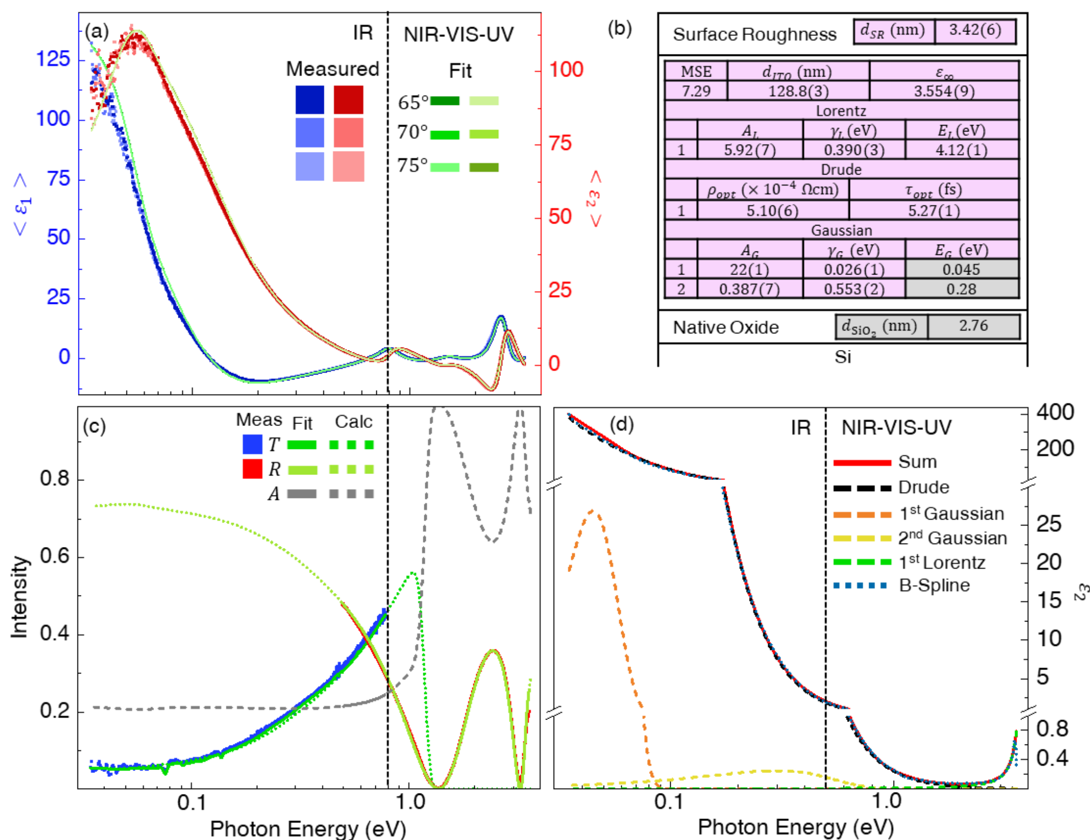

Fig. 4-15. Fitting report for the seed "optimised" ITO film fit using a generalised oscillator model with a single Drude term and fixed-position IR oscillators: (a) real (blue squares) and imaginary (red squares) parts of the *pseudo*-permittivity $< \tilde{\varepsilon} >$, with incident angles of 65° (darker shade), 70° (normal shade) and 75° (lighter shade). (b) The parameterised oscillator model utilised to fit the data, where the pink and grey areas indicate of the free and fixed parameters, respectively. (c) The corresponding measured IR transmission, $T_{IR}(E)$, (blue squares) and visible reflection, $R_{VIS}(E)$, (red squares). For reference, the calculated absorption, $A = 1 - (T_{IR} + R_{VIS})$, is shown with the solid grey line. In (a) and (c), the solid green lines indicate the fit to each collected data set. In (b), the dotted lines indicate that the values have been back-calculated outside of the measured spectral range. (d) The as-fit imaginary permittivity, $\varepsilon_2(E)$ (solid red line), of the optimised ITO film split into its individual components: a single Drude term (dashed black line), two Gaussian oscillators (dashed orange and yellow lines) and a single Lorentz oscillator (dashed green line). For comparison, dotted blue line presents the B-Spline fit. Note the changes of scale in the x-axis of (a), (c) and (d) at 0.8 eV, where the vertical dashed black line indicates the boundary between the IR and NIR-VIS spectral ranges, and in the y-axis at 1.0 and 30, used to show the maxima of each peak more clearly.

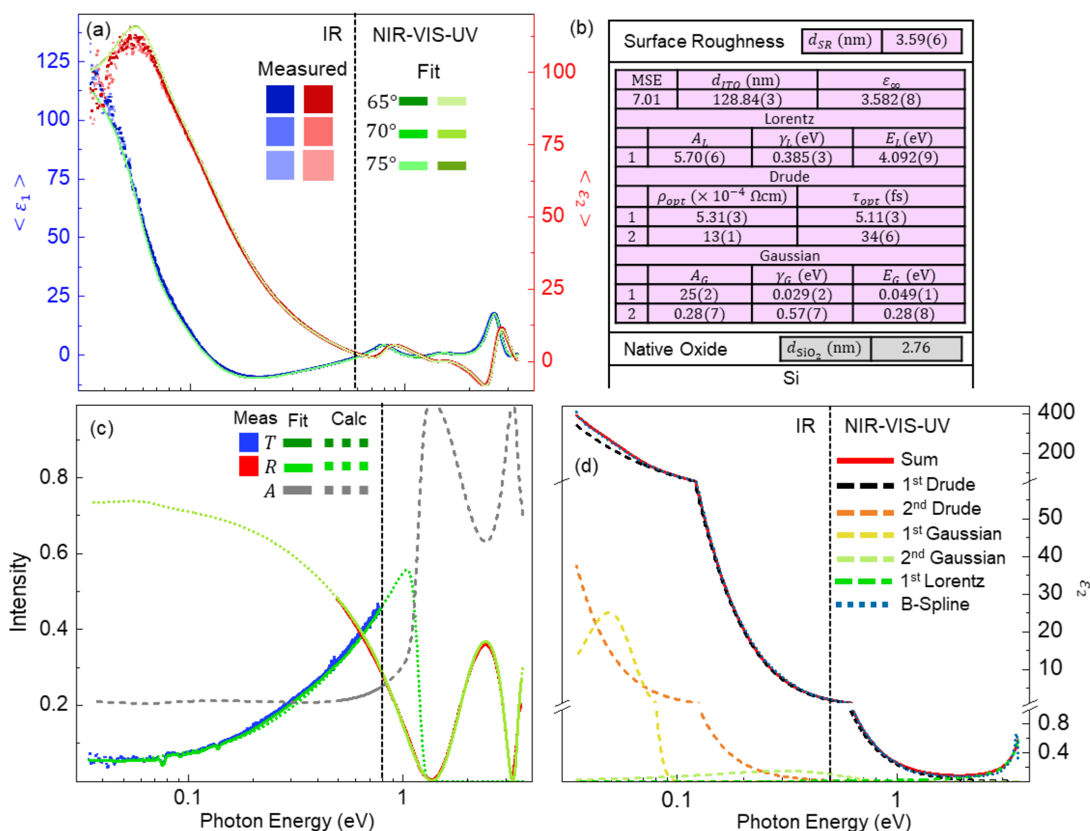

Fig. 4-16. Fitting report for the seed "optimised" ITO film fit using a generalised oscillator model with two Drude terms and free-position IR oscillators. (a) Real (blue squares) and imaginary (red squares) parts of the *pseudo*-permittivity $<\tilde{\varepsilon}>$, with incident angles of 65° (darker shade), 70° (normal shade) and 75° (lighter shade). (b) The parameterised oscillator model utilised to fit the data, where the pink and grey areas indicate of the free and fixed parameters, respectively. (c) The corresponding measured IR transmission, $T_{IR}(E)$, (blue squares) and visible reflection, $R_{VIS}(E)$, (red squares). For reference, the calculated absorption, $A = 1 - (T_{IR} + R_{VIS})$, is shown with the solid grey line. In (a) and (c), the solid green lines indicate the fit to each collected data set. In (b), the dotted lines indicate that the values have been back-calculated outside of the measured spectral range. (d) The as-fit imaginary permittivity, $\varepsilon_2(E)$ (solid red line), of the optimised ITO film split into its individual components: two Drude terms (dashed black and orange lines), two Gaussian oscillators (dashed yellow and light green lines) and a single Lorentz oscillator (dashed green line). For comparison, dotted blue line presents the B-Spline fit. Note the changes of scale in the x-axis of (a), (c) and (d) at 0.8 eV, where the vertical dashed black line indicates the boundary between the IR and NIR-VIS spectral ranges, and in the y-axis at 1.0 and 60, used to show the maxima of each peak more clearly.

The improvement of the fit and the reduction in the parameter correlation can be seen as evidence that the inclusion of a 2^{nd} Drude term is experimentally valid. However, it is important to consider whether this is also realistic. A summation of multiple Drude terms is warranted when there are multiple "carrier species" [105]. Usually, this represents distinct carrier species that account for electrons and holes, light and heavy holes, electrons in different conduction band valleys, s- and d- electrons, or bulk and surface electrons. A single Drude term is usually sufficient for n-type semiconductors with a single occupied conduction band valley, or for metals with a simple spherical Fermi surface (such as ITO) [105]. For now, the use of a 2^{nd} Drude term is justified by its ability to improve the fit and reduce parameter correlation. However, the nature of the distinct carrier species will be revealed later when a larger set of seed and laser processed films are considered (Chapter 5).

A final improvement can be made by expanding upon the default modelling of the surface roughness layer, using a distinct "surface layer" that comprises a linearly graded effective medium approximation (EMA) of the layer below and air with a single characteristic "surface" carrier species. The gradient exists in the % of each material of the EMA and is fixed from 0% of air at the bottom and 100% of air at the top of the layer so that the surface roughness is expressed as a series of repeating triangles of ITO on the surface. This is presented schematically in Fig. 4-17, for (a) a homogeneous EMA of 50% ITO and 50% air and (b) a graded EMA as used for the surface layer. The modelling of the roughness could be improved by using a non-linear gradient or by allowing the top % of air to be free parameters to change the shape of the surface roughness elements. However, this did not markedly improve the fit to justify inclusion for the samples investigated.

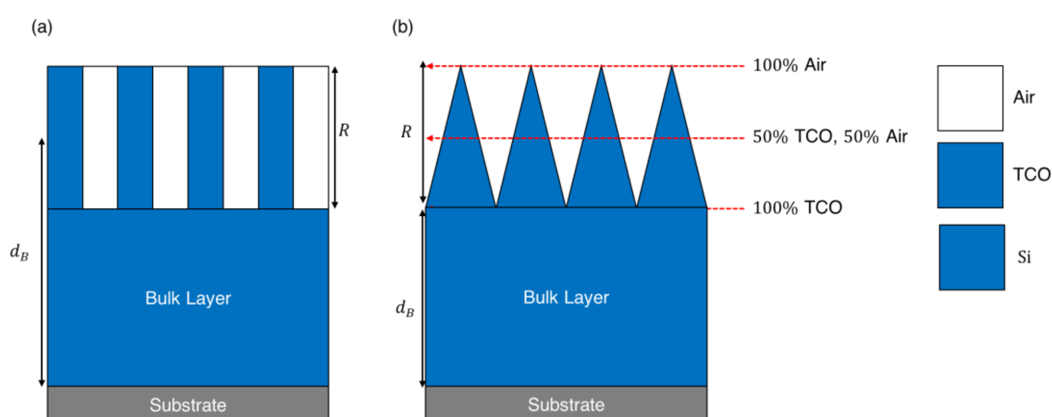

Fig. 4-17. Schematic of the (a) default surface roughness of CompleteEase™ comprising a uniform 50% material - 50% air EMA of and (b) the expanded surface roughness layer utilised in the remainder of this work, comprising a graded EMA layer where the air % variers from $0-100\%$ of the layer. Note how the precise definition of d_B changes between (a) and (b).

4.2.3. Accounting for depth Inhomogeneity of the carrier transport properties

Another potential non-ideality of the optical properties of TCOs and other materials that limits the ability to fit ellipsometric data using a simple, idealised model is the presence of non-uniformity or inhomogeneity in the film [91,92,102,299,360]. The non-uniformity may occur across the lateral dimensions of the sample, which gives rise to de-coherent reflections and depolarisation and makes ellipsometric modelling difficult [82], or across the depth of the film [102]. As the sputtered films used in this work were very uniform across the dimensions of the IRSE beam ($\sim 5 \times 5\ \mathrm{mm}^2$), only the depth-inhomogeneity is considered here.

The requirement to consider depth-inhomogeneity was encountered while fitting the seed un-optimised ITO thin films (Table 4-1), which is presented here as an exemplar case. The un-optimised ITO film was optically characterised *via* IRSE, NIR-VIS SE, ORS and IRT. The ORS and IRT measurements of R_{VIS} and T_{IR}, respectively, were appended to the SE data during fitting with a fit weighting of 30%. As outlined in Section 4.2.1, the first step in the fitting procedure for films with "unknown" optical constants is to perform a "B-Spline" fit to the data [84], where $\varepsilon_2(E)$ of the unknown layer is fit to the data using a series equally spaced of nodes. $\varepsilon_1(E)$ is calculated from $\varepsilon_2(E)$ using the Kramers-Kronig (KK) transformation [345,346] to ensure that $\tilde{\varepsilon}(E)$ is realistic. However, it was not possible to fit a KK-consistent B-Spline to the data. This is demonstrated in Fig. 4-18, which presents $< \varepsilon_2 >$ as measured for the un-optimised ITO film (red dots) and as fit with 3 different B-Spline configurations (dashed lines). The first attempt, presented as the dashed green line in Fig. 4-18, was to use a KK-consistent B-Spline to fit the data. It is observed that this results in an overestimation of $< \varepsilon_2 >$ at lower wavelengths, while $< \varepsilon_1 >$ (not shown for clarity) is adequately fit. One way to achieve a better fit is to not force KK-consistency (blue dashed line in Fig. 4-18), but this is a very strong indication that the assumption of an ideal film is wrong, and the optical constants extracted for the film are unphysical. However, a KK-consistent B-Spline fit can be achieved by introducing an angle offset, $\Delta\theta$, of $1°$ into the model. The angle offset is added to the angle of incidence, θ_0, in the optical model calculation is usually used to correct for machine or sample misalignment but can serve an indicator that the utilised model is not acceptable for a particular dataset [82,353].

The fit is improved further by allowing each angle to have a different offset in both the IR and NIR-VIS (Table 4-5). However, the sharp change in $\Delta\theta$ at the boundary of the spectral range breaks the continuity of the fit. This is accounted for by allowing $\Delta\theta$ to vary with E, *via*:

$$\Delta\theta(E) = mE + \Delta\theta_{0,j} \tag{4-2}$$

where m and $\Delta\theta_{0,j}$ are free parameters describing a linear gradient of $\Delta\theta(E)$.

Table 4-5. Angle offset at each angle and spectral range for the seed un-optimised ITO film.

Spectral Range	Angle Offset, $\Delta\theta$ (°)		
	$65°$	$70°$	$75°$
IR	1.54 ± 0.02	1.31 ± 0.02	1.02 ± 0.02
NIR-VIS	0.79 ± 0.04	0.69 ± 0.04	0.55 ± 0.03

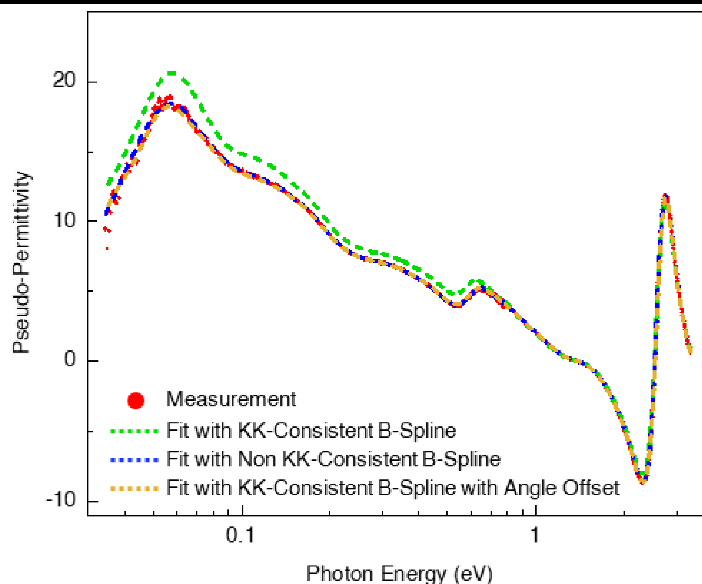

Fig. 4-18. Measured (red dot) and modelled (dashed lines) imaginary *pseudo*-permittivity, $< \varepsilon_2 >$. Three B-Spline configurations are presented: A Kramers-Kronig (KK) consistent B-Spline (green dashed line), a non-KK-consistent B-Spline (blue dashed line) and a KK-consistent B-Spline with an angle offset, $\Delta\theta$, included in the model (yellow dashed line).

Fig. 4-19 presents a schematic of the light reflecting from the sample in order to demonstrate why the requirement for an angle offset in the fit is in fact an indication that there potentially exist multiple distinct layers within the film. The schematic assumes that the film is split into two distinct layers. The first is a "bulk" layer which can be described by a single, uniform ideal B-Spline model described by a complex refractive index, $\tilde{n}_2(E)$, and the second layer is a "surface layer" that is described by a refractive index, $n_1(E)$. For simplicity, in this schematic n_1 is assumed to be purely real (*i.e.,* the surface layers are entirely transparent). The incoming light with an angle of incidence, θ_0, is refracted by the surface layer so that the "effective "angle of incidence at the surface of the bulk layer, θ_1, (the one being fit by the B-Spline) is less (if $n_0 < n_1$) or more (if $n_0 > n_1$), as according to Snell's Law [110]:

$$\frac{\sin(\theta_1)}{\sin(\theta_0)} = \frac{n_0}{n_1(E)} \tag{4-3}$$

Therefore, the angle offset, $\Delta\theta = \theta_1 - \theta_0$, will not be constant (as would be the case for sample or machine misalignment) but depend on θ_0. Furthermore, an energy dependence of the angle offset arises from how $n_1(E)$ is also dependent on the energy. In reality, n_1 would also be complex. This would affect the actual offset but is unimportant for this discussion. Provided

the bulk film is semi-transparent, a similar effect would also result if the layer existed below the "bulk" film of interest. The key takeaway is that if an angle dependence is required to achieve a good fit, and the machine alignment is verified to be correct, then it is likely that multiple layers and or some z-axis inhomogeneity is present in the sample.

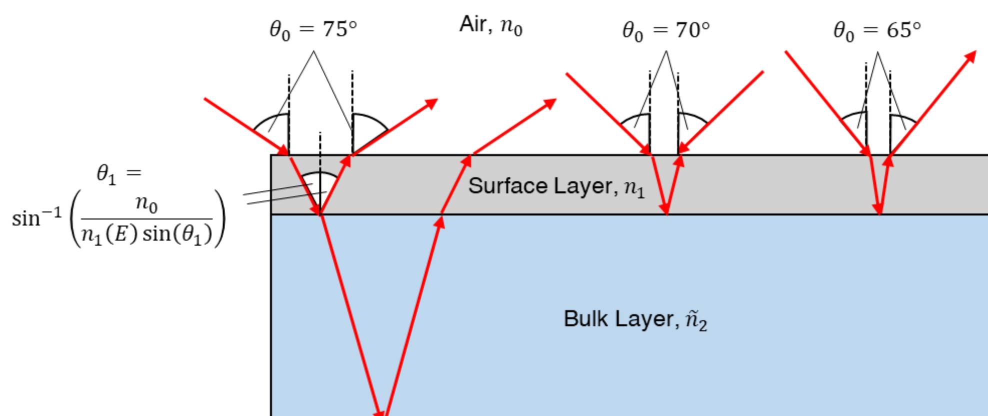

Fig. 4-19. Schematic for why a z-axis inhomogeneity can manifest as an angle offset, $\Delta\theta$. The incident light (with angle θ_1; red arrows) is refracted by the surface layer (with refractive index n_1; grey rectangle) so that the angle of incidence at the surface of the bulk layer, θ_1, (the layer being fit in an idealised model) is offset as according to Snell's law.

In order to better elucidate the optoelectronic properties of the un-optimised ITO film, the data was fit using a parameterised general oscillator layer. To achieve a good fit, the change in $\Delta\theta$ with θ_0 and E (Eq. (4-2)) was included into the model. As seen in the previous section, the addition of an extra Drude term improved the fit, reduced the parameter correlation, and stopped the phonon peak shifting to below the measurement range, and so two carrier species were included into the fit for the un-optimised ITO film. An additional, 3^{rd}, Gaussian oscillator at ~ 0.4 eV was also required to fit the data. Fig. 4-20 presents the fitting report for the seed un-optimised ITO thin film, using a model with 2 Drude oscillators, 3 Gaussian oscillators, a single Lorentz oscillator and an energy-dependent $\Delta\theta$.

A good fit to $< \tilde{\varepsilon} >$ is observed for the entire spectral range ($\mathrm{MSE} = 9.21$), with good overlap between the IR and NIR-VIS spectral regions as well as an agreement between ε_2 as fit by the generalised oscillator and B-Spline models. Despite the good fit to the SE data, the large, broad absorption at 0.5 eV predicted by fitting the SE data is not present in $T_{IR}(E)$. As seen above (Fig. 4-19), the requirement for an angle offset is a strong indication that there are multiple layers within the film. Therefore, the additional Gaussian at 0.335 ± 0.002 eV is likely not a real source of absorption but is being used to describe a feature of the *pseudo*-permittivity which arises from interference between the two layers. Another possibility is that there is very strong absorption peak within the surface layer. As SE relies on reflection from the surface, it

may be highly sensitive to such a peak. Conversely, $T_{IR}(E)$ is the sum of the total absorption across the entire depth of the film and so is mostly sensitive to the bulk of the film so that the absorption is not registered *via* IRT. However, including a very strong absorption peak at ~ 0.4 eV in the surface layer of the model did not improve the fit and there is no clear explanation for the physical origin of such a high intensity peak. Therefore, the 3$^{\mathrm{rd}}$ Gaussian oscillator used to fit the data is considered to be an "over-fit" feature that is actually due to z-axis inhomogeneity. The fit for the un-optimised ITO film can only be improved by removing the 3$^{\mathrm{rd}}$ Gaussian oscillator from the fit and setting up the model to include a z-axis inhomogeneity in place of the angle offset. This is done by splitting the ITO layer into two discrete layers: a "top" and "bottom" layer. The layers share the Gaussian and Lorentz terms describing the phonon and inter-band absorption, in order to reduce parameter coupling. For the sake of further reduction of the fitting parameters, the 2$^{\mathrm{nd}}$ Drude term is also coupled between the two layers (*i.e.,* the free carrier absorption of the 2$^{\mathrm{nd}}$ carrier species is assumed to be the same in both layers).

Fig. 4-21 presents the fitting report for the seed un-optimised ITO film, using a two-layer model with one independent and one shared Drude oscillator, 2 shared Gaussian oscillators, a single shared Lorentz oscillator. The individual oscillators of ε_2 are shown separately for both the (d) top and (e) bottom layers. The existence of two layers adequately describes the complex line shape around 0.5 eV, without the need for the 3$^{\mathrm{rd}}$ Gaussian oscillator. The IRT data is more accurately fit, confirmating that the data has not been over-fit. To verify this further, a B-spline fit was performed with two distinct layers (each with their own B-Spline; Fig. 4-21d-e). While the parameter correlation for the B-Spline was prohibitively large (usually one would not trust this type of fit), the results of the generalised oscillator model line up quite well with the 2 B-Spline layers. In contrast to Fig. 4-19, the smaller layer, which causes the angle offset, exist at the bottom of the film instead of the top. The bottom layer has a much ($\sim \times 10$) lower resistivity, ρ_{Bot}, and higher mean free time, τ_{Bot}. Using Eqs. (2-40) and (2-41), this translates to a higher "bottom layer" carrier concentration, $N_{Bot} = 2.31 \pm 0.02 \times 10^{20}$, and mobility, $\mu_{Bot} = 25.1 \pm 0.2$, as compared to the top layer $N_{Top} = 0.48 \pm 0.03 \times 10^{20}$, $\mu_{Top} = 10.6 \pm 0.7$. A further improvement ($\mathrm{MSE} = 12.2 \rightarrow 11.6$) of the fit is achieved by including an intermixing layer with thickness, $d_{mix} = 24 \pm 1$, between the bottom and top layers. d_{mix} is found to be almost the entire thickness of the bottom layer. Therefore, the bottom layer can be thought of as an "initial growth layer" that arises from the change in the effective substrate during deposition. Specifically, at the start of deposition, the ITO film is sputtered onto Si/SiO_2 substrate. The lattice mismatch between ITO and Si affects the initial growth. After the films few atomic layers are deposited, the atoms are instead sputtered onto the growing layer of ITO and the growth becomes more uniform.

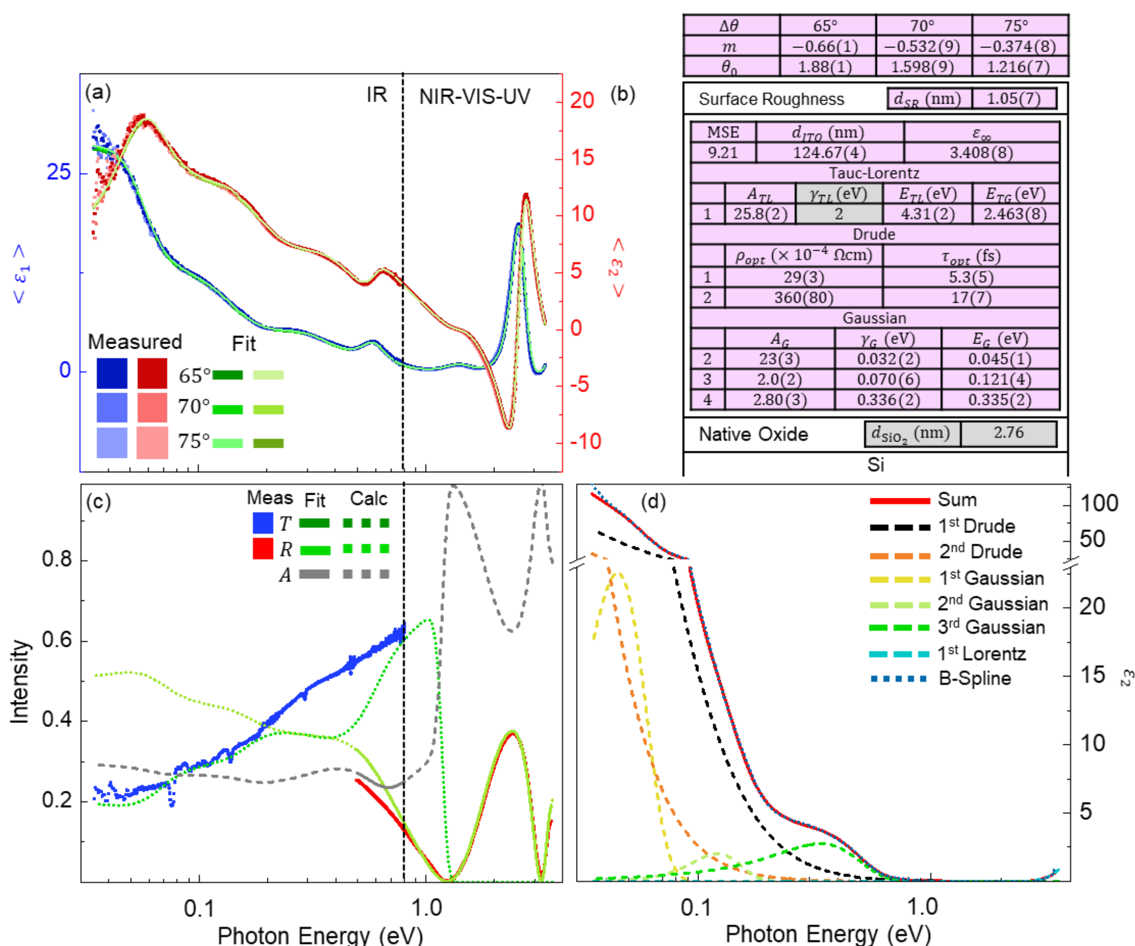

Fig. 4-20. Fitting report for the seed "un-optimised" ITO, fit using a generalised oscillator model with two Drude terms, a default surface roughness and an energy and incident angle dependent angle offset: (a) real (blue squares) and imaginary (red squares) parts of the *pseudo*-permittivity $<\tilde{\varepsilon}>$, at 65° (darker shade), 70° (normal shade) and 75° (lighter shade). (b) The parameterised oscillator model, where the pink and grey areas indicate of the free and fixed parameters, respectively. (c) The corresponding IR transmission, $T_{IR}(E)$, (blue squares) and visible reflection, $R_{VIS}(E)$, (red squares). For reference, the solid grey line shows the calculated absorption, A. In (a) and (c), the solid green lines indicate the fit to each collected data set. In (b), the dotted lines indicate that the values have been back-calculated from the as-fit imaginary permittivity $\varepsilon_2(E)$. (d) $\varepsilon_2(E)$ (solid red line) split into its individual components: 2 Drude terms (dashed black and orange lines), 3 Gaussian oscillators (dashed yellow, light green and green lines) and a single Lorentz oscillator (dashed light blue line). For comparison, the dotted blue line presents the B-Spline fit. Note the logarithmic scale in the x-axis of (a), (c) and (d), where the vertical dashed black lines indicate IR to NIR-VIS boundary, and the change of scale in the y-axis of (d) at 30, used to show the individual peaks more clearly.

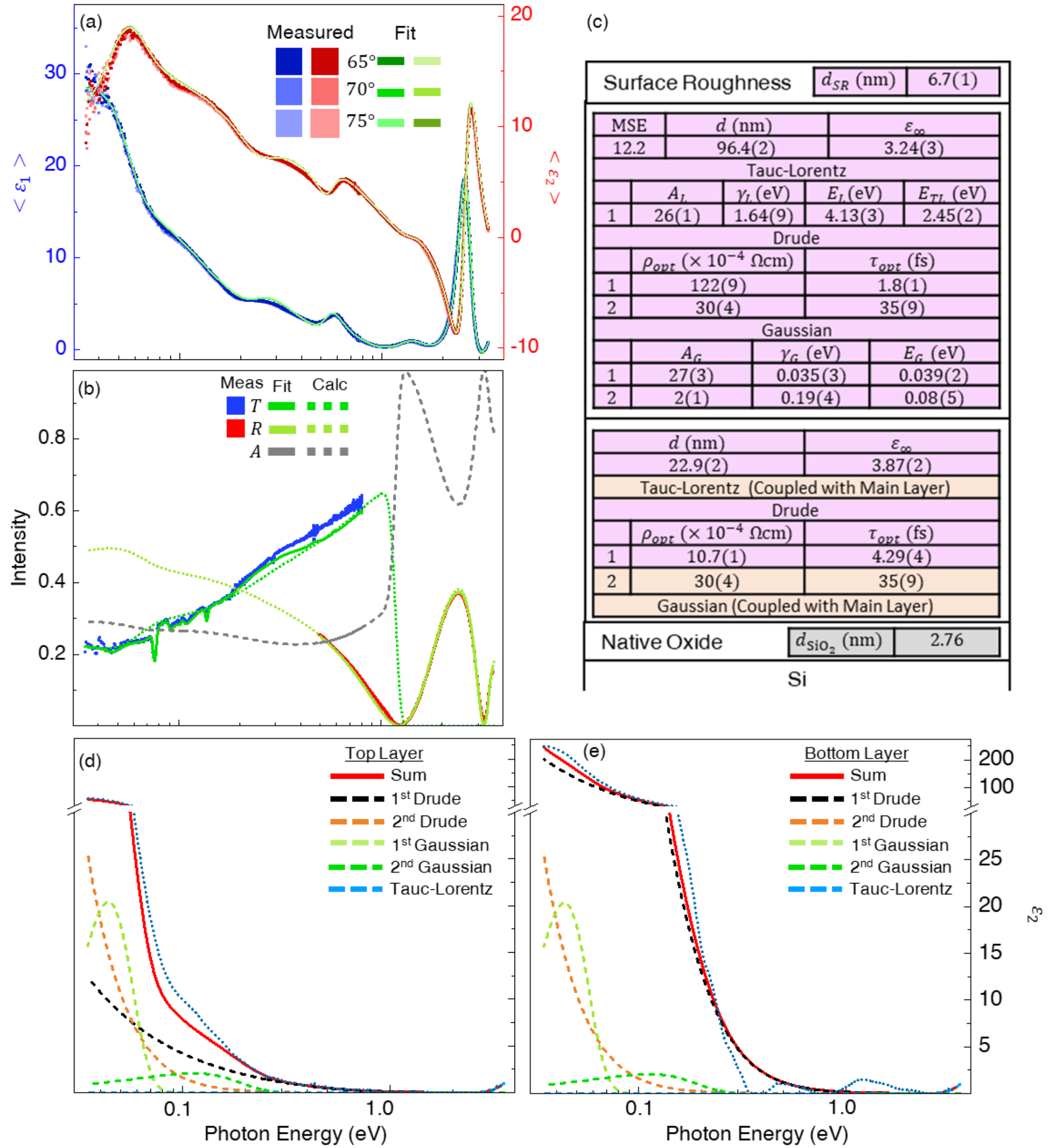

Fig. 4-21. Fitting report for the seed "un-optimised" ITO. (a) *Pseudo*-permittivity, $< \varepsilon_1 >$ (blue squares) and $< \varepsilon_2 >$ (red squares), at $65 - 75°$ (darker-lighter shades). (b) IR transmittance, $T_{IR}(E)$ (blue squares) and visible reflectance, $R_{VIS}(E)$ (red squares). The solid and doted green lines indicate the fit and the extrapolated values. The grey line shows the calculated absorption, A. (c) The parameterised oscillator model, where the pink, orange and grey areas indicate the free, coupled, and fixed parameters, respectively. $\varepsilon_2(E)$ (solid red line) for the (d) top and (e) bottom layers, split into its individual components (coloured dashed lines): 2 Drude terms (black and orange), 2 Gaussian oscillators (green) and a single Lorentz oscillator (blue). For comparison, the dotted line presents the B-Spline fit. Note the logarithmic scale in the x-axis and the change of scale in the y-axis of (d) and (e) at 30.

4.2.4. Accounting for non-parabolicity of the conduction band

As has been raised previously, the "optical" resistivity, ρ_{opt}, and scattering time, τ_{opt}, are extracted by fitting ellipsometric data. Generally, μ and N are calculated from τ and ρ *via* Eqs. (2-40) and (2-41), respectively [107]. To calculate the "optical" carrier concentration, N_{opt}, and mobility, μ_{opt}, one must know the electron effective mass, m_e^*, that has been shown to be directly dependent on N due to non-parabolicity in the conduction band (CB). The non-parabolicity is brought about by free carrier population of the CB and has been observed for ITO [118,361], AZO [362] and GZO [118,363]. The change in m_e^* with N is described by Eq. (4-4).

$$m_e^* = m_0^* \sqrt{1 + 2C\left(\frac{\hbar^2}{m_0^*}\right)(3\pi^2 N)^{\frac{2}{3}}} \tag{4-4}$$

where m_0^* is the parabolic effective electron mass (at low N) and C is a coefficient describing the rate of increase of m_e^* with N, where $C \approx 1/E_G$.

Clearly however, a problem arises as knowledge of N is required in order to determine m_e^*, and thus calculate N. Therefore, an alternate, precise, method for measuring N, such as Hall Effect, is necessary. By measuring ρ_{opt} and τ_{opt} alongside the "Hall" carrier concentration, N_{Hall}, m_e^* can be determined by employing Eqs. (2-40) and (2-41) independently for the SE and Hall Effect measurements. Then, if $N_{opt} = N_{Hall} = N$ an expression for m_e^* is derived:

$$m_e^* = N \cdot \rho_{opt} \cdot e^2 \cdot \tau_{opt} \tag{4-5}$$

where e is the charge of an electron.

For all samples, m_e^* is extracted with Eq. (4-5) and the results for ITO, AZO and GZO are presented as the grey squares in Fig. 4-22a-c, respectively. The resulting set of m_e^* are fitted with Eq. (4-4), using a Levenberg-Marquardt regression algorithm to determine the free parameters m_0^* and C. The fitting results to each material are shown with the dashed red lines in Fig. 4-22. The fitting parameters, m_0^* and C, are recorded in Table 4-6, alongside those that have been reported elsewhere [118,361,362]. It should be noted that for AZO and GZO, the two samples with the lowest N_{Hall} (indicated by red circles in Fig. 4-22) had to be excluded from the fit. The underestimated (for AZO) and overestimated (for GZO) values of m^* are due to the failure of IRSE to accurately determine ρ_{opt} and/or τ_{opt} (thus m_e^*) when μ has been suppressed by grain boundary scattering (GBS) [342] (see Section 7.6). This way, it is apparent how m_e^* changes with N, for each material. This trend is employed for all following analysis of TCOs *via* SE, for the cases where both Hall Effect and SE data are available.

Table 4-6. Fitting parameters, m_0^* and C, from this work and those reported elsewhere.

Parameter	Unit	ITO			AZO		GZO	
		This Work	Liu *et al.* [361]	Fujiwara *et al.* [118]	This Work	Romanyuk *et al.* [362]	This Work	Fujiwara *et al.* [118]
m_0^*/m_e		0.21 ± 0.02	0.263	0.297	0.24 ± 0.03	0.24	0.26 ± 0.02	0.280
C	eV^{-1}	0.4 ± 0.1	0.4191	0.180	0.6 ± 0.2	0.33	0.6 ± 0.1	0.142

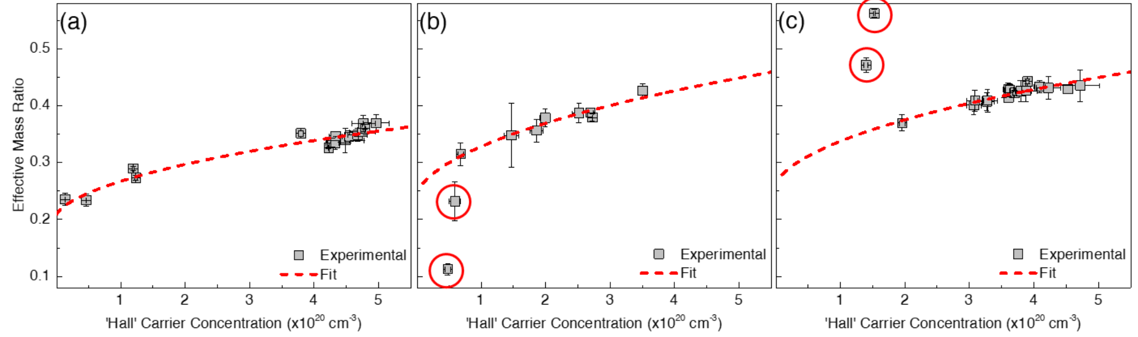

Fig. 4-22. Effective mass ratio, $m^* = m_e^*/m_e$, against the Hall carrier concentration, N_{Hall}, for the experimental set of (a) ITO, (b) AZO and (c) GZO. The fit of Eq. (4-4) is shown as the dotted red line. Erroneous samples, excluded from the fit, are indicated by the red circles.

There is a slight disagreement in the reported value of C (Eq. (4-4)), for AZO and GZO, between this work and previously published values (Table 4-6). This may be due to the relatively low number of sample sets considered by Liu *et al.* [361] and Romanyuk *et al.* [362]. Each study also relied upon reflectance measurements in the IR and/or VIS, which are well known to be less accurate than SE [297]. Fujiwara *et al.* [118] relied on NIR-VIS-UV-SE to determine the free carrier transport properties. Later in this work (Chapter 7) it is found that NIR-VIS-UV SE produces less reliable results (below 10% deviation from IR results) for samples where N is within a "region of uncertainty" below $(3.0 \pm 0.5) \times 10^{19}$ cm^{-3}, $(7 \pm 1) \times 10^{20}$ cm^{-3} and $(7 \pm 2) \times 10^{20}$ cm^{-3} for ITO, AZO and GZO, respectively, due to tailing of IR phonon and/or defect state absorption into the NIR. Some of the samples measured by Fujiwara *et al.* fall within this region [118]. This may explain the larger lower value of C compared to those of this work and Liu *et al.* [361] for ITO, alongside the observed poor agreement between m^* obtained experimentally and the theoretical model of a nonparabolic conduction band (Eq. (4-4)).

For each film, m_e^* is calculated using Eq. (4-4), where m_0^* and C have been fit to the entire data set for each material. N_{opt} and μ_{opt} are subsequently calculated from ρ_{opt} and τ_{opt} while μ_{Hall} is calculated from N_{Hall} and ρ_{Hall} using Eqs. (2-40) and (2-41) [107]. The "uncorrected" (assuming a constant m_e^*; red triangles) and "corrected" (using $m_e^*(N_{Hall})$; green dots) N_{opt} and N_{Hall} are compared for ITO, AZO and GZO in Fig. 4-23a-c, respectively. Fig. 4-23d-f correspondingly presents μ_{opt} against μ_{Hall} for ITO, AZO and GZO, respectively. The dashed

black lines indicate where $N_{opt} = N_{Hall}$ or $\mu_{opt} = \mu_{Hall}$. The assumed values for m_e^*, which are used to determine the uncorrected transport properties, are $0.30\, m_e$ for ITO and $0.28\, m_e$ for AZO and GZO. In Fig. 4-23a-c, it is observed how the correction for a non-parabolic effective mass brings N_{opt} into better agreement with N_{Hall}. In Fig. 4-23d-f, it is found that the correction makes, on average, little or no improvement to the agreement between μ_{Hall} and μ_{opt}, which was also reported by Fujiwara *et al*. [118]. However, it is entirely plausible that $\mu_{opt} \neq \mu_{Hall}$ due to variations in carrier transport in response to a direct current (DC) or optical electric field. As lower photon energies ever-more closely approximate DC electric fields during the short mean free time, the IR range should be preferred for more consistent measurements of μ_{opt} and μ_{Hall} [354]. Indeed, this is a documented advantage of IR (and more so THz) ellipsometry and the frequency dependence of μ_{opt} may even be accounted for in the model [151,354].

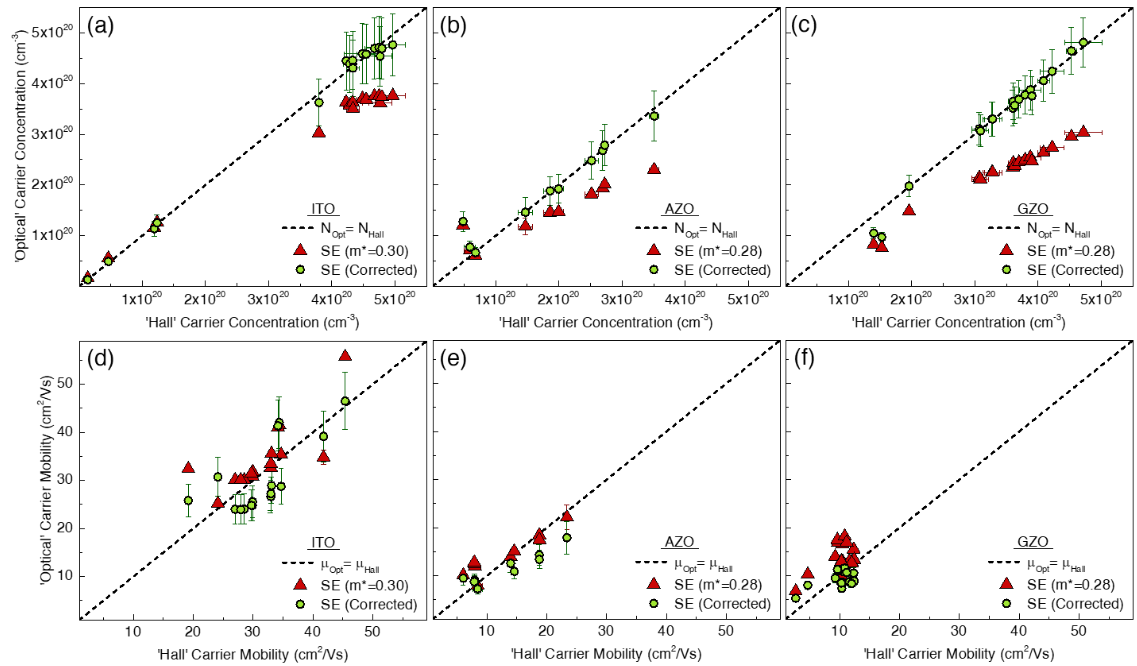

Fig. 4-23. (a-c) "Uncorrected" (red triangles) and "corrected" (green dots) optical carrier concentration, N_{opt}, against the Hall carrier concentration, N_{Hall}, for ITO, AZO and GZO, respectively. (d–f) optical mobility, μ_{opt}, against the Hall mobility, μ_{Hall}, for ITO, AZO and GZO, respectively. The dashed black lines indicate where $N_{opt} = N_{Hall}$ and $\mu_{opt} = \mu_{Hall}$.

4.2.5. Optical vs Hall carrier transport mechanisms

The approach outlined above is followed to combine Hall Effect and IRSE measurements to consider the change in m_e^* with N. Fig. 4-24 presents the optical (green dots) and Hall (yellow squares) carrier concentration and mobility of the sputtered (a) ITO, (b) AZO and (c) GZO films.

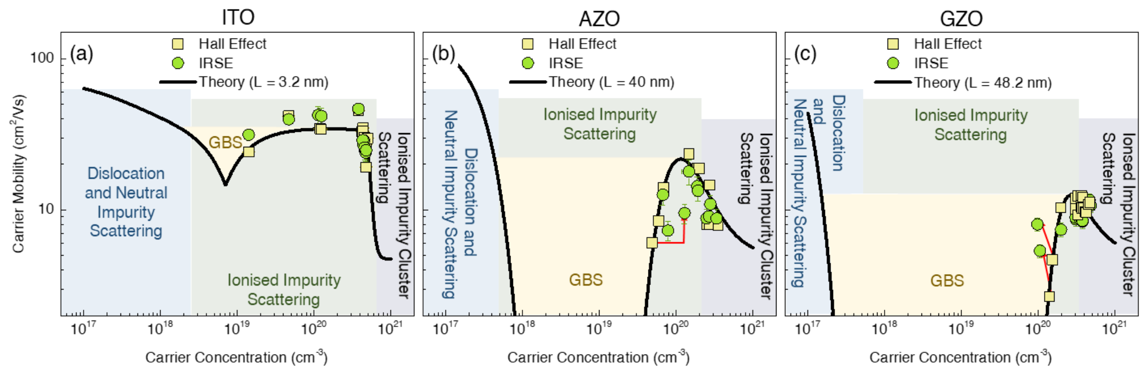

Fig. 4-24. (a-c) Carrier concentration, N, and mobility, μ, of sputtered ITO, AZO and GZO films, respectively, as determined by IRSE (green dots) and Hall Effect (yellow squares). The fit of $\mu(N)$ to the Hall Effect measurements is shown by the solid black line. The regions where different scattering mechanisms are dominant are highlighted by the different coloured shaded areas: blue for dislocation and neutral impurity scattering, green for ionised impurity scattering, yellow for grain boundary scattering (GBS) and grey for ionised impurity cluster scattering.

The relationship between μ and N follows the trend, described by Ellmer *et al.* [343] (solid black lines), as for the values determined *via* Hall Effect, discussed in Section 4.1.5. In Fig. 4-24b and Fig. 4-24c, few IRSE experimental points are observed ($N_{opt} = (8 \pm 1) \times 10^{19}$ cm^{-3} and $N_{opt} = (1.3 \pm 0.2) \times 10^{20}$ cm^{-3} for AZO and $N_{opt} = (1.0 \pm 0.1) \times 10^{20}$ cm^{-3} and $N_{opt} = (1.1 \pm 0.1) \times 10^{20}$ cm^{-3} for GZO) where there exist a deviation from the trend defined by the $\mu(N)$ relationship. Interestingly, these points do not agree with results from Hall Effect measurements (marked by red arrows in Fig. 4-24b-c), even after corrections have been applied considering how m_e^* varies with N. These points were also noted to produce erroneous values for m_e^* when evaluated against Hall Effect results (see Fig. 4-22). It is noted that for such points, N_{Hall} lies within the region of GBS (yellow shaded area in Fig. 4-24).

It follows that such results are likely invalid due to the diminished mobility invoked by GBS (Section 2.2.5). In order to verify where determination of the transport properties is possible, for both IR and NIR-VIS-UV SE, precise knowledge of N and μ is required. In addition, lower values of N than the range covered by the experimental set of films are required in order to verify that SE becomes viable below the region of GBS. In response to these limitations, an extensive ellipsometric theoretical experiment was employed that allows for an investigation

into the limitations of SE. This involved the simulation the permittivity of ITO, AZO and GZO, extending the range of N covered by the experimental dataset while carefully building, step-by-step, a set of rules that preserve the physical reality of such simulated data. This investigation is presented in Chapter 7.

4.3. Concluding Remarks

Chapter 4 was devoted to gaining precise knowledge of the optoelectronic and structural properties of the seed TCO films so that any following laser-induced modifications could be revealed. Room temperature deposition of ITO, AZO and GZO thin films onto Si substrates by radio frequency (RF) magnetron sputtering was performed for a range of deposition conditions including the applied RF power, the sputtering pressure, and the oxygen partial pressure. The effect of the sputtering conditions on the optoelectronic properties of TCOs was in good agreement with previous investigations [58,59,326]. The structure of the seed TCO films was analysed *via* X-ray diffractometry (XRD), and new insights were gained into the physical mechanisms behind the asymmetric peak for room temperature sputtered, amorphous, ITO.

Optical models were developed to fit ellipsometric measurements of a range of seed TCO films. For the seed TCOs utilised to elucidate the transport properties of TCOs and investigate the limitations of SE (Chapter 7), simple, ideal, models were sufficient to describe the optical constants, to reveal the IR and UV absorption centres, and to extract the carrier transport properties (mobility, carrier concentration, effective mass, scattering time). The transport properties of the room temperature sputter deposited ITO, AZO and GZO (collated *via* both SE and Hall Effect) sputtered across the range of sputtering conditions were used to determine the relation of both the effective mass and the carrier mobility to the carrier concentration. For ITO, however, in order to gain deeper insights into the precise nature of the conduction mechanisms and optoelectronic behaviour, the modelling required accounting for potential non-idealities such as multiple carrier species and film inhomogeneity to explain the ellipsometric results. This revealed new knowledge on the properties of TCOs such as the existence of an initial growth layer, multiple carrier transport mechanisms (explored further in Chapter 5) and a carrier-concentration dependent absorption in the IR.

5. Uncovering the physical mechanisms behind ReLA of ITO

5.1. Introduction

This chapter presents the investigation of the physical mechanisms that govern the conversion of the optoelectronic properties of indium tin oxide (ITO) during reactive laser annealing (ReLA). ReLA seeks to combine the advantages of reactive ambient thermal annealing (TA) and laser annealing (LA); utilising LA of room-temperature (RT) sputtered ITO thin films in pressurised, reactive environments to probe the films crystal structure and donor state variations. Specifically, 6.89×10^5 Pa (100 psig) of both oxidising (O_2) and reducing (5% H_2 in N_2) gasses were utilised within the pressure cell with a UV-transparent window during ReLA with varied laser fluence, J_L, from $25 - 125\ \mathrm{mJcm^{-2}}$ in steps of $25\ \mathrm{mJcm^{-2}}$. A $\times 1$ projection lens was used, providing a spot size of $(12.2 \pm 0.1) \times (12.2 \pm 0.1)\ \mathrm{mm^2}$ at the focal point (the sample surface). The desired fluence, lens, lens correction, spot area, required monitor energy and actual monitor energy and fluence are recorded in Table 5-1. Further details of the ReLA system were given in Section 3.1.2.

Table 5-1. Details of the varied sputtering conditions and corresponding film properties.

Desired Fluence ($\mathrm{mJcm^{-2}}$)	Lens Correction		Required Energy at Monitor (mJ)		Actual Monitor Energy (mJ)		Actual Fluence ($\mathrm{mJcm^{-2}}$)	
Value	c_{Lens}	Δc_{Lens}	Value	Error	Mean	Dev	Mean	Dev
25	1.211	0.004	44.4	0.5	43.6	0.2	25.1	0.3
50	1.211	0.004	88	1	87.9	0.4	49.7	0.8
75	1.211	0.004	133	2	131.2	0.7	75	1
100	1.211	0.004	177	2	176.9	0.7	100	2
125	1.211	0.004	222	3	222.7	0.9	124	2

To fully test the capability of ReLA and investigate how the film starting conditions affect the process, two films were deposited under different experimental of conditions (Table 4-1). The first seed material (the "optimised" film) represented the lowest resistivity, ρ, achievable for a RT sputtered thin film of ITO. The second seed material (the "un-optimised" film) was deposited with parameters chosen to produce a lower quality material with ρ being a magnitude greater than the optimised film. The investigation of the sputtering parameters was presented in Section 4.1.2. Prior to laser processing, the sputtered wafers were cleaved into ~ 50 "wafelets" with dimensions of $\sim(1 \times 1)\ \mathrm{cm^2}$ to guarantee that the entire wafelet was covered by the laser spot, ensuring a laterally uniform annealing. The wafelets used for laser processing were selected from a "ring" around the wafer (constant distance from the centre) to minimise the influence of the film inhomogeneity (see Section 4.1.5). Each of the above films occupies a section below (Sections 5.2 and 5.2.4, respectively). For both films, the optoelectronic properties of the processed films to the structural and compositional laser-induced modifications are

systematically investigated in order to gain knowledge of the physical mechanisms behind LA in reactive gas environments.

To reveal such properties, extensive characterisation was performed for the two ITO films, utilising: four-point probe (4pp), X-ray diffractometry (XRD), X-ray photon spectroscopy (XPS), transmission electron microscopy (TEM), energy-dispersive X-ray spectroscopy (EDX) and spectroscopic ellipsometry (SE) across the infrared (IR; $0.034 - 0.80\ \mathrm{eV}$) and near-IR-visible (NIR-VIS; $0.74 - 3.34\ \mathrm{eV}$) spectral ranges.

5.2. Reactive laser annealing of the optimised ITO film

5.2.1. Influence of ReLA on the optoelectronic characteristics

In order to reveal the properties of the ITO films subjected to ReLA the first consideration is the optoelectronic properties, which define the key characteristics of TCOs that are associated with most applications [110,165]. By fitting the complex permittivity of the ITO layer following the procedure outlined in Section 4.2, it was possible to extract the unknown variables in the model for all seed and laser processed ITO thin films. The variables of interest are the film thickness, d_B, surface roughness, d_R, "optical" resistivity ρ_{opt}, and scattering time τ_{opt},. For simplicity, this model accounted for a single carrier species (see Section 4.2.2) and a simple z-axis inhomogeneity described by the % deviation in the refractive index, $\tilde{n}$, across the film, $\%\tilde{n}_{Grad}$ [353], where the grading is accomplished by dividing the film into a series of discrete "slices" and $\%\tilde{n}_{Grad}$ is a positive number when the index is larger towards the surface of the film. The model that utilises two carrier species was also used for all seed and laser processed ITO films, but resulted in less precise values for the carrier transport properties. These results will be explored shortly, once a physical picture for the existence of two carrier species is fully elucidated. The "optical" free carrier concentration, N_{opt}, and mobility, μ_{opt}, are calculated from ρ_{opt} and τ_{opt} *via* Eqs. (2-40) and (2-41), where the effective electron mass, m_e^*, is determined for each sample by considering an increased non-parabolicity in the conduction band due to free carrier population [118], as outlined in Section 4.2.4.

To reveal the full picture of the transport properties of each seed and laser processed film, Fig. 5-1 presents μ_{opt} against N_{opt} and for the seed ITO thin films (grey stars) and those subject to single-pulse ReLA at $25 - 125\ \mathrm{mJcm^{-2}}$ in 5% H_2 in N_2 (red dots), 5% O_2 in N_2 (blue square) and O_2 (green triangles). The labels indicate the fluence used during laser processing of each sample. Three distinct examples of $\mu(N)$ are indicated by the black, purple, and orange dashed lines, respectively, in Fig. 5-1. Each example $\mu(N)$ is calculated using Eq. (2-49), Eq. (2-56) and Eqs. (2-58) to (2-61), considering $m_e^*(N)$ (Eq. (4-4)). The parameters describing $\mu(N)$ are individually fit to the 3 "clusters" of the films: $25 - 75\ \mathrm{mJcm^{-2}}$, $100\ \mathrm{mJcm^{-2}}$ and $125\ \mathrm{mJcm^{-2}}$,

using a Levenberg-Marquardt regression algorithm to determine the free parameters. Consequently, it is observed that the clusters to relate to groups of samples where the scattering mechanisms that influence μ_{opt} in relation to N are identical. When $N > 10^{20}\ \mathrm{cm}^{-3}$, the dominant scattering mechanism of ITO is ionised cluster scattering (ICS) [343] (Section 2.2.5). Therefore, the ionised impurity scattering (IIS) diminished mobility, μ_{min}, and the coefficient of ICS, α_{ICS}, are set as free parameters when fitting $\mu(N)$ to each cluster. These parameters are analogous to an intercept and gradient, respectively, of the near-straight lines of each cluster. All other parameters which define $\mu(N)$ are fixed from those found by examining a larger range of N [227,342,343]. The first cluster (dashed black line) is comprised of the seed films and those annealed in either 5% $\mathrm{H_2}$ in $\mathrm{N_2}$ (red dots) and $\mathrm{O_2}$ (green triangles) at lower J_L ($25 - 75\ \mathrm{mJcm^{-2}}$). Three seed films are shown to represent the range of transport properties of the seed ITO film, which arises from a non-uniformity across the $4''$ sputtered ITO wafer (see Section 4.1.5).

The films subject to ReLA at $25 - 75\ \mathrm{mJcm^{-2}}$ lie along the theoretical trend of $\mu(N)$, where $\mu_{min} = 55\ \mathrm{cm^2/Vs}$ and $\alpha_{ICS} = 11$, within the range of N covered by the seed films. Therefore, it is observed in Fig. 5-1 that single-pulse ReLA at $\leq 75\ \mathrm{mJcm^{-2}}$ provides no significant alteration of the conduction mechanisms from the seed optimised ITO film. ReLA at $125\ \mathrm{mJcm^{-2}}$ leads to a greater improvement of the film quality (μ_{min} is increased to $90\ \mathrm{cm^2/Vs}$) alongside an apparent reduction in the "strength" of ICS (*i.e.,* α_{ICS} is reduced from 11 to 6). These enhancements of the film quality at $100\ \mathrm{mJcm^{-2}}$ and $125\ \mathrm{mJcm^{-2}}$ likely arise from structural and/or compositional modifications. Furthermore, for the films annealed at $125\ \mathrm{mJcm^{-2}}$, a mobility-only translation (orange arrow) is not able to navigate the transport property modifications. To complete the navigation across Fig. 5-1 from the seed films to those annealed at $125\ \mathrm{mJcm^{-2}}$, an additional translation across the $\mu(N)$ trend is required. Vitally, this translation is ambient-dependent. Specifically, the increase in N in an oxidising environment ($\mathrm{O_2}$) is significantly less than in a reducing environment (5% $\mathrm{H_2}$ in $\mathrm{N_2}$). To assess the ambient-dependence further, an additional single-pulse ReLA at $125\ \mathrm{mJcm^{-2}}$ was performed in a mildly oxidising environment (5% $\mathrm{O_2}$ in $\mathrm{N_2}$) and is shown with the blue square in Fig. 5-1. The post-ReLA transport characteristics for this sample are found to lie on the same cluster with N between that of the samples annealed at $125\ \mathrm{mJcm^{-2}}$ in oxidising and reducing environments.

Therefore, ReLA is shown to induce modifications of the optoelectronic properties of the optimised ITO film. Vitally, this comprises an enhancement of μ_{opt} at $\geq 100\ \mathrm{mJcm^{-2}}$ coupled with an ambient-dependent modulation of N at $125\ \mathrm{mJcm^{-2}}$. The enhancement of N was increased for more reducing environments, indicating that ReLA at $125\ \mathrm{mJcm^{-2}}$ is able to

probe the oxygen vacancy concentration [52]. It has been shown previously that irradiation of amorphous In_2O_3 with UV light in reducing and oxidising environments could reversibly increase and decrease N [336]. However, an increase in N is observed even for the film subjected to ReLA in pure O_2, suggesting alternate donor state mechanisms are being probed.

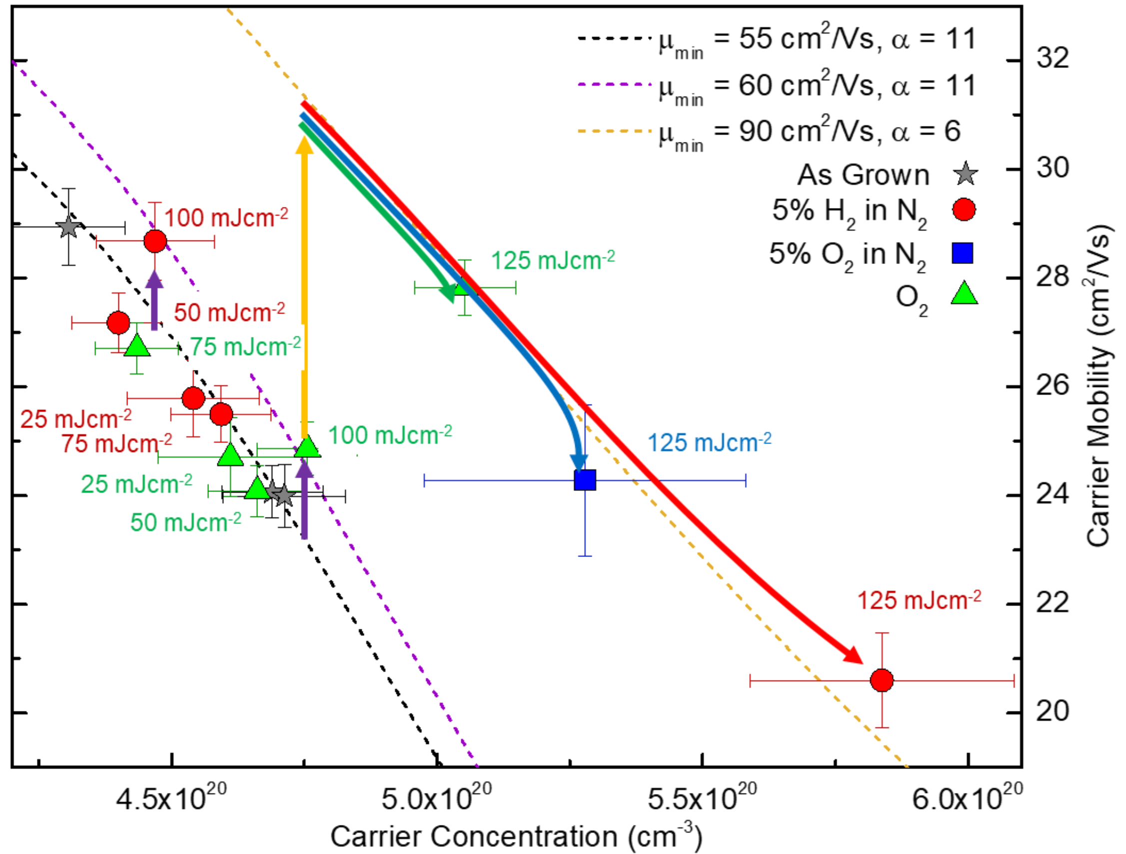

Fig. 5-1. "Optical" carrier concentration, N_{opt}, and mobility, μ_{opt}, of seed ITO thin films (grey stars) and those subject to single-pulse ReLA at $25 - 125\ \mathrm{mJcm^{-2}}$ in 5% H_2 in N_2 (red dots) and O_2 (green triangles). The sample processed with $125\ \mathrm{mJcm^{-2}}$ in 5% O_2 in N_2 is shown with the blue square. The dashed lines indicate the theoretical trend of $\mu(N)$ considering various scattering mechanisms. The parameters of $\mu(N)$ that indicate the ionised impurity scattering limited mobility, μ_{min}, and the ionised cluster scattering strength, α_{ICS}, are fit to the seed materials and those subject to ReLA at below $100\ \mathrm{mJcm^{-2}}$ (black dashed line), at $100\ \mathrm{mJcm^{-2}}$ (purple dashed line) and at $125\ \mathrm{mJcm^{-2}}$ (orange dashed line). The purple and orange arrows indicate the μ_{opt}-only transition to the next cluster and the green, blue and red arrows indicate the ambient dependent transition to higher N_{opt} after ReLA at $125\ \mathrm{mJcm^{-2}}$ in 5% H_2 in N_2, 5% O_2 in N_2 and O_2, respectively.

5.2.2. Influence of ReLA on the microstructure and morphology

A potential source for the ReLA-induced modifications of the optoelectronic properties of ITO is that the high energy dose and rapid annealing process has resulted in a change to the film crystallinity. To identify the crystal nature of the seed and processed samples, the seed and processed films were investigated with XRD. Fig. 5-2 presents the X-ray diffractograms for the seed optimised ITO film (grey squares) and the corresponding films processed with a single laser pulse at $25\ \mathrm{mJcm^{-2}}$ (red squares), $50\ \mathrm{mJcm^{-2}}$ (orange squares), $75\ \mathrm{mJcm^{-2}}$ (green squares), $100\ \mathrm{mJcm^{-2}}$ (teal squares) and $125\ \mathrm{mJcm^{-2}}$ (blue squares) in (a) $\mathrm{O_2}$ and in (b) $5\%\ \mathrm{H_2}$ in $\mathrm{N_2}$. The fitting of the broad asymmetric peak observed for the seed ITO films was achieved with a summation of two linked *pseudo*-Voigt functions (Eq. (3-13)), are presented alongside each diffractogram as the coloured solid lines. The nature of this peak was investigated in Section 4.1.4, where the large peak broadening and asymmetry for the seed film was found to arise from the nanocrystalline nature of the RT deposited ITO films. In this case, it is noted that the diffractograms of all measured seed and laser processed films in Fig. 5-2 are near identical and therefore the nanocrystalline nature appears unaffected during ReLA at $\leq 125\ \mathrm{mJcm^{-2}}$ in either $\mathrm{O_2}$ or $5\%\ \mathrm{H_2}$ in $\mathrm{N_2}$ ambient environments.

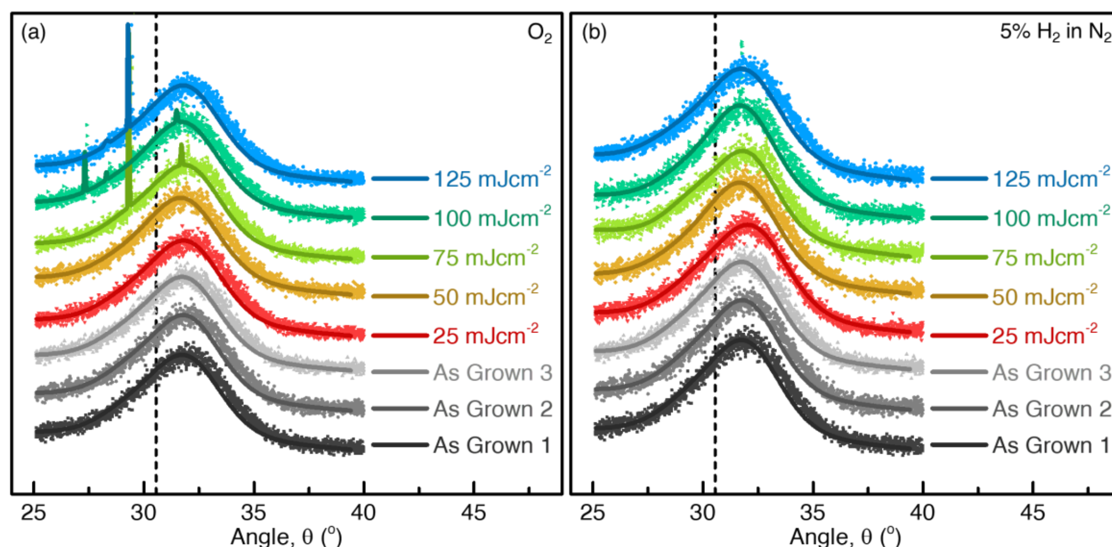

Fig. 5-2. X-ray diffractograms for the seed "optimised" ITO films (grey squares) and those subject to reactive laser annealing in (a) $\mathrm{O_2}$ and (b) $5\%\ \mathrm{H_2}$ in $\mathrm{N_2}$ between $25 - 125\ \mathrm{mJcm^{-2}}$ in steps of $25\ \mathrm{mJcm^{-2}}$ (red-blue squares). The fitting of two *pseudo*-Voigt functions to the asymmetric peak of each film is shown with the solid lines. The (100) Si peak at $32.9^0 - 33.1^0$ has been removed from all diffractograms.

However, XRD averages over the entire sample, and the modifications may be localised. To elucidate any microscopic modifications to the film structure, an examination of high-resolution TEM images was performed for the seed optimised ITO thin film (Fig. 5-3a) and the corresponding films subjected to single-pulse laser processing at $125\ \mathrm{mJcm^{-2}}$ in $\mathrm{O_2}$ (Fig. 5-3b) and $5\%\ \mathrm{H_2}$ in $\mathrm{N_2}$ (Fig. 5-3c) environments. All the samples are clearly amorphous and appear uniform across entire the sample depth, both before and after ReLA at $125\ \mathrm{mJcm^{-2}}$. Therefore, it is not possible to discriminate between the listed potential sources of the broad asymmetric XRD peak (Section 4.1.4) from the TEM images.

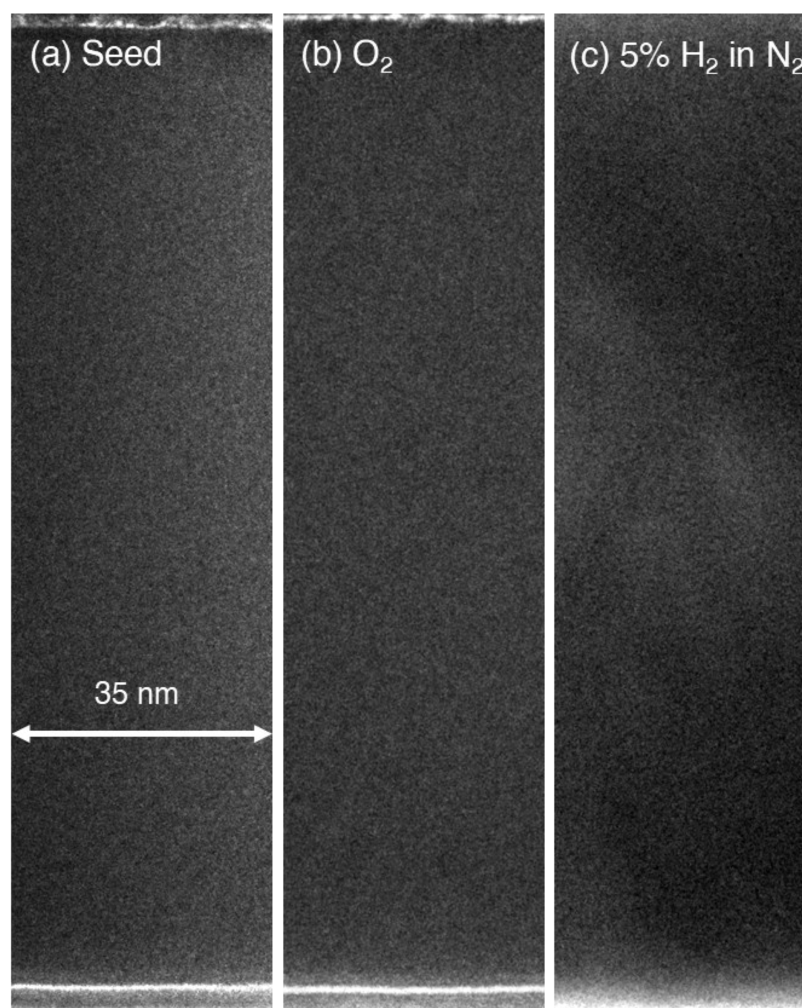

Fig. 5-3. TEM cross-sectional images of (a) seed "optimised" ITO thin film and those subject to a single laser pulse at $125\ \mathrm{mJcm^{-2}}$ in (b) $\mathrm{O_2}$ and (c) $5\%\ \mathrm{H_2}$ in $\mathrm{N_2}$. The white arrow indicates the scale of the image.

It should be noted that in previous reports on the LA of ITO, structural changes have been observed at lower fluences [66,67,364]. This discrepancy may be due to the change in the thickness of the ITO, the presence of an intermediate $\mathrm{SiO_2}$ layer (a thermal barrier for heat dissipation) and/or the solution process, which were used in the previous reports [66,364]. However, it should also be noted that an increased ambient pressure is typically employed in

order to suppress and/or eliminate sample ablation during LA [61,365]. Therefore, the pressurised environment reduces the stress inducing process of thermal expansion during ReLA. It is concluded that ReLA up to and including $125\ \mathrm{mJcm^{-2}}$ in 100 psig of either $5\%\ \mathrm{H_2}$ in $\mathrm{N_2}$ or $\mathrm{O_2}$ environments does not induce any significant changes to the crystal structure of the ITO films. Therefore, the annealing process at $\leq 125\ \mathrm{mJcm^{-2}}$ is low-stress and the ReLA-induced modifications to the optoelectronic properties cannot be explained through structural changes.

5.2.3. Influence of ReLA on the compositional properties

The other obvious source for the modifications is from changes to the material composition, which may also explain the ambient dependence of the N_{opt} modulation during ReLA (Fig. 5-1). To elucidate the compositional changes that govern the tailoring of the optical properties of ITO, an XPS survey was undertaken for one seed optimised ITO film and another film subject to single-pulse ReLA at $125\ \mathrm{mJcm^{-2}}$ in the reducing environment of $5\%\ \mathrm{H_2}$ in $\mathrm{N_2}$. The core-level X-ray photoelectron spectra of related to the (a-b) $\mathrm{Sn3d}$, (c-d) $\mathrm{O1s}$ and (e-f) $\mathrm{In3d}$ atomic orbital states for the seed and laser processed films, respectively, are presented with the black dots in Fig. 5-4. All the peaks show complex structures, where asymmetries are observed. These asymmetries require a multi-peak fitting to deconvolute the X-ray spectra into multiple sub-peaks, described by Gaussian-Lorentzian Sum (GLS) peaks (Eq. (3-18)) [293] with a fixed shape of 0.3 (30% Lorentzian and 70% Gaussian contribution). A very good fit is achieved for all peaks. The blue, green, cyan, and pink solid lines present the deconvoluted peaks for each core-level. The source of each sub-peak for each core level is discussed below. To improve the accuracy of the fit, the $\mathrm{3d_{5/2}}$ and $\mathrm{3d_{3/2}}$ peaks for both In and Sn were fit simultaneously, with a coupling of the peak broadening, area ratio, and 2^{nd} peak offset. Finally, the red solid lines in Fig. 5-4 present the cumulative fit to the data for each core-level X-ray photoelectron spectra.

The binding energy, E_B, of the $\mathrm{In3d_{5/2}}$ and $\mathrm{In3d_{5/2}}$ core levels are around 444 eV and 452 eV, corresponding to an $\mathrm{In_2O_3}$ host matrix [366]. The $\mathrm{In3d_{5/2}}$ and $\mathrm{In3d_{5/2}}$ peaks are each deconvoluted into two peaks ($\mathrm{In_I}$ and $\mathrm{In_{II}}$ for the $\mathrm{In3d_{5/2}}$ core level and $\mathrm{In_{III}}$ and $\mathrm{In_{IV}}$ for the $\mathrm{In3d_{5/2}}$ core level). The $\mathrm{In_I}$ and $\mathrm{In_{II}}$ peaks can be attributed to crystalline and amorphous ITO [367,368], respectively. The amorphous nature of the seed ITO films is highlighted by the large $\mathrm{In_I/In_{II}/In_I}$ ratio. Note that due to the coupling of the two core-levels, the $\mathrm{In_I}$ and $\mathrm{In_{III}}$ (and the $\mathrm{In_{II}}$ and $\mathrm{In_{IV}}$) peaks are identical in shape and relative peak position. The $\mathrm{In3d}$ peaks are largely insensitive to ReLA as peak shapes between Fig. 5-4e-f show no appreciable differences, indicating that the electronic environment of the $\mathrm{In^{3+}}$ ions is not significantly modified. This correlates with the finding of no significant structural change with during ReLA that was observed from XRD and TEM measurements.

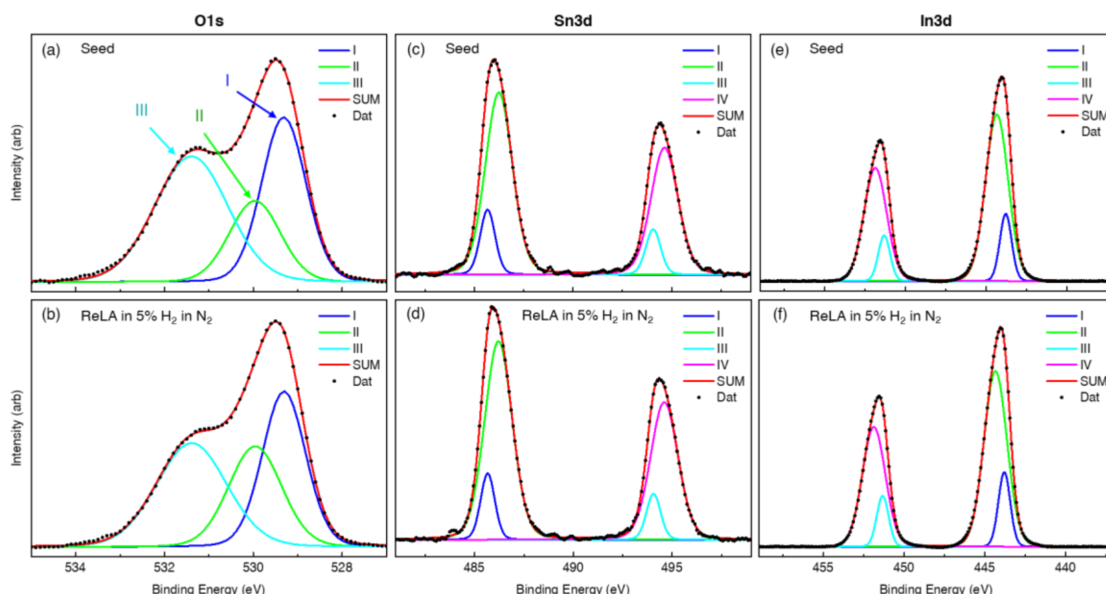

Fig. 5-4. High resolution (a-b) $\mathrm{Sn3d}$, (c-d) $\mathrm{O1s}$ and (e-f) $\mathrm{In3d}$ XPS spectra (black dots) for the optimised seed ITO films before and after laser processing with a single pulse at $125\ \mathrm{mJcm^{-2}}$ into an ambient atmosphere of 5% $\mathrm{H_2}$ in $\mathrm{N_2}$, respectively. The blue, green, cyan, and pink solid lines present the deconvoluted peaks for each core-level and the red solid line presents the cumulative fit to the data.

A key conduction mechanism in ITO is the introduction of the Sn dopant to $\mathrm{In_2O_3}$ [165] and so the investigation was devoted to the peak in the core-level X-ray photoelectron spectra that is related to Sn atoms (Fig. 5-4a-b). The $\mathrm{Sn3d_{5/2}}$ and $\mathrm{Sn3d_{3/2}}$ peaks are each deconvoluted into two peaks and the areal intensities of the $\mathrm{Sn^{4+}}$ and $\mathrm{Sn^{2+}}$ components are extracted. These components are related to the "activated" $\mathrm{SnO_2}$ and "un-activated" SnO states within the film, respectively [56]. As the donor state of ITO originates from $\mathrm{Sn^{4+}}$ ions substituting into $\mathrm{In^{3+}}$ and oxygen vacancy positions (becoming "activated"), the areal intensity of the $\mathrm{Sn^{4+}}$ component can be related to adjustments of N [216,369]. The areal intensities of the $\mathrm{Sn^{4+}}$ and $\mathrm{Sn^{2+}}$ components, in relation to the $\mathrm{Sn3d_{5/2}}$ peak, are presented in Fig. 5-5a. The $\mathrm{Sn^{2+}}$ component is dominant and there is an increased $\mathrm{Sn^{4+}}$ content after ReLA in 5% $\mathrm{H_2}$ in $\mathrm{N_2}$. Evidently, Sn activation at $125\ \mathrm{mJcm^{-2}}$ accounts for the enhancement of N_{opt} observed in Fig. 5-1. This corresponds to a removal O interstitials that activate the Sn donors [213] and marks the improvement in μ_{opt} observed in Fig. 5-1 (particularly the increased μ_{IIS}). It is inferred that a similar process of Sn activation occurs for the film processed in pure $\mathrm{O_2}$, resulting in the observed increase in N (Fig. 5-1). This is despite the highly oxidising environment, which is expected to reduce N by filling oxygen vacancies [52–55,79].

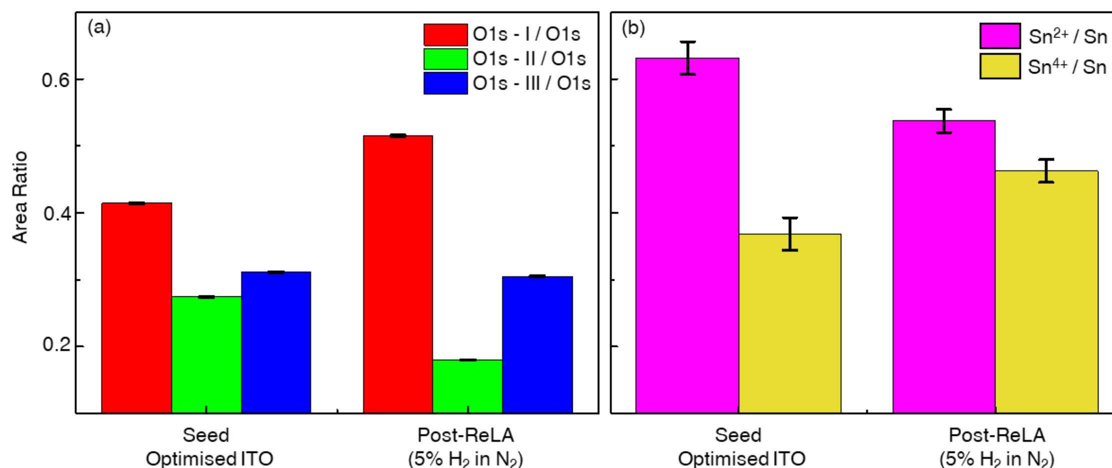

Fig. 5-5. Relative areal intensities of the deconvoluted component peaks of the core level X-ray photoelectron spectra for Sn: Sn^{2+} the (a) $\mathrm{O1s}$: $\mathrm{O_I}$ (red bar), $\mathrm{O_{II}}$ (green bar) and $\mathrm{O_{III}}$ (blue bar) and (b) Sn: Sn^{2+} (pink bar) and Sn^{4+} (yellow bar) peaks of the seed optimised ITO film and that subject to a single ReLA pulse at $125\ \mathrm{mJcm^{-2}}$ in $5\%\ \mathrm{H_2}$ in $\mathrm{N_2}$.

To investigate this possibility, the $\mathrm{O1s}$ core-level X-ray photoelectron peak (Fig. 5-4c-d) was studied. The $\mathrm{O1s}$ peak is de-convoluted into $\mathrm{O_I}$, $\mathrm{O_{II}}$ and $\mathrm{O_{III}}$ components [56]. The $\mathrm{O_I}$ and $\mathrm{O_{III}}$ components are related to the metal-oxide binding $(\mathrm{In-O})$ [369] and surface contaminants [370], respectively [364]. The origin of the $\mathrm{O_{II}}$ peak is commonly associated with oxygen atoms existing near to a neighbouring oxygen vacancy. However, this is still under debate and it is also possible that the $\mathrm{O_{II}}$ peak arises from oxygen atoms in the amorphous phase of ITO and/or oxygen atoms bound to Sn [53,177,367]. The relative areal intensities of the $\mathrm{O1s}$ components are shown in Fig. 5-5b. The films subject to ReLA in $5\%\ \mathrm{H_2}$ in $\mathrm{N_2}$ exhibit a significant enhancement of the metal oxide peak ($\mathrm{O_I}$; red bar in Fig. 5-5b) from the seed film. There is also a marked decrease in the relative areal intensity for the peak commonly associated with oxygen vacancies ($\mathrm{O_{II}}$, green bar in Fig. 5-5b). As this decrease corresponds to a decrease in the amount of oxygen (relative to In and Sn) and to an increase in N, it seems unlikely that the $\mathrm{O_{II}}$ peak is a result of oxygen vacancies. In addition, the lack of a significant change in the structure (Fig. 5-2 and Fig. 5-3) may eliminate the amorphous phase to be the source of the peak. The correlation between the reductions in the relative areal intensity of the $\mathrm{O_{II}}$ peak and the increase in the $\mathrm{Sn^{4+}/Sn^{2+}}$ ratio instead suggest that the oxygen atoms bound to Sn are the primary source. It is however very possible that the peak arises from a convolution of the above-mentioned sources that cannot be individually resolved during the peak fitting. Finally, there exist a small reduction in the surface containments after annealing in $5\%\ \mathrm{H_2}$ in $\mathrm{N_2}$ ($\mathrm{O_{III}}$; blue bar in Fig. 5-5b). This may indicate a reduction in the surface roughness due to the reduced surface area for contaminants. This may also correspond to an increased surface conductivity.

However, SE determines ρ_{opt} (a property of the entire ITO layer). Furthermore, during the SE analysis a z-axis inhomogeneity of the optical properties across the depth of the seed film was noted to improve the fit (Section 4.2.3) and the ReLA process itself is potentially highly depth-dependent [61]. The EDX capabilities of the system utilised to collect the TEM images presented in Fig. 5-3, enables an examination of the compositional modifications induced across the entire depth of the sample. Across the image, the average emitted X-ray intensity at the characteristic energy of each element within the sample is measured in order to create a depth profile of the relative elemental concentration across the film. To better compare the films, the intensity of each individual element is normalised to its peak value and the zero-point distance is set to the bottom of the film. The normalised grey value intensities for (a) Sn, (b) O, (c) In, (d) Pt and (e) Si from the bottom of the seed (grey squares) optimised ITO film and those subject to single-pulse ReLA at $125\ \mathrm{mJcm^{-2}}$ in 5% $\mathrm{H_2}$ in $\mathrm{N_2}$ (red squares) and (c) $\mathrm{O_2}$ (green squares) are presented in Fig. 5-6. Fig. 5-6f presents the bright field (BF) greyscale intensity, for reference. To calibrate the EDX intensities to the absolute surface region abundance determined *via* XPS, the surface region $\mathrm{O/(In + Sn)}$ ratio is calculated from the total areal intensities of the $\mathrm{O1s}$, $\mathrm{In3d_{5/2}}$, and $\mathrm{Sn3d_{5/2}}$ XPS peaks. Individual peak areas were corrected by their respective relative sensitivity factors [371,372]. The surface region $\mathrm{O/(In + Sn)}$ ratio is presented for the seed optimised ITO film (grey bar) and that subject to single-pulse ReLA at $125\ \mathrm{mJcm^{-2}}$ in 5% $\mathrm{H_2}$ in $\mathrm{N_2}$ (red bar) in Fig. 5-7a.

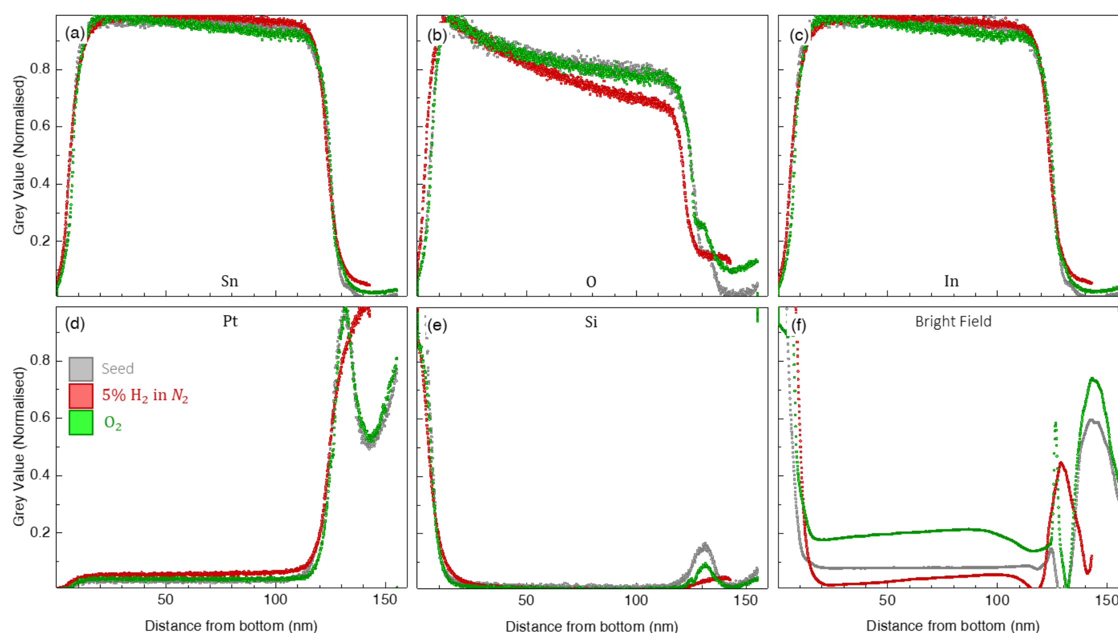

Fig. 5-6. Depth-profiles of the EDX intensity for the (a) Sn, (b) O, (c) In, (d) Pt, and (e) Si peaks of the seed "optimised" ITO thin film (grey squares) and those subject to a single laser pulse at $125\ \mathrm{mJcm^{-2}}$ in $\mathrm{O_2}$ (green squares) and 5% $\mathrm{H_2}$ in $\mathrm{N_2}$ (red squares). (f) Presents the depth profile of bright-field image greyscale intensity, for reference.

The likelihood that annealing in 5% H_2 in N_2 has created new oxygen vacancies, which complement the Sn activation for the increased N, observed in Fig. 5-1, [56] is supported by the significant drop in the relative O content, from 1.21 to 1.06, a significant departure from the stoichiometric case of $O/(In + Sn) = 1.5$ (dashed black line in Fig. 5-7). Significantly, the observed modulation of the oxygen vacancy contribution may give rise to the ambient dependence of the change in N during ReLA.

However, this is only relevant to the surface of the film and the ReLA process is likely to have a depth-dependence. Fig. 5-7a is used to calibrate the EDX-calculated depth profile of the normalised $O/(In + Sn)$ ratio across the sample depth for the optimised seed ITO film (grey stars) and those subject to single-pulse ReLA at $125\ mJcm^{-2}$ in 5% H_2 in N_2 (red dots) and in O_2 (green triangles). This is presented as a function of the distance from the bottom of the film in Fig. 5-7b. The EDX results are scaled so that the values of $O/(In + Sn)$ for the seed and 5% H_2 in N_2 annealed film, at roughly $10\ nm$ below the imaged surface (to account for the sampling depth [373]), match the values determined from XPS. These steps allow for an examination of how the oxygen content varies throughout the film.

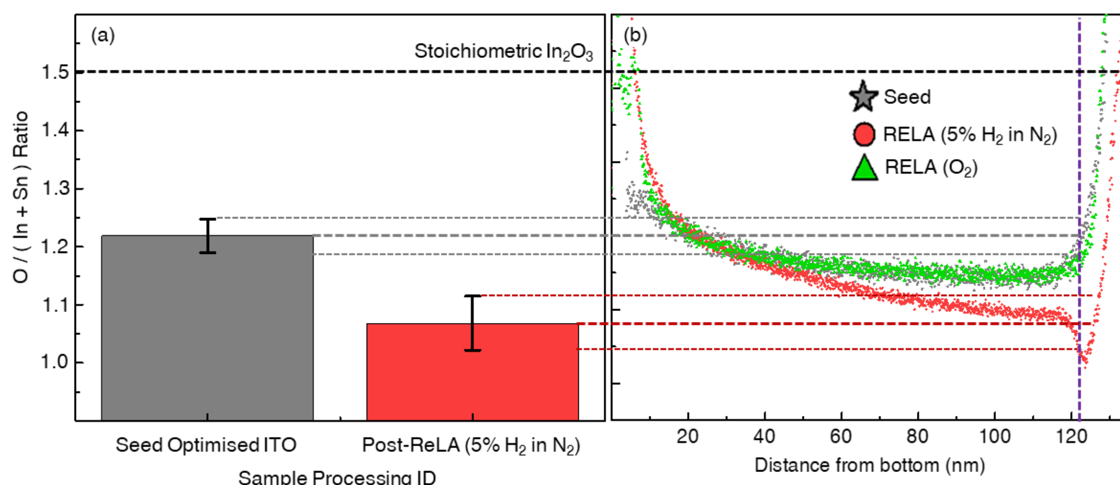

Fig. 5-7. (a) The $O/(In + Sn)$ ratio for the seed "optimised" ITO film (grey bar) and that subject to a single ReLA pulse at $125\ mJcm^{-2}$ in 5% H_2 in N_2 (red bar), calculated from surface-XPS results. (d) Depth profile of the $O/(In + Sn)$ ratio for the seed optimised ITO film (grey stars) and those subject to single ReLA pulse at $125\ mJcm^{-2}$ in 5% H_2 in N_2 (red dots) and O_2 (green stars), as calculated from EDX imaging. The $O/(In + Sn)$ ratio for a stoichiometric In_2O_3 film is indicated by the dashed black line. The XPS results are mapped onto the "surface" (purple dashed line) of the EDX depth profile with the grey and red dashed lines, where the grey and red dotted lines present the mapping of the errors.

In Fig. 5-7b, a smooth gradient is observed in the relative O concentration across the seed film. The gradient in $O/(In + Sn)$ is more significant for the film processed in 5% H_2 in N_2, and near the surface there is a sharp dip in $O/(In + Sn)$. Such a gradient has been reported previously using secondary ion mass spectroscopy [286], where the dip the $O/(In + Sn)$ ratio at the surface of the film was also found for reducing annealing environments. The gradient of the oxygen throughout the depth of the film is reflected in the presence of the simple graded inhomogeneity utilised during SE analysis.

5.2.4. Building a model for the ReLA process

To reflect the gradient in the oxygen content across the film (Fig. 5-7), an exponential gradient in ρ_{opt} and τ_{opt} across the depth of the ITO films was included in the optical analysis using Eq. (5-1) and Eq. (5-2).

$$\rho_{opt}(z) = \rho_0\left(1 + \frac{\rho_{\%Gr}}{100}\left(\frac{z}{d_B}\right)^{Exp}\right) \tag{5-1}$$

$$\tau_{opt}(z) = \tau_0\left(1 + \frac{\tau_{\%Gr}}{100}\left(\frac{z}{d_B}\right)^{Exp}\right) \tag{5-2}$$

where ρ_0 and τ_0 are the value of the resistivity and mean free time, respectively, at the bottom of the film (the ITO/Si interface). $\rho_{\%Gr}$ and $\tau_{\%Gr}$ are the percent gradient of the resistivity and mean free time, respectively, z is the distance from the bottom of the layer, d_B is the layer thickness, Exp is the exponent of the gradient. The gradient is described by a series of 100 discrete slices such that $z = (c + 0.5)/\mathrm{n}$ where c is the current slice, n is the total number of slices and z falls at the middle of each slice.

The resulting MSE for fitting this film using a gradient in ρ_{opt} and τ_{opt} was significantly reduced (from 14.7 to 10.3). The values of $N_{opt}(z)$ were calculated from $\rho_{opt}(z)$ and $\tau_{opt}(z)$ using Eq. (2-41) and are presented in Fig. 5-8 for the two of the seed optimised ITO films (black and grey line) and those subject to ReLA in 5% H_2 in N_2 (red line) and O_2 (green line) at $100\ \mathrm{mJcm^{-2}}$ (lighter shade) and $125\ \mathrm{mJcm^{-2}}$ (darker shade). The films annealed at $< 100\ \mathrm{mJcm^{-2}}$ showed a negligible change in the gradient of N_{opt} as compared to the seed films, and so are excluded from Fig. 5-8 for the sake of clarity. For the seed optimised ITO films (black and grey solid lines in Fig. 5-8), $N_{opt}(z)$ is larger towards the bottom of the film where it rapidly falls by $\sim 1 \times 10^{20}\ \mathrm{cm^{-3}}$ within the first $\sim 10\ \mathrm{nm}$ before plateauing. A sharper gradient in $N_{opt}(z)$ near the bottom of the film is observed for the film annealed at $100\ \mathrm{mJcm^{-2}}$ in both the reducing and oxidising environments (light shaded red and green, respectively, lines in Fig. 5-8).

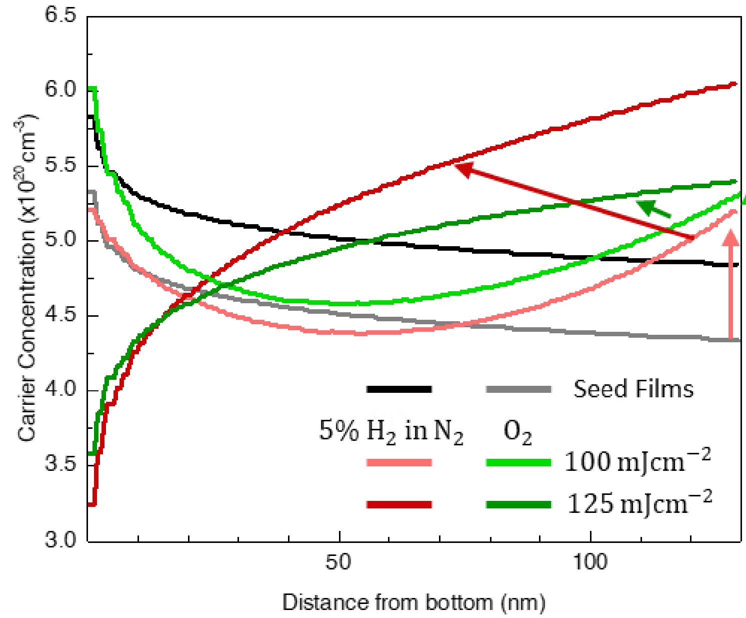

Fig. 5-8. Gradient of the optical carrier concentration as a function of the distance from the ITO/Si interface, $N_{opt}(z)$, for the seed optimised ITO film (grey line) and those subject to single-pulse ReLA at $125\ \mathrm{mJcm^{-2}}$ in 5% H_2 in N_2 (red line) and O_2 (green line).

At the surface of the film, however, N_{opt} is increased from the case of the seed films, and this results in an almost parabolic shape of $N_{opt}(z)$ across the film, where there is a lower N_{opt} near the middle of the film. As was seen in Fig. 5-1, the "average" N_{opt} of the film annealed at $100\ \mathrm{mJcm^{-2}}$ is larger for the film annealed in O_2 rather than 5% H_2 in N_2. However, a reasonable assumption can be made that the films used for laser processing in each ambient gas were slightly different (*i.e.,* sat at different points along $\mu(N)$ in Fig. 5-1). This can be seen to occur in Fig. 5-8 by how N_{opt} at the bottom of the film is larger for the film annealed in O_2, and how it is very similar to the seed film with the largest N_{opt} (black line). Conversely, for the annealed in 5% H_2 in N_2, $N_{opt}(z = 0)$ is very similar to the seed film with the smallest N_{opt} (black line). By accounting for this, it is seen that the increase of N_{opt} at the surface (relative to the seed film) is larger for the film annealed in 5% H_2 in N_2, than for the film annealed in O_2. This is indicated by the light shaded red and green arrows in Fig. 5-8. For the films annealed at $125\ \mathrm{mJcm^{-2}}$ in 5% H_2 in N_2 and O_2 (dark red and green lines in Fig. 5-8, respectively), N_{opt} at the surface is increased even further and the increase is, again, dependent on the ambient. The steepness of the $N_{opt}(z)$ curve for the seed and laser processed films agree well with the trend in the $\mathrm{O/(In + Sn)}$ ratio observed in Fig. 5-7b. This is expected from the increased likelihood of oxygen vacancy donors in the oxygen deficient lattice. Lower in the film, $N_{opt}(z)$ is reduced in comparison to the seed film for both the films annealed in 5% H_2 in N_2 and O_2. This is reflected by how the $\mathrm{O/(In + Sn)}$ ratio is increased at the bottom of the film (Fig. 5-7b). The overall trend

can be described by a shift of the gradient to lower in the film, so that the “dip” in N_{opt} lies near the bottom of the film.

These results can be used to build a physical interpretation of the ReLA process. A schematic diagram of the model used to explain the compositional changes to the ITO film during LA in a reactive ambient is presented in Fig. 5-9. A schematic for the composition of the seed film is shown in in Fig. 5-9a. The schematic highly simplifies the structure of ITO to a simple 2D array of In (green spheres) and oxygen (blue spheres) atoms where the oxygen atoms lie in the centre of four In atoms. Some of the In atoms sit at interstitial sites (light green spheres) and some of the oxygen sites are unfilled and so there exist oxygen vacancies (white spheres). In addition, some In atoms have been effective substituted with Sn atoms (orange spheres) and there also exist additional Sn atoms at interstitial positions. Finally, there may exist clusters or complexes of $\mathrm{In-O}$ and $\mathrm{Sn-O}$ that for simplicity are indicated as a molecule of InSnO in Fig. 5-9. The two rows in Fig. 5-9 show the seed film sat in the two utilised ambient environments: $5\%\ \mathrm{H_2}$ in $\mathrm{N_2}$ and pure $\mathrm{O_2}$, where the H and N atoms are indicated by the red and purple spheres, respectively.

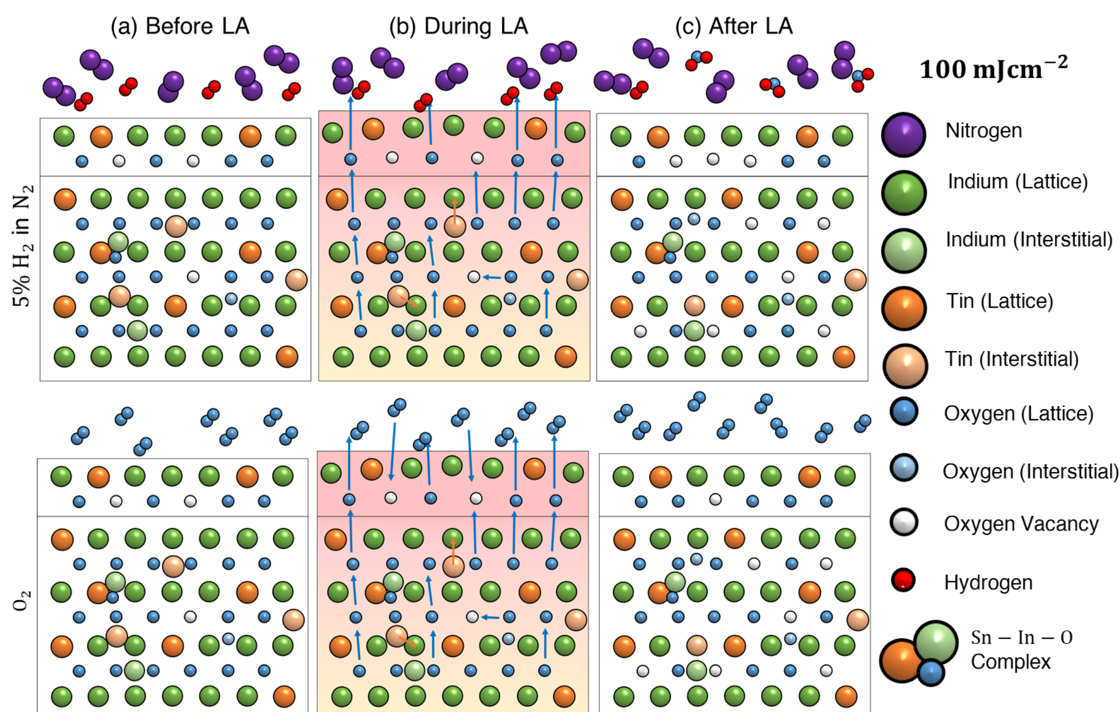

Fig. 5-9. Illustrative model for the compositional modifications of ITO during ReLA in (top row) $5\%\ \mathrm{H_2}$ in $\mathrm{N_2}$ and (bottom row) $\mathrm{O_2}$. The schematic of the composition of ITO is split into three parts: (a) before laser processing, (b) during laser processing and (c) after laser processing. The green, orange, blue, purple, and red spheres indicate In, Sn, O, N and H atoms, respectively. The lighter shaded symbols indicate the atoms are at interstitial positions in the lattice. The blue arrows show the migration of oxygen atoms during ReLA.

As detailed in Section 3.1.2, the heating mechanism of LA involves the absorption of laser photons within a penetration depth, δ_p, of the $5\ \mathrm{eV}$ KrF laser photons followed by a process of heat diffusion from the upper layer to the reset of the film [59] This results in a gradient of the thermal absorption, and thus the peak temperature reached during the annealing, as a function of the depth in the film (graded red-yellow shading in Fig. 5-9b). For "low" fluences ($\leq 100\ \mathrm{mJcm^{-2}}$), the thermal gradient is relatively small, and the thermal dose appears sufficient to modify N_{opt} within the top 90% of the film, through the creation of oxygen vacancies and/or the activation of $\mathrm{Sn^{4+}}$. Vitally, both effects require that the temperature be high enough that oxygen and/or Sn atoms become mobile within the lattice. Due to the lower atomic mass of oxygen, the oxygen atoms will become mobile at lower temperatures and be more mobile than In and Sn atoms within the lattice. The thermal expansion of the upper layers can create a pressure differential that may draw mobile oxygen atoms towards and out of the surface (blue arrows in Fig. 5-9b), leaving behind vacancies [254] and increasing N at the surface. The removal of oxygen into the pressure cell (out of the film), can exacerbate the pressure differential.

The oxygen atom mobility is induced across the entire depth of the film that reaches a critical temperature. Therefore, oxygen atoms that are removed from the surface may be replaced by those moving up from lower in the film, filling the vacancies and reducing N. As the ReLA process continues, the filled vacancies may again have their oxygen atom migrate upwards, which is indicated by the additional, cascading, blue arrows in Fig. 5-9b. This process continues while the temperature within the film is high enough to allow for the mobility of oxygen atoms throughout the lattice. At a time after the laser pulse, the thermal energy within the system becomes low enough to prevent the mobility of atoms through the lattice, marking the end of the "annealing period". The annealing period would depend on the peak temperature (*i.e.,* the fluence) and the cooling rate. At the end of the annealing period, the temperature gradient is also relaxed, and the lattice settles back to its equilibrium state (Fig. 5-9c). For low fluences ($\leq 100\ \mathrm{mJcm^{-2}}$), this time may be small enough that the some of the oxygen atoms from the bottom of the film have only just filled vacancies in the centre of the film. This can result in a middle portion of the film having fewer vacancies than both the top and the bottom of the films, resulting in a "dip" in N_{opt}, as seen in Fig. 5-8 for the films annealed at $100\ \mathrm{mJcm^{-2}}$. This situation arises from the competition between thermal gradient across the film (*i.e.*, more oxygen mobility, more blue arrows near the surface in Fig. 5-9b) and the amount of oxygen migrating from lower regions of the film. In the reducing environment, the hydrogen atoms enhance the extraction of oxygen atoms by reacting with the surface oxygen and escaping as water molecules. In the oxidising environment, a portion of the oxygen atoms that escape at the

surface are continually replaced with oxygen atoms from within the pressurised chamber (blue arrows going into the film in Fig. 5-9b). This reduces the net flux of oxygen from the surface, resulting in a lower N at the surface (relative to the bottom of the film) and a shallower gradient due to the reduced pressure differential. It should be noted that the additional oxygen can also form $\mathrm{Sn-O}$ complexes that can reduce N by "un-activating" Sn^{4+} dopants [130]. In other words, the modulation of N_{opt} may come from changing the $\mathrm{Sn}^{4+}:\mathrm{Sn}^{2+}$ ratio and not from the reduction in the oxygen vacancy density. Surface and/or depth-profile XPS of the film annealed in pure $\mathrm{O_2}$ would be required to test this possibility.

For the films annealed at $125\ \mathrm{mJcm^{-2}}$ (Fig. 5-10), the thermal dose at the top of the film is greater. A larger number of photons penetrate deeper into the film, increasing the depth of the film where the dominant heating mechanism is the absorption of the $5\ \mathrm{eV}$ KrF photons. Therefore, the peak temperature, thermal gradient and annealing time are all increased. The increased peak temperature increases the mobility of the atoms within the lattice during annealing and the increased thermal gradient enhances the pressure differential. Both effects result in a greater flux of oxygen through the film (increased number of cascading blue arrows in Fig. 5-10b). The increased thermal gradient can also change the balance of the oxygen migration within the film described above, so that the rate of oxygen leaving the film is greater than the rate at which oxygen is replenished from below. The result is that once the film has cooled and settled to its equilibrium state, there exist a strong gradient in the oxygen vacancy density across the depth of the film.

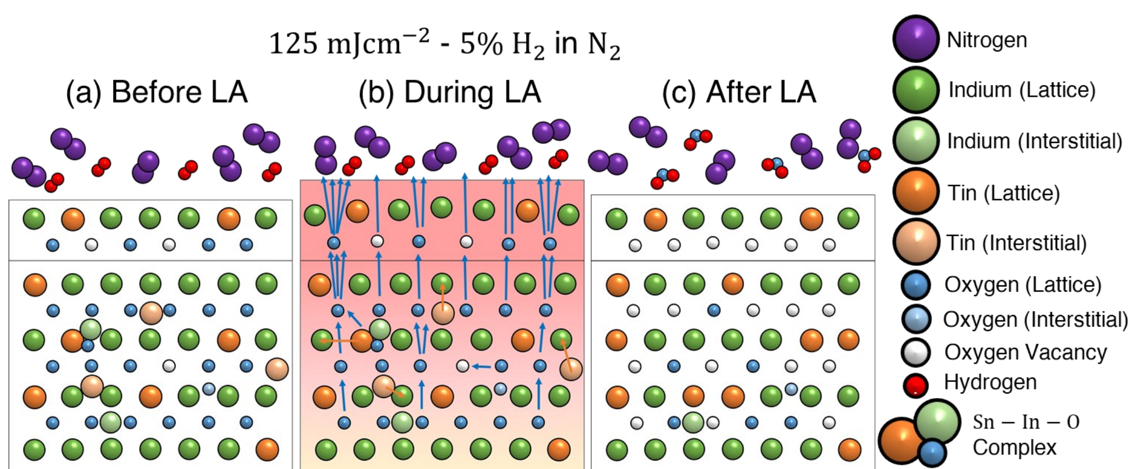

Fig. 5-10. Illustrative model for the compositional modifications of ITO during ReLA in 5% $\mathrm{H_2}$ in $\mathrm{N_2}$ and (bottom row) $\mathrm{O_2}$. The schematic of the composition of ITO is split into three parts: (a) before laser processing, (b) during laser processing and (c) after laser processing. The green, orange, blue, purple, and red spheres indicate In, Sn, O, N and H atoms, respectively. The lighter shaded symbols indicate the atoms are at interstitial positions in the lattice. The blue arrows show the migration of oxygen atoms during ReLA.

The higher temperature and the longer annealing period also enhance the processes of Sn activation and reduction of oxygen interstitials occurs simultaneously with the oxygen migration, further increasing the carrier concentration and the mobility, respectively. The outlined model would suggest that N of the laser processed film at all depths is increased from the case of the seed film. In Fig. 5-8, however, it is seen that N_{opt} near the bottom of the film is lower than for the seed film. Therefore, it appears that LA has a different effect for the region of the film near the ITO/Si interface than for the rest of the film. This may arise from the epitaxy of the ITO film near the interface. It is also possible that the oxygen is pulled from the thin native oxide layer into the ITO film, which may explain the peak in the $\mathrm{O}/(\mathrm{In}+\mathrm{Sn})$ ratio at the bottom of the film seen by EDX (Fig. 5-7). The precise nature of this effect, however, cannot currently be explained from the experimental data, and warrants further investigation. It should also be noted that depth-profile EDX does not elucidate whether the oxygen atoms within the film are more likely to end up in metal oxide or interstitial positions after ReLA. However, from the increased mobility observed in the optical results (Fig. 5-1) a reduction in oxygen interstitial concentration can be inferred as no structural modifications were observed (Fig. 5-2).

Finally, it is important to note that that annealing in hydrogen has a potential to promote hydrogen doping within the lattice [206,220,286]. This has been proposed to be a shallow donor of ITO that is more energetically favourable than oxygen vacancies [221]. This may explain why an ambient-dependent increase in N is observed alongside a reduction in the $\mathrm{O_{II}}$ peak that is commonly associated with oxygen vacancies but here viewed as resulting from $\mathrm{Sn-O}$. The effect of H-doping during ReLA in $5\%\ \mathrm{H_2}$ in $\mathrm{N_2}$ may further enhance the N modulation, but analysis of this mechanism is beyond the scope of this work. From this physical picture, it can be concluded that the ambient dependence of the free carrier modulation during ReLA arises primarily from the probing of the oxygen vacancies. The oxygen that becomes mobile in the film escapes, leaving behind increased oxygen vacancies and increasing N. The use of oxidising environments makes the increase in N less significant, as ambient oxygen atoms replenish the surface. Due to both the activation of $\mathrm{Sn^{4+}}$ and/or net oxygen flux out of the surface, an increase in N is noted even within oxidising environments. For applications where a lower N is desired, such as for low-loss NIR and IR plasmonics [15,28,51], a different strategy is required. Section 5.3 explores the case of starting from an ”un-optimised” seed ITO film, with much lower N, and filling the operational gap of N [41] *via* ReLA.

5.3. Reactive laser annealing of the un-optimised ITO film

A second seed ITO thin film was produced in order to further test the capability of ReLA and investigate how the film starting conditions affect the process. Furthermore, it was seen previously that due to Sn activation ReLA was only able to increase N. Therefore, a seed material with a lower N may allow for the bridging of the gap in the spectral windows for low loss plasmonics (Fig. 1-1), if μ_{opt} remains comparable to the optimised case. The identical conditions and characterisation techniques were applied to this film, and a much more complex story was revealed which builds upon the findings for the optimised film. The results and discussion are followed in the same way as presented above for the optimised film, noting any deviations from the previous case along the way.

5.3.1. Influence of ReLA on the optoelectronic characteristics

As discussed in Section 4.2.2, the optoelectronic properties of the ITO films are best described using three independent carrier "species" that define the optical carrier transport properties across the sample depth of the un-optimised ITO film. The optical transport properties for the 1^{st} and 2^{nd} top-layer species are compared in Fig. 5-11 alongside the case for the bottom layer in Fig. 5-12a. To compare optical and electronic results, Fig. 5-12b presents μ_{Hall} against N_{Hall}. The labels indicate the fluence used during laser processing of each sample and are coloured red or green for annealing in $5\%\ \mathrm{H_2}$ in $\mathrm{N_2}$ or $\mathrm{O_2}$, respectively. Due to the complexity introduced by the existence of multiple species of carriers across the film, the analysis requires careful, step-by-step, examination before summarising the overall picture. Firstly, the seed films (and those annealed at "low" fluences; $\leq 100\ \mathrm{mJcm^{-2}}$) are examined in order to investigate the difference between the optimised and un-optimised film and the identity of the two carrier species in the top layer. Subsequently, an examination is presented for how ReLA at higher fluences affects each layer and carrier species. Finally, the results for the top "bulk" layer are compared with those for the bottom "initial growth" layer and Hall Effect values of the transport properties.

Fig. 5-11 presents μ_{opt} against N_{opt} for the 1^{st} (darker shaded symbols) and 2^{nd} (lighter shaded symbols) carrier species that exist within the top layer of the seed un-optimised ITO films (grey stars) and those subject to single-pulse ReLA at $25 - 125\ \mathrm{mJcm^{-2}}$ in $5\%\ \mathrm{H_2}$ in $\mathrm{N_2}$ (red squares) and $\mathrm{O_2}$ (green triangles). For comparison, the case for the optimised ITO film (Fig. 5-1) are presented with the open symbols. As before, the example trends of $\mu(N)$ are shown with dashed lines. The parameters that define the trend are fit to particular "clusters" of data.

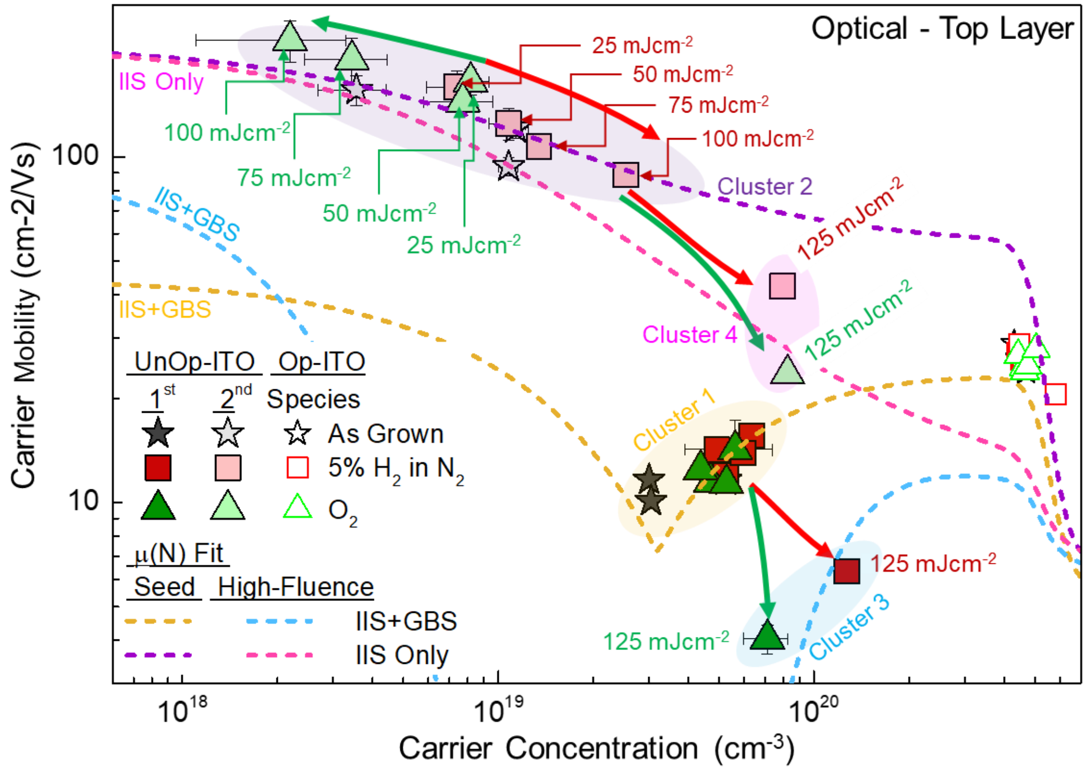

Fig. 5-11. "Optical" carrier concentration, N_{opt}, and mobility, μ_{opt}, of the seed "un-optimised" ITO thin films (grey stars) and those subject to single-pulse ReLA at $25 - 125\ \mathrm{mJcm^{-2}}$ in 5% H_2 in N_2 (red squares) and O_2 (green triangles). In (a), the 1^{st} and 2^{nd} carrier species are denoted by the dark and light symbol shades, respectively. For easy comparison, the open symbols show the corresponding transport mechanisms for the optimised ITO film, as presented in Fig. 5-1. The dashed lines indicate the theoretical trends of $\mu(N)$ considering various scattering mechanisms. The parameters of $\mu(N)_{IIS+GBS}$ that are related to grain boundary scattering (the grain size, D_{Gr}, and trap density, Q_t) are fit to the 1^{st} carrier species within the seed materials and those subject to ReLA at $\leq 100\ \mathrm{mJcm^{-2}}$ (gold dashed line) and at $125\ \mathrm{mJcm^{-2}}$ (cyan dashed line). The corresponding $\mu(N)_{IIS}$ relation, which ignores the effect of grain boundary scattering, for the films annealed at $100\ \mathrm{mJcm^{-2}}$ and $125\ \mathrm{mJcm^{-2}}$ are indicated by the purple and pink dashed lines, respectively. The green and red arrows indicate ambient-dependent transitions in N_{opt} after ReLA in 5% H_2 in N_2 and O_2, respectively.

The first cluster (indicated by the gold shaded area) represents the 1^{st} carrier species within the top layers of the seed un-optimised ITO films and those subject to ReLA at "low" fluence ($25 - 100\ \mathrm{mJcm^{-2}}$). A significantly lower N_{opt} is immediately noticed for the un-optimised film as for the optimised (Fig. 5-1), which is the source of the larger ρ_{opt} (Table 4-1). For these films, it is observed that μ_{opt} increases with N_{opt}. This indicates that in this case, as opposed to the optimised film, grain boundary scattering (GBS), and not ICS, is the dominant

scattering mechanism [227,342,343]. The trend of $\mu(N)$ fit to the 1^{st} cluster is indicated by the dashed gold line. Only the grain size, D_{Gr}, and trap density, Q_t, of the "scattering equation" (Eq. (2-49)) [227,342,343] were left free during the fit, and were determined to be 2.0 ± 0.2 nm and $(7.0 \pm 0.3) \times 10^{12}$ cm^{-2}, respectively. The other parameters were fixed to the values reported by Ellmer *et al.* [227] or to those fit to the optimised film (Fig. 5-1).

The very low D_{Gr} confirms that the seed un-optimised ITO film is amorphous, as seen by XRD (Fig. 4-3). In Fig. 5-11 it is also observed that the optimised ITO films lie slightly above the trend of $\mu(N)$ as fit to the un-optimised films (dashed gold line). This is because of the slightly larger D_{Gr} ($\sim$3.2 nm) for the optimised films [342]. The second cluster (purple shaded area in Fig. 5-11) represents the 2^{nd} carrier species (light symbols) within the top layers of the seed un-optimised ITO films and those subject to ReLA at lower fluences ($25 - 100$ mJcm^{-2}). The second cluster has considerably (approximately a factor of 10) lower N_{opt} and larger μ_{opt}. There is a negative trend of $\mu(N)$ which directly follows the trend of $\mu(N)$ for the first species if the influence of GBS is ignored, which are shown as the dashed purple line in Fig. 5-11. Indeed, the values of $\mu(N)$ for the 2^{nd} species agree well with those for epitaxial films of In_2O_3 and ITO [156,344,374]. From these observations, a picture for the physical mechanism behind the existence of two carrier species within the top layer can be established. Specifically, the first species experiences the influence of GBS whereas the 2^{nd} species does not. Therefore, the 1^{st} carrier species can be explained as the free carriers which oscillate, in response to the driving electromagnetic field, across the grain boundaries. Conversely, the 2^{nd} species oscillates within the individual grains.

Due to the amorphous (or more accurately, nanocrystalline [375]) nature of the RT deposited ITO films, the grains can be smaller than the (N-dependent) IIS-limited mean free path, $l_{e,IIS}(N)$, calculated using a highly degenerate electron gas model (Eq. (2-62)) [246–248]. This gives values of $l_{e,IIS} = 3.9 - 5.5$ nm for $N = 10^{18} - 2.7 \times 10^{19}$ cm^{-3} (the N-range of the 2^{nd} cluster), which are larger than D_{Gr}. At first glance, this suggest that all the carriers would be scattered by the grain boundaries before being scattered by ionised impurities. However, it must be noted that the scattering events which give rise to $l_{e,IIS}(N)$ are, inherently, statistical phenomena. Thus, even if $l_{e,IIS} > D_{Gr}$, a fraction of the carriers will be scattered off ionised impurities before the grain boundaries and another fraction will be scattered within the grain boundaries. The "transmitted" fraction of carriers, $T_{N,IIS}$, (*i.e.*, those that make it to the grain boundaries) can be described by:

$$T_{N,IIS} = \frac{\mathrm{N_{IIS}}}{\mathrm{N}} = e^{-D_{Gr}/l_{e,IIS}} \tag{5-3}$$

where N_{IIS} is the number of free carriers that make it to a grain boundary. From Eq. (5-3) it is calculated that $T_{N,IIS} = 67 - 69\ \%$ for $N = 3.5 \times 10^{18} - 1.1 \times 10^{19}\ \mathrm{cm^{-3}}$ (the N-range covered by the seed un-optimised films), meaning that $31 - 33\%$ of the free carriers will be scattered before a grain boundary. For the seed un-optimised ITO films, the population of the 2^{nd} carrier species is $11.7 - 36\ \%$ of the total free carrier population ($N_{opt} = N_1 + N_2$). The large range of the 2^{nd} carrier species population for the seed films is likely be due to distribution of D_{Gr} within and/or between each film *(i.e.* the average D_{Gr} is weighted by many small grains and fewer larger grains) [335]. These results build confidence that the two carrier species are indeed related to free carriers which oscillate within the grain boundaries before scattering off ionised impurities, and those that scatter at the grain boundaries. Therefore, here forth the 1^{st} and 2^{nd} carrier species are designated as the "inter-grain" and "intra-grain" carriers, respectively. It is also important to note that because D_{Gr} is so low, the picture of distinct grains with sharp grain boundaries may be misleading as the conductivity of amorphous TCOs arises from the direct overlap of large and non-directional metal atom s-states (Fig. 2-10) [178,376]. This suggest that GBS would play a minor role in the conduction mechanisms for amorphous ITO. However in Fig. 5-11 and in previous publications [342], it is seen that that the modelling of $\mu(N)$ with Seto's model of GBS (Fig. 2-11) [240] is empirically sufficient to fit the trend of the experimental films. Therefore, while there are not sharp grain boundaries where the crystal orientation of distinct grain changes, the amorphous film likely comprises localised regions of carrier traps where the carriers around the traps are depleted. Hereby, the carrier mobility through the film is affected in a similar fashion to GBS. The localised carrier traps can arise from neutral clusters of $(\mathrm{SnO_2})_2$ where the additional oxygen atoms play the role of electron traps [58,236]. Alternately, the two species may arise from carrier transport across the metal ns and the oxygen p-orbitals, respectively, in a way that is analogous to the dual-carrier species observed across different molecular chains in polymers [377]. As the precise mechanism of the physical mechanism behind the empirical adherence to Seto's model is currently unknown, the nomenclature of grains and grain boundaries will continue be used throughout the thesis.

The third and fourth clusters (light blue and pink shaded areas in Fig. 5-11, respectively) represent transitions to different "branches" of $\mu(N)$ brought on by ReLA at $125\ \mathrm{mJcm^{-2}}$. The population density for the intra-grain carriers is greatly increased, into the order of the inter-grain carriers. This indicates that the amount high mobility conduction pathways have increased, possibly by breaking up the neutral clusters of $(\mathrm{SnO_2})_2$. $\mu(N)$ is fit to the 3^{rd} and 4^{th} clusters simultaneously, both by taking into account only IIS (dashed pink line in Fig. 5-11) and by taking into account both IIS and GBS (dashed cyan line in Fig. 5-11). To do so, μ_{IIS} and $\mathrm{Q_t}$ are required to be free parameters. Due to the limited sample set, it is necessary to fix D_{Gr} at $6\ \mathrm{nm}$

(determined by XRD). μ_{IIS} and Q_t are subsequently determined to be $10 \pm 4\ \mathrm{cm^2/Vs}$, and $18.2 \pm 0.3 \times 10^{12}\mathrm{cm^{-2}}$, respectively. This represents a decrease in the IIS/lattice limited mobility and an increase in both D_{Gr} and $\mathrm{Q_t}$ after laser processing at $125\ \mathrm{mJcm^{-2}}$ and is indicative of a transition of the structure to one what contains more distinct and crystallised granular phases, with more "hard" grain boundaries, dispersed within the amorphous phase [58]. The lower value of μ_{IIS} also indicates an increased concentration of ionised impurities (activated $\mathrm{Sn^{4+}}$, interstitial In, or O vacancies) within the crystalline phases. For both the 1^{st} and 2^{nd} carrier species, the samples annealed in 5% $\mathrm{H_2}$ in $\mathrm{N_2}$ tend to show larger values of N_{opt} than for those annealed in $\mathrm{O_2}$. Indeed, for the un-optimised ITO film a potential decrease in N_{opt} with increasing fluence is seen for ReLA in $\mathrm{O_2}$. This is indicated with the red and green arrows in Fig. 5-11. Furthermore, the 1^{st} species annealed at $125\ \mathrm{mJcm^{-2}}$ shows an ambient dependence to the increase in N_{opt}, where there is a greater enhancement for the reducing environment.

The individual layers (top and bottom) can be compared with the results from Hall Effect measurements. Fig. 5-12a presents the bottom layer carrier mobility, μ_{Bot}, against the bottom layer carrier concentration, N_{Bot}, for the seed un-optimised ITO films (grey stars) and those subject to single-pulse ReLA at $25 - 125\ \mathrm{mJcm^{-2}}$ in 5% $\mathrm{H_2}$ in $\mathrm{N_2}$ (red squares) and $\mathrm{O_2}$ (green triangles). It is found that single species that lies within the bottom layer has significantly higher N (note the linear scale and change in range) than either (or both) species within the top layer. μ_{Bot} is larger than in the case for the 1^{st} species in the top film but much lower than for the 2^{nd} species. Furthermore, the "cluster" of the transport properties does not lie along one of the trends of $\mu(N)$ shown in Fig. 5-11, indicating that there are unique conduction mechanisms operating in this layer. There is no clear trend of N_{Bot} with the laser fluence. μ_{Bot} is found to vary between $38 - 54\ \mathrm{cm^2/Vs}$, where larger values of μ_{Bot} are observed for the films annealed in a reducing environment. Fig. 5-12b presents the corresponding set for μ_{Hall} and N_{Hall}. Here, an almost opposite trend is seen than for the previous case, where a near-constant μ_{Hall} ($\sim 35\ \mathrm{cm^2/Vs}$) and a variation in N_{Hall} ($0.5 - 1.6 \times 10^{20}\ \mathrm{cm^{-3}}$) with the ReLA fluence is observed. The Hall Effect results do not overlap with any individual carrier species across the sample. Instead, they appear to be influenced by contributions from both layers. For films with various carrier transport mechanisms, Hall Effect has been found to be more sensitive to the phase or layer with larger N [378]. This is found to be the case here, where N_{Hall} agrees most with the bottom optical layer. Again, a clear ambient dependence of N is observed, especially for the films annealed at $125\ \mathrm{mJcm^{-2}}$ where N_{Hall} is greater for the film annealed in 5% $\mathrm{H_2}$ in $\mathrm{N_2}$ than for that annealed in $\mathrm{O_2}$. μ_{Hall} is between the values found for the bottom optical layer and the 1^{st} species in the top optical layer. As the Hall Effect measurement using a direct

current (DC) electric field across the entire sample surface, it is expected that it is highly sensitive to GBS, and thus μ_{Hall} is far below the values found for the 2^{nd} (GBS insensitive) species.

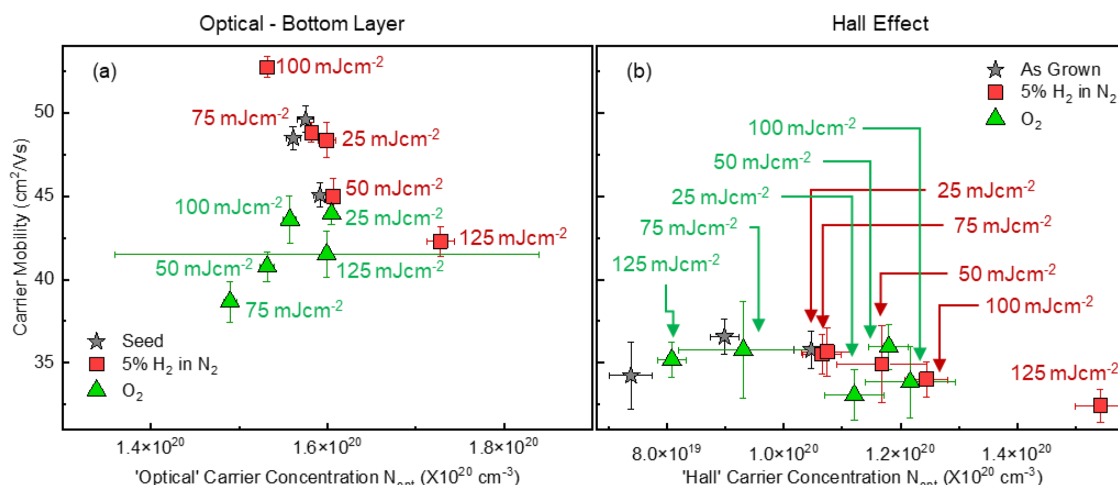

Fig. 5-12. (a) "Optical" bottom layer and (b) "Hall" carrier concentration, N, and mobility, μ, of the seed "un-optimised" ITO thin films (grey stars) and those subject to single-pulse ReLA at $25 - 125\ \mathrm{mJcm^{-2}}$ in 5% H_2 in N_2 (red squares) and O_2 (green triangles).

In summary, the optoelectronic properties of the un-optimised ITO film are far more complex than observed for the optimised film. The seed film has an inherent inhomogeneity (described by a gradient in the carrier transport properties) and multiple carrier species (due to "inter-grain" and "intra-grain" carrier species). This may be the first observation of the presence of a dual carrier species in ITO. Only by fitting a complex optical model, considering both multiple carrier species and a sharp gradient in N_{opt}, could a reliable fit to the ellipsometric and IRT measurements be achieved and thus accurate values for the carrier transport properties be extracted. Furthermore, only by investigating the resulting properties through the lens of the various scattering mechanisms at play could the physical picture of the electronic behaviour throughout the sample, and the influence of ReLA, be fully elucidated. Photo-induced modifications of the optoelectronic properties of the un-optimised ITO were revealed, with similar effects as found for the optimised film. An ambient-dependent modulation of N was noted at $125\ \mathrm{mJcm^{-2}}$, increased for more reducing environments, and, vitally, ReLA in O_2 was able to reduce N. For the un-optimised film, however, μ is reduced, not increased. From the knowledge gained by investigating the structure and composition of the optimised film, some of the underlying physical mechanisms behind the conversion of the optoelectronic properties during ReLA have been inferred. However, due to the complex nature of the film structure further experimental effort is required to fully elucidate the precise nature of such photo-induced modifications.

5.3.2. Influence of ReLA on the microstructure and morphology

As for the optimised ITO film (Section 5.2), the next step is to investigate whether ReLA has induced any modifications to the film crystallinity which may elucidate the changes to the optoelectronic properties observed in Fig. 5-11 and Fig. 5-12. The crystal structure of the seed and processed films was studied *via* XRD. Fig. 5-13a presents the X-ray diffractograms for the seed un-optimised ITO film (grey squares) and the corresponding films processed with 1 laser pulse at $125\ \mathrm{mJcm^{-2}}$ in $5\%\ \mathrm{H_2}$ in $\mathrm{N_2}$ (red squares) and in $\mathrm{O_2}$ (green squares). As for the optimised ITO films, the seed film shows a broad, asymmetric peak at centred at $\sim 32.5°$. The (222) and (400) peak positions for crystalline, unstressed $\mathrm{In_2O_3}$ at $30.607°$ and $35.49°$, respectively [285], are indicated with the dashed brown and purple lines, respectively, in Fig. 5-13a. The dark blue vertical dashed line indicates the peak likely due to a (321) preferred orientation for cubic $\mathrm{In_2O_3}$ within the amorphous film (Section 4.1.4). The X-ray diffractograms of the seed films and those processed at $\leq 100\ \mathrm{mJcm^{-2}}$ are almost identical to those for the optimised films (Fig. 5-2). Therefore, the requirement for two *pseudo*-Voigt functions that represent two distinct phases or regions with holds these are indicated by the gold and cyan dotted lines, respectively, in Fig. 5-13a. There is a striking difference for the un-optimised films annealed at $125\ \mathrm{mJcm^{-2}}$. Specifically, two new peaks emerge from the broad asymmetric peak, which has reduced in overall area, representing that the film now has a semi-crystalline nature [334]. The positions of these peaks more accurately reflect those for an unstressed, crystalline ITO film. Therefore, it is noted that ReLA has induced crystallisation of a portion of the ITO film. The *pseudo*-Voigt peaks that represent the crystallised (222) and (400) peaks are shown with the pink and purple dotted lines, respectively, in Fig. 5-13a.

The semi-crystalline nature of the films annealed at $125\ \mathrm{mJcm^{-2}}$ is confirmed by examining Fig. 5-13b-d, which presents the TEM cross-sectional images for the seed un-optimised ITO film and those subject to ReLA at $125\ \mathrm{mJcm^{-2}}$ in (c) $\mathrm{O_2}$ and (d) $5\%\ \mathrm{H_2}$ in $\mathrm{N_2}$. The seed film is highly uniform across the sample depth and no crystallisation can be observed, as for the optimised film (Fig. 5-3). However, for the film annealed at $125\ \mathrm{mJcm^{-2}}$ in $\mathrm{O_2}$, a clear region of distinct crystallites is observed within the top $\sim 67\ \mathrm{nm}$ of the film. The "fingerprint" like patterns which represent the grains are approximately $5 - 9\ \mathrm{nm}$ in diameter. This region can also be faintly observed for the film annealed in $5\%\ \mathrm{H_2}$ in $\mathrm{N_2}$, but determination of the crystallite size is inhibited by the lower image quality. This observation reveals that the two regions of an amorphous and crystalline character observed *via* XRD corresponds to the top and bottom layers of the film. The presence of distinct layers arises from the inherent depth-dependence of the ReLA thermal treatment.

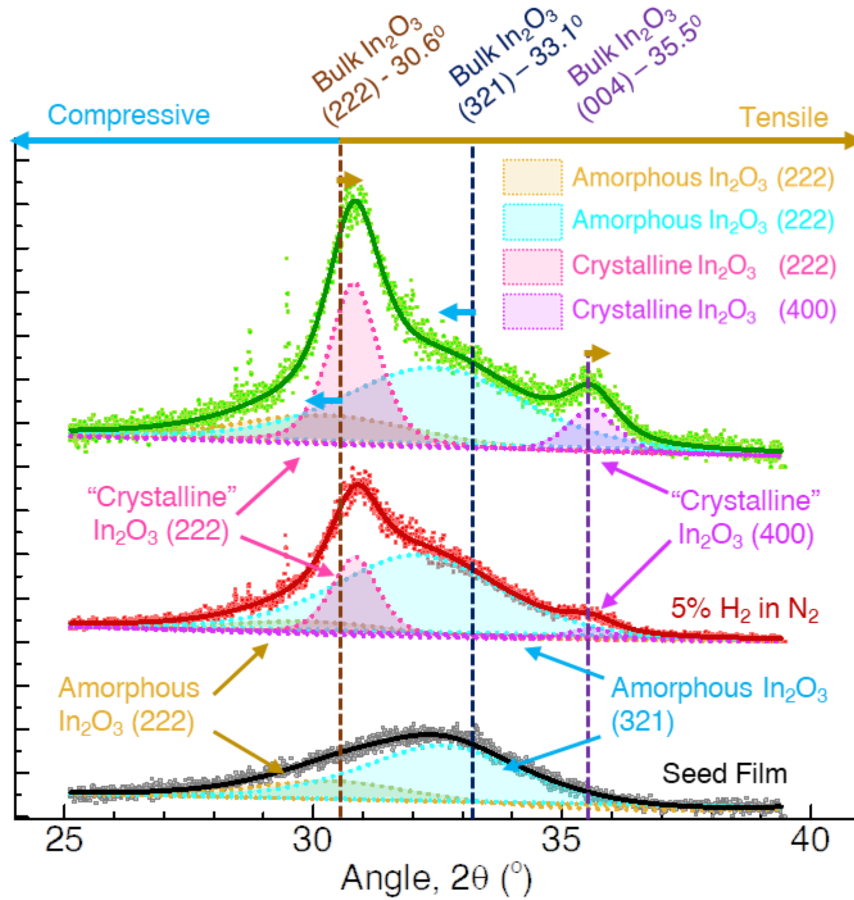

Fig. 5-13. X-ray diffractograms for seed "un-optimised" ITO (grey squares) and the film subject to single-pulse ReLA at $125\ \mathrm{mJcm^{-2}}$ in 5% H_2 in N_2 (red squares) and in O_2 (green squares). The two *pseudo*-Voight functions to the asymmetric peaks of each film are shown as the black, red, and green solid lines. The (100) Si peak at $32.9^0 - 33.1^0$ has been removed from all diffractograms.

The existence of a lower, amorphous layer and an upper, polycrystalline layer in the ITO film after ReLA can ascribed to the heating mechanism of LA [59]. This mechanism is presented schematically in Fig. 5-15 and is explained below. As detailed in Section 3.1.2, the penetration depth, δ_p, of the 5 eV KrF laser photons can be calculated from the complex permittivity, $\tilde{\varepsilon}(E) = \varepsilon_1(E) + i\varepsilon_2(E)$, *via* Eq. (5-4):

$$\delta_p(E) = \frac{1}{\alpha(E)} = \frac{\lambda}{4\pi}\kappa^{-1}(E) = \frac{hc}{2E}\frac{1}{\frac{1}{\sqrt{2}}\sqrt{\sqrt{\varepsilon_1{}^2(E) + \varepsilon_2{}^2(E)} - \varepsilon_1(E)}}\frac{1}{\frac{1}{\sqrt{2}}\sqrt{\sqrt{\varepsilon_1{}^2(E) + \varepsilon_2{}^2(E)} - \varepsilon_1(E)}} \tag{5-4}$$

The penetration depth (purple line in Fig. 5-15a) for the un-optimised ITO film cannot be directly calculated as the spectral range only extended to 3.4 eV. Therefore the "Low-N" ITO film that was measured *via* IRSE and NIR-VIS-UV SE (see Table 4-1), is used to find $\tilde{\varepsilon}$ at 5 eV and thus calculate that $\delta_{p,\mathrm{KrF}} = 43.2 \pm 0.1\ \mathrm{nm}$.

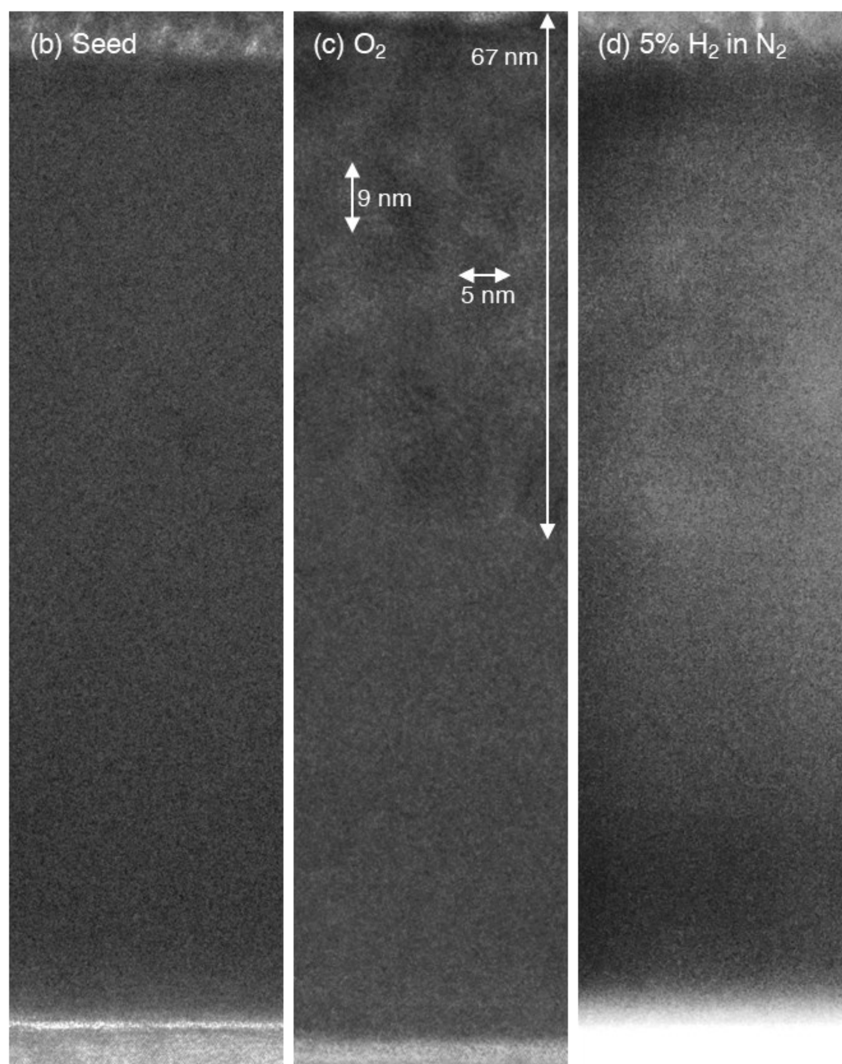

Fig. 5-14. TEM cross-sectional images of (a) seed "un-optimised" ITO film and those subject to ReLA at $1125\ \mathrm{mJcm^{-2}}$ in (b) $\mathrm{O_2}$ and (c) $5\%\ \mathrm{H_2}$ in $\mathrm{N_2}$. The white arrows in (b) indicate the scale (shared across the images) and, specifically, show an example grain size for the top layer and the depth of the semi-crystallised layer.

Within the region defined by the penetration depth, the heat is predominantly generated by the absorption of the KrF photons. This region is indicated by the purple shaded area in Fig. 5-15a. The lower portions of the film are then heated by heat diffusion from the top $\sim 67\ \mathrm{nm}$. The diffusion will also result in an exponential decay of the peak temperature as a function of δ (Fig. 5-15b). This region is indicated by the red shaded area in Fig. 5-15a. Below this region, the temperature increase would be insufficient to significantly affect the material. Depending on the thickness of the film, this threshold may occur within the film, or extend into the substrate itself so that the entire film is thermally affected. This region is indicated by the red shaded area in Fig. 5-15a. The reduced significance of the thermal annealing further down the film explains why the carrier transport mechanisms only vary by $\sim \pm 10\%$ for the bottom layer of the laser processed ITO films.

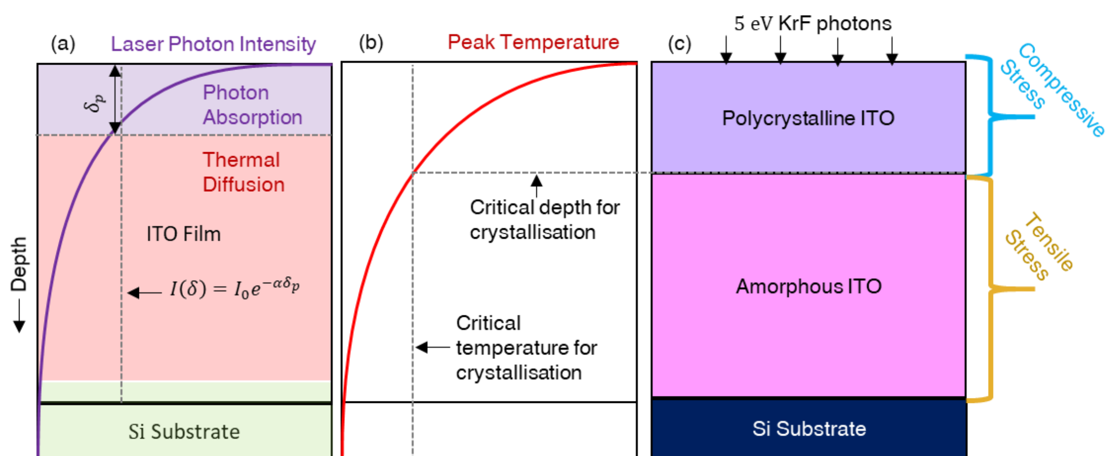

Fig. 5-15. Schematic of the depth dependence of LA.

In Fig. 5-14, however, it was seen that the region of polycrystallinity stops at a depth of ~ 67 nm, which is $\sim 60\%$ larger than the calculated δ_p. Of course, the absorption of the photons does not cut-off at the edge of the penetration depth. Instead, there is a smooth exponential gradient of the laser photon intensity (Fig. 5-15a) and thus temperature increase due to photon absorption. Across the film, the difference in the absorption would results in a gradient of the peak temperature reached during the laser annealing process. An illustration of the variation of the peak temperature, T_{Peak}, across the depth of the sample is shown as the solid red line Fig. 5-15b. The peak temperature closely follows the laser photon intensity. For a critical intensity of photons, T_{Peak} would be sufficiently high to induce a crystallisation of the ITO film. An example T_{Peak} is indicated by the vertical dashed line in Fig. 5-15b. Fig. 5-14 demonstrates that this critical temperature must be reached within the upper, polycrystalline region that extends ~ 67 nm into the film. This region is indicated with the purple slab in Fig. 5-15c. Below this region the peak temperature is insufficient to induce crystallinity and the layer remains amorphous. This is indicated with the pink slab in Fig. 5-15c.

It should be noted that the photon absorption relative to the incident photon intensity (*i.e.,* the laser fluence) as a function of the depth is dependent only on the material optical constants. However, the absolute absorption and thus the peak temperature as a function of the depth, $T_{peak}(\delta)$, would depend on the fluence and other properties of the material such as the thermal conductivity and entropy. Furthermore, the critical temperature for the promotion of crystallinity must depend on not only the absorption coefficient at 5 eV. This can be inferred by how the optimised film does not show an upper crystallised layer despite the fact that the optical constants in the UV (above the band gap) do not dramatically change (Fig. 4-9 and Fig. 4-10). To investigate the heating mechanism further, the illustrative example of Fig. 5-15 could be quantified by inputting specific material optical constants, thermal properties and the laser

fluence into numerical solutions to the $1D$ heat transport equation in order to extract the absolute values of $T_{peak}(\delta)$. This would allow for a correlation of the depth of the crystallised region with the $I(\delta)/I_0$ ratio and enable one to calculate the critical temperature for crystallisation [61].

The heating mechanism described above results in a depth-dependent modification of the microstructural and optoelectronic properties. Fig. 5-13 showed that the peak position of the (222) ITO peak for the seed un-optimised ITO film was lower than the bulk (222) peak position of $30.6°$. For films annealed at $125\ \mathrm{mJcm^{-2}}$, the (222) peak is split into two parts for both the amorphous and crystalline layers. The peak for the amorphous (bottom) layer exists below the bulk (222) position and thus remains under compressive stress. Conversely, the peak for the crystalline (top) layer exists above the bulk (222) peak position and indicates the top portion of the film is under a tensile stress. The change in the crystalline state between the top and bottom layers cautions a direct comparison of the XRD peaks. However, the compressive stress of the seed ITO film and lower region of the laser processed films likely arises from the interfacial mismatch between the atomic spacings for the Si and $\mathrm{In_2O_3}$ lattices [339]. Furthermore, the high oxygen content of the seed film (Fig. 5-16) would lead to a stretching of the lattice and a compressive stress, increasing the d-spacing and reducing $2\theta_{peak}$. For the upper layer, the reduction in oxygen and creation of oxygen vacancies can significantly reduce the d-spacing (see Fig. 2-7), resulting in a tensile stress. It should be noted that a model of the tensile and compressive stresses of the thermally affected and non-thermally affected layers of a laser processed film was developed by Elhamali to describe the asymmetry of the XRD peaks for laser processed AZO [59]. This model suggested that a compressive stress is introduced into the upper layer due to the expansion of the top layer parallel to the surface. The compression arises from the requirement that the length of the interface between the thermally affected and non-thermally affected regions is the same. However, the observed stresses for ITO are the opposite of those suggested by this model.

In summary, the structural modifications of the un-optimised ITO film were more significant and complex than for the optimised ITO film. Specifically, at higher fluences ($125\ \mathrm{mJcm^{-2}}$) in both reducing and oxidising ambient environments, a polycrystalline nature was introduced to the upper layer of the film (with a grain size of $\sim 5-9\ \mathrm{nm}$) while the lower layer remained amorphous. The depth of the polycrystalline layer was shown to result on the change in the photon absorption and peak temperature as a function of depth across the film. The depth-dependence of the LA process explains the minor changes to the bottom, "initial growth layer" of the un-optimised ITO film with ReLA. However, the modulation of the carrier

transport properties observed for the upper layer in Fig. 5-11 cannot be explained by a change in the structure alone. Furthermore, optical modelling revealed a high depth inhomogeneity in the seed un-optimised ITO film itself. To explain these observations, an extensive investigation into the compositional properties of the seed and laser processed films was required.

5.3.3. Influence of ReLA on the compositional properties

Fig. 5-16 presents the areal intensities of (a) the O_I (red bar), O_{II} (green bar) and O_{III} (blue bar) components of the $O1s$ core-level X-ray photoelectron spectra and (b) the Sn^{4+} (pink bar) and Sn^{2+} (yellow bar) components of the $Sn3d_{5/2}$ core-level X-ray photoelectron spectra for one seed un-optimised ITO film and another subject to single-pulse ReLA at $125\ mJcm^{-2}$ in the reducing environment of $5\%\ H_2$ in N_2. For comparison, the solid horizontal lines of each colour presented across each bar indicate the values for the optimised ITO film shown in Fig. 5-5 and Fig. 5-7. Inspection of the deconvoluted $O1s$ peaks reveals that the surface oxidations states for the seed un-optimised ITO film are very different to those of the optimised film. Specifically, in relation to the optimised ITO film: the O_I peak that is related to the metal oxide is significantly decreased while the O_{III} peak related to surface contaminants is increased and the O_{II} peak, likely related to $Sn-O$ [53] (Fig. 5-5), is largely the same. This suggests that the un-optimised ITO film is more entropic or amorphous than the optimised film [367], that there is a higher concentration of surface defects related to hydroxides [364] and/or a smaller presence of metallic In [254]. Inspection of the deconvoluted $Sn3d$ peaks for the seed un-optimised ITO film reveals that the Sn^{4+} states are reduced in comparison to the optimised film, partly explaining the lower values of N_{opt} and N_{Hall} observed in Fig. 5-11 and Fig. 5-12. The slight decrease in the O_{II} peak observed in (a) corresponds to the slight reduction in the Sn^{4+} peak observed in (b) and further highlights the case for $Sn-O$ bonds as the source of the O_{II} peak.

Laser processing of the seed un-optimised ITO film with a single ReLA pulse at $125\ mJcm^{-2}$ in the reducing environment of $5\%\ H_2$ in N_2, has a near-identical effect on the $O1s$ and Sn states as for the optimised ITO film. Specifically, the O_I peak is enhanced at the expense of the O_{II} peak, indicating an enhancement of the crystalline order and a reduction of $Sn-O$, and the surface defects (O_{III} peak). There is also a corresponding activation of Sn^{4+} donors, partially explaining the increase in N_{opt} and N_{Hall} observed after laser processing. As the concentration of oxygen vacancies cannot be reliably determined by de-convoluting the $O1s$ XPS peak, the abundance of oxygen relative to the abundance of the $O1s$, $In3d_{5/2}$ and $Sn3d_{5/2}$peaks, where the individual peak areas were corrected by their respective relative sensitivity factors [371,372].

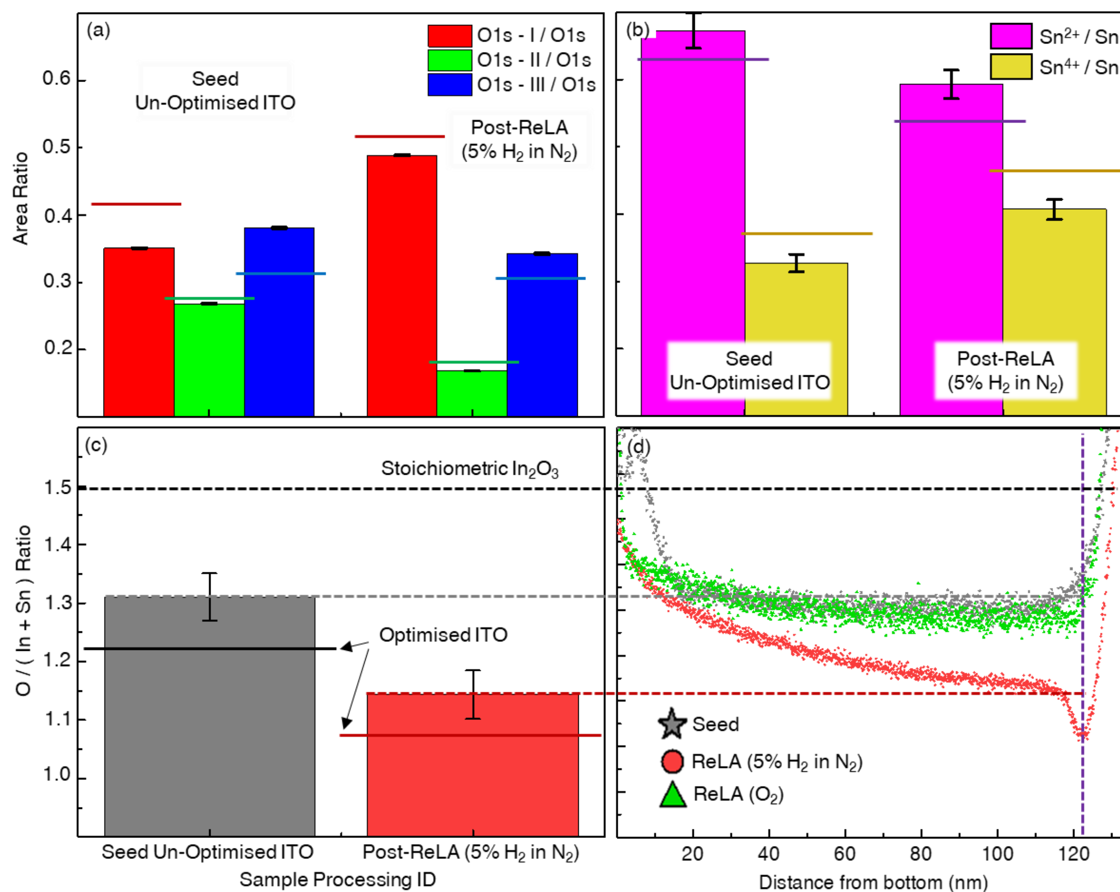

Fig. 5-16. Relative areal intensities of the deconvoluted component peaks of the core level X-ray photoelectron spectra for the (a) Sn^{2+} (pink bar) and Sn^{4+} (yellow bar) and the $\mathrm{O_I}$ (red bar), $\mathrm{O_{II}}$ (green bar) and $\mathrm{O_{III}}$ (blue bar) peaks for the seed "un-optimised" ITO film and that subject to a single ReLA pulse at $125\ \mathrm{mJcm^{-2}}$ in $5\%\ \mathrm{H_2}$ in $\mathrm{N_2}$. (c) The $\mathrm{O/(In + Sn)}$ ratio for the seed un-optimised ITO film (grey bar) and that subject to a single ReLA pulse at $125\ \mathrm{mJcm^{-2}}$ in $5\%\ \mathrm{H_2}$ in $\mathrm{N_2}$ (red bar), calculated from surface-XPS results. (d) Depth profile of the $\mathrm{O/(In + Sn)}$ ratio for the seed optimised ITO film (grey stars) and those subject to single ReLA pulse at $125\ \mathrm{mJcm^{-2}}$ in $5\%\ \mathrm{H_2}$ in $\mathrm{N_2}$ (red dots) and $\mathrm{O_2}$ (green stars), as calculated from EDX imaging. The $\mathrm{O/(In + Sn)}$ ratio for a stoichiometric $\mathrm{In_2O_3}$ film is indicated by the dashed black line. The XPS results are mapped onto the "surface" (purple dashed line) of the EDX depth profile with the grey and red dashed lines. The solid horizontal lines in (a-c) indicate the values for the optimised ITO film shown in Fig. 5-5 and Fig. 5-7.

The surface region $\mathrm{O/(In + Sn)}$ ratio is presented for the seed optimised ITO film (grey bar) and that subject to single-pulse ReLA at $125\ \mathrm{mJcm^{-2}}$ in $5\%\ \mathrm{H_2}$ in $\mathrm{N_2}$ (red bar) in Fig. 5-16c. The $\mathrm{O/(In + Sn)}$ ratio for the seed film (grey bar) is found to be larger than for the optimised ITO film (solid horizontal grey line) and is decreased by an amount identical amount by laser annealing (red bar where the solid horizontal red line indicates the post-ReLA $\mathrm{O/(In + Sn)}$ ratio

for the optimised ITO film). The higher, more stoichiometric (dashed black line), concentration of oxygen likely corresponds to a smaller density of oxygen vacancies, explaining the other cause of the lower N of the un-optimised film. The increase in the oxygen deficiency after ReLA correspondingly explains the increase of N after ReLA (alongside Sn^{4+} activation) and is likely the root of the ambient dependence of the N modulation, as detailed for the optimised ITO film.

The EDX-calculated depth profile of the normalised $\mathrm{O}/(\mathrm{In}+\mathrm{Sn})$ ratio (corrected to the XPS results; see Fig. 5-7) across the sample depth for the optimised seed ITO film (grey stars) and those subject to single-pulse ReLA at $125\ \mathrm{mJcm}^{-2}$ in 5% H_2 in N_2 (red dots) and in O_2 (green triangles) is presented as a function of the distance from the bottom of the film in Fig. 5-16d. Once again, a gradient of the carrier concentration is observed throughout the depth of the film. The sharp increase of the $\mathrm{O}/(\mathrm{In}+\mathrm{Sn})$ ratio at the bottom of the seed film may explain the existence of the bottom, "initial growth layer" required to model the optical properties of the film (Fig. 5-11). An identical behaviour to the modification of the gradient of the $\mathrm{O}/(\mathrm{In}+\mathrm{Sn})$ ratio with the ambient environment is found for the un-optimised ITO film as for the optimised. Specifically, the reducing environment creates a steeper reduction of the oxygen across the depth of the film. Thus, the model of oxygen mobility and Sn activation during ReLA outlined for the optimised ITO film (Section 5.2.4) equally works to describe the compositional modifications of the un-optimised ITO film.

5.4. Concluding remarks

It is concluded that ReLA offers a low-stress method to engineer the defects of the ITO films to enhance μ and selectively increase N. The modifications arise from a combination of Sn activation and a manipulation of the oxygen migration during the annealing process. The low-stress nature of the process mean that ReLA can promote defect mobility within the lattice without causing structural changes that may damage the film, especially if applied to more complex prefabricated nano/microstructures. Furthermore, the low-thermal budget of LA allows for the application of ReLA to annealing of materials on heat sensitive substrates, such as those used for flexible electronics [59,379,380]. It should be noted that this is just for a single pulse and as such, multi-pulse ReLA is likely to be able to enhance the capability to engineer the defects of TCOs and thus tailor their optoelectronic properties. Utilising multiple pulses may however require an adjustment of the utilised fluence to ensure the process remains low stress. This will be explored further for in Chapter 6.

Laser processing for a seed ITO material with a lower N was investigated in order to further reveal the physical mechanisms behind the conversion of the optical properties of ITO during ReLA and to see if such processing may allow for the bridging the gap in the spectral window for "low-loss plasmonic responses" (Fig. 1-1). The identical conditions and characterisation techniques that were used for the optimised ITO film were applied to this film, and a much more complex story was revealed that built upon the findings for the optimised film. Specifically, multiple charge species and a complex inhomogeneity were required to be considered in order to model the optical data. By examining the carrier transport mechanisms of the two carrier species for the larger set of seed and laser processed films, considering the effect of various scattering mechanisms, the nature of the multiple carrier species was revealed. Specifically, the two carrier species were found to arise from carriers that were scattered by ionised impurities and those that were scattered by grain boundaries or by clusters of defects that act like grain boundaries. Unlike the optimised film, clear structural modifications occurred when laser processing at a high fluence ($125\ \mathrm{mJcm^{-2}}$). Specifically, the upper layer of the film became polycrystalline (with grain sizes of $5 - 10\ \mathrm{nm}$) after ReLA. The depth dependence of the structural modifications was shown to arise from the change of the peak temperature across the film, due to the depth-dependence of the ReLA process. Despite the structural modifications, it was found that the compositional modifications induced by ReLA were near-identical to those for the optimised film. Specifically, the laser induced both an activation of Sn dopants and a modification of the oxygen vacancy concentration throughout the depth of the film. The modulation of the oxygen vacancies was deemed to be the likely candidate for the ambient-dependent modulation of N.

However, further work is required to fully elucidate the physical mechanisms that govern the modulation of the optoelectronic properties of ITO during ReLA. Specifically, XPS core-level spectra for the sample annealed in an oxidising environment would be essential to further test the role of oxygen vacancies as the source of the modulation of N. Depth-profile XPS would also enable more quantitative analysis of the gradient of N across the film. Theoretical modelling of the laser annealing process could be performed by solving the $1\mathrm{D}$ heat diffusion equation for the optimised and un-optimised films to find the thermal distribution across the depth of the film as a function of time and thus correlate the local temperature with the various compositional and structural modifications. Finally, the graded nature of the seed and laser processed ITO films, which is revealed optically and compositionally, may not be desirable for particular applications. Currently, the graded nature is compounded during laser processing and therefore methods to increase the depth uniformity would be greatly beneficial.

6. Ultrafast Multi-Beat Reactive Laser Annealing of ITO

6.1. Introduction

This chapter presents a broader investigation of the role of the laser annealing (LA) parameters (laser fluence, number of pulses and ambient composition) on the conversion of the optoelectronic properties of indium tin oxide (ITO) during LA. The aim was to reveal the full capabilities of reactive LA (ReLA) with multiple pulses and greater control on the ambient environment to tune the optoelectronic properties towards the requirements for IR plasmonic material components. Each parameter is investigated in turn, so that an "optimal" value can be found that maximises the change in the carrier concentration, N, can be used for investgating the subsequent LA parameter.

6.2. Influence of ReLA fluence

A selection of wafelets from the optimised "UMBReLA set" ITO film (see Table 4-1) were subjected to single pulse LA in pressured (100 psig) environment of pure Ar with increasing laser fluence, J_L, of $50 - 150\ \mathrm{mJcm^{-2}}$ with steps of $25\ \mathrm{mJcm^{-2}}$ using a $\times 1$ projection lens with a spot size of $(13 \pm 0.1) \times (13 \pm 0.3)\ \mathrm{mm^2}$ at the sample surface. A non-reactive environment of pure Ar was used to minimise the compositional changes of the thin film in this step. To investigate the role of larger J_L than investigated in Chapter 5, a $\times 1.7$ lens was used to provide a laser spot size of $(7.8 \pm 0.1) \times (8.0 \pm 0.3)\ \mathrm{mm^2}$. This enabled processing with fluences of $225 - 375\ \mathrm{mJcm^{-2}}$ in steps of $75\ \mathrm{mJcm^{-2}}$. The desired fluence, lens, lens correction, spot area, required monitor energy and actual monitor energy and fluence are recorded in Table 6-1.

After laser processing, the films were characterised with four-point probe (4pp), Hall Effect, IR transmission (IRT), optical reflectance spectroscopy (ORS) and IR spectroscopic ellipsometry (IRSE). This section investigates the effect of J_L on the resulting optoelectronic properties.

Table 6-1. Details of the varied sputtering conditions and corresponding film properties.

Desired Fluence ($\mathrm{mJcm^{-2}}$)	Lens			Spot Area ($\mathrm{cm^2}$)		Required Energy at Monitor (mJ)		Actual Monitor Energy (mJ)		Actual Fluence ($\mathrm{mJcm^{-2}}$)	
Value	Mag	c_{Lens}	Δc_{Lens}	Value	Error	Value	Error	Mean	Dev	Mean	Dev
50	$\times 1$	1.211	0.004	1.69	0.04	85	2	102	3	50	2
75	$\times 1$	1.211	0.004	1.69	0.04	127	3	153	4	75	3
100	$\times 1$	1.211	0.004	1.69	0.04	169	4	205	5	101	4
125	$\times 1$	1.211	0.004	1.69	0.04	211	5	256	6	125	4
150	$\times 1$	1.211	0.004	1.69	0.04	254	6	307	8	151	5
225	$\times 1.7$	1.16	0.01	0.62	0.02	140	6	162	7	230	10
300	$\times 1.7$	1.16	0.01	0.62	0.02	187	7	217	9	300	20
375	$\times 1.7$	1.16	0.01	0.62	0.02	234	9	270	10	380	20

Optical Modelling of ITO

During optical modelling of the IRSE measurements of $\Psi(E)$ and $\Delta(E)$ the IRT and ORS measurements were appended to the data with a fit weighting of 33%. The model that was utilised to fit the optical data built upon the findings of Chapter 4. Specifically, the model included two distinct layers for the ITO film; a "bulk" and a "surface" layer. The bulk layer is described by a summation of two distinct Drude terms, representing both the intra-grain and inter-grain carrier transport (see Section 5.3.1), a single Gaussian term for the phonon absorption of ITO around 0.05 eV [168,342,355] and a Tauc-Lorentz term that describes the interband absorption [354]. A high frequency permittivity, ε_∞, is used to describe the influence of the absorption at photon energies larger than the measured range $(0.034 - 5.0\ \mathrm{eV})$. The surface layer comprises a linearly graded effective medium approximation (EMA) of the layer below and air with a single characteristic "surface" carrier species, as outlined in Section 4.2.3. Vitally, the use of a two-layer, two-carrier species model removes the requirement for an additional Gaussian peak at ~ 0.2 eV, as was observed when considering ideal films only during optical modelling Section 4.2.1, and as has been reported previously [354].

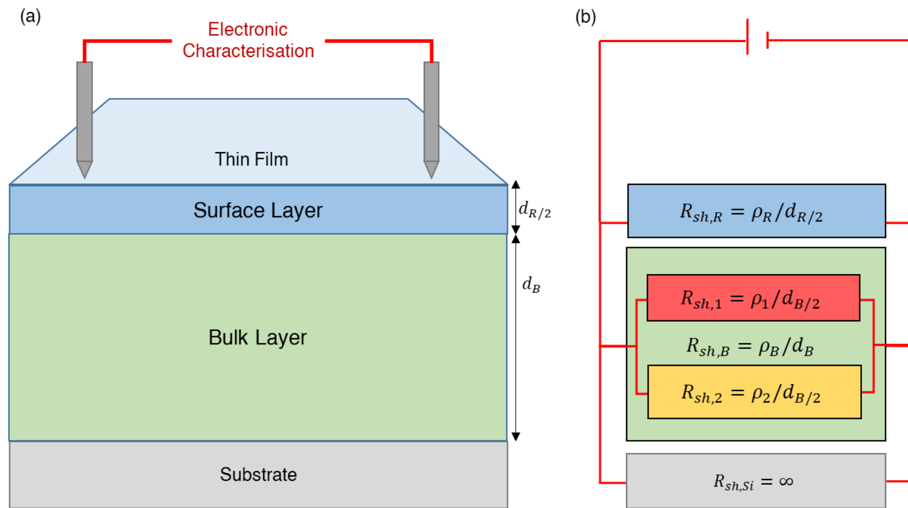

Fig. 6-1. Schematic illustration for electronic characterisation of a multilayer material: (a) the film geometry comprising a surface layer (blue slab), bulk layer (green slab) and a substrate (grey slab) measured with two current injecting probes (grey needles). (b) A model for the carrier transport where each layer is described by a resistor with a resistance, $R_{sh,j} = \rho_j d_j$. The bulk film itself can also be described by two parallel resistors (with $d_j = d_{B/2} = d_B/2$ for the 1^{st} (red rectangle) and 2^{nd} (yellow rectangle) carrier species.

The model extracts distinct values for the optical resistivity and mean free time for the two bulk and the surface layer carrier species. To compare the optical and DC resistivities it is necessary to "combine" the carrier species so that a "combined" optical resistivity and mean free time, ρ_{opt} and τ_{opt} respectively, can be calculated. To calculate ρ_{opt}, an approach is

followed that represents each carrier species as resistors in a parallel circuit in order to map the interaction of the current probes and the sample during a measurement of the resistivity. This model has been used previously to analyse Hall effect data for multilayer semiconductor structures with step-changed conductivity [378] and is shown schematically in Fig. 6-1.

As the sheet resistance for each layer, $R_{sh,j}$, is defined by the layer resistivity, ρ_l, and thickness, d_l, (where the subscript $l = B, R$ denotes the layer) it follows that Ohm's law for parallel circuits Eq. (6-1) can be used to calculate ρ_{opt} directly from the resistivity of the bulk and surface layers (ρ_B and ρ_R, respectively; Eq. (6-2)).

$$\frac{1}{R_{opt}} = \frac{1}{R_{sh,B}} + \frac{1}{R_{sh,R}} \tag{6-1}$$

$$\rho_{opt} = \frac{d_{B+R}}{\frac{d_B}{\rho_B} + \frac{d_R}{\rho_R}} \tag{6-2}$$

where $R_{sh,opt}$ is the "combined" sheet resistance and $R_{sh,B}$ and $R_{sh,R/2}$ are the sheet resistances of the bulk and surface, respectively. The optical carrier concentration, N_{opt}, is calculated by performing a summation of the number of carriers ($N_l d_l$, where the subscript l denotes the layer) in both layers the film, divided by the total thickness, $d_{B+R} = d_B + d_{R/2}$ (Eq. (6-3)). A surface layer thickness of $d_{R/2} = d_R/2$ is used to account for the fact that half the surface layer is air. The effective electron mass, $m_e^*(N)$, is determined for each sample by considering an increased non-parabolicity in the conduction band due to free carrier population [118], as outlined in Section 4.2.4.. The Hall Effect carrier concentration, N_{Hall}, is used to calculate the effective mass predicted from the trend of $m_e^*(N_{Hall})$ (Eq. (4-4)) for ITO (Table 4-6):

$$N_{opt} = N_B \mathrm{N_B} \frac{d_B}{d_{B+R}} + N_R \frac{d_{R/2}}{d_{B+R}} \frac{d_{R/2}}{d_{B+R}} = \frac{m_e^*}{e^2} \left(\frac{d_B}{\rho_B \tau_B} + \frac{d_{R/2}}{\rho_R \tau_R} \right) \cdot \frac{1}{d_{B+R}} \tag{6-3}$$

Performing this calculation requires an assumption that m_e^* is the same for each layer. τ_{opt} can then be back calculated from N_{opt} and ρ_{opt} *via* Eq. (6-4).

$$\tau_{opt} = \frac{\tau_B \tau_R (\rho_R d_B + \rho_B d_R)}{d_B \rho_R \tau_R + \frac{d_R}{2} \rho_B \tau_B} = \tau_B \left(\frac{N_B d_B}{d_{B+R}} \right) + \tau_R \left(\frac{N_R d_R}{d_{B+R}} \right) \tag{6-4}$$

Eq. (6-4) is be expressed in terms of ρ_j and τ_j only so that τ_B can be calculated without an assumption of m_e^*. Furthermore, Eq. (6-4) is an identical expression to if a weighted average of τ_B and τ_R is performed, where the weighting is defined by the total number of carriers in each layer. In this model, the bulk layer can also be thought of as an additional parallel circuit comprising one resistor for each charge species where $d_1 = d_2 = d_B/2$ (Fig. 6-1c), so that the bulk layer resistivity, ρ_B, carrier concentration, N_B, and mean free time, τ_B, are accounted for by Eq. (6-5), Eq. (6-6) and Eq. (6-7), respectively.

$$\rho_B = \frac{1}{\frac{1}{\rho_1} + \frac{1}{\rho_2}} \quad (6\text{-}5)$$

$$N_B = \sum(N_{j,B}) = N_1 + N_2 = \frac{m_e^*}{e^2}\left(\frac{1}{\rho_1\tau_1} + \frac{1}{\rho_2\tau_2}\right) \quad (6\text{-}6)$$

$$\tau_B = \sum\left(\tau_j \frac{N_j}{N_B}\right) = \tau_1 \frac{N_1}{N_B} + \tau_2 \frac{N_2}{N_B} = \frac{\tau_1\tau_2(\rho_1 + \rho_2)}{\rho_1\tau_1 + \rho_2\tau_2} \quad (6\text{-}7)$$

Comparing optical and DC Carrier transport of ITO

In order to see the full picture of the transport properties of each seed and laser processed film, Fig. 6-2 presents the optical (red squares) and Hall (green dots) (a) resistivity, and (b) carrier concentration for the seed optimised ITO films (star symbols with corresponding technique colour) and those subject to single-pulse ReLA in 100 psig of pure Ar with increasing fluence at $50 - 325\ \mathrm{mJcm^{-2}}$. For ρ (Fig. 6-2a), the results from 4pp are presented with the blue triangles. The 3 seed films that are presented are those that were covering the range of N_{opt} for the pre-processed wafelets.

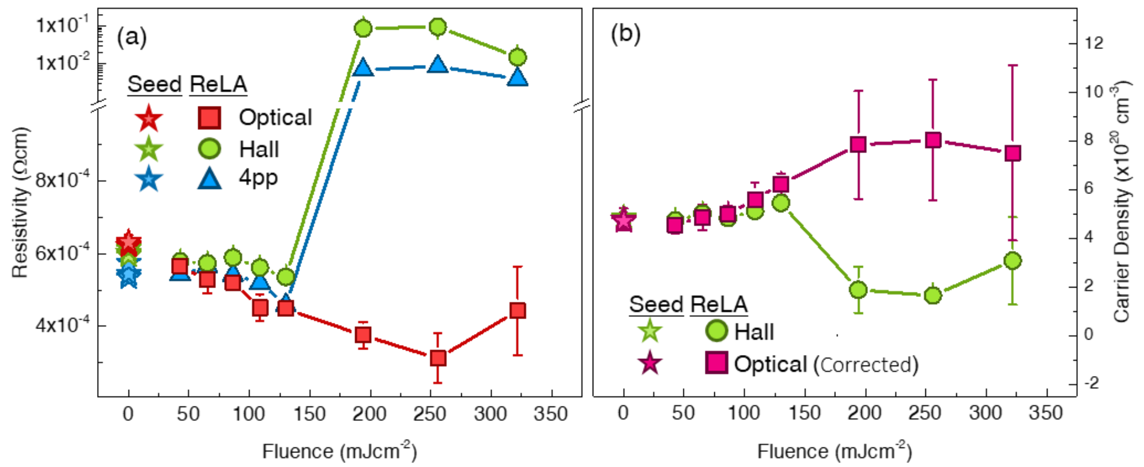

Fig. 6-2. Optoelectronic properties of the ITO films annealed with varied laser fluence, J_L. The Hall (green dots) and optical (red squares) (a) resistivity, ρ, and (b) carrier concentration, N, for the optimised ITO films subject to single-pulse laser annealing (LA) in 100 psig of pure Ar with increasing fluence at $50 - 325\ \mathrm{mJcm^{-2}}$. In (a), the blue triangles indicate the 4pp results. The green and red star symbols indicate Hall and optical values, respectively, for the 3 seed films that cover the range of N_{opt} for the pre-processed wafelets. Note the change in scale in (a) at $10^{-3}\ \Omega\mathrm{cm}$.

It is observed in Fig. 6-2a that annealing with a single pulse reduced ρ_{opt}, ρ_{Hall} and ρ_{4pp} of the ITO thin films as J_L was increased from $40\ \mathrm{mJcm^{-2}}$ to $130\ \mathrm{mJcm^{-2}}$ and the optical resistivity is reduced by $\sim 20\%$ at $130\ \mathrm{mJcm^{-2}}$ to a value of $(4.5 \pm 0.2) \times 10^{-4}\ \Omega\mathrm{cm}$. From Fig. 6-2b it is noted that the reduction in ρ below $130\ \mathrm{mJcm^{-2}}$ can attributed mainly to a rise in N from $(4.7 \pm 0.2) \times 10^{20}\ \mathrm{cm^{-3}}$ for the seed film to $(6.2 \pm 0.4) \times 10^{20}\ \mathrm{cm^{-3}}$ for the film

processed at $130\ \mathrm{mJcm^{-2}}$. This mirrors the case found for annealing of ITO in $5\%\ \mathrm{H_2}$ in $\mathrm{N_2}$ and $\mathrm{O_2}$ in Chapter 5. Therefore, the increase in N for ITO laser annealed at $40 - 130\ \mathrm{mJcm^{-2}}$ is attributed to an increase in the oxygen vacancy concentration and Sn dopant activation. When the J_L was increased above $130\ \mathrm{mJcm^{-2}}$, the change in the carrier transport properties with J_L was more erratic, with much larger errors. The optical resistivity continues to decrease with increasing J_L, with a minimum ρ_{opt} of $(3.1 \pm 0.7) \times 10^{-4}\ \Omega\mathrm{cm}$ and maximum N_{opt} of $(8 \pm 2) \times 10^{20}\ \mathrm{cm^{-3}}$ at $260\ \mathrm{mJcm^{-2}}$. The significant decrease in ρ_{opt} and increase in N_{opt} is also reflected in the IRT data (which effectively "averages" the free carrier absorption throughout the film) by the significantly diminished IR transmittance, T_{IR}, at lower photon energy, E. However, The DC resistivity as measured independently by 4pp and Hall Effect ascertain that the resistivity is vastly increased ($\times\ 10^2 - 10^3$) when $J_L > 130\ \mathrm{mJcm^{-2}}$. Hall Effect measurements reveal that this is due to both a significant reduction in both N_{Hall} and μ_{Hall}. Thus, Hall Effect and optical measurements of N disagree for the films annealed at $\geq 130\ \mathrm{mJcm^{-2}}$. This observation indicates that the film might have been damaged due to laser induced ablation effects, as has been reported elsewhere [59,66]. However, visual inspection of the laser processed films does not reveal any clear marks of such damage. Therefore, a further investigation into the optoelectronic properties of the films annealed at $> 130\ \mathrm{mJcm^{-2}}$ is warranted and follows.

Additional Film properties – Elucidating the nature of the "damaged" films.

Fig. 6-3 presents the (a) optical band gap, E_G, and (b) % inhomogeneity for the seed ITO films (star symbols) and those annealed with increasing J_L from $40\ \mathrm{mJcm^{-2}}$ to $320\ \mathrm{mJcm^{-2}}$. The % inhomogeneity is defined here as the % difference in $\tilde{\varepsilon}(E)$ between the bottom and top of the bulk layer. In Fig. 6-3a, a significant increase in E_G is observed for $J_L > 130\ \mathrm{mJcm^{-2}}$, as can be expected from a Burstein Moss shift due to the steadily increased N_{opt}. This suggest that the picture of a dramatically increased N, as extracted from IRSE data, is more realistic as the increase of E_G can again be explained through a Burstein Moss shift [182]. Therefore, Hall Effect and DC resistivity measurements have failed for films annealed at $\geq 130\ \mathrm{mJcm^{-2}}$, indicating the film structure may have been severely altered. From Fig. 6-3 it is observed that the bulk layer inhomogeneity remains at low and negative values up to $130\ \mathrm{mJcm^{-2}}$ but increases significantly for the films annealed at higher J_L. The negative values indicate that the optical absorption of the film is lower at the top of the film. The lower optical absorption likely arises from fewer carriers and/or a higher μ closer to the surface of the film, as seen optically and by EDX for the ITO films in Chapter 5. For $J_L > 200\ \mathrm{mJcm^{-2}}$, the inhomogeneity becomes positive (higher absorption towards the surface) and significantly (up to $\sim 90\%$ at $260\ \mathrm{mJcm^{-2}}$.

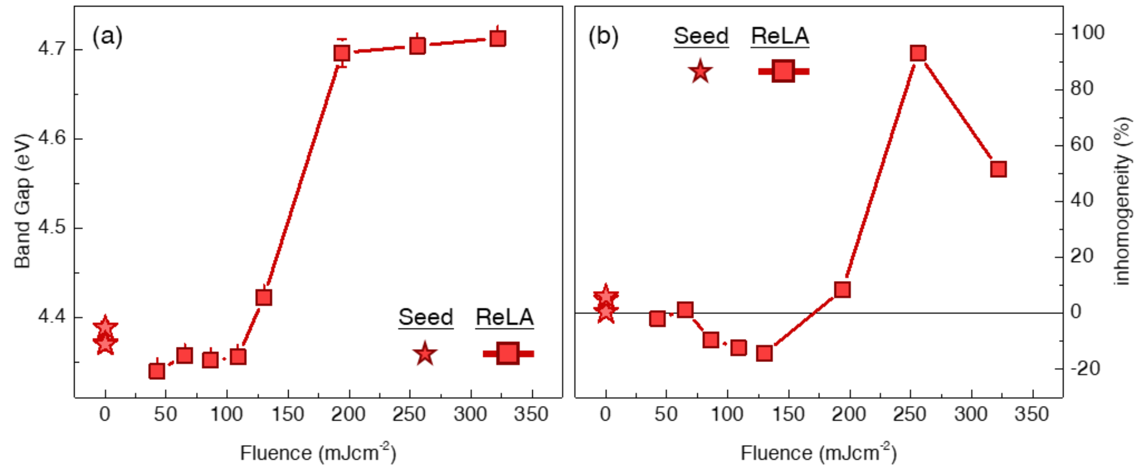

Fig. 6-3. (a) Band gap, E_G, and (b) percent inhomogeneity for the seed (red stars) optimised ITO films and those subject to single-pulse laser annealing (LA) in 100 psig of pure Ar with increasing fluence, J_L, at $50 - 325\ \mathrm{mJcm^{-2}}$ (red squares).

As mentioned above, previous reports that have utilised DC measurements of ρ_{4pp} and ρ_{VdP} have noted that damage to the film has occurred in the form of ablation [59,66]. This ablation is attributed to the high energy density delivered to the samples causing a rapid thermal expansion of the upper layers of the film [381,382]. This is reflected by how the total thickness, d_{Tot}, is increased when $J_L \geq 260\ \mathrm{mJcm^{-2}}$, despite a trend of steadily reducing d_{Tot} for lower J_L. The decreasing J_L between $40 - 130\ \mathrm{mJcm^{-2}}$ can be explained by an increase in the film density as the atomic structure is rearranged into a more energetically favourable structure during LA. This can arise from the reduction of oxygen interstitials and un-activated Sn dopants which act to increase the local lattice spacing (Fig. 5-15). At larger J_L the energy density is high enough to result in rapid thermal expansion of the upper layer manifesting as film ablation [59,66].

Carrier Species Transport properties

Further intuition for the modulation of the carrier transport mechanisms with LA with increasing fluence can be garnered from investigating the individual carrier species within the ITO film (ρ_j, N_j and μ_j). It must be noted that usually N_{Hall} is used to determine $m_e^*(N_{Hall})$ for the calculation of the combined transport properties. However, Hall Effect is unable to distinguish between the two carrier species. Therefore, a constant effective mass of $0.35\ m_e$ is used to calculate and present N and μ for each carrier species [361]. Fig. 6-4 presents ρ_j for the inter-grain (red squares), intra-grain (yellow dots) and surface layer (blue diamonds) carrier species within the optimised ITO processed with a single pulse in pure Ar with increasing fluence from $50 - 325\ \mathrm{mJcm^{-2}}$. The star symbols indicate the unprocessed, seed films. The green triangles and purple hexagons present the combined "bulk" and "optical" resistivity calculated with Eqs. (6-2) and (6-5), respectively, for reference.

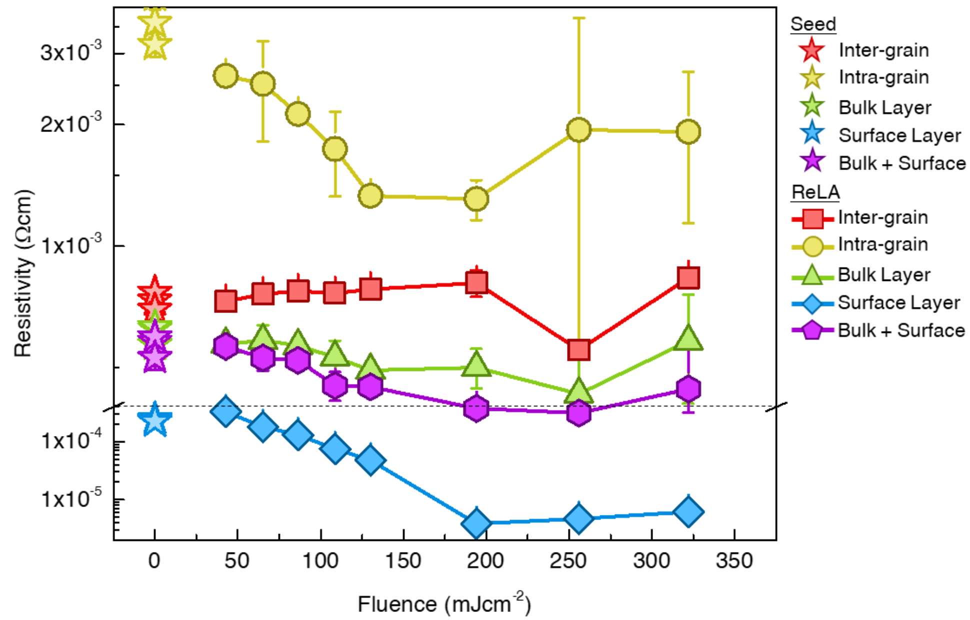

Fig. 6-4. The resistivity, ρ_j, of the individual carrier species for the seed optimised ITO films (star symbols with corresponding species colour) and those subject to single-pulse laser annealing (LA) in 100 psig of pure Ar with increasing laser fluence, J_L, at $50 - 325\ \mathrm{mJcm^{-2}}$. Specifically, the values of ρ_j are shown for the inter-grain (red squares), intra-grain (yellow dots), bulk layer (green triangles), surface layer (blue diamonds) and combined (purple hexagons) carrier species. Note the change in scale in the y-axis at $4 \times 10^{-4}\ \Omega\mathrm{cm}$.

It is seen in Fig. 6-4 that the decrease in the ρ_{opt} between $40 - 130\ \mathrm{mJcm^{-2}}$ arises primarily from a decrease in the resistivity of the intra-grain and the surface species. The resistivity of the surface layer for $J_L \geq 190\ \mathrm{mJcm^{-2}}$ is vastly decreased by a factor of ~ 100 down to $\sim 3 \times 10^{-6}\ \Omega\mathrm{cm}$. This observation gives a strong indication of why the physical measurements of the DC resistivity (4pp and Hall Effect) significantly over-estimated the resistivity and under-estimated N (Fig. 6-2). Specifically, due to the highly conductive nature of the surface layer, for the model of the current transport shown in Fig. 6-1, the current injected into the films, by the electrodes, would tend to follow the path of least resistance, through the top layer only. Ohm's law for parallel circuits [378] can be used to find that for the ITO film annealed at $190\ \mathrm{mJcm^{-2}}$, the majority of the current ($70 \pm 20\ \%$) passes through the surface layer. This means that for the film annealed at $\geq 190\ \mathrm{mJcm^{-2}}$, 4pp and Hall Effect measurements are measuring a sheet resistance, R_{sh}, that is primarily representative of the surface layer. However, the bulk thickness is generally being used to calculate the resistivity from R_{sh}, resulting in values of ρ_{4pp} and ρ_{Hall} far greater than the "real" values, as detected by IRSE and IRT measurements.

This can be further demonstrated by noting that the sheet resistance of this sample, as measured by 4pp, is $830 \pm 30\ \Omega\mathrm{cm}$. Assuming that R_{sh} is representative of the entire film

($d_{B+R} = 122.53$ nm), ρ_{4pp} is calculated to be $(9.1 \pm 0.4) \times 10^{-3}$ Ωcm (following the correction for the small sample size). This value is ~ 30 times larger than the reported ρ_{opt}. If, however, the thickness of the surface roughness layer is used then a value of $\rho_{4pp} = (2.9 \pm 0.2) \times 10^{-4}$ Ωcm is calculated instead, which is in far better agreement with the ellipsometrically determined $\rho_{opt} = (3.1 \pm 0.7) \times 10^{-4}$ Ωcm. Therefore, the existence of additional layers within the film explains the high DC resistivity and the disparity between optical and DC results. Previous reports, which relied on current-probe measurements of ρ and/or N, have identified that the films annealed at high fluences are entirely damaged due to ablation during LA [59,66]. However, the optical results indicate that the bulk and surface layer carrier transport properties *(i.e.,* below and within ablated area) may have been improved further than such techniques suggest. This may somewhat alter the conclusions of previous investigations and highlights the utility of SE to characterise the optoelectronic properties of TCOs and other materials. Despite this, the existence of multiple layers with detrimental effects in the ability to characterise the film strongly suggest detrimental effects to the films' potential for optoelectronic or plasmonic device applications. Therefore, these fluences are avoided for further laser processing.

Fig. 6-5 presents $\mu_{j/l}$ against $N_{j/l}$ for the inter-grain (red squares), intra-grain (yellow dots), surface layer (green triangles) and combined optical (blue diamonds) carrier species within the optimised ITO processed with a single pulse in 100% Ar with increasing fluence from $40 - 130$ mJcm^{-2}. The star symbols indicate the unprocessed, seed films. The fits of $\mu(N)$ to the seed films, for each carrier species, are indicated by the red, yellow, green, blue dashed lines, respectively. The films annealed above 130 mJcm^{-2} are excluded from this plot so that only the cases for the homogeneous films are considered. Finally, the solid-coloured arrows are a guide to the eye on how the transport properties of the samples translate across the $\mu(N)$ plot with increasing J_L. Such translations are discussed for each species, below.

The red squares in Fig. 6-5 represent the carrier concentration, N_1, and mobility, μ_j, for the inter-grain carrier species within the ITO films laser processed at fluences of $40 - 130$ mJcm^{-2}. N_1 is observed to increase steadily with fluence with a corresponding decrease in μ_1 so that all values lie along the $\mu_1(N_1)$ trend found for the seed films. An identical relation between J_L and the $\mu_2(N_2)$ values are observed for the second species. The translation across the $\mu(N)$ trend, as fit to the seed films, for both species strongly indicates that the increase in N_j arises from a purely compositional effect, likely from an increased activation of Sn^{4+} dopants and formation of oxygen vacancies, as was established from XPS and EDX of the optimised ITO film subject to ReLA in 5% H_2 in N_2 and O_2 (Chapter 5).

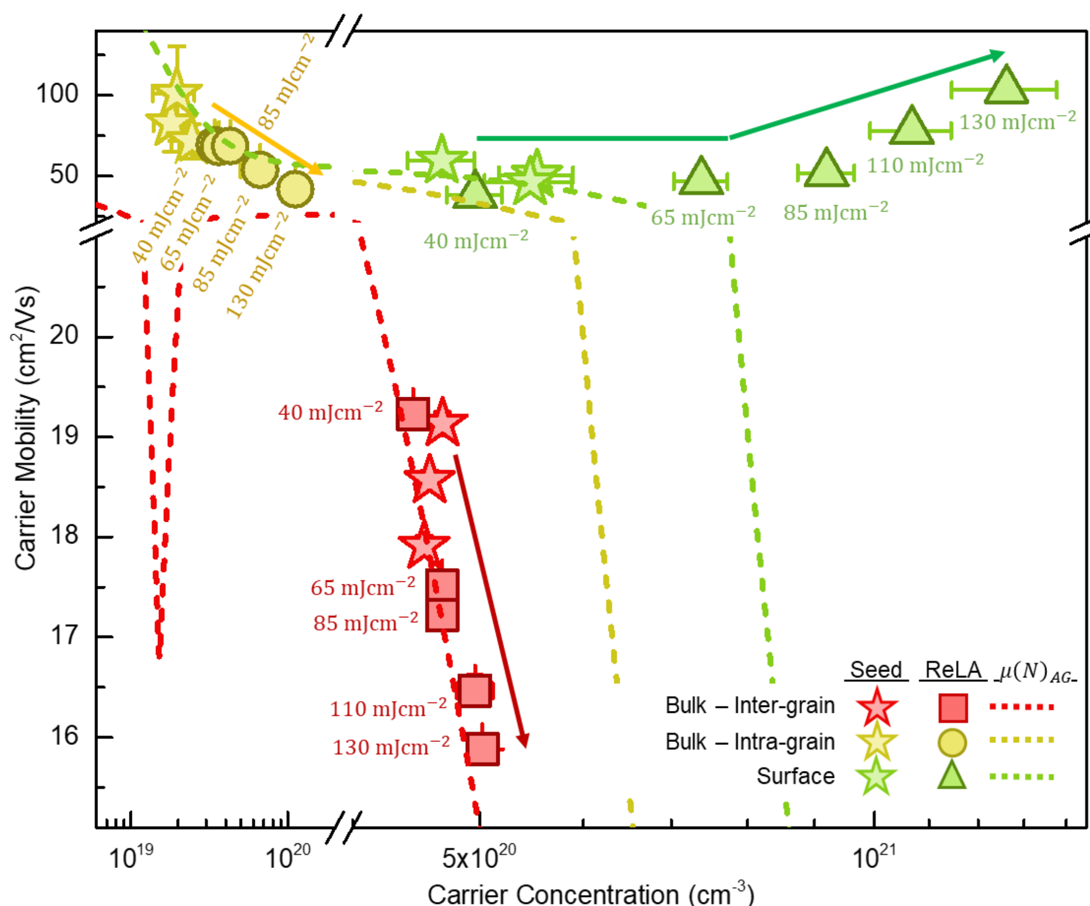

Fig. 6-5. The "optical" carrier mobility, μ_j, against the carrier concentration, N_j, of the individual carrier species, j, for the optimised ITO films subject to single-pulse laser annealing (LA) in $100\,\mathrm{psig}$ of pure Ar with increasing fluence, J_L, at $50-325\,\mathrm{mJcm^{-2}}$. Specifically, the values of resistivity, ρ_j, are shown for the inter-grain (red squares) intra-grain (yellow dots) and surface layer (green triangles) carrier species. The star symbols or each colour indicate μ_j and N_j for the seed films. The dashed lines of each colour indicate the fits of $\mu_j(N_j)$ to the entire set of seed films and the coloured arrows are a guide to the eye for how the laser processed samples translate from the seed film carrier transport properties. Note the gap and change in scale in the x-axis and the y-axis at $(2-4)\times10^{20}\,\mathrm{cm^{-3}}$ and $21\,\mathrm{cm^2/Vs}$, respectively.

The case is very different for the surface species (blue diamonds in Fig. 6-5). For laser pulses of $\leq 190\,\mathrm{mJcm^{-2}}$ an enhancement of both N_R and μ_R is observed. Furthermore, N_R is continually increased up to $(1.1\pm0.3)\times10^{22}\,\mathrm{cm^{-3}}$ at $260-330\,\mathrm{mJcm^{-2}}$ without the diminished mobility that would be expected for the increased number of ionised impurities, causing the values of $\mu_r(N_r)$ to translate away from the trend predicted for the seed films. In fact, μ_R is increased. Due to the ultra-thin nature of the surface layer ($\sim3\,\mathrm{nm}$), N_{opt} is only marginally increased from the bulk case (Eq. (6-3)). This highlights that LA has a significant effect

on the surface layer, not only manipulating its defects to increase the number of activated Sn^{4+} dopants and oxygen vacancies, but to significantly change the structure and/or density of neutral impurities ($Sn - O$ clusters and/or oxygen interstitials) resulting in a marked increase in μ_R.

The increased influence of LA on the surface of the film can be is assigned to the fact that the heat generated in the film during LA is dependent on the laser penetration depth through the processed sample, where the modification of the surface layer arises from the laser photon absorption while the rest of the film is less dramatically heated by the heat diffusion from the surface layer. The lower thermal dose to the bulk layer appears to be sufficient to activate Sn dopants and promote mobility of oxygen atoms (creating vacancies as they migrate out of the film) to increase N. However, the temperature reached appears insufficient to improve the crystal structure and/or break up the neutral impurity clusters. Furthermore, the existence of a thermal gradient between the surface layer and substrate explains the increase in the inhomogeneity across the z-axis of the film with increasing J_L (see Fig. 6-3). The thermal gradient results in a larger N near the top of the bulk layer, where the higher temperatures result in more energy for activation of Sn dopants. Furthermore, the higher peak temperature implies an increase in the length of time that the region of the sample spends hot enough to promote the mobility of atoms through the lattice. Using the model of the compositional modifications during ReLA that was developed in Chapter 5 (Fig. 5-9), this would likely result in an increase in the oxygen vacancy population as there is more time for the mobile oxygen in the film to escape into the Ar environment.

6.3. Influence of number of pulses

So far, only a single pulse has been applied. It was shown that larger fluences were not able to effectively improve the film properties and resulted in a complex geometry deemed not useful for optoelectronic or plasmonics applications. To demonstrate if the properties of ITO can be further enhanced, and to potentially improve the depth uniformity, it is necessary to focus the efforts on processing the ITO films with an increased number of pulses. An additional selection of wafelets from the "UMBReLA" ITO film (see Table 4-1) were subjected to ultrafast ($10\ \mathrm{Hz}$), multi-beat LA in pressured ($100\ \mathrm{psig}$) environment of pure Ar with $J_L = 100\ \mathrm{mJcm^{-2}}$ using a $\times 1$ projection lens with a spot size of $\sim(15.5 \times 15.5\ )\ \mathrm{mm^2}$ at the sample surface, entirely covering the $\sim(8 \times 8\ )\ \mathrm{mm^2}$ wafelets ensuring a uniform annealing across the dimensions of the wafelet. The films were processed with 1, 5, 10, 50, 100, 500, 1000 and 5000 pulses. On the first attempt, the films were annealed at the "optimal" J_L of $130\ \mathrm{mJcm^{-2}}$, found in Section 6.2, above, to provide the greatest increase in N without introducing a complex structure/geometry that interferes with DC measurements of the resistivity. However, damage, in the form of a complex geometry explored above, to the film occurred with only 5 laser pulses. Therefore, a lower J_L of $102 \pm 4\ \mathrm{mJcm^{-2}}$ (referred to henceforth as $100\ \mathrm{mJcm^{-2}}$) was utilised instead to promote a less intense LA treatment over a greater period in an attempt to more uniformly improve the film properties. After laser processing, the films were characterised with 4pp, Hall Effect, IRT, ORS and IRSE. This section investigates the effect of the number of laser pulses on the resulting optoelectronic and structural properties.

Optical Modelling of ITO

The model that was near-identical to fit the optical data ($\Psi(E)$, $\Delta(E)$, $T_{IR}(E)$ and $R_{VIS}(E)$) of the previous section, enabling extraction of the geometric features of the film, the parameters describing the phonon and interband absorption (A_n, Γ_n and $E_{0,\mathrm{n}}$, where n denotes the oscillator) and ρ_j and τ_j for each carrier species ($j = 1$, $j = 2$ and $j = R$ for the 1^{st} bulk, 2^{nd} bulk and surface layer carrier species, respectively). To reflect the detection of a z-axis inhomogeneity in the transport properties of the laser processed ITO films, a gradient was more rigorously applied within the model using Eq. (5-1) and Eq. (5-2). As before, ρ_{opt}, τ_{opt} and N_{opt} (*i.e.* the "combined" transport properties for the entire system) are calculated from Eq. (6-2) to Eq. (6-7) in order to better compare optical, 4pp and Hall Effect measurements.

Comparing optical and DC carrier transport

Fig. 6-6 presents the Hall (green dots) and optical (red squares) (a) resistivity and (b) carrier concentration for the seed optimised ITO films (star symbols with corresponding technique colour) and those subject to multi-pulse LA at $100\ \mathrm{mJcm^{-2}}$ in $100\ \mathrm{psig}$ of pure Ar with

increasing number of pulses from $1 - 5000$. The 3 seed films that are presented are those that were covering the range of N_{opt} for the laser annealed wafelets, prior to processing. It is observed in Fig. 6-6a that annealing with a single pulse reduced ρ_{opt} and ρ_{Hall} and ρ_{4pp} of the ITO thin films with an increasing number of pulses. ρ_{opt} is reduced by $\sim 50\%$ at 5000 pulses to a value of $(3.0 \pm 0.5) \times 10^{-4}\ \Omega\text{cm}$. From Fig. 6-6b it is noted that the reduction in the resistivity can again be primarily attributed to a steady rise in the carrier concentration from $(4.9 \pm 0.4) \times 10^{20}\ \text{cm}^{-3}$ for the seed films to $(13 \pm 0.4) \times 10^{20}\ \text{cm}^{-3}$ for the film processed at 5000 pulses. The trends in ρ_{opt} and N_{opt} agree very well with the results from Hall Effect.

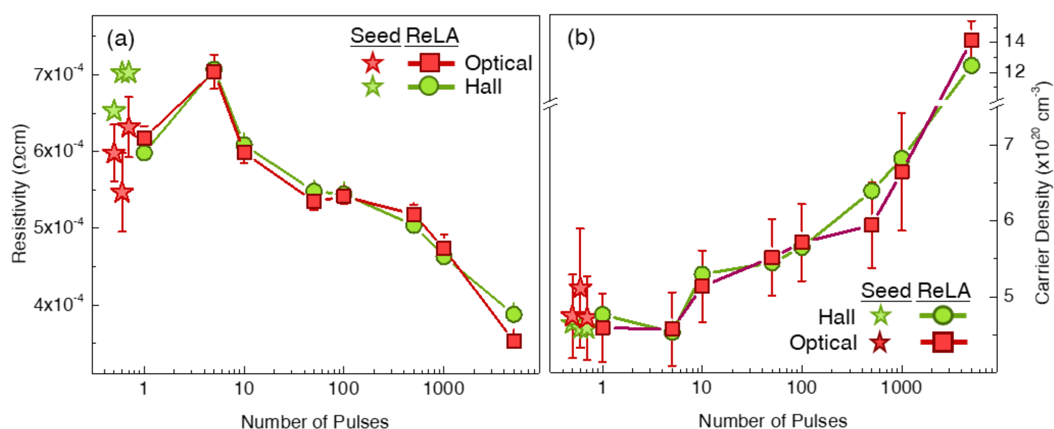

Fig. 6-6. Optoelectronic properties of the ITO films annealed with varied number of laser pulses. The Hall (green dots) and optical (red squares) (a) resistivity, ρ, and (b) carrier concentration, N, for the optimised ITO films subject to $1 - 5000$ laser pulses in 100 psig of pure Ar with a laser fluence, J_L, of $100\ \text{mJcm}^{-2}$. The green and red stars indicate Hall and optical values, respectively, for the 3 seed films that cover the range of N_{opt} for the pre-processed wafelets. Note the logarithmic scale in the x-axis and the change in scale in the y-axs of (b) at $8 \times 10^{20}\ \text{cm}^{-3}$.

As before, deeper understanding of the modulation of the carrier transport mechanisms with LA with increasing number of pulses is found by examining the individual optical carrier species within the ITO film (ρ_j, N_j and μ_j). Fig. 6-7a presents the optical resistivity and for the inter-grain (red squares), intra-grain (yellow dots) and surface layer (green triangles) carrier species within the optimised ITO processed in 100% Ar with a fluence of $100\ \text{mJcm}^{-2}$ with an increasing number of pulses from $1 - 5000$. Fig. 6-7b presents the carrier mobility against the concentration for the equivalent data points in (a), where the labels indicate the number of pulses. In both (a) and (b), the star symbols indicate the unprocessed, seed films. The blue diamonds present the combined “optical” values, for reference. The fits of $\mu(N)$ to the seed films, for each carrier species, are indicated by the red, yellow, green, and blue dashed lines, respectively, in Fig. 6-7b. Finally, the coloured arrows are a guide to the eye to how the transport properties of the samples translate across the $\mu(N)$ plot with increasing laser fluence.

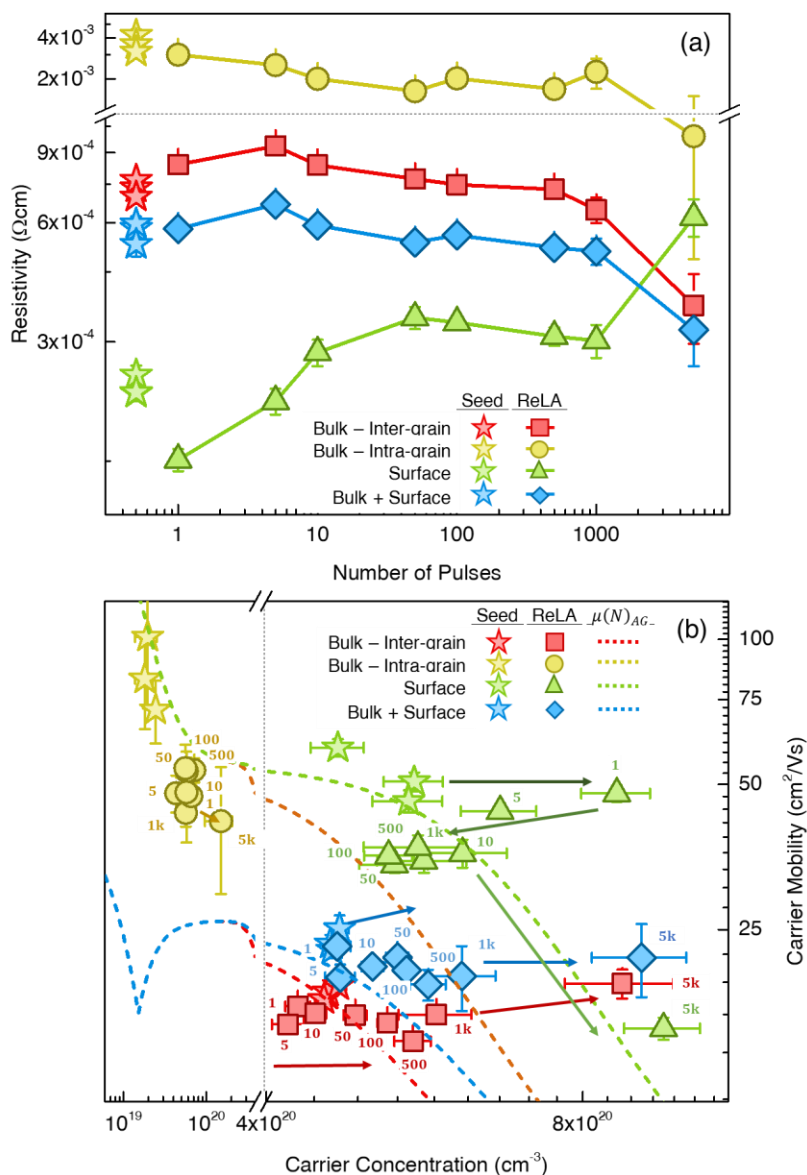

Fig. 6-7. (a) The "optical" resistivity, ρ_j, against the number of pulses and (b) the optical carrier mobility, μ_j, against the carrier concentration, N_j, of the individual carrier species, j, for the optimised ITO films subject to $1 - 5000$ laser pulses in 100 psig of pure Ar with a fluence, J_L, of $100\ \mathrm{mJcm^{-2}}$. Specifically, the values of resistivity are shown for the inter-grain (red squares), intra-grain (yellow dots), bulk layer (green triangles), surface layer (blue diamonds) and combined (purple hexagons) carrier species. The star symbols or each colour indicate μ_j and N_j for the seed films. The dashed lines of each colour indicate the fits of $\mu_j(N_j)$ to the entire set of seed films and the coloured arrows are a guide to the eye for how the laser processed samples translate from the trends found for the seed films. Note the changes in scale in the y-axis in (a) at $1.1 \times 10^{-3}\ \Omega\mathrm{cm}$ and in the x-axis of (b) at $4 \times 10^{20}\ \mathrm{cm^{-3}}$.

In opposition to the films annealed with increasing fluence, the modulation of the combined optical resistivity, in this case, is dominated by a change in the bulk, inter-grain species, owing to the much larger sheet carrier concentration ($N_{sh,j} = N_j d_j$) of the 1^{st} (inter-grain) carrier species. The change of the 2^{nd} (intra-grain) charge species is less significant than that observed for increasing fluence. However, a general trend of decreasing resistivity is observed for both the bulk species. In Fig. 6-7b, it is demonstrated that the resistivity reduction is a result of the simultaneous enhancement of both the carrier concentration and mobility. The increase of the carrier concentration can be explained using the model developed in Section 5.2.4 (Fig. 5-9): a larger number of pulses increases the annealing time, where the temperature is high enough to permit the mobility of oxygen vacancies. As before, this results in an increased carrier concentration as oxygen has escapes into the ambient. While the absolute values of the mobility for each charge species remain relatively constant, an apparent improvement in the mobility relative to carrier concentration is increased. This manifest as the translation to a much larger N off the line of predicted $\mu(N)$ for the inter-grain and combined species without a significant loss in μ as would be expected from ionised cluster scattering (ICS). This translation is indicated with the red and blue arrows in Fig. 6-7b.

A significant change in the film is observed for the film annealed with 5000 pulses. Specifically, the resistivity of the inter-grain and intra-grain carrier species is significantly lower than the films annealed at lower number of pulses. From Fig. 6-7b it is noted that the reduction in resistivity is primarily a result of an increase in N_1 from $(5.2 \pm 0.4) \times 10^{20}\ \mathrm{cm}^{-3}$ (for the film annealed with 1000 pulses) to $(9 + 2) \times 10^{20}\ \mathrm{cm}^{-3}$. It should be noted that the jump in N_1 and N_{opt} between 1000 and 5000 pulses is unusual. This is because the energy dose of each pulse is identical and the relatively low repetition rate ($10\ \mathrm{Hz}$) compared to laser pulse length ($25\ \mathrm{ns}$) implies that the film has effectively cooled between each pulse. Therefore, any thermally induced modifications to the film should be gradual with the number of pulses. Instead, there is a critical number of pulses where the steady modulation of the carrier transport properties is interrupted and a more significant change to the film is induced. The exact mechanism which causes this critical point is currently unknown and requires further investigation.

However, it is possible that the cooling rate is just low enough that some residual thermal energy remains in the film at the time of the next pulse. Eventually, at a critical number of pulses, the peak temperature would be more comparable to if a larger fluence was used for each pulse and would enable additional modifications to the film. Alternatively, the changes to the optoelectronic properties film after each pulse could modify the precise nature of the laser absorption heating process for the subsequent pulses. These possibilities could be tested by

solving the 1D heat transport equation [61] in order to extract the cooling rate and peak temperature across the film for a single pulse to find the thermal energy in the system at the time of the second pulse. For a single pulse there is a reduction in the resistivity of the surface layer due to a large increase in N_R (dark green arrow in Fig. 6-7b). For $5-100$ pulses, the resistivity increases beyond that of the seed films as both N_R is reduced back down to $(5.2 \pm 0.3) \times 10^{20}\ \mathrm{cm}^{-3}$ (green arrow in Fig. 6-7b). At $500-1000$ pulses, the trend is reversed again as N_R slightly increases to $(5.7 \pm 0.5) \times 10^{20}\ \mathrm{cm}^{-3}$. Vitally, the resistivity of the surface layer approaches the resistivity of the bulk film, indicating that the total film uniformity has improved. To analyse the film uniformity further, it is useful to examine the gradient of the carrier concentration across the bulk layer of the ITO film. $N_1(z)$ is calculated from in $\rho_1(z)$ and $\tau_1(z)$ and presented as a function of the distance from the substrate, z, in Fig. 6-8 for the optimised ITO films laser processed $1-5000$ number of pulses (red-purple line).

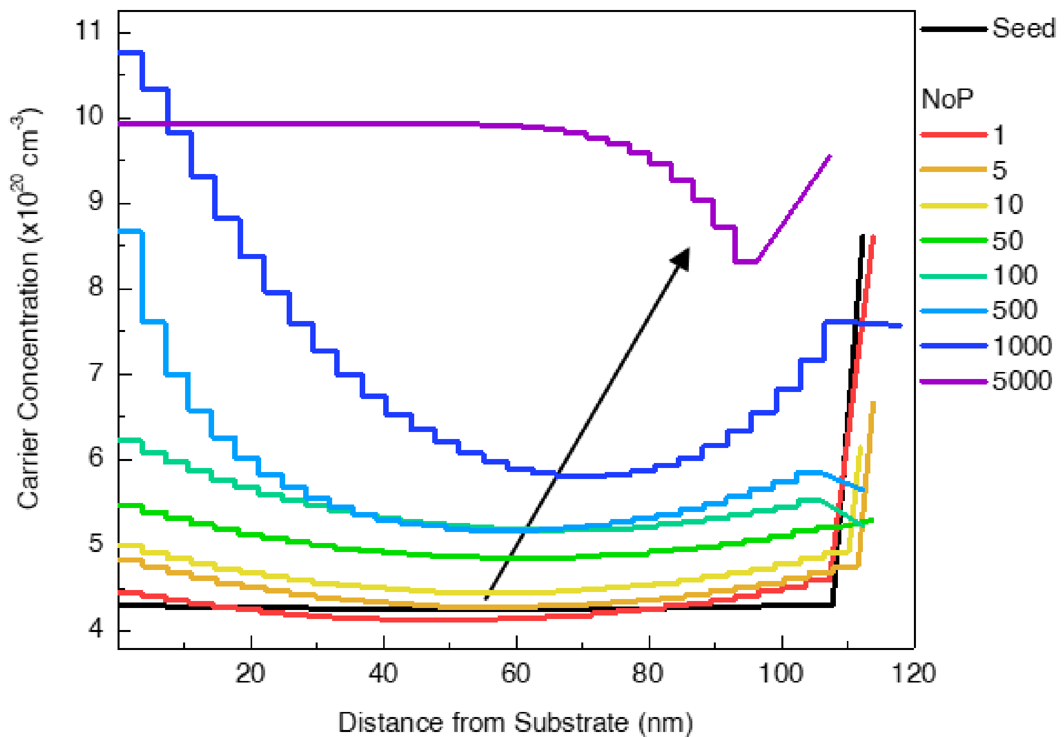

Fig. 6-8. Gradient of the inter-grain species carrier concentration, N_1, as a function of the distance from the ITO/Si interface, z, for the seed optimised ITO film (black line) and those subject to 1 (red line), 5 (orange line), 10 (yellow line), 50 (green line), 100 (turquoise line), 500 (light blue line), 1000 (blue line) and 5000 (purple line) laser pulses in 100 psig of pure Ar with a fluence, J_L, of $100\ \mathrm{mJcm}^{-2}$. The black arrows indicate the shift of the "dip" in N_1 to higher up in the film with an increasing number of pulses.

The film annealed with a single pulse has an increased $N_1(z)$ both at the bottom and the top of the bulk layer. This results in a "dip" in $N_1(z)$ near the centre of the film, as was seen for the films annealed at $100\ \mathrm{mJcm^{-2}}$ in 5% $\mathrm{H_2}$ in $\mathrm{N_2}$ and $\mathrm{O_2}$ in Fig. 5-8. This dip was stated to arise from how due to the short annealing time, the oxygen pulled from the bottom of the film had only just reached the middle, filling the vacancies and reducing N_1. The increase in the average $N_1(z)$ can also be ascribed to the activation of $\mathrm{Sn^{4+}}$ dopants (Section 5.2.4). Further pulses up to 100 pulses act to increase the average carrier concentration across the film, as was observed in Fig. 6-7. The film inhomogeneity is largely constant between $1 - 100$ pulses, but the "dip" in $N_1(z)$ is shifted to a slightly higher position within the film with each new step in the number of pulses. This minor change in the uniformity and dip position suggest that, for the relatively low fluence of $100\ \mathrm{mJcm^{-2}}$, the process of the oxygen vacancy migration (Fig. 5-9) is relatively weak and that the activation of $\mathrm{Sn^{4+}}$ dominates the creation of oxygen vacancies.

At $500 - 1000$ pulses, however, the inhomogeneity is greater as $N_1(z)$ at the bottom and top regions of the film significantly increases. At 5000 pulses, $N_1(z)$ in most of the film (from $0\% - {\sim}70\%$) remains nearly constant at ${\sim}9.5 \times 10^{20}\ \mathrm{cm^{-3}}$. Therefore, an equilibrium of the oxygen vacancy density is reached up to ${\sim}70\%$ of the film thickness. The dip in $N_1(z)$ is shifted all the way to the surface of the film, as can be expected from the longer annealing time for the oxygen atoms from the bottom to be pulled out of the surface. This is supported by how the carrier concentration at the bottom of the film slowly approaches a maximum of ${\sim}10^{21}\ \mathrm{cm^{-3}}$ between $500 - 1000$ pulses. This maximum represents that all the available Sn atoms are activated as $\mathrm{Sn^{4+}}$ and that no more oxygen vacancies can be created.

It should be noted that these conclusions are, presently, speculative. However, they could be experimentally verified by investigating the X-ray photoelectron spectra across the entire depth of the seed and laser processed ITO films. Therefore, one could corroborate the existence of the critical number of pulse thresholds for the activation of interstitial Sn ($>$ 1 pulse) and the enhancement of oxygen atom migration ($500 - 1000$ pulses). Furthermore, a more detailed understanding of the thermal and pressure gradients within the film during LA could re-enforce the model of oxygen mobility presented schematically in Fig. 5-9. Finally, if multiple phases of compositional changes are due to the residual heat in the film at the time of the next pulse, the critical number of pulses would depend on the repetition rate. Therefore, an investigation of the effect of the repetition rate on $N_1(z)$ is warranted.

6.4. Influence of ReLA ambient composition

So far in this chapter, the laser processing of the optimised film has occurred in a non-reactive ambient environment of pure Ar. However, Chapter 5 demonstrated that for a single pulse, the use of reactive ambient environments enables one to modulate N. This process was designated as "Reactive LA" (ReLA). However, for single pulse ReLA the overall change in N was small and increased even in pure $\mathrm{O_2}$ environments. In was noted that this was due to activation of Sn dopants within the film and that with increased pulses one may complete the Sn activation and allow for further manipulation of the oxygen vacancies by the reactive environments to further increase, or potentially decrease, N. The competition of Sn activation, a more intense modulation of the oxygen stoichiometry throughout the film and a more uniform distribution of N throughout the film was, indeed, found to occur when annealing in Ar with 5000 pulses in the previous section. Here forth, the process of performing multi pulse (or beat) reactive laser annealing is designated as "ultrafast multi-beat reactive laser annealing" or UMBReLA. To elucidate the role of the ambient environment further, a further investigation utilising various mixtures of reactive (and non-reactive) gasses within the pressure cell. An additional selection of wafelets from the optimised "UMBReLA set" ITO film (ITO-56) were subjected to ultrafast ($10\ \mathrm{Hz}$), multi-beat LA in pressured ($100\ \mathrm{psig}$) environment of $5\%\ \mathrm{H_2}$ in $\mathrm{N_2}$, pure $\mathrm{N_2}$, pure Ar, $5\%\ \mathrm{O_2}$ in Ar and $20-100\%\ \mathrm{O_2}$ in Ar with 5000 laser pulses at a fluence of $100\ \mathrm{mJcm^{-2}}$.

Fig. 6-9 presents the optical (red squares) and Hall (green dots) (a) resistivity, (b) carrier density and (c) carrier mobility for the seed optimised ITO films (star symbols with corresponding technique colour) and those subject to UMBReLA in a pressured ($100\ \mathrm{psig}$) environment of $5\%\ \mathrm{H_2}$ in $\mathrm{N_2}$, pure $\mathrm{N_2}$, pure Ar, $5\%\ \mathrm{O_2}$ in Ar and $20-100\%\ \mathrm{O_2}$ in Ar with 5000 laser pulses at a fluence of $100\ \mathrm{mJcm^{-2}}$. For ρ (Fig. 6-9a), the results from 4pp are presented with the blue triangles. The 3 seed films that are presented are those that were covering the range of N_{opt} for the laser annealed wafelets, prior to processing. It is observed (Fig. 6-9) that there is a clear dependence of ρ_{opt}, N_{opt}, μ_{opt} on the ambient environment. Specifically, the largest optical resistivity is found when performing ReLA into an environment of 60% oxygen and is decreased for lower and higher oxygen partial pressures. The greatest reduction in the resistivity is found when processing the ITO films in pure $\mathrm{N_2}$. This trend is found in Hall Effect, optical and 4pp measurements. However, the absolute values of ρ disagree between measurements. This likely arises from the complicated structure of the laser processed films [378].

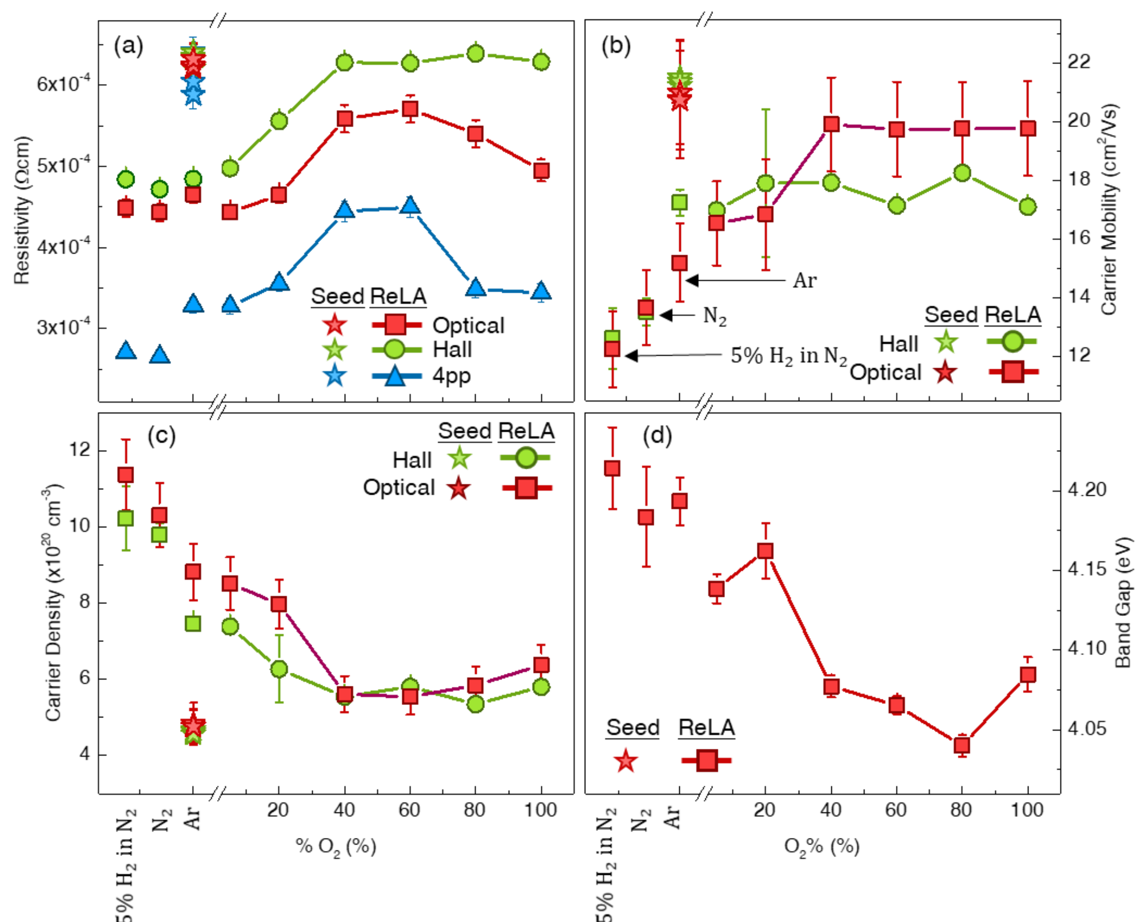

Fig. 6-9. Optoelectronic properties of the ITO films annealed in varied ambient environments. The Hall (green dots with green line) and optical (red squares with red line) (a) resistivity, ρ, and (b) carrier mobility, μ, and (c) carrier concentration, N, for the optimised ITO films subject to 5000 laser pulses with a laser fluence, J_L, of $100\ \mathrm{mJcm^{-2}}$ into 100 psig of $5-100\%$ O_2 in Ar. The blue triangles in (a) indicate the 4pp measurements of ρ. The green, red and blue stars indicate Hall, optical and 4pp values, respectively, for the 3 seed films that cover the range of N_{opt} for the pre-processed wafelets. The unconnected symbols present the results for the films annealed in 5% H_2 in N_2, pure N_2 and pure Ar. Finally, (d) presents the optical band gap for each film, found by fitting the linear region of $(E\alpha)^2$ vs E.

The modulation of ρ cannot be primarily attributed to either a change in N or μ alone but depends on the balance between each. This is because, generally, the mobility is decreased with N due to the increased influence of ICS. In Fig. 6-9c, a smooth trend of N_{Hall} (green dots) and N_{opt} (red and purple squares for the uncorrected and corrected values) is observed with changing $O_2\%$ from $0-100\%$ (points connected by solid lines). From $5-60\%$ O_2 in Ar, there is a decrease in N with increasing $O_2\%$. This decrease is likely due to the increased $O_2\%$ changing the balance of the oxygen atom migration outlined in Fig. 5-9. Specifically, the larger

percentage of oxygen in the ambient reduces the creation of oxygen vacancies throughout the film, resulting in lower values of N. However, for ambient environments with $> 60\%$ O_2 in Ar, the trend reverses and N is slightly increased with the $O_2\%$. For such oxygen partial pressures, the mobility remains constant instead of decreasing. This indicates that the concentration of ionised clusters is reduced as these samples translate away from the trend of $\mu(N)$ predicted from ICS. However, the relatively minor increase in N_{opt} between $60 - 100\%$ O_2 in Ar indicates that there is a limit to the modulation of the oxygen vacancies with the ambient environment. If the filling of oxygen vacancies is coming from the ambient oxygen being incorporated in the film, then there is, equally, a limit to the amount that can be incorporated. Due to the likely complete activation of all Sn^{4+} after 5000 laser pulses, the existence of such a limit for oxygen incorporation means that there is always an increase in N from the seed films. Therefore, the use of an increased number of pulses was not able to overcome the activation of Sn to reduce N and therefore expand reduce the free carrier absorption further into the IR. It would be of great interest to determine if the limit for oxygen incorporation can be altered by changing the fluence. This could be elucidated by performing a further experiment using UMBReLA with 5000 pulses and $75 - 125$ $mJcm^{-2}$ in 60%, 80% and 100% O_2 in Ar. If not, the strategy of starting from an "un-optimised" film with lower N and increasing N with ReLA, as presented in Section 5.2.4, is required instead.

In addition to laser processing in $5 - 100\%$ O_2 in Ar, the films were annealed in reducing environments of pure Ar, pure N_2 and 5% H_2 in N_2. These are shown as the un-connected symbols in Fig. 6-9. As expected, the use of reducing environments further enhances N due to the increased creation of oxygen vacancies. Interestingly, the environment of pure N_2 provides a greater enhancement of N than the pure Ar environment. Moreover, the addition of 5% H_2 into the N_2 environment only slightly enhances N futher. This indicates that the N_2 environment is not entirely un-reactive but the incorporation of N_2 into the film may aid the activation of Sn, aid the creation of oxygen vacancies or the nitrogen atoms may form donor states themselves. It is also possible that the deviation of the carrier concentration between the N_2 and Ar environments is due to the lower mass of N_2. Therefore, it is apparent that the precise mechanism for the increase of N for a pure N_2 environment, is not currently understood and warrants further investigation. Finally, it is noted that the modulation of N with the ambient environment, as detailed above, is also reflected in the change in the band gap, as shown in Fig. 6-9d. This is due to the Burstein-Moss effect and may result in an enhancement in the visible transmission for the films annealed in a reducing environment [185].

6.5. Concluding Remarks

In summary, an investigation of the influence of the fluence, number of pulses and ambient environment on the laser annealing of ITO was undertaken. Firstly, laser processing of ITO was performed in $100\ \mathrm{psig}$ of Ar between $40-330\ \mathrm{mJcm^{-2}}$. The larger fluences applied (than those explored in Chapter 5) and the use of a non-reactive environment allowed for a better examination of the influence of LA on the optoelectronic properties of ITO. An optical model was developed that described the seed and laser processed ITO films, building on the knowledge gained from Chapter 4 and Chapter 5. The model consisted of multiple carrier species: 2 species representing inter-grain and intra-grain transport in a bulk layer and one species to describe the free carriers in a surface roughness layer. A process of "combining" the carrier species in a way that reflected how a current would interact with the film was laid out and used to effectively compare 4pp and Hall Effect measurements of the multilayer system with the optical results.

The ITO films subject to non-reactive LA at $\leq 130\ \mathrm{mJcm^{-2}}$ showed a great agreement with the results for ReLA in $5\%\ \mathrm{H_2}$ in $\mathrm{N_2}$ and $\mathrm{O_2}$ (Chapter 5). Specifically, there was a steady increase in N with laser fluence, which was likely due to the activation of $\mathrm{Sn^{4+}}$ dopants and increase in oxygen vacancy density within the film during LA. The ITO films laser annealed at above $130\ \mathrm{mJcm^{-2}}$ were extensively investigated in order to elucidate the precise nature of the film "damage" that occurs at high fluences. Vitally, by considering the individual carrier species alongside the calculated "optical" transport properties, it was shown that the common conception that the film is damaged at high fluences may be misleading. The carrier transport properties across the film were indeed improved, but the depth-effects of the LA process introduced a complex geometry into the film that interfere with 4pp and Hall Effect measurements. This complex geometry should be directly observable *via* transmission electron microscopy.

A greater focus was given to investigation the effect of laser fluence on each of the carrier species. N_j and μ_j for the bulk layer species, j, were found to shift across the predicted trend of $\mu(N)$ as if there was an increase in the number of clustered ionised impurities, resulting from Sn activation and formation of oxygen vacancies. The surface layer saw a dramatic increase in N and μ simultaneously. A gradient in N_1 in the bulk film was noted and it was observed that the shape of the gradient is highly dependent on the laser fluence. These results explained the processes of LA that lead to a modification of the composition of the ITO film during LA in Ar, providing a strong framework to understand the modification of the optoelectronic properties of ITO during ReLA *via* optical measurements alone.

Next, ITO films were processed at a relatively low laser fluence ($100\ \mathrm{mJcm^{-2}}$) with a range of pulses from $1 - 5000$ pulses in a pressure cell of $100\ \mathrm{psig}$ of Ar. A steady decrease in ρ was observed with increasing number of pulses. Hall and SE were in excellent agreement, indicating the films were uniform. The decrease in ρ was attributed primarily to a steady increase in the carrier concentration of the inter-grain carrier species, N_1. The dependence of $N_1(z)$ on the number of pulses was understood using the model of Sn activation and oxygen migration developed in Chapter 5. Specifically, it was found that there existed a critical number of pulses where the general trend of $N_1(z)$ changes. This indicated either that residual heat is built up between each pulse so that the "effective" fluence increases with each pulse, or that the gradual change in the properties of the laser processed film modified the heating process. It was noted that further depth-profile XPS and simulations of the thermal treatment would be necessary to gain further insights into the precise nature of the LA process with increasing pulses.

Finally, a further investigation was performed into the LA of ITO utilising various mixtures of reactive (and non-reactive) gasses within the pressure cell with many pulses (5000), in an attempt to both improve the depth-uniformity of the annealing process and enhance the modulation of N than could be achieved for a single pulse. A clear dependence of the annealing environment on the resulting optoelectronic properties was found. Specifically, there was a steady trend in increasing N with a decreasing oxygen partial pressure below $60\%\ \mathrm{O_2}$ in Ar. Interestingly, annealing at higher oxygen partial pressures did not decrease N further, indicating that there may be a limit to the oxygen incorporation during ReLA. This meant that N was always increased in relation to the seed film, and to expand the range of low-loss plasmonic responses further into the IR a strategy of starting with a low-N film is required. Annealing in reducing environments of pure Ar, $\mathrm{N_2}$ and $5\%\ \mathrm{H_2}$ in $\mathrm{N_2}$ greatly enhanced N up to $\sim 10^{21}\ \mathrm{cm^{-3}}$ ($\sim 3 \times$ higher than the seed films).

7. When ellipsometry really works

7.1. Introduction

The following section is devoted to investigating the mechanisms that produce limitations of spectroscopic ellipsometry (SE), and thus define any potential "detection limits" of infrared (IR) and near-IR-visible-ultraviolet (NIR-VIS-UV) SE. This chapter is based on the publication "When Ellipsometry Works Best – A case study with Transparent Conductive Oxides" (J. A. Hillier *et al.*, ACS Photonics) [342]. The chapter builds upon the finding of Chapter 4. It starts by building simulated data sets of SE data (Section 7.2) to expand the range of carrier concentrations experimentally achieved to investigate limitations of ellipsometry to reveal the transport properties of transparent conductive oxides (TCOs). It starts from most simple, idealised, cases and then investigates the additional complications arising from the above-mentioned knowledge of sputtered indium tin oxide (ITO), aluminium-doped zinc oxide (AZO) and gallium-doped zinc oxide (GZO) thin films. Specifically, the following sections explore the influence of the: computational limits and random noise (Section 7.3), presence of substrate and thin film thickness (Section 7.4), presence of additional oscillators within and outside the measurement range (Section 7.5) and the effect of the carrier mobility (Section 7.6) Finally, all these concepts are applied to the experimentally produced films to conclude when ellipsometry really works for the case of the TCOs (Section 7.7).

7.2. Simulating ellipsometric data

The simulations are performed in an identical manner to the modelling of SE data. Specifically, the geometric model is set up to include the substrate (with the native oxide) optical constants as well as a thin film on top, where the optical constants can be described by a generalised oscillator model. The difference is that there is no data to fit, but the parameters of the generalised oscillator model are set to their desired value for each simulation and the ellipsometric angles $\Psi(E)$ and $\Delta(E)$ are calculated by solving the matrix method for p- and s-polarised light that is incident on the surface of the material at a specified angle (Section 3.2.5).

For each "data set", two distinct simulations are performed, reflecting the ranges defined by the two individual ellipsometers ($0.034 - 0.8$ eV for the IRSE and $0.775 - 6.5$ eV for the NIR-VIS-UV SE) [353]. Both spectral ranges are simulated with 2000 steps so that the calculated MSE (which depends on the number of steps; Eq. (3-55)) can be reliably compared. This results in a step size of 0.00038319 eV and 0.0028639 eV for the IR and NIR-VIS-UV spectral ranges, respectively. All simulations are performed using 3 distinct angles of incidence: $65°$, $70°$ and $75°$.

The parameterised models used simulate the optical constants for ITO, AZO and GZO (Section 7.7) take into account the influence of the scattering mechanisms (Section 2.2.5) on carrier mobility, μ, and the influence of the non-parabolicity of the conduction band on the carrier effective mass, m_e^*, (Section 4.2.4) with the carrier concentration, N. Noise, in the form of a standard deviation of Ψ and Δ around the calculated value, can also be introduced. The noise is described by a single parameter of a noise percentage, $\%_{Noise}$; the maximum and minimum range used to generate Ψ and Δ at each photon energy and for each angle using a random number generator. $\%_{Noise}$ is defined in a way that for a sufficiently large number of data points, the standard deviation will be $\%_{Noise}/10^4$. The calculated values of Ψ and Δ are saved as a measurement file so that they can be loaded into CompleteEASE™ software and fit, just as if they were a standard SE measurement [353]. When fitting the simulated data sets, an identical model to that which performed the simulation is used. However, all parameters that describe the material are left free and the cross-parameter calculations (such as $\mu(N)$) are disabled.

7.3. Computational Limits and Noise

To explore the fundamental computational limits and those presented by SE measurement random noise, the first step was to simulate a data set comprising of a bulk film (a single generalised oscillator layer of infinite thickness) with only a Drude term (Section 2.1.4). The "simulated" carrier concentration, N_{sim}, is varied between $10^{10} - 10^{23}$ cm^{-3}, μ is fixed at 210 cm^2/Vs (an indicative "maximum" μ for ITO, AZO and GZO [342,343]) and m_e^* is fixed at $0.3\ m_e$ [182]. Presently, no random noise is included in the simulation ($\%_{Noise} = 0$). The limits for accurate determination of the carrier transport properties will also depend on μ, which will vary with N according to what scattering mechanism are at play (Section 2.2.5). The independent influence of μ is investigated in Section 7.6. Fig. 7-1a presents the "optical" (fitted) carrier concentration, N_{opt}, against the N_{sim} that have been independently simulated in the IR (red dots) and in the NIR-VIS-UV (blue squares). The dashed black lines indicate the ideal case where $N_{opt} = N_{sim}$, which is valid for high enough N. In this scenario, there is a limit at $\sim 10^{11}$ cm^{-3} and $\sim 10^{13}$ cm^{-3} for the IR and NIR-VIS-UV spectral ranges, respectively, where $N_{opt} \neq N_{sim}$. In theory, N_{opt} should be identical to N_{sim} for all nonzero N_{sim} in both spectral ranges. However, the data cannot reasonably be simulated (or of course, measured) to infinite precision. In the case of these simulations, round off errors become significant when the permittivity, at the lowest considered frequency, is below $\sim 10^{-7}$. The exponential tail of the Drude term is, by definition, larger at the lowest energy point for the IR (0.034 eV) as to the NIR-VIS-UV (0.775 eV), resulting in better sensitivity in N in the IR range.

Fig. 7-1b presents the "free carrier detectability", S_{Drude}, within the IR (dark red line with dot symbols) and NIR-VIS-UV (dark blue line with square symbols) spectral ranges. S_{Drude} is defined as the numerical integration of the free carrier contribution to the permittivity within each spectral range. The threshold in S_{Drude} in Fig. 7-1b occurs at when $N_{opt} \neq N_{sim}$ in Fig. 7-1a. This limit is found at higher N in cases where a fixed percentage of random noise is also manually included across the entire spectral range of the data (more closely representing a real measurement). It should be noted that for real measurements the noise is generally greater at the edges of the spectral ranges, which will compound this issue. It is apparent that for materials with a low N, reducing the percentage of noise in the data (especially at low photon energy) is vital for accurate determination of N and thus, if the measured spectral range cannot be brought to lower energies, an increased number of scans to average should take precedence over increased resolution. The benefit of utilizing terahertz (THz) SE for materials with $N < 10^{18}\ \text{cm}^{-3}$ is also apparent from these results.

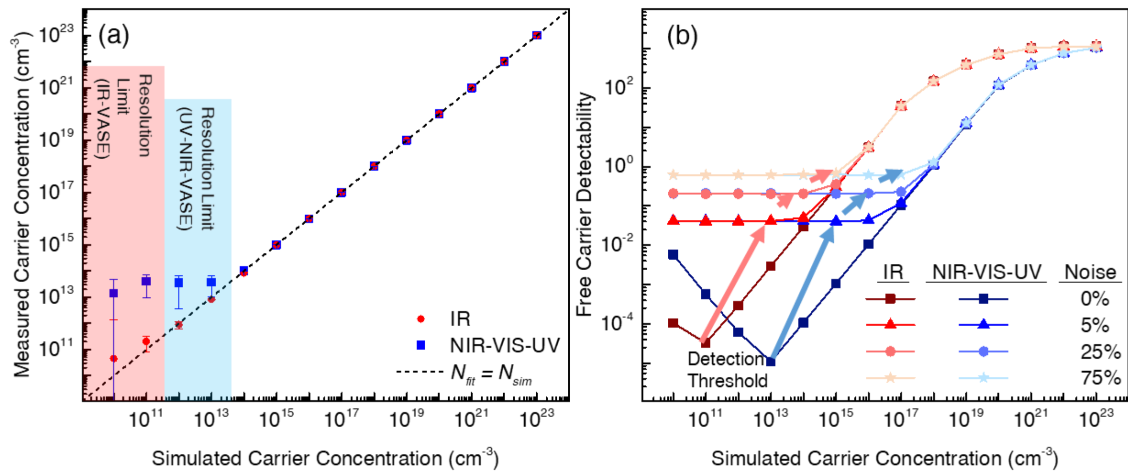

Fig. 7-1. (a) 'Optical' carrier concentration, N_{opt}, against the simulated carrier concentration, N_{sim}, for the case of fitting the data simulated in the IR (red dots) and in the NIR-VIS-UV (blue squares). The dashed black lines indicate the ideal case where $N_{opt} = N_{sim}$. (b) Free carrier detectability, S_{Drude}, of the fit within the NIR-VIS-UV (dark blue line with square symbols) and IR (dark red line with circle symbols) spectral ranges to the free carrier contribution to the simulated data set.

7.4. Substrate and Film Thickness

Fig. 7-2a presents S_{Drude} against N_{sim} for a bulk material (black line with star symbols) and for thin film materials of various thickness, in nm, (purple to dark red lines with square symbols) on top of a Si wafer with a 2 nm native oxide on top. The simulated measurements did not include noise and only included a Drude oscillator where the mobility is fixed at $210\ \text{cm}^2/\text{Vs}$ and N_{sim} was varied from $10^7 - 10^{17}\ \text{cm}^{-3}$. It is found that the free carrier detection threshold, where S_{Drude} plateaus to a minimal value, is increased from $\sim 10^{11}\ \text{cm}^{-3}$ for a bulk film to

$\sim 10^{13}\ \mathrm{cm^{-3}}$ for a $1\ \mathrm{nm}$ film. If the thickness of the film is increased further, the threshold is reduced until matching that of the bulk film for a thickness of $100\ \mathrm{nm}$. Furthermore, it is found that for a larger thickness, the threshold is reduced below that of a bulk film. The cause for this is apparent from Fig. 7-2b, where the simulated imaginary *pseudo*-permittivity, $< \varepsilon_2 >_{sim}$, is presented for four distinct films:

i. a $100\ \mathrm{nm}$ film where $N_{sim} = 1 \times 10^{11}\ \mathrm{cm^{-3}}$ (solid black line in Fig. 7-2b),
ii. a $100\ \mathrm{\mu m}$ film where $N_{sim} = 1 \times 10^{11}\ \mathrm{cm^{-3}}$ (solid red line in Fig. 7-2b),
iii. a $100\ \mathrm{nm}$ film where $N_{sim} = 0.9 \times 10^{11}\ \mathrm{cm^{-3}}$ (dashed green line in Fig. 7-2b),
iv. a $100\ \mathrm{\mu m}$ film where $N_{sim} = 0.9 \times 10^{11}\ \mathrm{cm^{-3}}$ (dashed blue line in Fig. 7-2b).

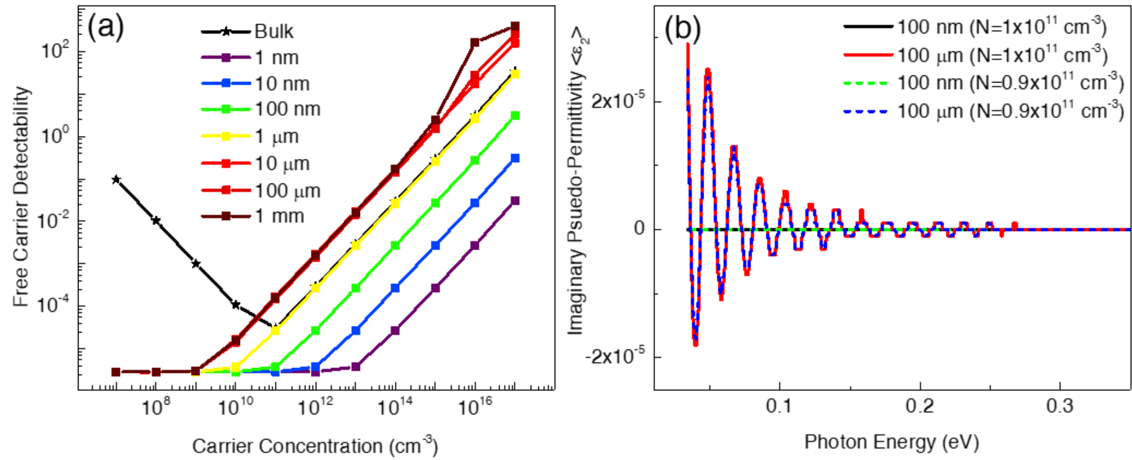

Fig. 7-2. (a) S_{Drude} against N_{Sim} for a bulk material (black line with star symbols) and for thin film materials of various thickness, in nm, (purple-dark red lines with square symbols) on top of a Si wafer with a 2 nm native oxide. (b) Simulated imaginary *pseudo*-permittivity, $< \varepsilon_2 >$, of four distinct films: a $100\ \mathrm{nm}$ film where $N_{sim} = 1 \times 10^{11}\ \mathrm{cm^{-3}}$, a $100\ \mathrm{\mu m}$ film where $N_{sim} = 1 \times 10^{11}\ \mathrm{cm^{-3}}$, a $100\ \mathrm{nm}$ film where $N_{sim} = 0.9 \times 10^{11}\ \mathrm{cm^{-3}}$ and a $100\ \mathrm{\mu m}$ film where $N_{sim} = 0.9 \times 10^{11}\ \mathrm{cm^{-3}}$.

It is observed that $< \varepsilon_2 >_{sim}$ is below the resolvable limit for $E \geq 0.034\ \mathrm{eV}$ and so the free carrier contribution to $< \varepsilon_2 >_{sim}$ cannot be fit, N_{opt} cannot be resolved and the two films with a thickness of $100\ \mathrm{nm}$ appear identical. However, for the film simulated with a thickness of $100\ \mathrm{\mu m}$, the reflections from the material/substrate interface produce an interference pattern at low energy. Importantly, the interference pattern is very sensitive to changes in N_{opt} and so there are resolvable differences between the film simulated with $0.9 \times 10^{11}\ \mathrm{cm^{-3}}$ and $1 \times 10^{11}\ \mathrm{cm^{-3}}$. This results in the reduction of the threshold limit below that of the bulk case observed in Fig. 7-2a. Vitally, the same effect can be achieved by utilising transparent or semi-transparent substrates or intermediate layers (*i.e.* optical spacers) [383].

7.5. Additional Oscillators within and outside the measurement range

The simulations so far have been performed for films with only a Drude contribution to the permittivity of the material. In practice, phonons and or defect states will be present in the IR that reduce the sensitivity of IRSE to the free electron contribution. This arises from a combination of reduced resolution (*i.e.,* there is a larger % difference between 0.01 and 0.1 to between 10.01 and 10.1) and coupling between parameters (*i.e.,* the amplitude of a phonon peak near the edge of the spectral range can be mistaken for increased free carrier absorption, and vice versa). The effect of the additional oscillators within the measurement range on the detection limits for the carrier transport properties will depend on the peak size, broadening and the central energy. Because of this, a simple correlation of each parameter with the detection limits is not possible.

If the oscillators have a central energy below the measured spectral range (*e.g.,* in the IR), then only the tail edge of the absorption can be seen within the measured spectral range (the NIR-VIS-UV). This results in a permittivity near the low-energy edge of the measured range that resembles free electron absorption but is the result of additional oscillators at lower energies. For example, Uprety and colleagues demonstrated how the NIR absorption observed in NIR-VIS-UV SE should be interpreted as a combination of tailing effects from free carriers, phonons and/or low-energy defect states [306,354]. The effect of NIR tailing on the detection limits of the carrier transport properties will be fully dependent on the precise nature of the IR oscillators, and so is investigated in more detail for the ITO, AZO and GZO thin films in Section 7.7.

7.6. Influence of the carrier mobility

Previously, it has been assumed that the mobility is constant and a very high value of $210\ \mathrm{cm}^2/Vs$ has been used to demonstrate the examples regarding the influence of the computational limits, measurement noise, presence of a substrate and the film thickness. However, the line shape of the free carrier absorption and especially the absolute value of ε_1 and ε_2 at the smallest measured E, which actually determines the detection limit (Fig. 7-1), also depend on μ (Eq. (2-43)). As μ defines the broadening of the peak, its effect on the absolute values of $\varepsilon_1(E)$ and $\varepsilon_2(E)$ at a particular photon energy, E, depends on the value of E itself. This is demonstrated in Fig. 7-3a, which presents an example set of $\varepsilon_2(E)$ with varying μ (from $25 - 200\ \mathrm{cm}^2/\mathrm{Vs}$ in steps of $25\ \mathrm{cm}^2/\mathrm{Vs}$). N and m_e^* for these simulated permittivity's are $10^{18}\ \mathrm{cm}^{-3}$ and $0.3\ m_e$, respectively. As the mobility increases, the Drude absorption peak (centred at $0\ \mathrm{eV}$) becomes sharper. Initially, this causes ε_2 at low energy ($0.034\ \mathrm{eV}$) to rapidly increase. At larger energies, the relative increase in ε_2 is not as significant. After a point ($\mu = 100\ \mathrm{cm}^2/\mathrm{Vs}$), the

trend reverses and $\varepsilon_2(E = 0.034\ \text{eV})$ starts to slowly decrease. At higher E, the inflection point is seen to occur at smaller values of μ. This trend is shown more clearly in Fig. 7-3b, which presents the values of ε_1 (blue squares) and ε_2 (red dots) at 0.034 eV as a function of μ.

From Eq. (2-45) it can be derived that the maximum and/or minimum $\varepsilon_2(\gamma_p)$ occurs at:

$$\frac{d\varepsilon_2(\gamma_p)}{d\gamma_p} = \frac{E^2 - \gamma_p^2}{\left(E^2 + \gamma_p^2\right)^2} = 0 \ , \tag{7-1}$$

which is satisfied when $\gamma_p = E$, or $\gamma_p = \infty$. The former depicts the maxima observed in Fig. 7-3, such that the inflection point of the mobility is given by $\mu_{\varepsilon_2(E),max}(E) = (e/m_e^*\hbar)E$. The $\hbar$ in the denominator of the conversion indicates that E is expressed in eV. It should be noted that this has important consequences for the defect engineering of materials for optoelectronic applications and/or as alternative materials for plasmonics. Specifically, the key focus to reduce the losses of potential plasmonic devices is to minimise ε_2. Usually, this is done by seeking ways to increase μ. However, Fig. 7-3 demonstrates that for materials seeking to be a component of a device operating at E, if $\mu < (e/m_e^*\hbar)E$ then reducing μ is more desirable. Finally, to better reflect how this affects the detection limits for N, S_{Drude} is calculated from ε_1 and ε_2 ($S_{Drude} = \sqrt{\varepsilon_1^2 + \varepsilon_1^2}$). Despite the up and down of ε_2, the absolute values of ε_1 always increase with μ, increasing $S_{Drude}$with μ up to a plateau. Therefore, increasing μ will increase S_{Drude}.

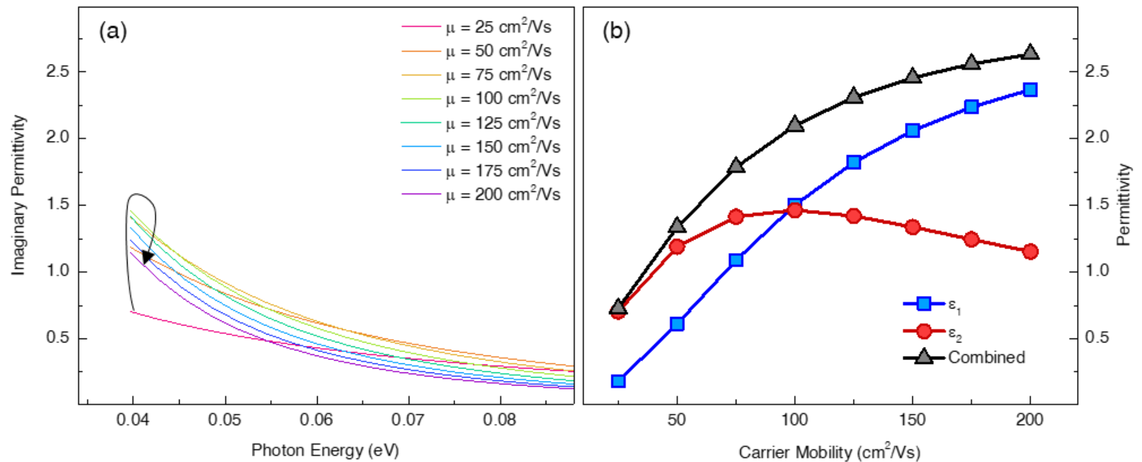

Fig. 7-3. (a) Imaginary permittivity, $\varepsilon_2(E)$, for an example material with carrier concentration, $N = 10^{18}\ \text{cm}^{-3}$, and carrier effective mass, $m_e^* = 0.3\ m_e$. The carrier mobility, μ, is set to $25\ \text{cm}^2/\text{Vs}$ (pink line), $50\ \text{cm}^2/\text{Vs}$ (orange line), $75\ \text{cm}^2/\text{Vs}$ (gold line), $100\ \text{cm}^2/\text{Vs}$ (green line), $125\ \text{cm}^2/\text{Vs}$ (teal line), $150\ \text{cm}^2/\text{Vs}$ (light blue line), $175\ \text{cm}^2/\text{Vs}$ (blue line) and $200\ \text{cm}^2/\text{Vs}$ (purple line) The black arrow illustrates how the peak value of $\varepsilon_2(E = 0.034\ \text{eV})$ originally increases with μ before decreasing rapidly when $\mu > (e/m_e^*\hbar)E$. (b) ε_1 (blue squares), ε_2 (red dots) and $S_{Drude} = \sqrt{\varepsilon_1^2 + \varepsilon_1^2}$ (grey triangles) at 0.034 eV as a function of μ.

7.7. Limits of SE for TCOs

This section applies all the concepts outlined above to more realistic simulations of ITO, AZO and GZO films (based on the experimental results outlined throughout the thesis) in order to conclude when ellipsometry really works for TCOs. To produce simulated data sets of the bulk permittivity, for ITO, AZO and GZO, N_{sim} is varied between $10^{17} - 10^{21}$ cm^{-3} in steps of $10^{0.5}$ cm^{-3}. μ_{sim} is calculated using Eq. (2-49), Eq. (2-56) and Eqs. (2-58) to (2-61), considering $m_e^*(N)$. Subsequently, ρ_{sim} and τ_{sim} are calculated from N_{opt} and μ_{opt} *via* Eq. (2-40) and Eq. (2-41). This brings the resistivity range between $10^{-4} - 10^{7}$ Ωcm. In order to ensure the simulated data sets accurately described the absorption of the phonon and/or defects states for each material, the oscillator parameters resulting from fitting the "low-N" films (see Table 4-2). For the purpose of highlighting the limitations of SE, the generalised oscillator parameters as extracted by the "idealised" models of Section 4.2.1 were considered sufficient to describe the optical constants of the Low-N ITO (Fig. 4-10), AZO (Fig. 4-12) and GZO (Fig. 4-14) films. The permittivity is built from the summation of the IR and UV oscillators of each material and the Drude term defined by N_{sim} and μ_{sim} for each simulated data set, as per Eq. (3-54). These steps, alongside those applied to establish $\mu(N)$ and $m_e^*(N)$, ensured that the simulated data are self-consistent and as much as possible represent realistic optical constants for ITO, AZO and GZO materials with varying N. For every increment of N_{sim}, two distinct data sets are simulated, reflecting the ranges defined by two individual ellipsometers ($0.034 - 0.8$ eV for the IR and $0.775 - 6.5$ eV for the NIR-VIS-UV).

7.7.1. Limitations of SE to determine the carrier concentration.

To elucidate the limitation of the capabilities of IR and NIR-VIS-UV SE to extract N_{opt}, the simulated data sets are fit and the 'optical' carrier concentration, N_{opt}, is recorded as the value of N that fits the simulated data sets. The results from fitting the NIR-VIS-UV (blue squares) and IR (red dots) simulated data sets for ITO, AZO and GZO are presented in Fig. 7-4a, Fig. 7-4b and Fig. 7-4c, respectively. The dashed black lines indicate the ideal case where $N_{opt} = N_{sim}$, which is valid for high enough N. As N_{sim} decreases, three distinct areas where $N_{opt} \neq N_{sim}$ are observed. Each area is colour coded in a way that distinguishes between different mechanisms.

IR detection limit

For the data sets simulated in the IR, a deviation from the diagonal dashed line, coupled with a significantly increased error bar, is noted for $N_{sim} \approx 10^{17}$ cm^{-3}. This is indicated as the red shaded areas in Fig. 7-4a-c, where $N_{opt} \neq N_{sim}$ is due to the "IR detection limit". This is a photon energy dependent limit that is due to rounding errors for simulated bulk films and thus is identical for ITO, AZO and GZO. The previous sections of this chapter demonstrated that, for

practical measurements the detection limit varies significantly due to a combination of the presence of noise, material/substrate reflections and/or IR absorption centres. Additionally, the IR detection limit can be reduced by utilising films, substrates or optical spacers with a thickness sufficient to produce interference effects within the measured spectral range.

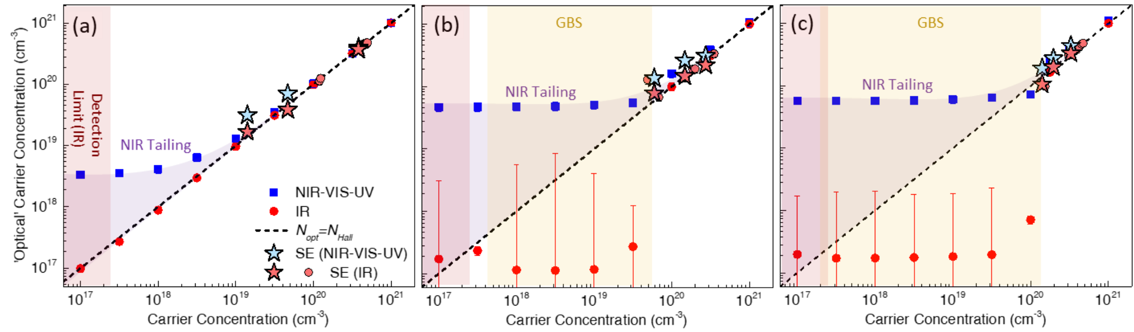

Fig. 7-4. "Optical" carrier concentration, N_{opt}, as determined by fitting each simulated dataset of N_{sim} for (a) ITO, (b) AZO and (c) GZO, respectively. The result from fitting the data simulated in the IR (red dots) and in the NIR-VIS-UV (blue squares) are shown alongside $N_{opt} = N_{sim}$ (black dashed diagonal line). The influence of the NIR tailing and GBS are indicated by the purple and yellow shaded areas, respectively. The results for the low-N, mid-N and high-N experimental films as measured with IRSE, NIR-VIS-UV SE and Hall Effect are displayed with light red and light, blue-bordered star symbols, respectively. The films measured with IRSE and Hall Effect only are displayed with the light red, bordered circle symbols. For the experimental films, the x-axis "real" carrier concentration, N, is set to the Hall carrier concentration, N_{Hall}, and for the simulated films $N = N_{sim}$.

Material structure limit

An additional case where $N_{opt} \neq N_{sim}$ arises when fitting AZO in the IR. When $N_{sim} = 10^{18} - 10^{19.5}\ cm^{-3}$, N_{opt} is considerably underestimated and the error in N_{opt} is enormous (yellow shaded area in Fig. 7-4b). This region directly overlaps the region where μ is diminished by the influence of GBS (Section 4.1.6). This diminished mobility produces an extremely damped Drude term which becomes undetectable within either (or in fact any) spectral windows. It is apparent that in order to determine N_{opt} of a material *via* SE, the $N_{Hall} = N$ must fall outside the window of GBS. It should be noted that the simulation has assumed that the grain size and trap density do not change with N. However, in Section 4.1.6 it was seen that a variation in the grain size shifts the lower edge (in terms of N) of the mobility hole that is associated with GBS (Fig. 4-7). If the edge of the mobility hole is higher than the detection limit of IRSE ($\sim 10^{17}\ \mathrm{cm}^{-3}$ in the presented cases), accurate determination of the transport properties is possible below the GBS threshold (see the point $\mathrm{N_{sim}} = 10^{17.5}\ \mathrm{cm}^{-3}$ in Fig. 7-4b). Similar results are found for

GZO, with the exception that the window of GBS is large enough to overlap with the fundamental detection limits so that there is no region of $N_{opt} = N_{sim}$ below $10^{20.5}$ cm^{-3}.

NIR-VIS-UV detection limit

As N_{sim} falls below a certain threshold (varied for each material) it is noticed that N_{opt}, as determined by fitting the data simulated in the NIR-VIS-UV (blue squares), deviates from the diagonal dashed line. This is indicated as the purple shaded areas in Fig. 7-4a-c, where $N_{opt} \neq N_{sim}$ is exclusively due to NIR tailing effects (a NIR permittivity that resembles free electron absorption but is, instead, the result of additional oscillators in the IR; Section 7.5). However, the results from fitting the NIR-VIS-UV data sets maintain a negligible error in N_{opt}. This manifests a potential "false positive" of NIR-VIS-UV SE. At larger N, the free carrier absorption sufficiently screens the other contributions in the IR, ensuring a more accurate determination of the carrier transport properties. To highlight the effect of NIR tailing, it is useful to examine the permittivity of the materials as seen by both ellipsometers.

Fig. 7-5 presents the (a-c) real, $\varepsilon_1(E)$, and (d-f) imaginary, $\varepsilon_2(E)$, permittivity of the low-N (darker shaded lines) and high-N (lighter shaded lines) ITO, AZO and GZO films (see Table 4-1), respectively, from fitting IR (red lines) and NIR-VIS-UV SE (blue lines) measurements separately. Fig. 7-5 also shows only the Drude term that was determined *via* IRSE (dashed black lines) alongside the extrapolation of the permittivity determined by NIR-VIS-UV into the IR (dashed blue lines). The region between the measured permittivity and the expected permittivity, if only free carriers were present, is highlighted by the purple shaded region. This region indicates the contribution of the IR oscillators to the NIR absorption and thus defines the NIR tailing effects. The high-N ITO film is the only experimental material which does not show clearly visible NIR tailing and, therefore, IR and NIR-VIS-UV-SE agree to within 10% (Fig. 7-4a). The NIR tailing is more significant for the doped-ZnO films than for ITO, due to the increased intensity of the absorption peak at ~ 0.12 eV. The increased tailing results in the higher value of N_{opt} when fitting the doped-ZnO simulated data sets in the NIR-VIS-UV that is observed in Fig. 7-4a-c. This, subsequently, results in a larger limit for accurate extraction of the carrier transport properties as a higher free carrier absorption is required to screen the tailing of the IR absorption.

It is noticed in Fig. 7-5 that, for the doped-ZnO materials, the absorption peak at ~ 0.05 eV results in a region of positive real permittivity for lower energies. This observation is important as it reveals that any exploitation of plasmonic behaviour in the far-IR is impossible. Conversely, for the low-N ITO, AZO and GZO films, the additional absorption peaks in the IR results in a window (or two distinct windows) of negative permittivity which is not present when

only the free carrier absorption is considered. Therefore, exploitation of plasmonic (or in this case phononic [41,384,385]) behaviour is possible despite the insufficient conductivity.

In summary, NIR tailing causes NIR-VIS-UV SE to become increasingly ambiguous for metal oxides where N lies within a "region of uncertainty", which is tied to an application-specific "acceptable deviation" in N. By taking advantage of the high accuracy of IRSE to determine the optical constants of ITO, AZO and GZO in the IR, it is possible to quantify the boundary of such a region of uncertainty.

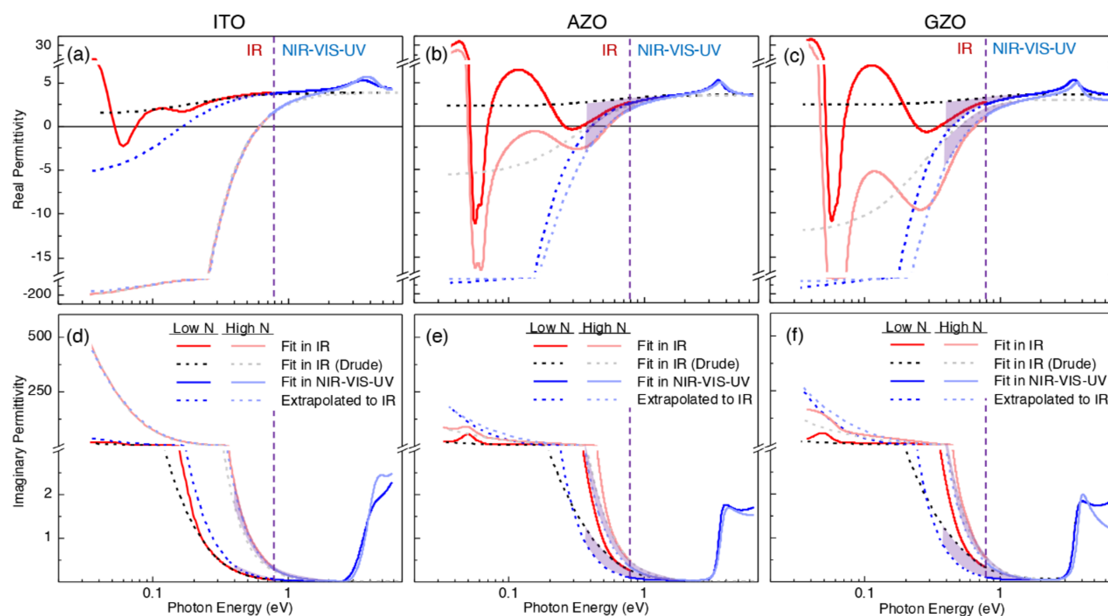

Fig. 7-5. (a-c) Real, $\varepsilon_1(E)$, and (d-f) imaginary, $\varepsilon_2(E)$, parts of the complex permittivity for the sputtered ITO, AZO and GZO films, respectively, as fit in the IR (solid red lines), as fit in the NIR-VIS-UV (solid blue lines), *via* extrapolation of the NIR-VIS-UV into the IR (dashed blue lines), and as simulated with only the Drude term of the IR fitted (dashed black/grey lines). "Low-N" (darker lines) and "High-N" (lighter lines) represent two distinct films of each material which cover the experimental range of carrier concentration. The purple shaded region highlights the difference between the simulated and fitted Drude contribution in the NIR, where tailing effects of the IR absorption centres are mistaken for free carrier absorption when fitting in the NIR-VIS-UV. Please note the changes in scale at −17 and 7 for the real permittivity and at 3 for the imaginary permittivity.

7.7.2. Quantifying the limits of NIR-VIS-UV SE

The competition between the free carrier absorption and other factors of NIR tailing affects the final determination of N with the ratio N_{opt}/N_{sim} (the ratio of NIR-tailing affected carrier concentration to the "actual" carrier concentration). The ratio N_{opt}/N_{sim} is calculated, where N_{opt} is determined from fitting the data sets simulated in the NIR-VIS-UV. The calculated N_{opt}/N_{sim} is presented as the grey squares in Fig. 7-6a-c for ITO, AZO and GZO, respectively. A logistic function (Eq. (7-2)) is fit to the calculated N_{opt}/N_{sim} (red dashed line in Fig. 7-6) using a Levenberg-Marquardt regression algorithm to determine the free parameters N_0 and p. For AZO and GZO, the points within the region of grain boundary scattering (GBS; yellow shaded area in Fig. 7-6) are ignored during the fit of Eq. (7-2) the data (both NIR-VIS-UV SE and IRSE fail within this region (Section 7.7.1)). For illustration, the value of N_{sim} is calculated when $N_{opt}/N_{sim} = 1.1$ (N_{opt} is 10% greater than N_{sim}), $N_{opt}/N_{sim} = 1.5$ (N_{opt} is 50% greater than N_{sim}), $N_{opt}/N_{sim} = 2$ (N_{opt} is 100% greater than N_{sim}) and $N_{opt}/N_{sim} = 10$ (N_{opt} is an order of magnitude, or 900%, higher than N_{sim}). These values of N_{sim}, for when N_{opt}/N_{sim} is below a given "acceptable deviation", can be used to define the upper boundary of a "region of uncertainty", where one might have doubts on the validity of NIR-VIS-UV-SE to determine the carrier concentration.

Here, a concept of the application-specificity for the region of uncertainty is introduced, allowing for the provision of a confidence factor for NIR-VIS-UV-SE that can be applied on a case-by-case basis. A relatively low acceptable deviation of 10% is deemed suitable for plasmonics, as the plasmonic properties are very sensitive to the carrier concentration (see below). For other applications, however, the acceptable deviation may differ, resulting in an application-specific upper boundary of N for the region of uncertainty. The acceptable N_{opt}/N_{sim} ratio (or ρ_{sim}/ρ_{opt} ratio) can become an adjustable parameter and thus fixed to the requirements of an application. For example, sheet resistances of $150 - 450\ \Omega/\square$ are considered sufficient for flat panel display electrode applications [386], resulting in an acceptable deviation of 200%. In addition, commercial grade ITO films are specified at $(1-2) \times 10^{-4}\ \Omega\text{cm}$ (a 100% deviation) [124]. This provides an application-specific confidence factor for NIR-VIS-UV SE. Table 7-1 shows the fitting parameters of Eq. (7-2) and the N_{sim} thresholds for a set of example acceptable deviations of N_{opt}/N_{sim} during NIR-VIS-UV SE for ITO, AZO and GZO. The regions of uncertainty for example acceptable deviations of 10%, 50%, 100% and 900% (greater than N_{sim}) are indicated by the green, blue, red and purple shaded areas, respectively, in Fig. 7-6a-c. It should be noted that the influence of GBS overrides the influence of NIR tailing when defining where NIR-VIS-UV-SE is unable to determine, unambiguously, the carrier transport properties. Therefore, for AZO and

GZO, NIR-VIS-UV-SE will fail for larger N thresholds than expressed in the 900% (for AZO) and 900%, 100% and 50% (for GZO) acceptable deviations.

$$\frac{N_{opt}}{N_{sim}} = 1 + \frac{10^6}{1 + \left(\frac{N_{sim}}{N_0}\right)^p} \qquad (7\text{-}2)$$

Table 7-1. Free parameters of Eq. (7-2) and the N_{sim} thresholds for a set of example acceptable deviations of N_{opt}/N_{sim} during NIR-VIS-UV-SE.

Parameter	Unit	Material		
		ITO	AZO	GZO
$\boldsymbol{N_0}$	$\times 10^{12}\ cm^{-3}$	3.7 ± 0.4	33 ± 2	45 ± 2
$\boldsymbol{p}$		1.013 ± 0.009	0.959 ± 0.007	0.97 ± 0.01
$\boldsymbol{N\ (N_{opt}/N_{sim} = 1.1) - 10\%}$	$\times 10^{20}\ cm^{-3}$	0.30 ± 0.05	7 ± 1	7 ± 2
$\boldsymbol{N\ (N_{opt}/N_{sim} = 1.5) - 50\%}$	$\times 10^{19}\ cm^{-3}$	0.6 ± 0.1	12 ± 2	14 ± 3
$\boldsymbol{N\ (N_{opt}/N_{sim} = 2) - 100\%}$	$\times 10^{18}\ cm^{-3}$	3.1 ± 0.5	59 ± 8	70 ± 10
$\boldsymbol{N\ (N_{opt}/N_{sim} = 10) - 900\%}$	$\times 10^{17}\ cm^{-3}$	3.6 ± 0.5	60 ± 7	70 ± 10

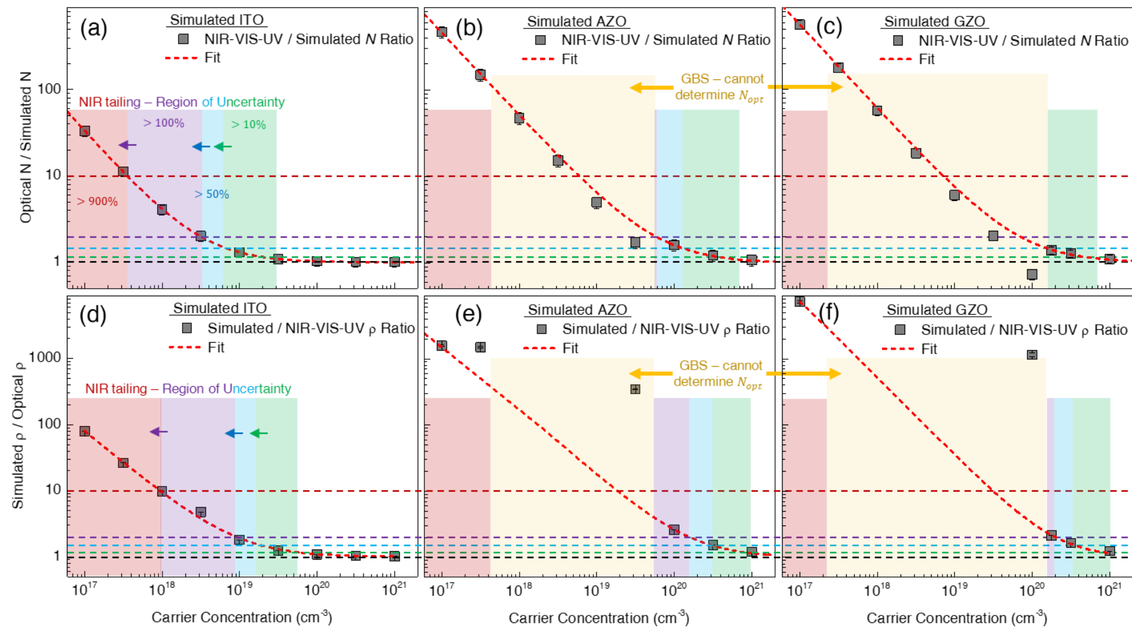

Fig. 7-6. (a-c) Ratios of N_{opt}, as fit in the NIR-VIS-UV, to N_{sim} (grey squares) for (a) ITO, (b) AZO and (c) GZO. (d-f) The corresponding ratios of ρ_{sim} to ρ_{opt}, as fit in the NIR-VIS-UV, (grey squares) for (d) ITO, (e) AZO and (f) GZO. Also shown is the fit to the data (red dashed line), ignoring the points within the region of GBS (yellow shaded area) where SE fails regardless of the measured spectral range. The points where (a-c) N_{opt}/N_{sim} or (d-f) ρ_{sim}/ρ_{opt} is equal to 1.0, 1.1 (10% agreement), 1.5 (50% agreement) and 10 (order of magnitude agreement) are indicated with the black, green, blue and purple dashed lines, respectively. The regions of uncertainty where N_{opt} (or ρ_{sim}) is 10%, 50%, 100% and 900% larger than N_{sim} (ρ_{opt}) are indicated with the green, blue, purple and red shaded areas, respectively.

For example, the limit of NIR-VIS-UV SE to accurately determine the transport properties can be defined to be the point where the deviation between N_{opt} and N_{sim} is below 10%. For ITO, this limit is found to be $(3.0 \pm 0.5) \times 10^{19}\ \mathrm{cm}^{-3}$. For AZO (Fig. 7-4b), the limit for inaccurate determination of N *via* NIR-VIS-UV-SE is higher (in terms of N) than for ITO (Fig. 7-4a). Due to the increased intensity of the absorption peak at $\sim 0.12\ \mathrm{eV}$, the threshold where N_{opt} is within 10% of N_{sim} for AZO is found to be $(7 \pm 1) \times 10^{20}\ \mathrm{cm}^{-3}$. The NIR tailing effects for GZO are near identical to those for AZO (see Section 4.2.1) and so has an equal threshold (but larger error) of $(7 \pm 2) \times 10^{20}\mathrm{cm}^{-3}$. A measurement of the carrier transport porperties of ITO *via* NIR-VIS-UV-SE below this limit has, as-of-yet, not been found within the literature. This is likely because the most prominent implementation of TCOs has been electronic applications [68,70,123,145], or plasmonics at the telecom wavelengths [27,42], where a larger N is desired. However, there is a collection of studies which extract the carrier transport properties of AZO and GZO from NIR-VIS-UV-SE or VIS-NIR reflection measurements while N is close-to or under the limit of $(7 \pm 1) \times 10^{20}\ \mathrm{cm}^{-3}$ [19,28,163,348,359,387]. Furthermore, as the plasmonic community explores materials with lower N, the requirement for IRSE becomes even more pronounced. Fig. 7-6d-f presents the corresponding case for comparing the deviation in resistivity. An identical procedure as outlined above is followed. However, the ratio ρ_{sim}/ρ_{opt} is used instead of N_{opt}/N_{sim} on the left-hand side of Eq. (7-2). The case is more complex as ρ_{sim} is calculated from N_{sim}, $\mu_{sim}(N)$ and $m_e^*(N)$. This causes many data points to be shifted to much larger ρ_{sim}/ρ_{opt} within (and near) the region of GBS. To account for this, the data is fit only for $N_{sim} = 10^{17}\ \mathrm{cm}^{-3}$ and $N_{sim} > 10^{20}\ \mathrm{cm}^{-3}$, where the influence of GBS on μ_{sim} is less significant. It is seen that, due to the additional influence of the mobility, the regions of uncertainty are shifted to larger N_{sim}. This indicates that the considerations of the spectral range for the validity of SE depends not only on the material properties, but also on the targeted application (*e.g.,* when deviations in ρ_{opt} are more important than in N_{opt}).

Justifying a $\mathbf{10}\%$ acceptable deviation limit for plasmonic applications

The use of a 10% acceptable deviation of N is justified by investigating the effect of a variation in N_{opt} on the Figure of Merits (FoMs) for near field enhancement and localised heating. Two widely used FoMs evaluate the quality of both localised and propagating SPP, which are calculated from the $\varepsilon_1(E)$ and $\varepsilon_2(E)$. Lallise *et al.* [349] introduced two more useful FoMs, namely Faraday, $Fa(E)$, and Joule, $Jo(E)$, numbers which quantify the ability of a nanoparticle to enhance the optical near field and produce heat, respectively. These FoMs consider the refractive index of the local dielectric medium and light source by introducing or removing a $1/n_s$ term in the Fa or Jo number, respectively. They drew up the values of the non-

retarded resonance wavelength and Fa and Jo number at this wavelength for a large set of materials with plasmonic responses in the visible.

$$Fa(E) = |1 + 2\xi(E)|^2 \tag{7-3}$$

$$Jo(E) = \frac{e\varepsilon_2(E)}{n_s}|\xi(E) - 1|^2 \tag{7-4}$$

where n_s the refractive index of the surrounding medium and $\xi(E)$ is the enhancement factor, given by:

$$\xi(E) = \frac{\varepsilon_1(E) + i\varepsilon_2(E) - \varepsilon_M}{\varepsilon_1(E) + i\varepsilon_2(E) + 2\varepsilon_M} \tag{7-5}$$

where ε_M is the permittivity of the local dielectric medium. The high-N ITO film (see Table 4-2) is used here as an indicative example case. Fig. 7-7 presents (a) $Fa(E)$ and (c) $Jo(E)$ for the high-N ITO thin film (pink line). The orange, yellow, green, turquoise, blue and purple lines represent the calculation of the FoMs for the same material but with a 10%, 20%, 30%, 40%, 50% and 100% deviation in the carrier concentration, respectively. It is seen that the peak positions for $Fa(E)$ and $Jo(E)$ are noticeably shifted with increasing N. Fig. 7-7b presents the energy where $Fa(E)$ and $Jo(E)$ are at their maxima, $E(Fa^0)$ (red squares) and $E(Jo^0)$ (blue squares) for each deviation of N. The peak energy increases following the relation:

$$E_{FoM^0} = a\big(100(1 + N_{opt}/N_{sim})\big)^b + c \tag{7-6}$$

where the values a, b and c for each FoM are presented within Fig. 7-7b. The increase is almost linear, and so setting an acceptable deviation based on the maximum acceptable shift in the peak energy will always have an arbitrary element. For a given photon energy that is desired for a specific application (e.g., a targeted molecular absorption) this peak shift also manifests as a deviation in the absolute values of $Fa(E)$ and $Jo(E)$ at that energy. Fig. 7-7d shows the Faraday (red squares) and Joule (blues squares) numbers at 0.49 eV and 0.51 eV, respectively. These photon energies correspond to the peak positions, $E(Fa^0)$ and $E(Jo^0)$, for the un-deviated high-N ITO film. When the deviation is $0 - 5\%$, it is observed that $Fa(0.49\text{ eV})$ and $Jo(0.51\text{ eV})$ are almost identical to the original material. For deviations greater than 5%, the values start to rapidly decline, indicating the sensitive nature of both FoMs to N. This value provides a natural point to set the acceptable deviation. However, by considering that the energy for an application usually is not discrete but exists within a narrow spectral window, a slightly larger acceptable deviation of 10% was deemed adequate. For a deviation of 20% a 29% decrease in $Jo(0.51\text{ eV})$ is noted, which is a significant underestimation that arises from the miscalculation of the N_{opt} by ellipsometry. Finally, an additional indication of the application-specificity of the acceptable deviation is observed from the fact that the Faraday and Joule numbers drop with the N deviation at different rates. Indeed, the application-specificity applies even between different applications within the field of plasmonics.

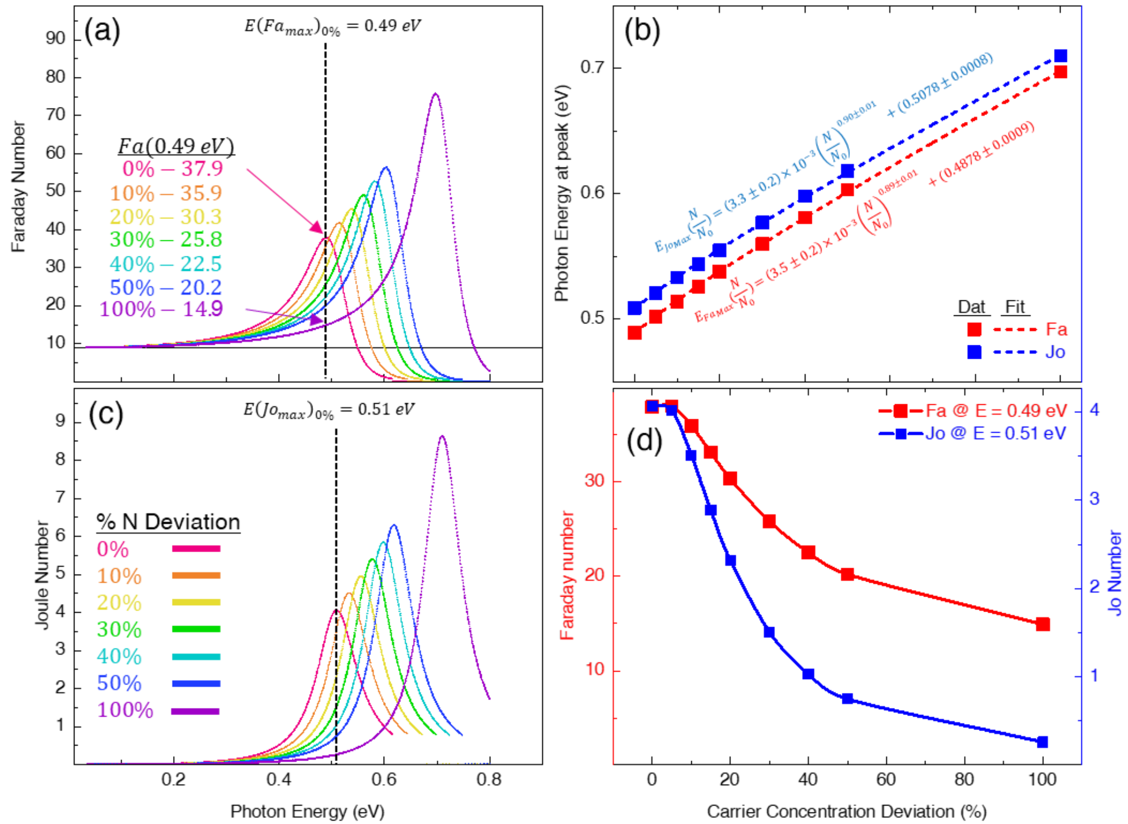

Fig. 7-7. (a) Faraday and (c) Joule numbers of the "high-N" ITO thin film (pink line). The orange, yellow, green, turquoise, blue and purple lines represent the calculation of the FoM for the same material but with a 10%, 20%, 30%, 40%, 50% and 100% deviation in the carrier concentration, N, respectively. In (a) the absolute values of the Faraday number at 0.49 eV are shown for each deviation of N. (b) $E(Fa^0)$ (red squares) and $E(Jo^0)$ (blue squares) for each devation of N. The dashed red and blue lines are the fit of $E_{FoM^0} = a\left(100(1 + N_{opt}/N_{sim})\right)^b + c$ to the data. (d) Faraday (red line, square symbols) and Joule (blues line, square symbols) numbers at 0.49 eV and 0.51 eV, respecitevly, for each deviation of N.

7.8. Concluding Remarks

In this chapter, the limitations of SE were investigated with a theoretical experiment to detail the limits of IR and NIR-VIS-UV SE due to noise, effect of a substrate, oscillators outside of the spectral range, oscillators within the spectral range, the carrier mobility and grain boundary scattering. Then, the established $\mu(N)$ and $m_e^*(N)$ relationships and the determined absorption centres for the seed TCO films explored in Chapter 4 were utilised to simulate a set of SE measurements covering a wide range of N for ITO, AZO and GZO.

Three vital factors that clarify when SE correctly determines the transport properties of low carrier concentration materials were documented: NIR tailing, GBS and spectral sensitivity. By considering each case, confidence can be built for the material properties extracted *via* SE. For the TCO candidates investigated, the tailing of the IR absorption into the NIR results in an overestimation of the Drude contribution to the permittivity.

Only when the free carrier absorption dominated the spectrum in the NIR, could one achieve an unambiguous determination of the carrier transport properties. These cases occurred only when outside the "region of uncertainty", bounded by an adjustable "acceptable deviation" of N from the actual (simulated) value. The concept of the application-specificity for the region of uncertainty was introduced, providing a confidence factor for NIR-VIS-UV SE that can be applied on a case-by-case basis. For plasmonic applications, an acceptable deviation of 10% was justified. This identified the region of uncertainty as $N \leq (3.0 \pm 0.5) \times 10^{19}\,\mathrm{cm}^{-3}$, $N \leq (7 \pm 1) \times 10^{20}\,\mathrm{cm}^{-3}$ and $N \leq (7 \pm 2) \times 10^{20}\,\mathrm{cm}^{-3}$ for ITO, AZO and GZO, respectively. Within these regions, IRSE measurements become of utmost importance.

Moreover, it was revealed how the material structure always requires great consideration as both IR and NIR-VIS-UV-SE fail for materials where GBS is a dominant scattering mechanism. Finally, it was noted how measurements of the permittivity of TCOs *via* NIR-VIS-UV SE overestimates their plasmonic quality and that the additional absorption peaks in the IR can prevent the exploitation of plasmonic phenomena in the far-IR but can create pocket of negative real permittivity for metal oxide films with low conductivity, allowing for exploitation of phononic behaviour in the IR.

8. Conclusions and Future Perspectives

8.1. Introduction

The research carried out in this Ph.D. was aimed at investigating how laser annealing (LA) in reactive environments can probe the defect state variations of key transparent conducting oxides (TCO) materials in order to tailor their opto-electronic properties and further demonstrate their applicability to IR plasmonics. Seed indium tin oxide (ITO), aluminium-doped zinc oxide (AZO) and gallium-doped zinc oxide (GZO) thin films were fabricated *via* radio frequency magnetron sputtering at room temperature. The microstructural and optoelectronic properties of the three TCO films were investigated in order to build knowledge of the optoelectronic character of ITO, AZO and GZO films with a wide range of carrier concentrations, N. Specifically, an in-depth approach to modelling the optical properties of TCOs with spectroscopic ellipsometry (SE) across a very wide spectral range ($0.034 - 6.5$ eV) was undertaken to gain deeper insights into the optical behaviour of TCOs and their applicability to IR plasmonics. On the way to achieving this goal, there were further insights into the strengths and weaknesses of SE to determine the optoelectronic properties of TCOs, and how the measured spectral range during SE affects this process.

Finally, the seed ITO thin films were then processed with single pulse reactive (5% H_2 in N_2 and pure O_2) LA (ReLA) for a range of LA conditions. Microstructural, compositional, electrical, and optical properties of the laser processed films were systematically investigated as a function of the laser fluence in two (reducing and oxidising) extremes of ambient environment. Subsequently, a deeper investigation into the role of the LA parameters on the optoelectronic properties of ITO was undertaken to reveal the influence of high fluences, number of pulses and a wider set of ambient environments. This chapter presents the research conclusions, key outcomes, as well as some thoughts for future work.

8.2. Conclusions

The main conclusion of this research is that ReLA can serve as an effective and versatile tool to modulate the optoelectronic properties of TCOs in order to tune them towards the requirements of IR plasmonic material components. One, final, figure is presented here to summarise this point. Fig. 8-1 presents the Faraday number, $Fa(E)$, (Eq. (7-3)) for all the seed and laser processed ITO films (thin dashed light grey lines), processed with various fluences, number of pulses and in varied ambient environments, as presented throughout Chapter 5 and 6. The thick solid light and dark blue lines indicate the Low-N and High-N ITO films of Chapter 7. The value of Fa at a specific photon energy, E, is indicative of how the material would perform as a material component for exploiting the plasmonic resonance of the material-based

nanoparticles enhance the electronic field close to the nanoparticle. These phenomena can only be exploited when the real permittivity, $\varepsilon_1(E)$, is less than zero and thus E is below the plasma energy, E_p. Such phenomena are more efficient within the region of “low-loss plasmonics” or “epsilon-near-zero” (ENZ) outlined in Fig. 1-1. In this way, examining the Faraday number for all the seed and laser processed films brings us full circle to contemplate how the presented research has found new pathways to overcome the current roadblock of plasmonics: finding new, more effective material components for IR plasmonics. The changes in the peak height and position of Fa depend on the specific changes to the complex permittivity, $\tilde{\varepsilon}$, of the material. Such changes in the IR primarily arise from modulation of the carrier transport properties. Throughout the thesis, ReLA has been shown to be able to finely control the carrier transport properties of ITO and thus modulate the permittivity and consequently the Fa number. The specific changes related to the laser parameters have been overviewed in Chapters 5 and 6. Here, we present a holistic view of the laser processed materials.

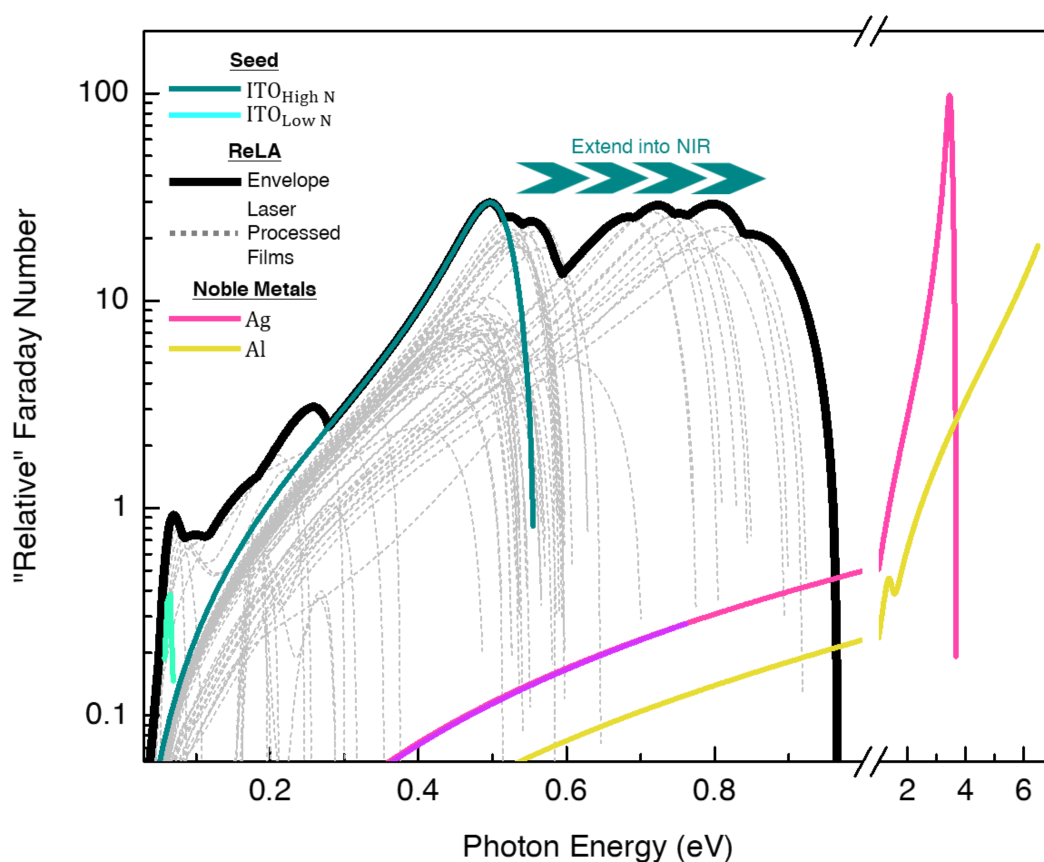

Fig. 8-1. “Relative” Faraday numbers, $Fa_{Rel} = Fa(E) - 9$, for the seed and laser processed ITO films (thin light grey dashed lines). The thick black line covers the maximum $Fa_{Rel}(E)$ across all samples. For reference, the experimental seed “SE Set” ITO films are shown with the blue solid lines, respectively. The shade differentiates between the High-N and Low-N films. $Fa_{Rel}(E)$ for Ag and Al are shown with the solid pink and yellow lines, respectively. Note the logarithmic scale in the y-axes and the change in scale in the x-axis at 1 eV.

Specifically, by collating $Fa(E)$ for all materials, one can map the maximum Fa for ITO. This is presented with the thick solid black line in Fig. 8-1. In this way, it is useful to think of the black line as an "effective" FoM for ITO. By carefully selecting the seed film deposition and LA parameters, one can fabricate an ITO based material with the maximum possible value of Fa (defined by the black solid line) at the desired E for a given device or application. From this perspective, it is seen that ReLA can somewhat bridge the gap of low loss plasmonic response in the NIR (dark blue arrow in Fig. 8-1). While ReLA was not able to reduce the carrier concentration and thus peak photon energy position, the strategy of laser processing an "un-optimised" ITO film with lower carrier concentration started to enhance $Fa(E)$ further into the IR.

It is apparent that that it is not necessary to find or invent new materials. There are already enough materials to play around with, and such materials have very interesting properties that have not fully been exploited. Developing further insights into the fundamentals of TCOs and employing various tools like LA will be able to push the boundaries of plasmonics and enable the proliferation of commercial devices. It should be noted that the modulation and enhancement of the optoelectronic properties of ITO have important implications for technologies beyond plasmonics alone. For example, the expansion of the optical bandgap (thus visible transparency) and the resistivity for all laser processed films can enhance the TCO performance for a multitude of optoelectronic applications (*e.g.,* photovoltaic devices).

Furthermore, the combination of ReLA with SE across a wide spectral range of $0.034 - 6.5$ eV can be a very useful tool in further material science studies into the, still not fully understood, conduction mechanisms of TCOs. Specifically, the high-throughput, fast and localised nature of ReLA allows for the rapid fabrication of a very large set of films with slightly modified transport properties for a single deposited film and the non-destructive and self-referencing nature of SE provides an unrivalled tool to determine the precise nature of the laser induced modifications of the optoelectronic properties. Indeed, by examining a set of seed films along, many insights were gained into the carrier transport mechanisms of TCOs and how the defect states, phonons and structural properties of ITO, AZO and GZO define their behaviour in optoelectronic and plasmonic devices [342].

8.3. Future perspectives

As in most Ph.D. research programmes, the observed results have revealed pathways for new research questions and experiments. Some thoughts for future work are listed below.

1. An extended investigation into a wide range of LA parameters (number of pulses, ambient pressure, pulse repetition rate, additional ambient environments, see Fig. 1-2), particularly for the un-optimised ITO film, in order to better fill the gap of "low-loss plasmonic response" or, equally, low $Fa(E)$ further into the IR.
2. Experimental investigations into ReLA of AZO and GZO thin films, which have also been highlighted as potential plasmonic material components in the IR. However, care will be needed when looking into reducing the carrier concentration of these materials, as eventually plasmonic effects will be prevented from the strong IR phonon absorption of ZnO and from grain-boundary scattering of the polycrystalline films.
3. X-ray photoelectron spectroscopy (XPS) depth profile studies should be performed on the optimised and un-optimised ITO samples before and after ReLA to find out how the changes in oxygen stoichiometry observed by Energy-dispersive X-ray (EDX) translate affect the density of oxygen vacancies and interstitials and thus change the carrier concentration in the bulk region of the ITO films.
4. Utilise thermal simulations (solving the $1\mathrm{D}$ heat transport equation) to investigate the depth-profile of the laser-induced heating of the ITO thin films. From such simulations, reveal how the starting film conditions and applied laser fluence affect the peak temperature and annealing time. From this correlate the peak temperature with the observed critical thresholds for Sn activation and oxygen atom migration throughout the film. Finally, incorporate the change in the optical properties with each pulse into the simulation to reveal the distinct "phases" of changes to the film that arise from an increasing number of pulses.
5. Elucidate the build-up of thermal energy in the system during multiple pulses, by investigating the influence of the repetition rate on the ReLA process, and the effect of rapid thermal expansion and ablation, by investigating the role of the ambient pressure.
6. Perform further investigations on the influence of highly oxidising environments to determine if there is a limit on the oxygen incorporation into the film and thus determine if it is possible to reduce the carrier concentration of the seed ITO films with ReLA in oxidising environments. If so, investigate whether ReLA can be used to switch the carrier concentration back and forth with subsequent pulses in different atmospheres.

7. As the activation of Sn provides only an increase in the carrier concentration, investigate simply removing Sn from the equation by investigating the role of ReLA on In_2O_3 thin films. Specifically, investigate how far ReLA can modulate the oxygen deficiency of In_2O_3 and how this translates to changes in the carrier concentration. This may provide multiple benefits: removing IR absorption peaks associated with Sn (reducing IR absorption), lowering the window of low loss plasmonics further into the IR and providing a simpler case study to further elucidate the physical mechanisms behind the ReLA induced conversion of the optoelectronic properties of TCOs.
8. Further SE investigations of TCOs for a larger variation in the carrier concentration may allow for correlation of the individual IR peaks with the carrier concentration to gain insights into whether the peaks arise from defect states arising from substitutional metal ion dopants or even oxygen vacancies. Such work may help reveal the precise source of the conductivity of TCOS, which is currently still under debate.
9. To improve the depth uniformity of post-ReLA Ito films, investigate "Layer by layer ReLA". Specifically, perform ReLA in-between rounds of thin film deposition of multiple layers where each layer is comparable to the penetration depth of the KrF laser photons in the material.

9. References

1. H. L. Lord, W. Zhan, and J. Pawliszyn, "Fundamentals and applications of needle trap devices. A critical review," Anal. Chim. Acta **677**(1), 3–18 (2010).
2. S. A. Maier, *Plasmonics: Fundamentals and Applications* (Springer US, 2007).
3. D. K. Gramotnev and S. I. Bozhevolnyi, "Plasmonics beyond the diffraction limit," Nat. Photonics **4**(2), 83–91 (2010).
4. E. Ozbay, "Plasmonics: Merging photonics and electronics at nanoscale dimensions," Science (80-.). **311**(5758), 189–193 (2006).
5. M. L. Brongersma, V. M. Shalaev, C. Rietbergen, and M. Moerbeek, "The case for plasmonics," Science (80-.). **328**(5977), 440–441 (2010).
6. H. A. Atwater and A. Polman, "Plasmonics for improved photovoltaic devices," Nat. Mater. **9**(3), 205–213 (2010).
7. S. V. Boriskina, M. A. Green, K. Catchpole, E. Yablonovitch, M. C. Beard, Y. Okada, S. Lany, T. Gershon, A. Zakutayev, M. H. Tahersima, V. J. Sorger, M. J. Naughton, K. Kempa, M. Dagenais, Y. Yao, L. Xu, X. Sheng, N. D. Bronstein, J. A. Rogers, A. P. Alivisatos, R. G. Nuzzo, J. M. Gordon, D. M. Wu, M. D. Wisser, A. Salleo, J. Dionne, P. Bermel, J. J. Greffet, I. Celanovic, M. Soljacic, A. Manor, C. Rotschild, A. Raman, L. Zhu, S. Fan, and G. Chen, "Roadmap on optical energy conversion," J. Opt. (United Kingdom) **18**(7), 0 (2016).
8. K. M. Mayer and J. H. Hafner, "Localized surface plasmon resonance sensors," Chem. Rev. **111**(6), 3828–3857 (2011).
9. R. Ziblat, V. Lirtsman, D. Davidov, and B. Aroeti, "Infrared surface plasmon resonance: A novel tool for real time sensing of variations in living cells," Biophys. J. **90**(7), 2592–2599 (2006).
10. A. Siozios, D. C. Koutsogeorgis, E. Lidorikis, G. P. Dimitrakopulos, T. Kehagias, H. Zoubos, P. Komninou, W. M. Cranton, C. Kosmidis, and P. Patsalas, "Optical encoding by plasmon-based patterning: Hard and inorganic materials become photosensitive," Nano Lett. **12**(1), 259–263 (2012).
11. F. Pincella, K. Isozaki, and K. Miki, "A visible light-driven plasmonic photocatalyst," Light Sci. Appl. **3**(e113), 1–6 (2014).
12. V. A. Zenin, S. Choudhury, S. Saha, V. M. Shalaev, A. Boltasseva, and S. I. Bozhevolnyi, "Hybrid plasmonic waveguides formed by metal coating of dielectric ridges," Opt. Express **25**(11), 12295 (2017).
13. J. A. Schuller, E. S. Barnard, W. Cai, Y. C. Jun, J. S. White, and M. L. Brongersma, "Plasmonics for extreme light concentration and manipulation," Nat. Mater. **9**(3), 193–204 (2010).
14. S. V. Boriskina, H. Ghasemi, and G. Chen, "Plasmonic materials for energy: From physics to applications," Mater. Today **16**(10), 375–386 (2013).
15. U. Guler, A. V. Kildishev, A. Boltasseva, and V. M. Shalaev, "Plasmonics on the slope of enlightenment: The role of transition metal nitrides," Faraday Discuss. **178**, 71–86 (2015).
16. A. Fafin, S. Yazidi, S. Camelio, and D. Babonneau, "Near-Field Optical Properties of AgxAu1−x Nanoparticle Chains Embedded in a Dielectric Matrix," Plasmonics **11**(5), 1407–1416 (2016).
17. A. Alù, M. G. Silveirinha, A. Salandrino, and N. Engheta, "Epsilon-near-zero metamaterials and electromagnetic sources: Tailoring the radiation phase pattern," Phys. Rev. B - Condens. Matter Mater. Phys. **75**(15), 1–37 (2007).
18. K. Marchuk and K. A. Willets, "Localized surface plasmons and hot electrons," Chem. Phys. **445**, 95–104 (2014).
19. J. Kim, G. V. Naik, N. K. Emani, U. Guler, and A. Boltasseva, "Plasmonic resonances in nanostructured transparent conducting oxide films," IEEE J. Sel. Top. Quantum Electron. **19**(3), (2013).
20. K. M. McPeak, S. V. Jayanti, S. J. P. Kress, S. Meyer, S. Iotti, A. Rossinelli, and D. J. Norris,

"Plasmonic films can easily be better: Rules and recipes," ACS Photonics **2**(3), 326–333 (2015).

21. D. A. Bobb, G. Zhu, M. Mayy, A. V. Gavrilenko, P. Mead, V. I. Gavrilenko, and M. A. Noginov, "Engineering of low-loss metal for nanoplasmonic and metamaterials applications," Appl. Phys. Lett. **95**(15), 15–18 (2009).
22. J. B. Khurgin and A. Boltasseva, "Reflecting upon the losses in plasmonics and metamaterials," MRS Bull. **37**(8), 768–779 (2012).
23. Editor, "Where now for plasmonics?," Nat. Nanotechnol. **11**(1), 1 (2016).
24. M. Kumar, N. Umezawa, S. Ishii, and T. Nagao, "Examining the Performance of Refractory Conductive Ceramics as Plasmonic Materials: A Theoretical Approach," ACS Photonics **3**(1), 43–50 (2016).
25. P. R. West, S. Ishii, G. V. Naik, N. K. Emani, V. M. Shalaev, and A. Boltasseva, "Searching for better plasmonic materials," Laser Photonics Rev. **4**(6), 795–808 (2010).
26. N. Kinsey, C. Devault, J. Kim, M. Ferrera, V. M. Shalaev, and A. Boltasseva, "Epsilon-near-zero Al-doped ZnO for ultrafast switching at telecom wavelengths," Optica **2**(7), 616 (2015).
27. M. A. Noginov, L. Gu, J. Livenere, G. Zhu, A. K. Pradhan, R. Mundle, M. Bahoura, Y. A. Barnakov, and V. A. Podolskiy, "Transparent conductive oxides: Plasmonic materials for telecom wavelengths," Appl. Phys. Lett. **99**(2), 2–5 (2011).
28. G. V. Naik, V. M. Shalaev, and A. Boltasseva, "Alternative plasmonic materials: Beyond gold and silver," Adv. Mater. **25**(24), 3264–3294 (2013).
29. A. Boltasseva and H. A. Atwater, "Low-loss plasmonic metamaterials," Science (80-.). **331**(6015), 290–291 (2011).
30. V. E. Babicheva, A. Boltasseva, and A. V. Lavrinenko, "Transparent conducting oxides for electro-optical plasmonic modulators," Nanophotonics **4**(1), 165–185 (2015).
31. J. M. McMahon, G. C. Schatz, and S. K. Gray, "Plasmonics in the ultraviolet with the poor metals Al, Ga, In, Sn, Tl, Pb, and Bi," Phys. Chem. Chem. Phys. **15**(15), 5415–5423 (2013).
32. D. Zhao, Z. Lin, W. Zhu, H. J. Lezec, T. Xu, A. Agrawal, C. Zhang, and K. Huang, "Recent advances in ultraviolet nanophotonics: From plasmonics and metamaterials to metasurfaces," Nanophotonics **10**(9), 2283–2308 (2021).
33. S. Kassavetis, B. D. Ozsdolay, N. Kalfagiannis, A. Habib, J. H. Tortai, S. Kerdsongpanya, R. Sundararaman, M. Stchakovsky, D. V. Bellas, D. Gall, and P. Patsalas, "Near-Zero Negative Real Permittivity in Far Ultraviolet: Extending Plasmonics and Photonics with B1-MoN x," J. Phys. Chem. C **123**(34), 21120–21129 (2019).
34. G. V. Naik and A. Boltasseva, "Semiconductors for plasmonics and metamaterials," Phys. Status Solidi - Rapid Res. Lett. (2010).
35. D. Li and C. Z. Ning, "All-semiconductor active plasmonic system in mid-infrared wavelengths," Opt. Express (2011).
36. A. S. Karimullah, C. Jack, R. Tullius, V. M. Rotello, G. Cooke, N. Gadegaard, L. D. Barron, and M. Kadodwala, "Disposable Plasmonics: Plastic Templated Plasmonic Metamaterials with Tunable Chirality," Adv. Mater. (2015).
37. Y. R. Leroux, J. C. Lacroix, K. I. Chane-Ching, C. Fave, N. Félidj, G. Lévi, J. Aubard, J. R. Krenn, and A. Hohenau, "Conducting polymer electrochemical switching as an easy means for designing active plasmonic devices," J. Am. Chem. Soc. (2005).
38. L. Gu, J. Livenere, G. Zhu, E. E. Narimanov, and M. A. Noginov, "Quest for organic plasmonics," Appl. Phys. Lett. **103**(2), (2013).
39. S. Chen, E. S. H. Kang, M. Shiran Chaharsoughi, V. Stanishev, P. Kühne, H. Sun, C. Wang, M. Fahlman, S. Fabiano, V. Darakchieva, and M. P. Jonsson, "Conductive polymer nanoantennas for dynamic organic plasmonics," Nat. Nanotechnol. (2020).
40. G. V Naik, J. Kim, A. Boltasseva, S. Kehr, Y. Liu, L. Martin, P. Yu, M. Gajek, S. Yang, C. Yang, M. Wenzel, R. Jacob, H. von Ribbeck, M. Helm, X. Zhang, L. Eng, R. Ramesh, K. Lim, H. Cho, T. Kim, S. Jang, Y. Suh, V. Misra, I. Yeo, J. Roh, J. W. Park, H. Yoon, K. Kim, K. Park,

and D. Ma, "Oxides and nitrides as alternative plasmonic materials in the optical range," Int. Sci. Technol. A J. Phys. D Appl. Phys (2001).

41. Y. Zhong, S. D. Malagari, T. Hamilton, and D. Wasserman, "Review of mid-infrared plasmonic materials," J. Nanophotonics **9**(1), 093791 (2015).
42. V. E. Babicheva, N. Kinsey, G. V. Naik, M. Ferrera, A. V. Lavrinenko, V. M. Shalaev, and A. Boltasseva, "Towards CMOS-compatible nanophotonics: Ultra-compact modulators using alternative plasmonic materials," Opt. Express **21**(22), 27326 (2013).
43. C. Haffner, D. Chelladurai, Y. Fedoryshyn, A. Josten, B. Baeuerle, W. Heni, T. Watanabe, T. Cui, B. Cheng, S. Saha, D. L. Elder, L. R. Dalton, A. Boltasseva, V. M. Shalaev, N. Kinsey, and J. Leuthold, "Low-loss plasmon-assisted electro-optic modulator," Nature **556**(7702), 483–486 (2018).
44. Z. Ma, Z. Li, K. Liu, C. Ye, and V. J. Sorger, "Indium-Tin-Oxide for High-performance Electro-optic Modulation," Nanophotonics **4**(1), 198–213 (2015).
45. S. Kim, J. M. Kim, J. E. Park, and J. M. Nam, "Nonnoble-Metal-Based Plasmonic Nanomaterials: Recent Advances and Future Perspectives," Adv. Mater. **30**(42), 1–24 (2018).
46. C. Rhodes, S. Franzen, J. P. Maria, M. Losego, D. N. Leonard, B. Laughlin, G. Duscher, and S. Weibel, "Surface plasmon resonance in conducting metal oxides," J. Appl. Phys. **100**(5), 054905 (2006).
47. T. Minami, "New n-type transparent conducting oxides," MRS Bull. (2000).
48. D. S. Ginley, *Handbook of Transparent Conductors* (Springer, 2011).
49. S. C. Dixon, D. O. Scanlon, C. J. Carmalt, and I. P. Parkin, "N-Type doped transparent conducting binary oxides: An overview," J. Mater. Chem. C **4**(29), 6946–6961 (2016).
50. A. Calzolari, A. Ruini, and A. Catellani, "Transparent Conductive Oxides as Near-IR Plasmonic Materials: The Case of Al-Doped ZnO Derivatives," ACS Photonics **1**(8), 703–709 (2014).
51. Z. Wang, C. Chen, K. Wu, H. Chong, and H. Ye, "Transparent Conductive Oxides and Their Applications in Near Infrared Plasmonics," Phys. Status Solidi Appl. Mater. Sci. **216**(5), 1–12 (2019).
52. Y. Wang, A. C. Overvig, S. Shrestha, R. Zhang, R. Wang, N. Yu, and L. Dal Negro, "Tunability of indium tin oxide materials for mid-infrared plasmonics applications," Opt. Mater. Express **7**(8), 2727 (2017).
53. N. Mori, S. Ooki, N. Masubuchi, A. Tanaka, M. Kogoma, and T. Ito, "Effects of postannealing in ozone environment on opto-electrical properties of Sn-doped In2O3 thin films," in *Thin Solid Films* (2002), **411**(1), pp. 6–11.
54. M. Kanehara, H. Koike, T. Yoshinaga, and T. Teranishi, "Indium tin oxide nanoparticles with compositionally tunable surface plasmon resonance frequencies in the near-IR region," J. Am. Chem. Soc. **131**(49), 17736–17737 (2009).
55. S. Q. Li, P. Guo, L. Zhang, W. Zhou, T. W. Odom, T. Seideman, J. B. Ketterson, and R. P. H. Chang, "Infrared plasmonics with indium-tin-oxide nanorod arrays," ACS Nano **5**(11), 9161–9170 (2011).
56. J. W. Kim, H. Kim, M. Y. Lee, D. Y. Lee, J. S. Lee, Y. H. Jang, J. S. Bae, J. S. Lee, and S. Park, "Atomistic aspects of carrier concentration variation in post-annealed indium tin oxide films," J. Phys. D. Appl. Phys. **48**(39), (2015).
57. S. J. Wakeham, M. J. Thwaites, B. W. Holton, C. Tsakonas, W. M. Cranton, D. C. Koutsogeorgis, and R. Ranson, "Low temperature remote plasma sputtering of indium tin oxide for flexible display applications," Thin Solid Films **518**(4), 1355–1358 (2009).
58. G. Giusti, "Deposition and Characterisation of Functional Ito Thin Films," University of Birmingham (2011).
59. S. O. Elhamali, "Material Deposition and Laser Annealing of Metal Oxide Thin Films for Electronics Fabricated At Low Temperature," Nottingham Trent University (2016).
60. M. C. Choi, Y. Kim, and C. S. Ha, "Polymers for flexible displays: From material selection

to device applications," Prog. Polym. Sci. (2008).
61. E. Yarali, C. Koutsiaki, H. Faber, K. Tetzner, E. Yengel, P. Patsalas, N. Kalfagiannis, D. C. Koutsogeorgis, and T. D. Anthopoulos, "Recent Progress in Photonic Processing of Metal-Oxide Transistors," Adv. Funct. Mater. **30**(20), 1–37 (2020).
62. A. Siozios, D. C. Koutsogeorgis, E. Lidorikis, G. P. Dimitrakopulos, N. Pliatsikas, G. Vourlias, T. Kehagias, P. Komninou, W. Cranton, C. Kosmidis, and P. Patsalas, "Laser-matter interactions, phase changes and diffusion phenomena during laser annealing of plasmonic AlN:Ag templates and their applications in optical encoding," J. Phys. D. Appl. Phys. **48**(28), 285306 (2015).
63. H. Palneedi, J. H. Park, D. Maurya, M. Peddigari, G. T. Hwang, V. Annapureddy, J. W. Kim, J. J. Choi, B. D. Hahn, S. Priya, K. J. Lee, and J. Ryu, "Laser Irradiation of Metal Oxide Films and Nanostructures: Applications and Advances," Adv. Mater. **30**(14), 1–38 (2018).
64. G. J. Bonami, *Heat Treatment: Theory, Techniques and Applications* (2011).
65. G. M. Alonzo-Medina, A. González-González, J. L. Sacedón, and A. I. Oliva, "Understanding the thermal annealing process on metallic thin films," in *IOP Conference Series: Materials Science and Engineering* (2013).
66. M. Noh, I. Seo, J. Park, J. S. Chung, Y. S. Lee, H. J. Kim, Y. J. Chang, J. H. Park, M. G. Kang, and C. Y. Kang, "Spectroscopic ellipsometry investigation on the excimer laser annealed indium tin oxide sol-gel films," Curr. Appl. Phys. **16**(2), 145–149 (2016).
67. M. Noh, Y. S. Lee, J. Park, J. S. Chung, J. K. Yang, B. W. Ko, J. W. Kim, S. Park, H. J. Kim, and Y. J. Chang, "Post-annealing effect on the optical property of indium tin oxide sputtered films," Curr. Appl. Phys. **16**(12), 1576–1580 (2016).
68. S. M. De Nicolás, D. Muñoz, C. Denis, J. F. Lerat, and T. Emeraud, "Optimisation of ITO by excimer laser annealing for a-Si:H/c-Si solar cells," in *Energy Procedia* (2012), **27**(0), pp. 586–591.
69. B. J. Li, M. Zhou, M. Ma, W. Zhang, and W. Y. Tang, "Effects of nanosecond laser irradiation on photoelectric properties of AZO/FTO composite films," Appl. Surf. Sci. **265**, 637–641 (2013).
70. S. O. El Hamali, W. M. Cranton, N. Kalfagiannis, X. Hou, R. Ranson, and D. C. Koutsogeorgis, "Enhanced electrical and optical properties of room temperature deposited Aluminium doped Zinc Oxide (AZO) thin films by excimer laser annealing," Opt. Lasers Eng. **80**, 45–51 (2016).
71. G. Barbillon, *Nanoplasmonics - Fundamentals and Applications* (InTech, 2017).
72. D. M. Mattox, *Handbook of Physical Vapor Deposition (PVD) Processing* (2007).
73. J. A. Thornton, "Magnetron Sputtering: Basic Physics and Application To Cylindrical Magnetrons.," J Vac Sci Technol **15**(2), 171–177 (1978).
74. A. L. Dawar and J. C. Joshi, "Semiconducting transparent thin films: their properties and applications," J. Mater. Sci. (1984).
75. W. Kern and J. L. Vossen, *Thin Film Processes II* (2012).
76. D. Basting and G. Marowsky, *Excimer Laser Technology* (2005).
77. M. S. Brown and C. B. Arnold, "Fundamentals of Laser-Material Interaction and Application to Multiscale Surface Modification," in *Springer Series in Materials Science* (2010).
78. T. T. Chen and C. Y. Chang, "The effects of annealing parameters on the evolution of surface morphology of A-Si thin films irradiated by ArF excimer laser," Chung Cheng Ling Hsueh Pao/Journal Chung Cheng Inst. Technol. **34**(2), 171–184 (2006).
79. M. Warzecha, J. I. Owen, M. Wimmer, F. Ruske, J. Hotovy, and J. Hüpkes, "High mobility annealing of transparent conductive oxides," in *IOP Conference Series: Materials Science and Engineering* (2012), **34**(1).
80. R. P. Howson, "The reactive sputtering of oxides and nitrides," Pure Appl. Chem. (1994).
81. D. Depla, S. Mahieu, and J. E. Greene, "Sputter Deposition Processes," in *Handbook of Deposition Technologies for Films and Coatings* (2010).

82. H. G. Tompkins, *Handbook of Ellipsometry* (Springer, 2005).
83. H. G. Tompkins and J. N. Hilfiker, *Spectroscopic Ellipsometry Practical Application to Thin Film Characterization* (Momentum Press, 2016).
84. J. W. Weber, T. A. R. Hansen, M. C. M. Van De Sanden, and R. Engeln, "B-spline parametrization of the dielectric function applied to spectroscopic ellipsometry on amorphous carbon," J. Appl. Phys. (2009).
85. D. Gonçalves and E. A. Irene, "Fundamentals and applications of spectroscopic ellipsometry," Quim. Nova (2002).
86. L. Dominici, F. Michelotti, T. M. Brown, A. Reale, and A. Di Carlo, "Plasmon polaritons in the near infrared on fluorine doped tin oxide films," Opt. Express **17**(12), 10155 (2009).
87. S. G. Lim, S. Kriventsov, T. N. Jackson, J. H. Haeni, D. G. Schlom, A. M. Balbashov, R. Uecker, P. Reiche, J. L. Freeouf, and G. Lucovsky, "Dielectric functions and optical bandgaps of high- K dielectrics for metal-oxide-semiconductor field-effect transistors by far ultraviolet spectroscopic ellipsometry," J. Appl. Phys. (2002).
88. D. E. Aspnes, J. B. Theeten, and F. Hottier, "Investigation of effective-medium models of microscopic surface roughness by spectroscopic ellipsometry," Phys. Rev. B (1979).
89. A. A. Y. Guilbert, M. Schmidt, A. Bruno, J. Yao, S. King, S. M. Tuladhar, T. Kirchartz, M. I. Alonso, A. R. Goñi, N. Stingelin, S. A. Haque, M. Campoy-Quiles, and J. Nelson, "Spectroscopic evaluation of mixing and crystallinity of fullerenes in bulk heterojunctions," Adv. Funct. Mater. (2014).
90. A. M. Jubb and H. C. Allen, "Vibrational spectroscopic characterization of hematite, maghemite, and magnetite thin films produced by vapor deposition," ACS Appl. Mater. Interfaces (2010).
91. E. H. Korte and A. Röseler, "Infrared spectroscopic ellipsometry: A tool for characterizing nanometer layers," in *Analyst* (1998).
92. M. Thönissen, S. Billat, M. Krüger, H. Lüth, M. G. Berger, U. Frotscher, and U. Rossow, "Depth inhomogeneity of porous silicon layers," J. Appl. Phys. (1996).
93. A. Kasic, M. Schubert, S. Einfeldt, D. Hommel, and T. E. Tiwald, "Free-carrier and phonon properties of n- and p-type hexagonal GaN films measured by infrared ellipsometry," Phys. Rev. B - Condens. Matter Mater. Phys. **62**(11), 7365–7377 (2000).
94. L. A. A. Pettersson, F. Carlsson, O. Inganäs, and H. Arwin, "Spectroscopic ellipsometry studies of the optical properties of doped poly(3,4-etnylenedioxythiophene): An anisotropic metal," Thin Solid Films (1998).
95. B. Drévillon, "Spectroscopic ellipsometry in the infrared range," Thin Solid Films (1998).
96. M. F. Saenger, M. Schädel, T. Hofmann, J. Hilfiker, J. Sun, T. Tiwald, M. Schubert, and J. A. Woollam, "Infrared ellipsometric characterization of silicon nitride films on textured Si photovoltaic cells," in *Materials Research Society Symposium Proceedings* (2009).
97. H. G. Tompkins, T. Tiwald, C. Bungay, and A. E. Hooper, "Use of Molecular Vibrations to Analyze Very Thin Films with Infrared Ellipsometry," J. Phys. Chem. B (2004).
98. T. I. Willett-Gies, C. M. Nelson, L. S. Abdallah, and S. Zollner, "Two-phonon absorption in LiF and NiO from infrared ellipsometry," J. Vac. Sci. Technol. A Vacuum, Surfaces, Film. (2015).
99. K. moh Lin, S. W. Wu, S. B. Wang, L. Y. Li, and Y. Sawada, "Spectroscopic ellipsometry study of compound-induced changes in chemical and optical properties of In2O3:Sn–ZnO:Al films," Thin Solid Films **618**, 107–113 (2016).
100. K. Postava, H. Sueki, M. Aoyama, T. Yamaguchi, K. Murakami, and Y. Igasaki, "Doping effects on optical properties of epitaxial ZnO layers determined by spectroscopic ellipsometry," Appl. Surf. Sci. (2001).
101. S. Schöche, T. Hofmann, V. Darakchieva, N. Ben Sedrine, X. Wang, A. Yoshikawa, and M. Schubert, "Infrared to vacuum-ultraviolet ellipsometry and optical Hall-effect study of free-charge carrier parameters in Mg-doped InN," J. Appl. Phys. **113**(1), (2013).
102. T. E. Tiwald, D. W. Thompson, J. A. Woollam, W. Paulson, and R. Hance, "Application of

IR variable angle spectroscopic ellipsometry to the determination of free carrier concentration depth profiles," Thin Solid Films **313**–**314**, 661–666 (1998).

103. A. A. Kukharskii, "Plasmon-phonon coupling in GaAs," Solid State Commun. **13**(11), 1761–1765 (1973).
104. F. Gervais and J. F. Baumard, "Lo phonon-plasmon coupling in non-stoichiometric rutile TiO2," Solid State Commun. (1977).
105. S. Zollner, P. P. Paradis, F. Abadizaman, and N. S. Samarasingha, "Drude and Kukharskii mobility of doped semiconductors extracted from Fourier-transform infrared ellipsometry spectra," J. Vac. Sci. Technol. B **37**(1), 012904 (2019).
106. A. A. Toropov and T. V. Shubina, *Plasmonic Effects in Metal-Semiconductor Nanostructures* (Oxford University Press, 2015).
107. M. Fox, *Optical Properties of Solids* (Oxford Univeristy Press, 2010).
108. D. J. Griffiths, *Introduction to Electrodynamics*, 4th ed. (Cambridge University Press, 2017).
109. V. Barcilon and N. Bleistein, "Mathematical Methods for Wave Phenomena.," Math. Comput. (1986).
110. M. Fox and G. F. Bertsch, *Optical Properties of Solids* (Oxford Univeristy Press, 2016).
111. M. N. Berberan-Santos, "Beer’s law revisited," J. Chem. Educ. (1990).
112. J. Chalker, "Quantum Theory of Condensed Matter," Michaelmas Term (2013).
113. S. Kasap, *Principles of Electronic Materials and Devices*, Fourth (McGraw-Hill Education, 2017).
114. G. D. Mahan and F. Claro, "Nonlocal theory of thermal conductivity," Phys. Rev. B (1988).
115. R. J. Mendelsberg, G. Garcia, and D. J. Milliron, "Extracting reliable electronic properties from transmission spectra of indium tin oxide thin films and nanocrystal films by careful application of the Drude theory," J. Appl. Phys. **111**(6), (2012).
116. Y. K. Koh and D. G. Cahill, "Frequency dependence of the thermal conductivity of semiconductor alloys," Phys. Rev. B - Condens. Matter Mater. Phys. (2007).
117. D. K. Schroder, *Semiconductor Material and Device Characterization: Third Edition* (2005).
118. H. Fujiwara and M. Kondo, "Effects of carrier concentration on the dielectric function of ZnO:Ga and In 2O 3:Sn studied by spectroscopic ellipsometry: Analysis of free-carrier and band-edge absorption," Phys. Rev. B - Condens. Matter Mater. Phys. **71**(7), 1–10 (2005).
119. I. R. Hooper and W. L. Barnes, "The basics of plasmonics," in *Handbook of Surface Science* (Elsevier B.V., 2014), **4**, pp. 37–74.
120. A. Siozios, "Wide-band gap semiconductors with noble metals for photonic applications.," University of Ioannina (2014).
121. D. Slocombe, A. Porch, M. Pepper, and P. P. Edwards, "The Mott transition and optimal performance of transparent conducting oxides in thin-film solar cells," Energy Environ. Sci. (2012).
122. B. Szyszka, P. Loebmann, A. Georg, C. May, and C. Elsaesser, "Development of new transparent conductors and device applications utilizing a multidisciplinary approach," Thin Solid Films **518**(11), 3109–3114 (2010).
123. H. Liu, V. Avrutin, N. Izyumskaya, Ü. Özgr, and H. Morkoç, "Transparent conducting oxides for electrode applications in light emitting and absorbing devices," Superlattices Microstruct. **48**(5), 458–484 (2010).
124. K. Ellmer, "Past achievements and future challenges in the development of optically transparent electrodes," Nat. Photonics **6**(12), 809–817 (2012).
125. C. G. Granqvist, "Transparent conductors as solar energy materials: A panoramic review," Sol. Energy Mater. Sol. Cells (2007).
126. C. G. Granqvist, "Electrochromics for smart windows: Oxide-based thin films and devices," Thin Solid Films (2014).
127. C. G. Granqvist, "Transparent conductors for solar energy and energy efficiency: A broad-brush picture," Int. J. Nanotechnol. (2009).

128. O. Warschkow, L. Miljacic, D. E. Ellis, G. González, and T. O. Mason, "Interstitial oxygen in tin-doped indium oxide transparent conductors," J. Am. Ceram. Soc. **89**(2), 616–619 (2006).
129. M. Bazzani, A. Neroni, A. Calzolari, and A. Catellani, "Optoelectronic properties of Al:ZnO: Critical dosage for an optimal transparent conductive oxide," Appl. Phys. Lett. **98**(12), (2011).
130. J. E. Medvedeva and C. L. Hettiarachchi, "Tuning the properties of complex transparent conducting oxides: Role of crystal symmetry, chemical composition, and carrier generation," Phys. Rev. B - Condens. Matter Mater. Phys. **81**, (2010).
131. A. Janotti and C. G. Van De Walle, "Oxygen vacancies in ZnO," Appl. Phys. Lett. **87**(12), 1–3 (2005).
132. J. Buckeridge, C. R. A. Catlow, M. R. Farrow, A. J. Logsdail, D. O. Scanlon, T. W. Keal, P. Sherwood, S. M. Woodley, A. A. Sokol, and A. Walsh, "Deep vs shallow nature of oxygen vacancies and consequent n -type carrier concentrations in transparent conducting oxides," Phys. Rev. Mater. **2**(5), 054604 (2018).
133. J. R. Bellingham, A. P. Mackenzie, and W. A. Phillips, "Precise measurements of oxygen content: Oxygen vacancies in transparent conducting indium oxide films," Appl. Phys. Lett. **58**(22), 2506–2508 (1991).
134. S. Nigo, M. Kubota, Y. Harada, T. Hirayama, S. Kato, H. Kitazawa, and G. Kido, "Conduction band caused by oxygen vacancies in aluminum oxide for resistance random access memory," J. Appl. Phys. **112**(3), 033711 (2012).
135. H. Hosono, "Recent progress in transparent oxide semiconductors: Materials and device application," Thin Solid Films (2007).
136. Z. Z. You and G. J. Hua, "Electrical, optical and microstructural properties of transparent conducting GZO thin films deposited by magnetron sputtering," J. Alloys Compd. **530**, 11–17 (2012).
137. S. H. Keshmiri, M. Rezaee-Roknabadi, and S. Ashok, "A novel technique for increasing electron mobility of indium-tin-oxide transparent conducting films," Thin Solid Films **413**(1–2), 167–170 (2002).
138. V. Teixeira, H. N. Cui, L. J. Meng, E. Fortunato, and R. Martins, "Amorphous ITO thin films prepared bya DC sputtering for electrochromic applications," Thin Solid Films **420**–**421**, 70–75 (2002).
139. S. A. Kamaruddin, K. Y. Chan, H. K. Yow, M. Zainizan Sahdan, H. Saim, and D. Knipp, "Zinc oxide films prepared by sol-gel spin coating technique," Appl. Phys. A Mater. Sci. Process. **104**(1), 263–268 (2011).
140. Y. Natsume and H. Sakata, "Zinc oxide films prepared by sol-gel spin-coating," Thin Solid Films **372**(1), 30–36 (2000).
141. B. Stjerna, E. Olsson, and C. G. Granqvist, "Optical and electrical properties of radio frequency sputtered tin oxide films doped with oxygen vacancies, F, Sb, or Mo," J. Appl. Phys. **76**(6), 3797–3817 (1994).
142. M. F. A. M. Van Hest, M. S. Dabney, J. D. Perkins, D. S. Ginley, and M. P. Taylor, "Titanium-doped indium oxide: A high-mobility transparent conductor," Appl. Phys. Lett. (2005).
143. M. Batzill and U. Diebold, "The surface and materials science of tin oxide," Prog. Surf. Sci. (2005).
144. J. E. Medvedeva and A. J. Freeman, "Combining high conductivity with complete optical transparency: A band structure approach," Europhys. Lett. **69**(4), 583–587 (2005).
145. G. J. Exarhos and X. D. Zhou, "Discovery-based design of transparent conducting oxide films," Thin Solid Films **515**(18), 7025–7052 (2007).
146. M. Khuili, N. Fazouan, H. A. El Makarim, G. El Hallani, and E. H. Atmani, "First principle study of structural, electronic, optical and electrical properties of Ga doped ZnO with GGA and mBJ approximations," in *Journal of Physics: Conference Series* (2016), **758**(1).
147. A. Jiamprasertboon, A. Waehayee, N. Chanlek, N. Yong, S. Suthirakun, and T. Siritanon,

"Understanding structure, optical, and electrical properties of In4Sn3O12 and In4.5Sn2M0.5O12 (M = Nb and Ta)," J. Alloys Compd. **783**(December), 28–36 (2019).
148. O. Warschkow, D. E. Ellis, G. B. González, and T. O. Mason, "Defect Structures of Tin-Doped Indium Oxide," J. Am. Ceram. Soc. **706**(10), 1700 (2003).
149. A. Catellani, A. Ruini, G. Cicero, and A. Calzolari, "First principles description of the electronic properties of doped ZnO," Phys. Status Solidi Basic Res. **250**(10), 2106–2109 (2013).
150. A. Catellani, A. Ruini, and A. Calzolari, "Optoelectronic properties and color chemistry of native point defects in Al:ZnO transparent conductive oxide," J. Mater. Chem. C **3**(32), 8419–8424 (2015).
151. E. L. Runnerstrom, A. Bergerud, A. Agrawal, R. W. Johns, C. J. Dahlman, A. Singh, S. M. Selbach, and D. J. Milliron, "Defect Engineering in Plasmonic Metal Oxide Nanocrystals," Nano Lett. **16**(5), 3390–3398 (2016).
152. A. Zunger, "Practical doping principles," Appl. Phys. Lett. **83**(1), 57–59 (2003).
153. C. Agashe, O. Kluth, J. Hüpkes, U. Zastrow, B. Rech, and M. Wuttig, "Efforts to improve carrier mobility in radio frequency sputtered aluminum doped zinc oxide films," J. Appl. Phys. **95**(4), 1911–1917 (2004).
154. D. S. Ginley and C. Bright, "Transparent conducting oxides," MRS Bull. **25**(8), 15–21 (2000).
155. M. Lorenz, M. S. Ramachandra Rao, T. Venkatesan, E. Fortunato, P. Barquinha, R. Branquinho, D. Salgueiro, R. Martins, E. Carlos, A. Liu, F. K. Shan, M. Grundmann, H. Boschker, J. Mukherjee, M. Priyadarshini, N. Dasgupta, D. J. Rogers, F. H. Teherani, E. V. Sandana, P. Bove, K. Rietwyk, A. Zaban, A. Veziridis, A. Weidenkaff, M. Muralidhar, M. Murakami, S. Abel, J. Fompeyrine, J. Zuniga-Perez, R. Ramesh, N. A. Spaldin, S. Ostanin, V. Borisov, I. Mertig, V. Lazenka, G. Srinivasan, W. Prellier, M. Uchida, M. Kawasaki, R. Pentcheva, P. Gegenwart, F. Miletto Granozio, J. Fontcuberta, and N. Pryds, "The 2016 oxide electronic materials and oxide interfaces roadmap," J. Phys. D. Appl. Phys. **49**(43), 433001 (2016).
156. O. Bierwagen and J. S. Speck, "High electron mobility In2O3(001) and (111) thin films with nondegenerate electron concentration," Appl. Phys. Lett. **97**(7), 3–6 (2010).
157. W. Seiler, M. Nistor, C. Hebert, and J. Perrière, "Epitaxial undoped indium oxide thin films: STRUCTURAL and physical properties," Sol. Energy Mater. Sol. Cells **116**, 34–42 (2013).
158. Y. Zhang, J. Xu, S. Shi, Y. Gao, C. Wang, X. Zhang, S. Yin, and L. Li, "Development of Solution-Processed ZnO Nanorod Arrays Based Photodetectors and the Improvement of UV Photoresponse via AZO Seed Layers," ACS Appl. Mater. Interfaces **8**(34), 22647–22657 (2016).
159. S. Dellis, N. Pliatsikas, N. Kalfagiannis, O. Lidor-Shalev, A. Papaderakis, G. Vourlias, S. Sotiropoulos, D. C. Koutsogeorgis, Y. Mastai, and P. Patsalas, "Broadband luminescence in defect-engineered electrochemically produced porous Si/ZnO nanostructures," Sci. Rep. (2018).
160. S. Dellis, N. Kalfagiannis, S. Kassavetis, C. Bazioti, G. P. Dimitrakopulos, D. C. Koutsogeorgis, and P. Patsalas, "Photoluminescence enhancement of ZnO via coupling with surface plasmons on Al thin films," J. Appl. Phys. (2017).
161. European Commission, "Critical raw materials for the EU," Eucom (2010).
162. B. Azzopardi, C. J. M. Emmott, A. Urbina, F. C. Krebs, J. Mutale, and J. Nelson, "Economic assessment of solar electricity production from organic-based photovoltaic modules in a domestic environment," Energy Environ. Sci. (2011).
163. G. V. Naik, J. Liu, A. V. Kildishev, V. M. Shalaev, and A. Boltasseva, "Demonstration of Al:ZnO as a plasmonic component for near-infrared metamaterials," Proc. Natl. Acad. Sci. U. S. A. **109**(23), 8834–8838 (2012).
164. Y. Wang, A. Capretti, and L. Dal Negro, "Wide tuning of the optical and structural properties of alternative plasmonic materials," Opt. Mater. Express **5**(11), 2415 (2015).

165. J. Gao, K. Kempa, M. Giersig, E. M. Akinoglu, B. Han, and R. Li, "Physics of transparent conductors," Adv. Phys. **65**(6), 553–617 (2016).
166. N. Nadaud, N. Lequeux, M. Nanot, J. Jové, and T. Roisnel, "Structural studies of tin-doped indium oxide (ITO) and In4Sn3O12," J. Solid State Chem. **135**(1), 140–148 (1998).
167. M. Marezio, " Refinement of the crystal structure of In 2 O 3 at two wavelengths ," Acta Crystallogr. (1966).
168. M. Jothibas, C. Manoharan, S. Ramalingam, S. Dhanapandian, S. Johnson Jeyakumar, and M. Bououdina, "Preparation, characterization, spectroscopic (FT-IR, FT-Raman, UV and visible) studies, optical properties and Kubo agap analysis of In 2O3 thin films," J. Mol. Struct. **1049**, 239–249 (2013).
169. A. S. A. C. Diniz and C. J. Kiely, "Crystallisation of indium-tin-oxide (ITO) thin films," Renew. Energy **29**(13), 2037–2051 (2004).
170. K. Naoi, Y. Nagano, and W. Naoi, "Transparent Conductors - A Status Review," Thin Solid Films **102**(256), 1–3 (2013).
171. A. Rogozin, M. Vinnichenko, N. Shevchenko, U. Kreissig, A. Kolitsch, and W. Möller, "Real-time evolution of electrical properties and structure of indium oxide and indium tin oxide during crystallization," Scr. Mater. **60**(4), 199–202 (2009).
172. T. J. Coutts, D. L. Young, and T. A. Gessert, "Modeling, Characterization, and Properties of Transparent Conducting Oxides," in *Handbook of Transparent Conductors* (2011).
173. Ü. Özgür, Y. I. Alivov, C. Liu, A. Teke, M. A. Reshchikov, S. Doğan, V. Avrutin, S. J. Cho, and H. Morkọ, "A comprehensive review of ZnO materials and devices," J. Appl. Phys. **98**(4), 1–103 (2005).
174. D. R. Lide, "CRC Handbook of Chemistry and Physics, Internet Version 2005," CRC Press. Taylor Fr. Boca Rat. FL (2005).
175. J. Klingshirn, C.F., Waag, A., Hoffman, A., Geurts, *Zinc Oxide Zinc Oxide From Fundamental Properties Towards Novel Applications* (2013).
176. S. Jin, Y. Yang, J. E. Medvedeva, J. R. Ireland, A. W. Metz, J. Ni, C. R. Kannewurf, A. J. Freeman, and T. J. Marks, "Dopant ion size and electronic structure effects on transparent conducting oxides. Sc-doped CdO thin films grown by MOCVD," J. Am. Chem. Soc. **126**(42), 13787–13793 (2004).
177. J. C. C. Fan and J. B. Goodenough, "X-ray photoemission spectroscopy studies of Sn-doped indium-oxide films," J. Appl. Phys. **48**(8), 3524–3531 (1977).
178. H. Hosono, M. Yasukawa, and H. Kawazoe, "Novel oxide amorphous semiconductors: Transparent conducting amorphous oxides," J. Non. Cryst. Solids (1996).
179. K. Nomura, H. Ohta, A. Takagi, T. Kamiya, M. Hirano, and H. Hosono, "Room-temperature fabrication of transparent flexible thin-film transistors using amorphous oxide semiconductors," Nature (2004).
180. T. Kamiya and H. Hosono, "Material characteristics and applications of transparent amorphous oxide semiconductors," NPG Asia Mater. (2010).
181. T. Kamiya, K. Nomura, and H. Hosono, "Origins of High Mobility and Low Operation Voltage of Amorphous Oxide TFTs: Electronic Structure, Electron Transport, Defects and Doping*," J. Disp. Technol. (2009).
182. H. Odaka, Y. Shigesato, T. Murakami, and S. Iwata, "Electronic structure analyses of Sn-doped In2O3," Japanese J. Appl. Physics, Part 1 Regul. Pap. Short Notes Rev. Pap. (2001).
183. Y. Mi, H. Odaka, and S. Iwata, "Electronic structures and optical properties of ZnO, SnO2 and In2O3," Japanese J. Appl. Physics, Part 1 Regul. Pap. Short Notes Rev. Pap. (1999).
184. O. N. Mryasov and A. J. Freeman, "Electronic band structure of indium tin oxide and criteria for transparent conducting behavior," Phys. Rev. B - Condens. Matter Mater. Phys. (2001).
185. M. Feneberg, J. Nixdorf, C. Lidig, R. Goldhahn, Z. Galazka, O. Bierwagen, and J. S. Speck, "Many-electron effects on the dielectric function of cubic In2 O3: Effective electron mass, band nonparabolicity, band gap renormalization, and Burstein-Moss shift," Phys. Rev. B

93(4), (2016).

186. A. Walsh, J. L. F. Da Silva, S.-H. Wei, C. Körber, A. Klein, L. F. J. Piper, A. DeMasi, K. E. Smith, G. Panaccione, P. Torelli, D. J. Payne, A. Bourlange, and R. G. Egdell, "Nature of the Band Gap of <math display="inline"> <msub> <mi>In</mi> <mn>2</mn> </msub> <msub> <mi mathvariant="normal">O</mi> <mn>3</mn> </msub> </math> Revealed by First-Principles Calculations and X-Ray Spectroscopy," Phys. Rev. Lett. (2008).
187. M. Batzill and U. Diebold, "The surface and materials science of tin oxide," Prog. Surf. Sci. **79**(2–4), 47–154 (2005).
188. F. A. Kröger and H. J. Vink, "Relations between the Concentrations of Imperfections in Crystalline Solids," Solid State Phys. - Adv. Res. Appl. (1956).
189. N. F. Mott, "Metal-Insulator Transitions," Pure Appl. Chem. (1980).
190. N. F. Mott, "Conduction in non-crystalline materials," Philos. Mag. (1969).
191. K. H. L. Zhang, D. J. Payne, R. G. Palgrave, V. K. Lazarov, W. Chen, A. T. S. Wee, C. F. McConville, P. D. C. King, T. D. Veal, G. Panaccione, P. Lacovig, and R. G. Egdell, "Surface structure and electronic properties of in2O3(111) single-crystal thin films grown on Y-stabilized zrO2(111)," Chem. Mater. (2009).
192. J. C. Inkson and D. Ter Haar, " Many-Body Theory of Solids: An Introduction ," Phys. Today (1985).
193. I. Hamberg and C. G. Granqvist, "Evaporated Sn-doped In2O3 films: Basic optical properties and applications to energy-efficient windows," J. Appl. Phys. (1986).
194. B. E. Sernelius, K. F. Berggren, Z. C. Jin, I. Hamberg, and C. G. Granqvist, "Band-gap tailoring of ZnO by means of heavy Al doping," Phys. Rev. B (1988).
195. V. A. Fonoberov and A. A. Balandin, "ZnO Quantum Dots: Physical Properties and Optoelectronic Applications," J. Nanoelectron. Optoelectron. (2006).
196. P. P. Edwards and M. J. Sienko, "Universality aspects of the metal-nonmetal transition in condensed media," Phys. Rev. B (1978).
197. A. Kohan, G. Ceder, D. Morgan, and C. G. Van de Walle, "First-principles study of native point defects in ZnO," Phys. Rev. B - Condens. Matter Mater. Phys. (2000).
198. A. Schleife, F. Fuchs, J. Furthmüller, and F. Bechstedt, "First-principles study of ground- and excited-state properties of MgO, ZnO, and CdO polymorphs," Phys. Rev. B - Condens. Matter Mater. Phys. (2006).
199. C. G. Van De Walle, "Hydrogen as a cause of doping in zinc oxide," Phys. Rev. Lett. (2000).
200. D. C. Look, J. W. Hemsky, and J. R. Sizelove, "Residual native shallow donor in ZnO," Phys. Rev. Lett. **82**(12), 2552–2555 (1999).
201. P. D. C. King, R. L. Lichti, Y. G. Celebi, J. M. Gil, R. C. Vilão, H. V. Alberto, J. Piroto Duarte, D. J. Payne, R. G. Egdell, I. McKenzie, C. F. McConville, S. F. J. Cox, and T. D. Veal, "Shallow donor state of hydrogen in In2 O3 and SnO2: Implications for conductivity in transparent conducting oxides," Phys. Rev. B - Condens. Matter Mater. Phys. **80**(8), 1–4 (2009).
202. Ç. Kılıç and A. Zunger, "Origins of coexistence of conductivity and transparency in SnO2," Phys. Rev. Lett. **88**(9), 955011–955014 (2002).
203. D. C. Look, G. C. Farlow, P. Reunchan, S. Limpijumnong, S. B. Zhang, and K. Nordlund, "Evidence for native-defect donors in n-type ZnO," Phys. Rev. Lett. **95**(22), 1–4 (2005).
204. E. A. Davis, S. P. Cottrell, P. J. King, J. S. Lord, J. M. Gil, H. V. Alberto, R. C. Vilão, J. Piroto Duarte, N. Ayres de Campos, A. Weidinger, R. L. Lichti, S. J. Irvine, and S. F. Cox, "Experimental confirmation of the predicted shallow donor hydrogen state in zinc oxide," Phys. Rev. Lett. (2001).
205. D. M. Hofmann, A. Hofstaetter, F. Leiter, H. Zhou, F. Henecker, B. K. Meyer, S. B. Orlinskii, J. Schmidt, and P. G. Baranov, "Hydrogen: A Relevant Shallow Donor in Zinc Oxide," Phys. Rev. Lett. (2002).
206. S. Husein, M. Stuckelberger, B. West, L. Ding, F. Dauzou, M. Morales-Masis, M. Duchamp, Z. Holman, and M. I. Bertoni, "Carrier scattering mechanisms limiting mobility in hydrogen-doped indium oxide," J. Appl. Phys. **123**(24), 245102 (2018).

207. J. H. Noh, H. S. Jung, J. K. Lee, J. Y. Kim, C. M. Cho, J. S. An, and K. S. Hong, "Reversible change in electrical and optical properties in epitaxially grown Al-doped ZnO thin films," J. Appl. Phys. **104**(7), 073706 (2008).
208. A. Janotti and C. G. Van De Walle, "Hydrogen multicentre bonds," Nat. Mater. **6**(1), 44–47 (2007).
209. J. J. Meléndez and M. Wierzbowska, "In2O3 Doped with Hydrogen: Electronic Structure and Optical Properties from the Pseudopotential Self-Interaction Corrected Density Functional Theory and the Random Phase Approximation," J. Phys. Chem. C (2016).
210. O. Caporaletti, "Electrical and optical properties of bias sputtered ZnO thin films," Sol. Energy Mater. (1982).
211. Z. Yuan, X. Zhu, X. Wang, X. Cai, B. Zhang, D. Qiu, and H. Wu, "Annealing effects of In2O3 thin films on electrical properties and application in thin film transistors," Thin Solid Films (2011).
212. K. Ellmer, "Resistivity of polycrystalline zinc oxide films: Current status and physical limit," J. Phys. D. Appl. Phys. **34**(21), 3097–3108 (2001).
213. J. H. W. De Wit, "Electrical properties of In2O3," J. Solid State Chem. (1973).
214. Z. Ovadyahu, B. Ovryn, and H. W. Kraner, "Microstructure and Electro-Optical Properties of Evaporated Indium-Oxide Films," J. Electrochem. Soc. (1983).
215. C. A. Pan and T. P. Ma, "High-quality transparent conductive indium oxide films prepared by thermal evaporation," Appl. Phys. Lett. (1980).
216. G. B. González, T. O. Mason, J. P. Quintana, O. Warschkow, D. E. Ellis, J. H. Hwang, J. P. Hodges, and J. D. Jorgensen, "Defect structure studies of bulk and nano-indium-tin oxide," J. Appl. Phys. **96**(7), (2004).
217. T. Minami, T. Kakumu, Y. Takeda, and S. Takata, "Highly transparent and conductive ZnO�In2O3 thin films prepared by d.c. magnetron sputtering," Thin Solid Films **290**–**291**, 1–5 (1996).
218. F. Ye, X. M. Cai, X. Zhong, X. Q. Tian, S. Y. Jing, L. B. Huang, V. A. L. Roy, D. P. Zhang, P. Fan, J. T. Luo, Z. H. Zheng, and G. X. Liang, "The electrical and optical properties of Cu-doped In2O 3 thin films," Thin Solid Films **556**, 44–47 (2014).
219. C. Manoharan, M. Jothibas, S. J. Jeyakumar, and S. Dhanapandian, "Structural, optical and electrical properties of Zr-doped In2O3 thin films," Spectrochim. Acta Part A Mol. Biomol. Spectrosc. **145**, 47–53 (2015).
220. B. Macco, H. C. M. Knoops, and W. M. M. Kessels, "Electron Scattering and Doping Mechanisms in Solid-Phase-Crystallized In2O3:H Prepared by Atomic Layer Deposition," ACS Appl. Mater. Interfaces **7**(30), 16723–16729 (2015).
221. S. Limpijumnong, P. Reunchan, A. Janotti, and C. G. Van De Walle, "Hydrogen doping in indium oxide: An ab initio study," Phys. Rev. B - Condens. Matter Mater. Phys. (2009).
222. Y. R. Park, D. Jung, K. C. Kim, S. J. Suh, T. S. Park, and Y. S. Kim, "Physical properties of transparent conducting indium doped zinc oxide thin films deposited by pulsed DC magnetron sputtering," J. Electroceramics **23**(2–4), 536–541 (2009).
223. T. Minami, H. Sato, H. Nanto, and S. Takata, "Highly conductive and transparent silicon doped zinc oxide thin films prepared by rf magnetron sputtering," Jpn. J. Appl. Phys. **25**(9), L776–L779 (1986).
224. T. Minami, T. Yamamoto, and T. Miyata, "Highly transparent and conductive rare earth-doped ZnO thin films prepared by magnetron sputtering," Thin Solid Films **366**(1–2), 63–68 (2000).
225. H. Liang and R. G. Gordon, "Atmospheric pressure chemical vapor deposition of transparent conducting films of fluorine doped zinc oxide and their application to amorphous silicon solar cells," J. Mater. Sci. (2007).
226. T. Minami, "New n-type transparent conducting oxides," MRS Bull. **25**(8), 38–44 (2000).
227. K. Ellmer and R. Mientus, "Carrier transport in polycrystalline ITO and ZnO:Al II: The influence of grain barriers and boundaries," Thin Solid Films **516**(17), 5829–5835 (2008).

228. K. Ellmer, "Resistivity of polycrystalline zinc oxide films: Current status and physical limit," J. Phys. D. Appl. Phys. (2001).
229. A. Bikowski, "The Relation between the Deposition Process and the Structural , Electronic , and Transport Properties of Magnetron Sputtered Doped ZnO and Zn 1-x Mg x O Films," Humboldt-Universität zu Berlin (2014).
230. J. R. Bellingham, W. A. Phillips, and C. J. Adkins, "Electrical and optical properties of amorphous indium oxide," J. Phys. Condens. Matter (1990).
231. E. Conwell and V. F. Weisskopf, "Theory of impurity scattering in semiconductors," Phys. Rev. (1950).
232. D. Chattopadhyay and H. J. Queisser, "Electron scattering by ionized impurities in semiconductors," Rev. Mod. Phys. (1981).
233. W. Shockley and W. T. Read, "Statistics of the recombinations of holes and electrons," Phys. Rev. (1952).
234. G. Masetti, M. Severi, and S. Solmi, "Modeling of Carrier Mobility Against Carrier Concentration in Arsenic-, Phosphorus-, and Boron-Doped Silicon," IEEE Trans. Electron Devices **30**(7), 764–769 (1983).
235. T. E. Haynes and D. C. Paine, "Lattice Defects in OC Implanted Tin-Doped Indium Oxide Films," Jpn. J. Appl. Phys. (1993).
236. G. Frank and H. Köstlin, "Electrical properties and defect model of tin-doped indium oxide layers," Appl. Phys. A Solids Surfaces (1982).
237. C. Erginsoy, "Neutral impurity scattering in semiconductors," Phys. Rev. (1950).
238. J. Nomoto, H. Makino, and T. Yamamoto, "Carrier mobility of highly transparent conductive Al-doped ZnO polycrystalline films deposited by radio-frequency, direct-current, and radio-frequency-superimposed direct-current magnetron sputtering: Grain boundary effect and scattering in the grain bulk," J. Appl. Phys. **117**(4), (2015).
239. Z. Zhang, C. Bao, W. Yao, S. Ma, L. Zhang, and S. Hou, "Influence of deposition temperature on the crystallinity of Al-doped ZnO thin films at glass substrates prepared by RF magnetron sputtering method," Superlattices Microstruct. **49**(6), 644–653 (2011).
240. J. Y. W. Seto, "The electrical properties of polycrystalline silicon films," J. Appl. Phys. **46**(12), 5247–5254 (1975).
241. K. Ellmer, A. Klein, and B. Rech, "Transparent Conductive Zinc Oxide Basics and Applications in Thin Film Solar Cells," Springer **239**(4836), 125 (1988).
242. D. H. Zhang, "Adsorption and photodesorption of oxygen on the surface and crystallite interfaces of sputtered ZnO films," Mater. Chem. Phys. (1996).
243. T. Minami, H. Sato, K. Ohashi, T. Tomofuji, and S. Takata, "Conduction mechanism of highly conductive and transparent zinc oxide thin films prepared by magnetron sputtering," J. Cryst. Growth (1992).
244. G. Baccarani, B. Riccò, and G. Spadini, "Transport properties of polycrystalline silicon films," J. Appl. Phys. (1978).
245. R. B. H. Tahar, T. Ban, Y. Ohya, and Y. Takahashi, "Optical, structural, and electrical properties of indium oxide thin films prepared by the sol-gel method," J. Appl. Phys. (1997).
246. Y. Shigesato and D. C. Paine, "Study of the effect of Sn doping on the electronic transport properties of thin film indium oxide," Appl. Phys. Lett. (1993).
247. J. W. Bae, S. D. Park, N. G. Cho, D. H. Lee, and G. Y. Yeom, "Effects of tin concentration on the electrical properties of room-temperature ion-beam-assisted-evaporation-deposited indium oxide thin films," Japanese J. Appl. Physics, Part 2 Lett. **41**(9 A/B), 6–9 (2002).
248. C. Kittel, "Introduction to Solid State Physics 8th ED," Solid-State Phys. (Fourth Extensively Updat. Enlarg. Ed. An Introd. to Princ. Mater. Sci. (2010).
249. S. A. Maier, *World Scientific Handbook of Metamaterials and Plasmonics* (World Scientific, 2017), **1**.

250. U. Guler, V. M. Shalaev, and A. Boltasseva, "Nanoparticle plasmonics: Going practical with transition metal nitrides," Mater. Today **18**(4), 227–237 (2015).
251. M. Henini, "Handbook of Thin-Film Deposition Processes and Techniques," Microelectronics J. (2000).
252. S. R. Thomas, P. Pattanasattayavong, and T. D. Anthopoulos, "Solution-processable metal oxide semiconductors for thin-film transistor applications," Chem. Soc. Rev. (2013).
253. S. Dellis, I. Isakov, N. Kalfagiannis, K. Tetzner, T. D. Anthopoulos, and D. C. Koutsogeorgis, "Rapid laser-induced photochemical conversion of sol-gel precursors to In2O3 layers and their application in thin-film transistors," J. Mater. Chem. C **5**(15), 3673–3677 (2017).
254. R. X. Wang, C. D. Beling, S. Fung, A. B. Djurišic, C. C. Ling, and S. Li, "Influence of gaseous annealing environment on the properties of indium-tin-oxide thin films," J. Appl. Phys. **97**(3), (2005).
255. M. Nakata, K. Takechi, T. Eguchi, E. Tokumitsu, H. Yamaguchi, and S. Kaneko, "Flexible high-performance amorphous InGaZnO4 thin-film transistors utilizing excimer laser annealing," Jpn. J. Appl. Phys. (2009).
256. W. Yang, Z. Liu, D. L. Peng, F. Zhang, H. Huang, Y. Xie, and Z. Wu, "Room-temperature deposition of transparent conducting Al-doped ZnO films by RF magnetron sputtering method," Appl. Surf. Sci. **255**(11), 5669–5673 (2009).
257. M. Nisha and M. K. Jayaraj, "Influence of RF power and fluorine doping on the properties of sputtered ITO thin films," Appl. Surf. Sci. **255**(5 PART 1), 1790–1795 (2008).
258. N. Akin, B. Kinaci, Y. Ozen, and S. Ozcelik, "Influence of RF power on the opto-electrical and structural properties of gallium-doped zinc oxide thin films," J. Mater. Sci. Mater. Electron. **28**(10), 7376–7384 (2017).
259. S. Swann, "Magnetron sputtering," Phys. Technol. **19**(2), 67–75 (1988).
260. K. S. Sree Harsha, *Principles of Vapor Deposition of Thin Films* (2006).
261. J. Ungula, B. F. Dejene, and H. C. Swart, "Effect of annealing on the structural, morphological and optical properties of Ga-doped ZnO nanoparticles by reflux precipitation method," Results Phys. **7**, 2022–2027 (2017).
262. C. S. Huang and C. C. Liu, "The optical and electrical properties of gallium-doped ZnO thin film with post-annealing processes of various atmospheres," Microelectron. Eng. **148**, 59–63 (2015).
263. Z. Xu, P. Chen, Z. Wu, F. Xu, G. Yang, B. Liu, C. Tan, L. Zhang, R. Zhang, and Y. Zheng, "Influence of thermal annealing on electrical and optical properties of indium tin oxide thin films," Mater. Sci. Semicond. Process. **26**(1), 588–592 (2014).
264. W. Yang, Z. Wu, Z. Liu, A. Pang, Y. L. Tu, and Z. C. Feng, "Room temperature deposition of Al-doped ZnO films on quartz substrates by radio-frequency magnetron sputtering and effects of thermal annealing," Thin Solid Films (2010).
265. R. H. Horng, S. L. Ou, C. Y. Huang, P. Ravadgar, and C. I. Wu, "Effects of Ga concentration and rapid thermal annealing on the structural, optoelectronic and photoluminescence properties of Ga-doped ZnO thin films," Thin Solid Films **605**, 30–36 (2016).
266. S. Cho, "Effects of rapid thermal annealing on the properties of In 2O3 thin films grown on glass substrate by rf reactive magnetron sputtering," Microelectron. Eng. **89**(1), 84–88 (2012).
267. L. Correra and L. Pedulli, "Incoherent-light-flash annealing of phosphorus-implanted silicon," Appl. Phys. Lett. (1980).
268. H. Pan, D. Lee, S. H. Ko, C. P. Grigoropoulos, H. K. Park, and T. Hoult, "Fiber laser annealing of indium-tin-oxide nanoparticles for large area transparent conductive layers and optical film characterization," Appl. Phys. A Mater. Sci. Process. (2011).
269. W. M. Cranton, S. L. Wilson, R. Ranson, D. C. Koutsogeorgis, K. Chi, R. Hedgley, J. Scott, S. Lipiec, A. Spiller, and S. Speakman, "Excimer laser processing of inkjet-printed and sputter-deposited transparent conducting SnO2:Sb for flexible electronics," Thin Solid Films **515**(24 SPEC. ISS.), 8534–8538 (2007).

270. M. Park, B. H. Chon, H. S. Kim, S. C. Jeoung, D. Kim, J. I. Lee, H. Y. Chu, and H. R. Kim, "Ultrafast laser ablation of indium tin oxide thin films for organic light-emitting diode application," Opt. Lasers Eng. (2006).
271. F. Rahman, "Zinc oxide light-emitting diodes: a review," Opt. Eng. (2019).
272. S. Acharya, S. Chouthe, H. Graener, T. Böntgen, C. Sturm, R. Schmidt-Grund, M. Grundmann, and G. Seifert, "Ultrafast dynamics of the dielectric functions of ZnO and BaTiO3 thin films after intense femtosecond laser excitation," J. Appl. Phys. (2014).
273. C. Hammond, *The Basics of Crystallography and Diffraction*, 2nd ed. (Oxford Univeristy Press, 2002).
274. M. Birkholz, *Thin Film Analysis by X-Ray Scattering* (Wiley, 2005).
275. D. L. L. Dorset, "X-ray Diffraction: A Practical Approach," Microsc. Microanal. **4**(5), 513–515 (1998).
276. B. D. Cullity and J. W. Weymouth, "Elements of X-Ray Diffraction," Am. J. Phys. (1957).
277. J. Als-Nielsen and D. McMorrow, *Elements of Modern X-ray Physics*, 2nd ed. (Wiley, 2011).
278. K. Ellmer, "Magnetron sputtering of transparent conductive zinc oxide: Relation between the sputtering parameters and the electronic properties," J. Phys. D. Appl. Phys. **33**(4), 17–32 (2000).
279. G. K. Williamson and W. H. Hall, "Discussion of the Theories of Line Broadening," Acta Metall. (1953).
280. U. Holzwarth and N. Gibson, "The Scherrer equation versus the "Debye-Scherrer equation,"" Nat. Nanotechnol. **6**(9), 534 (2011).
281. A. R. Stokes and A. J. C. Wilson, "The diffraction of x rays by distorted crystal aggregates - I," Proc. Phys. Soc. (1944).
282. B. W. Young and B. W. Young, "Biaxial Stress and Strain," in *Essential Solid Mechanics* (1976).
283. R. Cebulla, R. Wendt, and K. Ellmer, "Al-doped zinc oxide films deposited by simultaneous rf and dc excitation of a magnetron plasma: Relationships between plasma parameters and structural and electrical film properties," J. Appl. Phys. (1998).
284. T. H. de Keijser, J. I. Langford, E. J. Mittemeijer, and A. B. P. Vogels, "Use of the Voigt function in a single-line method for the analysis of X-ray diffraction line broadening," J. Appl. Crystallogr. (1982).
285. Y. Hu, X. Diao, C. Wang, W. Hao, and T. Wang, "Effects of heat treatment on properties of ITO films prepared by rf magnetron sputtering," Vacuum **75**(2), 183–188 (2004).
286. K. Zhang, F. Zhu, C. H. A. Huan, and A. T. S. Wee, "Indium tin oxide films prepared by radio frequency magnetron sputtering method at a low processing temperature," Thin Solid Films (2000).
287. K. Park, "Cross-Sectional TEM Specimen Preparation of Semiconductor Devices by Focused Ion Beam Etching," MRS Proc. (1990).
288. G. Friedbacher and H. Bubert, *Surface and Thin Film Analysis: A Compendium of Principles, Instrumentation, and Applications, Second Edition* (2011).
289. J. C. Vickerman and I. S. Gilmore, *Surface Analysis - The Principal Techniques: Second Edition* (2009).
290. J. F. Watts and J. Wolstenholme, *An Introduction to Surface Analysis by XPS and AES* (2019).
291. H. Bubert, J. C. Rivière, and W. S. M. Werner, "X-Ray Photoelectron Spectroscopy (XPS)," in *Surface and Thin Film Analysis: A Compendium of Principles, Instrumentation, and Applications, Second Edition* (2011).
292. P. Patsalas, M. Handrea, S. Logothetidis, M. Gioti, S. Kennou, and W. Kautek, "A complementary study of bonding and electronic structure of amorphous carbon films by electron spectroscopy and optical techniques," Diam. Relat. Mater. (2001).
293. V. Jain, M. C. Biesinger, and M. R. Linford, "The Gaussian-Lorentzian Sum, Product, and

Convolution (Voigt) functions in the context of peak fitting X-ray photoelectron spectroscopy (XPS) narrow scans," Appl. Surf. Sci. (2018).
294. F. M. Smits, "Measurement of Sheet Resistivities with the Four-Point Probe," Bell Syst. Tech. J. (1958).
295. L. J. van der Pauw, "A method of measuring specific resistivity and Hall effect of discs of arbitrary shapes," Philips Res. Rep. (1958).
296. M. Born, E. Wolf, and E. Hecht, " Principles of Optics: Electromagnetic Theory of Propagation, Interference and Diffraction of Light ," Phys. Today (2000).
297. H. Fujiwara, *Spectroscopic Ellipsometry* (John Wiley & Sons, Ltd, 2007).
298. H. Wöhler, G. Haas, M. Fritsch, and D. A. Mlynski, "Faster 4 × 4 matrix method for uniaxial inhomogeneous media," J. Opt. Soc. Am. A **5**(9), 1554 (1988).
299. O. S. Heavens, "Optical properties of thin films," Rep. Prog. Phys. (1960).
300. H. P. Gavin, "The Levenburg-Marqurdt Algorithm For Nonlinear Least Squares Curve-Fitting Problems," Duke Univ. (2019).
301. C. M. Herzinger, B. Johs, W. A. McGahan, J. A. Woollam, and W. Paulson, "Ellipsometric determination of optical constants for silicon and thermally grown silicon dioxide via a multi-sample, multi-wavelength, multi-angle investigation," J. Appl. Phys. **83**(6), 3323–3336 (1998).
302. D. De Sousa Meneses, M. Malki, and P. Echegut, "Structure and lattice dynamics of binary lead silicate glasses investigated by infrared spectroscopy," J. Non. Cryst. Solids **352**(8), 769–776 (2006).
303. B. D. Johs, W. A. McGahan, and J. A. Woollam, "Optical analysis of complex multilayer structures using multiple data types," Thin Solid Films (1994).
304. R. A. Synowicki, "Suppression of backside reflections from transparent substrates," in *Physica Status Solidi (C) Current Topics in Solid State Physics* (2008).
305. G. E. Jellison and F. A. Modine, "Parameterization of the optical functions of amorphous materials in the interband region," Appl. Phys. Lett. **69**(3), 371–373 (1996).
306. P. Uprety, M. M. Junda, K. Ghimire, D. Adhikari, C. R. Grice, and N. J. Podraza, "Spectroscopic ellipsometry determination of optical and electrical properties of aluminum doped zinc oxide," Appl. Surf. Sci. **421**, 852–858 (2017).
307. D. Panti, "Handbook on semiconductors," Microelectronics J. **29**(11), 940 (1998).
308. W. Hume-Rothery and H. M. Powell, "On the Theory of Super-Lattice Structures in Alloys," Zeitschrift für Krist. - Cryst. Mater. (2014).
309. S. H. Jeong, B. N. Park, S. B. Lee, and J. H. Boo, "Metal-doped ZnO thin films: Synthesis and characterizations," Surf. Coatings Technol. (2007).
310. Y. Shigesato, Y. Hayashi, and T. Haranoh, "Doping mechanisms of tin-doped indium oxide films," Appl. Phys. Lett. (1992).
311. H. Köstlin, R. Jost, and W. Lems, "Optical and electrical properties of doped In2O3 films," Phys. status solidi **29**(1), 87–93 (1975).
312. H. Kim, C. M. Gilmore, A. Piqué, J. S. Horwitz, H. Mattoussi, H. Murata, Z. H. Kafafi, and D. B. Chrisey, "Electrical, optical, and structural properties of indium-tin-oxide thin films for organic light-emitting devices," J. Appl. Phys. **86**(11), 6451–6461 (1999).
313. T. Minami, "Present status of transparent conducting oxide thin-film development for Indium-Tin-Oxide (ITO) substitutes," Thin Solid Films (2008).
314. O. Gürbüz, I. Kurt, S. Çalişkan, and S. Güner, "Influence of Al concentration and annealing temperature on structural, optical, and electrical properties of Al co-doped ZnO thin films," Appl. Surf. Sci. **349**, 549–560 (2015).
315. V. Bhosle, A. Tiwari, and J. Narayan, "Electrical properties of transparent and conducting Ga doped ZnO," J. Appl. Phys. **100**(3), (2006).
316. K. M. Sandeep, S. Bhat, S. M. Dharmaprakash, and K. Byrappa, "Influence of Ga doping ratio on the saturable absorption mechanism in Ga doped ZnO thin solid films processed

by sol-gel spin coating technique," J. Phys. D. Appl. Phys. **50**(9), (2017).

317. K. H. Patel and S. K. Rawal, "Influence of power and temperature on properties of sputtered AZO films," Thin Solid Films **620**, 182–187 (2016).
318. S. Rahmane, M. A. Djouadi, M. S. Aida, N. Barreau, B. Abdallah, and N. Hadj Zoubir, "Power and pressure effects upon magnetron sputtered aluminum doped ZnO films properties," Thin Solid Films (2010).
319. R. Kitamura, L. Pilon, and M. Jonasz, "Optical constants of silica glass from extreme ultraviolet to far infrared at near room temperature," Appl. Opt. (2007).
320. H. Han, Y. Zoo, S. K. Bhagat, J. S. Lewis, and T. L. Alford, "Influence of defects and processing parameters on the properties of indium tin oxide films on polyethylene napthalate substrate," J. Appl. Phys. **102**(6), (2007).
321. C. Guillén and J. Herrero, "Influence of oxygen in the deposition and annealing atmosphere on the characteristics of ITO thin films prepared by sputtering at room temperature," Vacuum **80**(6), 615–620 (2006).
322. S. Elhalawaty, K. Sivaramakrishnan, N. D. Theodore, and T. L. Alford, "The effect of sputtering pressure on electrical, optical and structure properties of indium tin oxide on glass," Thin Solid Films (2010).
323. D. M. Mattox, "Particle bombardment effects on thin-film deposition: A review," J. Vac. Sci. Technol. A Vacuum, Surfaces, Film. (1989).
324. J. Gwamuri, M. Marikkannan, J. Mayandi, P. K. Bowen, and J. M. Pearce, "Influence of oxygen concentration on the performance of ultra-thin RF magnetron sputter deposited indium tin oxide films as a top electrode for photovoltaic devices," Materials (Basel). (2016).
325. Y. Matsuda, Y. Yamori, M. Muta, S. Ohgushi, and H. Fujiyama, "Relation between plasma parameters and film properties in DC reactive magnetron sputtering of indium-tin-oxide," Japanese J. Appl. Physics, Part 1 Regul. Pap. Short Notes Rev. Pap. **36**(7 SUPPL. B), 4922–4927 (1997).
326. C. Charpentier, "Investigation of deposition conditions and annealing treatments on sputtered ZnO:Al thin films: Material properties and application to microcristalline silicon solar cells," Ecole Polytechnique X (2012).
327. F. Greuter and G. Blatter, "Electrical properties of grain boundaries in polycrystalline compound semiconductors," Semicond. Sci. Technol. (1990).
328. A. Spadoni and M. L. Addonizio, "Effect of the RF sputtering power on microstructural, optical and electrical properties of Al doped ZnO thin films," Thin Solid Films (2015).
329. P. Patsalas, N. Kalfagiannis, S. Kassavetis, G. Abadias, D. V. Bellas, C. Lekka, and E. Lidorikis, "Conductive nitrides: Growth principles, optical and electronic properties, and their perspectives in photonics and plasmonics," Mater. Sci. Eng. R Reports **123**, 1–55 (2018).
330. K. H. Ri, Y. Wang, W. L. Zhou, J. X. Gao, X. J. Wang, and J. Yu, "The structural properties of Al doped ZnO films depending on the thickness and their effect on the electrical properties," Appl. Surf. Sci. **258**(4), 1283–1289 (2011).
331. J. Meija, T. B. Coplen, M. Berglund, W. A. Brand, P. De Bièvre, M. Gröning, N. E. Holden, J. Irrgeher, R. D. Loss, T. Walczyk, and T. Prohaska, "Atomic weights of the elements 2013 (IUPAC Technical Report)," Pure Appl. Chem. (2016).
332. R. W. Balluffi, S. M. Allen, and W. C. Carter, *Kinetics of Materials* (John Wiley & Sons, Inc., 2005).
333. W. J. Heward and D. J. Swenson, "Phase equilibria in the pseudo-binary In2O3-SnO 2 system," J. Mater. Sci. **42**(17), 7135–7140 (2007).
334. F. Mei, T. Yuan, and R. Li, "Effects of second-phase particles and elemental distributions of ITO targets on the properties of deposited ITO films," Ceram. Int. **43**(12), 8866–8872 (2017).
335. F. Mei, T. Yuan, R. Li, K. Qin, and J. Huang, "Microstructure evolution and grain orientation

in ITO targets and their effects on the film characteristics," J. Mater. Sci. Mater. Electron. **29**(17), 14620–14634 (2018).

336. H. Fritzsche, B. Pashmakov, and B. Claflin, "Reversible changes of the optical and electrical properties of amorphous InOx by photoreduction and oxidation," Sol. Energy Mater. Sol. Cells **32**(4), 383–393 (1994).
337. P. Thilakan and J. Kumar, "Investigations on the annealing effects on reactively deposited ITO thin films," Phys. Status Solidi Appl. Res. **160**(1), 97–104 (1997).
338. A. Walsh and D. O. Scanlon, "Polymorphism of indium oxide: Materials physics of orthorhombic In 2O3," Phys. Rev. B - Condens. Matter Mater. Phys. **88**(16), 1–4 (2013).
339. A. Bouhdjer, H. Saidi, A. Attaf, A. Yahia, M. S. Aida, O. Benkhetta, and L. Bouhdjer, "Effects of lattice mismatches in In2O3 / substrate structures on the structural, morphological and electrical properties of In2O3 films," **20**(May), (2020).
340. F. Wang, M. Z. Wu, Y. Y. Wang, Y. M. Yu, X. M. Wu, and L. J. Zhuge, "Influence of thickness and annealing temperature on the electrical, optical and structural properties of AZO thin films," in *Vacuum* (2013), **89**(1), pp. 127–131.
341. H. Mahdhi, J. L. Gauffier, K. Djessas, and Z. Ben Ayadi, "Thickness dependence of properties Ga-doped ZnO thin films deposited by magnetron sputtering," J. Mater. Sci. Mater. Electron. **28**(6), 5021–5028 (2017).
342. J. A. Hillier, S. Camelio, W. Cranton, A. V. Nabok, C. J. Mellor, D. C. Koutsogeorgis, and N. Kalfagiannis, "When ellipsometry works best: A case study with transparent conductive oxides," ACS Photonics **7**(10), 2692–2702 (2020).
343. K. Ellmer and R. Mientus, "Carrier transport in polycrystalline transparent conductive oxides: A comparative study of zinc oxide and indium oxide," Thin Solid Films **516**(14), 4620–4627 (2008).
344. M. V. Frischbier, H. F. Wardenga, M. Weidner, O. Bierwagen, J. Jia, Y. Shigesato, and A. Klein, "Influence of dopant species and concentration on grain boundary scattering in degenerately doped In2O3 thin films," Thin Solid Films **614**, 62–68 (2016).
345. C. F. Bohren, "What did Kramers and Kronig do and how did they do it?," Eur. J. Phys. (2010).
346. A. B. Kuzmenko, "Kramers-Kronig constrained variational analysis of optical spectra," Rev. Sci. Instrum. (2005).
347. A. Manjavacas, J. G. Liu, V. Kulkarni, and P. Nordlander, "Plasmon-induced hot carriers in metallic nanoparticles," ACS Nano **8**(8), 7630–7638 (2014).
348. S. Xiao, V. P. Drachev, A. V. Kildishev, X. Ni, U. K. Chettiar, H. K. Yuan, and V. M. Shalaev, "Loss-free and active optical negative-index metamaterials," Nature **466**(7307), 735–738 (2010).
349. A. Lalisse, G. Tessier, J. Plain, and G. Baffou, "Quantifying the Efficiency of Plasmonic Materials for Near-Field Enhancement and Photothermal Conversion," J. Phys. Chem. C **119**(45), 25518–25528 (2015).
350. B. Doiron, M. Mota, M. P. Wells, R. Bower, A. Mihai, Y. Li, L. F. Cohen, N. M. N. Alford, P. K. Petrov, R. F. Oulton, and S. A. Maier, "Quantifying Figures of Merit for Localized Surface Plasmon Resonance Applications: A Materials Survey," ACS Photonics **6**(2), 240–259 (2019).
351. J. A. Lock and G. Gouesbet, "Generalized Lorenz-Mie theory and applications," J. Quant. Spectrosc. Radiat. Transf. **110**(11), 800–807 (2009).
352. G. Gonçalves, E. Elangovan, P. Barquinha, L. Pereira, R. Martins, and E. Fortunato, "Influence of post-annealing temperature on the properties exhibited by ITO, IZO and GZO thin films," Thin Solid Films **515**(24 SPEC. ISS.), 8562–8566 (2007).
353. J. A. W. Co., "CompleteEASE ^{TM} Data Analysis Manual," misc (2008).
354. P. Uprety, M. M. Junda, H. Salmon, and N. J. Podraza, "Understanding near infrared absorption in tin doped indium oxide thin films," J. Phys. D. Appl. Phys. **51**(29), (2018).
355. I. Hamberg and C. G. Granqvist, "Dielectric function of “undoped” In2O3," Thin Solid Films

105(2), (1983).
356. Y. Huang, M. Liu, Z. Li, Y. Zeng, and S. Liu, "Raman spectroscopy study of ZnO-based ceramic films fabricated by novel sol-gel process," Mater. Sci. Eng. B Solid-State Mater. Adv. Technol. **97**(2), 111–116 (2003).
357. C. Bundesmann, N. Ashkenov, M. Schubert, D. Spemann, T. Butz, E. M. Kaidashev, M. Lorenz, and M. Grundmann, "Raman scattering in ZnO thin films doped with Fe, Sb, Al, Ga, and Li," Appl. Phys. Lett. **83**(10), 1974–1976 (2003).
358. N. Ashkenov, B. N. Mbenkum, C. Bundesmann, V. Riede, M. Lorenz, D. Spemann, E. M. Kaidashev, A. Kasic, M. Schubert, M. Grundmann, G. Wagner, H. Neumann, V. Darakchieva, H. Arwin, and B. Monemar, "Infrared dielectric functions and phonon modes of high-quality ZnO films," J. Appl. Phys. **93**(1), 126–133 (2003).
359. H. Zheng, R. J. Zhang, D. H. Li, X. Chen, S. Y. Wang, Y. X. Zheng, M. J. Li, Z. G. Hu, N. Dai, and L. Y. Chen, "Optical Properties of Al-Doped ZnO Films in the Infrared Region and Their Absorption Applications," Nanoscale Res. Lett. **13**, (2018).
360. K. von Rottkay, M. Rubin, and N. Ozer, "Optical indices of tin-doped indium oxide and tungsten oxide electrochromic coatings," in *Materials Research Society Symposium - Proceedings* (1996), **403**, pp. 551–556.
361. X. Liu, J. Park, J. H. Kang, H. Yuan, Y. Cui, H. Y. Hwang, and M. L. Brongersma, "Quantification and impact of nonparabolicity of the conduction band of indium tin oxide on its plasmonic properties," Appl. Phys. Lett. **105**(18), (2014).
362. V. Romanyuk, N. Dmitruk, V. Karpyna, G. Lashkarev, V. Popovych, M. Dranchuk, R. Pietruszka, M. Godlewski, G. Dovbeshko, I. Timofeeva, O. Kondratenko, M. Taborska, and A. Ievtushenko, "Optical and electrical properties of highly doped ZnO:Al films deposited by atomic layer deposition on Si substrates in visible and near infrared region," Acta Phys. Pol. A **129**(1), A36–A40 (2016).
363. Y. Wang, W. Tang, J. Liu, and L. Zhang, "Stress-induced anomalous shift of optical band gap in Ga-doped ZnO thin films: Experimental and first-principles study," Appl. Phys. Lett. **106**(16), (2015).
364. H. J. Kim, M. J. Maeng, J. H. Park, M. G. Kang, C. Y. Kang, Y. Park, and Y. J. Chang, "Chemical and structural analysis of low-temperature excimer-laser annealing in indium-tin oxide sol-gel films," Curr. Appl. Phys. **19**(2), 168–173 (2019).
365. A. Siozios, N. Kalfagiannis, D. V. Bellas, C. Bazioti, G. P. Dimitrakopulos, G. Vourlias, W. M. Cranton, E. Lidorikis, D. C. Koutsogeorgis, and P. Patsalas, "Sub-surface laser nanostructuring in stratified metal/dielectric media: A versatile platform towards flexible, durable and large-scale plasmonic writing," Nanotechnology (2015).
366. C. J. Powell, "Elemental binding energies for X-ray photoelectron spectroscopy," Appl. Surf. Sci. (1995).
367. J. H. Park, C. Buurma, S. Sivananthan, R. Kodama, W. Gao, and T. A. Gessert, "The effect of post-annealing on Indium Tin Oxide thin films by magnetron sputtering method," Appl. Surf. Sci. **307**, 388–392 (2014).
368. M. H. Rein, M. V. Hohmann, A. Thøgersen, J. Mayandi, A. O. Holt, A. Klein, and E. V. Monakhov, "An in situ x-ray photoelectron spectroscopy study of the initial stages of rf magnetron sputter deposition of indium tin oxide on p-type Si substrate," Appl. Phys. Lett. (2013).
369. D. Mergel, M. Schenkel, M. Ghebre, and M. Sulkowski, "Structural and electrical properties of In2O3:Sn films prepared by radio-frequency sputtering," Thin Solid Films **392**(1), 91–97 (2001).
370. J. S. Kim, P. K. H. Ho, D. S. Thomas, R. H. Friend, F. Cacialli, G. W. Bao, and S. F. Y. Li, "X-ray photoelectron spectroscopy of surface-treated indium-tin oxide thin films," Chem. Phys. Lett. **315**(5–6), 307–312 (1999).
371. C. D. Wagner, "Sensitivity factors for XPS analysis of surface atoms," J. Electron Spectros. Relat. Phenomena (1983).

372. C. J. Powell, "Recommended Auger parameters for 42 elemental solids," J. Electron Spectros. Relat. Phenomena (2012).
373. C. J. Powell and A. Jablonski, "Progress in quantitative surface analysis by X-ray photoelectron spectroscopy: Current status and perspectives," J. Electron Spectros. Relat. Phenomena (2010).
374. T. Koida and M. Kondo, "High electron mobility of indium oxide grown on yttria-stabilized zirconia," J. Appl. Phys. **99**(12), 1–7 (2006).
375. J. I. Gersten and W. S. Frederick, *The Physics and Chemistry of Materials* (John Wiley & Sons, 2001).
376. H. Hosono, N. Kikuchi, N. Ueda, and H. Kawazoe, "Working hypothesis to explore novel wide band gap electrically conducting amorphous oxides and examples," J. Non. Cryst. Solids (1996).
377. Y. Kudo, K. Kawabata, and H. Goto, "A possibility for generation of two species of charge carriers along main-chain and side-chains for a π-conjugated polymer," in *Journal of Physics: Conference Series* (2013).
378. E. Valcheva, B. Arnaudov, S. Evtimova, B. Monemar, T. Paskova, and M. Heuken, "Multilayer model for Hall effect data analysis of semiconductor structures with step-changed conductivity," Phys. Rev. B - Condens. Matter Mater. Phys. (2003).
379. S. Kim and Y. K. Choi, "Resistive switching of aluminum oxide for flexible memory," Appl. Phys. Lett. **92**(22), (2008).
380. N. Gergel-Hackett, B. Hamadani, B. Dunlap, J. Suehle, C. Richter, C. Hacker, and D. Gundlach, "A flexible solution-processed memristor," IEEE Electron Device Lett. **30**(7), 706–708 (2009).
381. Q. Nian, M. Y. Zhang, B. D. Schwartz, and G. J. Cheng, "Ultraviolet laser crystallized ZnO:Al films on sapphire with high Hall mobility for simultaneous enhancement of conductivity and transparency," Appl. Phys. Lett. (2014).
382. C. Charpentier, R. Boukhicha, P. Prod'Homme, T. Emeraud, J. F. Lerat, P. R. I. Cabarrocas, and E. V. Johnson, "Evolution in morphological, optical, and electronic properties of ZnO:Al thin films undergoing a laser annealing and etching process," Sol. Energy Mater. Sol. Cells **125**, 223–232 (2014).
383. G. Ndong, A. Lizana, E. Garcia-Caurel, V. Paret, G. Melizzi, D. Cattelan, B. Pelissier, and J.-H. Tortai, "Use of optical spacers to enhance infrared Mueller ellipsometry sensitivity: application to the characterization of organic thin films," Appl. Opt. **55**(12), 3323 (2016).
384. J. B. Khurgin, "Relative merits of phononics vs. plasmonics: The energy balance approach," Nanophotonics **7**(1), 305–316 (2018).
385. N. Kalfagiannis, J. L. Stoner, J. Hillier, I. Vangelidis, and E. Lidorikis, "Mid- to far-infrared sensing: SrTiO3, a novel optical material," J. Mater. Chem. C **7**(26), 7851–7857 (2019).
386. V. Sharma, S. Singh, K. Asokan, and K. Sachdev, "A study on 100 MeV O7+ irradiated SnO2/Ag/SnO2 multilayer as transparent electrode for flat panel display application," Nucl. Instruments Methods Phys. Res. Sect. B Beam Interact. with Mater. Atoms **379**, 141–145 (2016).
387. H. Kim, M. Osofsky, S. M. Prokes, O. J. Glembocki, and A. Piqué, "Optimization of Al-doped ZnO films for low loss plasmonic materials at telecommunication wavelengths," Appl. Phys. Lett. **102**(17), 1–5 (2013).